Homogeneous catalysts for the ROCOP of CO_2 and epoxides

Natalia Vieira Reis



The Queen's College

Department of Inorganic Chemistry

University of Oxford

September 2020

A thesis submitted in partial fulfilment of the requirements for the degree of Doctor of Philosophy in Chemistry

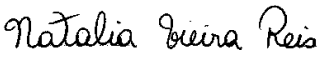
For my family and friends

"Putting your goal into words is
the first step towards realizing
one's dreams".
Naruto Shippuden

Declaration

The work presented in this thesis was conducted at the University of Oxford. This is the work of the author unless otherwise stated.

The copyright of this thesis rests with the author and is made available under a Creative Commons Attribution Non-Commercial no Derivatives licence. Researches are free to copy, distribute or transmit the thesis on the condition that they attribute it, that they do not use it for commercial purposes and that they do not alter, transform or build-upon it. For any reuse or distribution, researchers must make clear to others the licence terms of this work.



Natalia Vieira Reis

Abstract

The ring-opening copolymerisation of carbon dioxide and epoxides, yielding aliphatic polycarbonates, is a useful means to valorise waste gas and to reduce pollution in polymer manufacturing. Key to the success of this polymerization is the catalyst controlling both rate and selectivity. This thesis details the synthesis, characterisation and application of various inorganic complexes as homogeneous catalysts for these copolymerisations. Two different classes of catalysts are examined: (1) Heterodinuclear complexes, combining Mg(II) and various first-row transition metal(II) elements, are investigated to understand the potential for bimetallic synergy. Overall, the thesis provides insight into catalyst mechanisms and future design options. (2) Mononuclear indium(III) complexes.

Chapter 1 contains a literature review of existing catalysts and mechanisms. It ends with an overview of the thesis aims and rationale for the selection of the catalysts.

Chapter 2 provides an overview of selected material characterisation methods relevant to both the inorganic catalysts and the polymerisation catalysis.

Chapter 3 compares catalysis using a series of heterodinuclear complexes of the form MgM where M = Mg(II), Cr(II), Mn(II), Fe(II), Co(II), Ni(II), Cu(II) and Zn(II). The most active catalysts are MgFe or MgCo – both show very high activity and selectivity for cyclohexene oxide / carbon dioxide ROCOP. The catalysts are also active using vinyl cyclohexene oxide, cyclopentene oxide and 3,4-epoxytetrahydrofuran/CO_2 and for norbornene anhydride/CHO.

Chapter 4 describes the synthesis and characterisation of a series of salen and salan In(III) catalysts. The influence of electron donation of both the imine backbone (C=N,

C–N and C–NMe) and *para*-phenolate position (^{t}Bu, OMe and Me) upon the catalysis are compared. The optimum catalysis conditions are under 40 bar carbon dioxide pressure and with a PPNCl cocatalyst.

Chapter 5 provides and overall conclusion and outlook to the research presented in this thesis.

Chapter 6 describes the experimental methods and techniques used in this thesis.

Acknowledgments

I would like to thank Prof. Charlotte Williams and Prof. Philip Mountford for giving me the opportunity to work in their groups, thank you both for the guidance and support. I also want to express my gratitude to Manuja for all her help with academic bureaucracy.

I would like to thank the Williams group, both past and present, for all your help, guidance and for making work an enjoyable place: Leti, Sumesh, Duncan, Patrick, Ryan, Andy, Tim, Chris, Alice, Arron, Lisa, Wilf, Greg, Gloria, Joost, Sebastian, Wouter, Said, Georgina, Peck, Alex, Holly, Jamie, Emma, Nathan and Tom. A special thanks to Lisa, Wouter and Ryan for all help and chats. I would also like to thank my friends from Mountford group for all the support and good time: Peace, Archie, David, Martin, Simona, Helen, Insun, Bowen, Adan, Karen, Ben and Theresa.

To all my friends that I had the opportunity to meet in Oxford throughout the years, I am really thankful to all you for making my time here memorable: Ari, Rosi, Rafa, Vinicius, Barbara, Luana, Mari, Eduardo, Rafael, Darlan, Lívia, Luci, Henrique, William, Vanessa, Pri, Sargento, Tulio, Marcela, Tim, Jost, Alex, Suelen, Sergio, Isa, Ana, Carol, Adir and Luiza.

The final part of my acknowledgments will be dedicated to my family and friends in Brazil and it will be written in Portuguese.

Primeiramente gostaria de agradecer aos meus pais e minha irmã por todo apoio e por sempre acreditarem e confiarem em mim, devo o que tenho e o que sou ao que vocês me ensinaram. Gostaria também de agradecer ao Mario e ao Lourenço (meu sobrinho e afilhado) que nasceu durante o meu doutorado e veio me visitar antes mesmo de

nascer, espero que um dia você possa entender porque a maioria das nossas fotos foram por Skype. Também agradeço a toda a minha família que sempre estão ao meu lado e me motivam a seguir em frente e claro, ao Spock!

Gostaria de agradecer aos meus amigos que deixei no Brasil mas que de alguma forma estão sempre ao meu lado, especialmente um certo disco voador! São amigos de longa data que gostaria de expressar a minha gratidão por todo apoio: Vitor, Polly, Taniris, Alexandre, Cris, Raphael, Wdeson, Tat, Raoni, Ana, Ingrid, Ivo, Fernanda, Nat Moreira (obrigada por me permitir ser sua madrinha de casamento mesmo por Skype!), Nat Tavares, Nat Pinheiro, Wally, William e Camila Van.

Abbreviations

ATR-IR	Attenuated Total Reflectance Infrared
BDI	β-Diiminate
BDE	Bond dissociation enthalpy
DMF	Dimethylformamide
Boc	*Tert*-Butyloxycarbonyl
C	Currie constant
Conv.	Conversion
χ	Magnetic Susceptibility
χ_m	Molar Magnetic Susceptibility
Cat	Catalyst
CHD	Cyclohexene-1,2-diol
CHO	Cyclohexene Oxide
CPO	Cyclopentene Oxide
CTA	Chain Transfer Agent
CV	Cyclic Voltammetry
D	Diffusion Coefficient
Đ	Dispersity
DCM	Dichloromethane
DMAP	4-dimethylaminopyridine
DOSY	Diffusion Ordered NMR Spectroscopy
emu	Electromagnetic unit
equiv.	Equivalent
ETHF	3,4-Epoxytetrahydrofuran

Fc	Ferrocene
GPC	Gel Permeation Chromatography
IR	Infrared
k_{obs}	Observed Rate Constant
L	Ligand
M	Metal centre
M	mol L^{-1}
M_n	Number of average molar mass
μ_B	Bohr magneton
μ_{eff}	Effective magnetic moment
MALDI	Matrix Assisted Lased Desorption Ionisation
Me	Methyl
MeOH	Methanol
M_w	Mass average molar mass
n	Number of unpaired electrons
N-MeIm	*N*-methylimidazole
NA	Norbornene Anhydride
NMR	Nuclear Magnetic Resonance
OAc	Acetate
PCHC	Poly(cyclohexene carbonate)
PO	Propylene Oxide
PPNCl	Bis(triphenylphosphoranylidene)ammonium chloride
ROCOP	Ring Opening Copolymerisation
S.D.	Standard deviation

S.E.	Standard error
SEC	Size Exclusion Chromatography
SO	Spin-only
SQUID	Superconducting Quantum Interference Device
θ	Curie-Weiss constant
τ	Structural parameter
^{t}Bu	*Tert*-Butyl
THF	Tetrahydrofuran
TM	Transition metal
ToF	Time of Flight
TOF	Turn Over Frequency
TON	Turn Over Number
vCHO	4-Vinyl-1-Cyclohexene-1,2-Epoxide
WERC	Water exchange rate constant
X	Co-ligand

List of Figures, Schemes and Tables

Chapter 1: Introduction

Figure 1.1. a) Distribution of European plastic converters demand by segment in 2018; b) Plastic relative demand by type in Europe.

Figure 1.2. Ring-opening copolymerisation of epoxide (PO and CHO) and CO_2.

Figure 1.3. Initiation step for CO_2/CHO ROCOP and PCHC formation during propagation step for a ROCOP of CHO and CO_2 with excess of epoxide. Growing chain denoted as 'R'.

Figure 1.4. Possible side reactions during the propagation step of ROCOP CO_2/CHO. Formation of *cis* and *trans* cyclic product and polyether.

Figure 1.5. a) Aluminium tetraphenyl-porphyrin. b) Zinc bis(phenoxide).

Figure 1.6. Three main families of catalysts discussed in this chapter. Figure adapted from Williams et al.

Figure 1.7. Examples of bifunctional/two components catalysts reported in the literature by Darenbourg; Lu and Coates with co-workers with bis(salicylaldimine) and cocatalysts. DMAP (4-dimethyl(amino)pyridine); N-MeIm (N-methylimidazole) and PPNCl (Bis(triphenylphosphoranylidene)ammonium chloride).

Figure 1.8. (salan)Cr(III)Cl catalysts developed by Darensbourg and co-workers.

Figure 1.9. Figure adapted from Darensbourg et al, showing the *cis*-coordination conformation adopted by the salan-Cr catalyst.

Figure 1.10. Epoxide ring-opening step at the bimetallic mechanism. Nu = anionic co-catalyst or growing carbonate polymer chain.

Figure 1.11. Epoxide ring-opening step at the bicomponent mechanism. Nu = anionic co-catalyst or carbonate polymer chain.

Figure 1.12. Two-component single catalyst with a derivative from (salcy)–Co with piperidinium 'arm'.

Figure 1.13. Examples of catalysts with two ammonium groups and (salen)Co reported in the literature.

Figure 1.14. Al(III)porphyrin with quaternary ammonium halide as tethered co-catalyst.

Figure 1.15. Representation of a) bifunctional catalyst; b) binary catalyst. Figure adapted from Ema et al.

Figure 1.16. Zinc β-diiminate (BDI) catalyst.

Figure 1.17. Representation of dinuclear catalysts: Singe ligand, dimeric and tethered catalysts. Figure adapted from Williams et al.

Figure 1.18. Dinuclear catalysts reported in the literature.

Figure 1.19. Range of single ligand bimetallic catalysts developed by Lee and co-workers. a) Di-zinc with acyclic bis(anilido-aldimine); b) Di-zinc macrocycle with bis(anilido-aldimine).

Figure 1.20. Dinuclear catalysts macrocycle explored for ROCOP of CO_2 and epoxide.

Figure 1.21. Heterometallic catalyst with a macrocyclic tris(salen)-based ligand with three Zn(II) and a Ln(III).

Figure 1.22. a) Tetranuclear with tris(N_2O_2) hexaoxime macrocycle. b) (salen)Co(II) mononuclear catalyst.

Figure 1.23. Examples of selected other dimeric catalysts reported in the literature.

Figure 1.24. Examples of tethered catalysts with different bridges flexibility.

Figure 1.25. Examples of tethered catalysts with different linker lengths.

Figure 1.26. Chain-shuttling mechanism. The ligand scaffold is depicted as a curve line and the growing chain denoted as 'R'. Figure adapted from Williams et al.

Figure 1.27. Systems explored in this thesis.

Chapter 2: Methodology

Figure 2.1. Diamagnetic correction calculated for a Mg(II)Mn(II) macrocycle. The values for the Pascal's constants for the diamagnetic susceptibility for each atom were taken from Gordon A. Bain et al.

Figure 2.2. Representation of χ^{-1} *vs.* T and μ_{eff} *vs.* T graphs and large domains of magnetic dipoles for paramagnetic, ferromagnetic and antiferromagnetic materials.

Figure 2.3. Example of magnetic susceptibility experiment for a Mg(II)Mn(II) macrocycle system. a) Inverse of molar susceptibility *vs*. temperature. ∘ experimental data, – fitting of the curve. b) Effective magnetic moment *vs.* temperature calculated from susceptibility experiment.

Table 2.1. Theoretical values obtained using spin-only equation for different oxidation states of manganese.

Figure 2.4. a) Representation of the three electrodes in a cell for cyclic voltammetry. b) Generic voltammogram experiments with formal potential ($E_{1/2}$), peak cathodic and anodic currents ($i_{p,c}$,$i_{p,a}$) and

potential for oxidation and reduction. Figures adapted from Dempsey et al. and Skoog (*Principles of Instrumental Analysis*).

Figure 2.5. Example of cyclic voltammogram calibration with ferrocene. a) Cyclic voltammogram before calibration. b) Cyclic voltammogram with the Fc^+/Fc signal. c) Cyclic voltammogram after calibration.

Figure 2.6. a) Illustration of a ATR set up with a representation of the evanescent wave (Figure adapted from literature). b) Representation of a ReactIR equipment with a probe for *in situ* IR studies. c) Example of a 3D graph obtained in the experiment.

Figure 2.7. a) Example of absorbance vs. time plot for PCHC (every 10^{th} point displayed). b) Normalised conversion vs. time plot for PHCH (every 10^{th} point displayed), total conversion of 55 % calculated by ^1H NMR.

Figure 2.8. Example of logarithm of epoxide concentration vs. time plot and k_{obs} obtained from the linear fit of the curve.

Chapter 3: Heterodinuclear Catalysts for the Ring-Opening Copolymerisation of CO_2/Epoxide

Figure 3.1. Chapter 3 summary.

Scheme 3.1. Synthesis of complex **1**. I) $ZnEt_2$, THF, RT, 16 h; II) $MgBr_2$, THF, –78 °C → RT, 1 h; III) KOAc, THF, RT, 16h.

Scheme 3.2. Synthesis of di-magnesium complex **2** and heterodinuclear catalysts **3–8**. i) $Mg(N(SiMe_3)_2)_2$, $M(OAc)_2$, THF, 100 °C, 16 h.*MgCr complex were synthesised at room temperature, 72 h, due to decomposition.

Figure 3.2. Cyclic voltammograms of complexes **2**, **7** and **8** showing only oxidations of the ligand phenolate to phenoxyl radicals.

Figure 3.3. Cyclic voltammograms for complexes **3–6**, performed in THF.

Table 3.1. Redox values of the complexes **3–6**.

Figure 3.4. Inverse of molar susceptibility *vs*. temperature for MgFe complex **5**.

Table 3.2. Values of Curie constant (C) and Curie-Weiss constant (θ) for complexes **3–8.**

Figure 3.5. Effective magnetic moment *vs.* temperature graph for complex **5**.

Table 3.3. Theoretical and experimental values obtained for magnetic susceptibility for complexes **3–8** and some values reported in the literature for the same metal centres in different complex environment.

Figure 3.6. a) Molecular structures of the complex MgFe (**5**) represented as ball & stick to clarify due to disorder. (b) Representation of acetate bridging two macrocycles. (c) Angle between the planes from different macrocycle. H-atoms and crystallisation solvent (toluene) were omitted to clarify.

Figure 3.7. a) Molecular structures of the complex MgNi (**7**) (b) Representation of acetate bridging two macrocycles. (c) Angle between the planes from different macrocycle. Thermal ellipsoids represented at 40 % probability. H-atoms and crystallisation solvent (toluene) were omitted to clarify.

Table 3.4. Selected bond distances, for complexes **5** and **7**.

Figure 3.8. MALDI-ToF spectra of MgZn, MgMg, MgCr, MgMn, MgFe and MgCo with the experimental (above peak) and theoretical (top left of each graph) values. The simulated isotopic distribution is also represented on the bottom of each graph.

Figure 3.9. MALDI-ToF spectra of MgNi and MgCu, complexes **7** and **8** showing the water adduct $[LMg_2(OAc)(OH_2)]^+$, with the experimental (written on top of the peak) and theoretical (top left of each graph) values. The simulated isotopic distribution is also represented on the bottom of each graph.

Figure 3.10. Comparison between infrared spectra of the pro-free ligand H_2L and complex **5**. Highlighted bands are discussed in the text; 3298 cm^{-1}, 1590 cm^{-1}, 1440 cm^{-1}, 924 cm^{-1}, 707 cm^{-1}.

Figure 3.11. Comparison of the infrared spectra for complexes **1**–**8** obtained in solid-state.

Table 3.5. The resonance frequencies (cm^{-1}) obtained from the solid-state infrared spectra for complexes **1**–**8**.

Figure 3.12. a) Absorbance vs. time plot for PCHC (every 4^{th} point displayed). b) Normalised conversion vs. time plot for PHCH (every 4^{th} point displayed). c) Logarithm of epoxide concentration vs. time for PCHC. d) Logarithm of epoxide concentration vs. time for three ROCOP runs with MgFe, complex **5**.

Table 3.6. CO_2/CHO copolymerisation at 1 bar CO_2 with catalysts **1–8** and literature reported complexes ZnZn, CoCo and LFe_2Cl_4.

Figure 3.13. Graph of CHO conversion against time for CO_2/CHO copolymerisation using complexes **1–8**.

Figure 3.14. GPC traces for complexes **1**–**8**.

Figure 3.15. TOFs values obtained from ROCOP of CO_2/CHO for complexes **1–8** represented in following MgMg and the first-row of transition metals MgM(II) (M(II) = Cr, Mn, Fe, Co, Ni, Cu, Zn).

Figure 3.16. Comparison of BDEs (M–O), Mulliken electronegativity and oxophilicity through the fist-row transition metals. Graph adapted from Moltved et al.

Figure 3.17. Graph comparing the catalyst activity with BDEs (M–O) values reported in the literature. Due to a non-agreement in the Cr and Ni BDEs values, both values found in the literature (---) were reported in the graph, and the values suggested by Keep and co-workers are connected by a full line (–).

Figure 3.18. Graph comparing the catalyst activity with WERC values, plotted on a log scale.

Figure 3.19. Comparison between pK_a values reported in the literature and TOFs for the series of metal ions.

Figure 3.20. Structures of different epoxides investigated for ROCOP. Cyclohexene oxide (CHO); vinyl cyclohexene oxide (vCHO); 3,4-epoxytetrahydrofuran (ETHF); cyclopentene oxide (CPO).

Table 3.7. CO_2/Epoxides ROCOP with MgCo (**6**). For individual polymerisation plots (conversion *vs.* time), see Appendix Figure A.15 and for GPC see Figure A.17.

Table 3.8. CO_2/Epoxides ROCOP with MgFe (**5**). For individual polymerisation plots (conversion *vs.* time), see Appendix Figure A.16 and for GPC see Figure A.18.

Scheme 3.3. Ring-opening co-polymerisation of CHO and NA.

Table 3.9. CHO/NA ROCOP data for MgM(II) (M(II) = Mg, Cr, Mn, Fe, Co, Ni, Cu).

Scheme 3.4. Synthesis of FeIIFeIII complex **10** with unisolable complex **9** intermediate. I) 2 $Fe(OAc)_2$ in THF at 100 °C for 16 h with the

formation of HOAc. II) Excess of HOAc formed from the first reaction.

Scheme 3.5. Synthesis of FeIIFeII complex **9**. I) $K(N(SiMe_3)_2)$ in THF at 100 °C for 16 h. II) $Fe(OAc)_2$ in THF at 100 °C for 16h.

Figure 3.21. Cyclic voltammograms of complexes **5**, **9** and **10** in THF at scan rate 0.1 V, calibrated against Fc^+/Fc.

Table 3.10. Redox values of the complexes **9** and **10**.

Figure 3.22. a) Inverse of molar susceptibility *vs*. temperature for complex **9**. ◦ experimental data, – fitting of the curve. b) Effective magnetic moment *vs.* temperature plot for complex **9**.

Figure 3.23. a) Inverse of molar susceptibility *vs*. temperature for complex **10**. ◦ experimental data, – fitting of the curve. b) Effective magnetic moment *vs.* temperature plot for complex **10**.

Figure 3.24. Crystal structure obtained for the complex FeIIFeIII (**10**) by Dr. Arron Deacy (University of Oxford). Thermal ellipsoids represented at 40 % probability. H-atoms and THF crystallization solvent were omitted to clarify.

Table 3.11. Selected distances for complex **10**.

Figure 3.25. MALDI-ToF spectra of complexes **9** and **10** with signals at 721.3 *m/z*.

Figure 3.26. Comparison among infrared spectrum for complexes **5, 9**,**10** and pro-ligand H_2L.

Table 3.12. Main bands of infrared spectrum for complexes **5, 9** and **10.**

Chapter 4: Investigations into backbone modifications in In-salan complexes for epoxide/CO_2 ROCOP

Figure 4.1. a) Structure of the In-phosphasalen and mononuclear mechanism for CO_2/epoxide ROCOP using indium catalyst. R = Growing polymer chain. Figure based on C. K. William, 2018. b) Three possible configurations (*trans*, *cis*-β and *cis*-α) for tetradentate Schiff base ligand in an octahedral complex.

Figure 4.2. Catalyst designing explored in this chapter.

Scheme 4.1. Synthesis of ligands $^{Et}\mathbf{L_RH_2}$ and $^{Pr}\mathbf{L_RH_2}$, R = tBu, Me or OMe. i) formaldehyde and the correspondent amine, reflux in methanol for 17 h.

Scheme 4.2. Synthesis of ligands $^{MePr\text{-}a/b}\mathbf{L_{tBu}H_2}$ and $^{Bu\text{-}a/b}\mathbf{L_{tBu}H_2}$**.** i) Correspondent amine, reflux in ethanol for 2 h. ii) $NaBH_4$ in methanol for 16 h.

Figure 4.3. Infrared spectra for a) $^{MePr\text{-}a/b}\mathbf{L_{tBu}H_2}$ and b) $^{Bu\text{-}a/b}\mathbf{L_{tBu}H_2}$.

Table 4.1. Selected resonance frequencies (cm^{-1}) obtained from the solid state infrared spectra for ligands $^{MePr\text{-}a/b}\mathbf{L_{tBu}H_2}$ and $^{Bu\text{-}a/b}\mathbf{L_{tBu}H_2}$

Scheme 4.3. Attempted methylation of $^{MePr\text{-}b}\mathbf{L_{tBu}H_2}$ and $^{Bu\text{-}b}\mathbf{L_{tBu}H_2}$. i) Acetic acid, formaldehyde and $NaBH_4$.

Scheme 4.4. Synthesis of C3 backbone amine. i) HCOOMe, neat amine, reflux for 12 h. ii) $LiAlH_4$ in Et_2O, 0 °C → RT, 20 h.

Scheme 4.5. Synthesis of C4 backbone amine. i) $(CH_3)_3COCOOC_6H_5$, in DMF with a catalytic amount of Et_3N during 16h. ii) $LiAlH_4$ in THF, reflux 18h.

Scheme 4.6. Synthesis of amine. i) Di-tert-butyl decarbonate, methanol 48 h. ii) NaH, MeI in DMF, 12h. iii) 2 M HCl in ether, 5h.

Scheme 4.7. Synthesis of $^{Et}\mathbf{L_RInCl}$ and $^{Pr}\mathbf{L_RInCl}$ (R = ^{t}Bu, Me or OMe) complexes. i) $KN[Si(CH_3)_3]_2$, $InCl_3$, THF.

Figure 4.4. Comparison between ^{1}H NMR spectrum (C_6D_6, 298 K) for $^{Et}L_{tBu}H_2$ (bottom spectrum) and $^{Et}L_{tBu}InCl$ (top spectrum).

Figure 4.5. a) and b) Molecular structures of $^{Pr}L_{tBu}InCl$. c) In(III) environment and atom labels for complex $^{Pr}L_{tBu}InCl$. Thermal ellipsoids represented at 40 % probability. H–atoms and crystallisation solvent (THF) were omitted to clarity.

Table 4.2. Selected bond distances and angles for $^{Pr}L_{tBu}InCl$.

Figure 4.6. a) Molecular structures of $^{Et}L_{Me}InCl$. b) In(III) environment and bond angles used to calculate τ factor. Thermal ellipsoids represented at 40 % probability. H–atoms and crystallisation solvent (benzene) were omitted to clarity.

Table 4.3. Selected bond distances and angles for $^{Et}L_{Me}InCl$.

Scheme 4.8. Synthesis of $^{MePr-a/b}L_{tBu}InCl$ and $^{Bu-a/b}L_{tBu}InCl$ complexes. i) $KN[Si(CH_3)_3]_2$, $InCl_3$, THF.

Figure 4.7. Comparison between ^{1}H NMR spectrum (C_6D_6, 298 K) for $^{MePr-a}L_{tBu}H_2$ (bottom spectrum) and $^{MePr-a}L_{tBu}InCl$ (top spectrum). * Residual water from C_6D_6.

Figure 4.8. a) Molecular structures of $^{MePr-a}L_{tBu}InCl$. b) In(III) environment for complex $^{MePr-a}L_{tBu}InCl$ (left) and $^{Pr}L_{tBu}InCl$ (right). Thermal ellipsoids represented at 40 % probability. H–atoms and crystallisation solvent (THF) were omitted to clarity.

Table 4.4. Selected bond distances and angles for $^{MePr-a}L_{tBu}InCl$.

Figure 4.9. ^{1}H NMR spectrum for $^{MePr-b}L_{tBu}InCl$, (C_6D_6, 500 Hz, 298 K). The signal at 7.16 ppm is from C_6D_6 solvent.

Figure 4.10. Variable temperature ^{1}H NMR spectrum for $^{MePr\text{-}b}$**L$_{tBu}$InCl**, (Toluene-d$_8$, 500 Hz, 298; 273 and 248 K). Signals at 7.09; 7.01; 6.95 and 2.05 ppm are solvent residual signal from Toluene-d$_8$ solvent.

Figure 4.11. Variable temperature ^{1}H NMR spectrum for $^{Bu\text{-}b}$**L$_{tBu}$InCl**, (Toluene-d$_8$, 500 Hz, 298; 273 and 248 K). Signals at 7.09; 7.01; 6.95 and 2.05 ppm (*) are from Toluene-d$_8$ solvent.

Scheme 4.9. Synthesis of ^{Et}**L$_{tBu}$InO^{t}Bu** complexes. i) KO^{t}Bu, THF, RT, 4 h.

Scheme 4.10. Synthesis of ^{Et}**L$_{tBu}$ScCl**. i) KN[Si(CH$_3$)$_3$]$_2$, ScCl$_3$(THF)$_3$, THF.

Figure 4.12. Variable temperature ^{1}H NMR spectrum in THF-*d*$_8$, 400 Hz of ^{Et}**L$_{tBu}$ScCl**. Temperatures: 298, 273, 248, 223 and 198 K.

Figure 4.13. ^{1}H NMR spectrum of ^{Et}**L$_{tBu}$ScCl** in toluene-d$_8$ and THF-*d*$_8$. Toluene-*d*$_8$ (bottom) fist sample run. Toluene-d$_8$ (top) second sample run (after dry the sample used in THF-*d*$_8$ and re-dissolve in toluene-*d*$_8$).

Figure 4.14. Variable temperature ^{1}H NMR spectrum in toluene-d$_8$, 400 Hz of ^{Et}**L$_{tBu}$ScCl**. Temperatures: 298, 323, 353, 363 and 373 K.

Figure 4.15. Complexes reported in the literature by Williams et al.

Table 4.5. CO$_2$/CHO ROCOP catalysed by ^{Y}**L$_{tBu}$InCl** (Y = Et, Pr, MePr-a/b or Bu-a/b) at 1 bar CO$_2$, without the addition of co-catalyst.

Table 4.6. CO$_2$/CHO ROCOP catalysed by a series of ^{Et}**L$_R$InCl** (R = ^{t}Bu, Me or OMe) complexes at 1 bar CO$_2$, without the addition of co-catalyst.

Table 4.7. CO$_2$/CHO ROCOP catalysed by ^{Y}**L$_R$InCl** (Y = Et or Pr; R = tBu, Me or OMe), at 40 Bar CO$_2$.[a]

Chapter 5: Conclusions and Outlook

Figure 5.1. Summary of the catalysts reported in this thesis.

Figure 5.2. TOFs *vs.* heterodinuclear complexes Mg(II)M(II) with M = Mg, Cr, Mn, Fe, Co, Ni, Cu and Zn, ordered by atomic number.

Figure 5.3. Summary of mononuclear In(III) complexes tested for ROCOP of CHO/CO_2, without co-catalyst addition, and their respective activity and selectivity.

Scheme 5.1. Potential heterodinuclear macrocycle catalysts systems.

Scheme 5.2. Potential multinuclear catalysts.

Figure 5.4. Summary of In(III) catalysts systems with diamine backbone and nitrogen environment variations. Highlighted the systems that were not accessed and tested yet.

Figure 5.5. Summary of In(III) catalysts systems with diamine backbone and *para*-phenolate sites variations (for N–Me systems). Highlighted the systems that were not accessed and tested yet.

Figure 5.6. Potential future catalysts obtained from the optimized ligand structure.

Table of Contents

Declaration 3

Abstract 4

Acknowledgments 6

Abbreviations 8

List of Figures, Schemes and Tables 11

Chapter 1 Introduction 29

1.1. Polymers 30

1.3. Ring-opening copolymerisation of CO_2/Epoxide 32

1.4 Catalysts for copolymerisation of CO_2 and epoxides 36

1.5. Bifunctional/Two components catalysis 38

1.5.1 Examples of Bifunctional catalysts 38

1.5.2. Mechanisms for two component catalysis 41

1.7. Bifunctional catalysts – Two-component single catalyst 42

1.6. Dinuclear catalysts 47

1.6.1. Single ligand bimetallic catalysts 48

1.6.2. Dimeric catalyst 55

1.6.3. Tethered Catalysts 56

1.6.4. Dinuclear catalyst mechanism – Polymer chain shuttling mechanism 59

1.8. Aims 61

1.9. References 64

Chapter 2 Methodology **70**

2.1. Superconducting Quantum Interference Device Magnetometry 71

2.2. Cyclic Voltammetry 76

2.3. Reaction monitoring – *in situ* Attenuated Total Reflectance – Infrared spectroscopy (ATR–IR) 78

2.4. References 82

Chapter 3 Heterodinuclear Catalysts for the Ring-Opening Copolymerisation of CO_2/Epoxide **83**

3.1. Introduction 84

3.2. Aims 85

3.3. Synthesis and Characterisation of Heterometallic $LMgM(OAc)_2$ complexes (where M = Cr, Mn, Fe, Co, Ni, Cu, Zn) 87

3.3.1. Synthesis of complex **1** 87

3.3.2. Synthesis of complexes **2–8** 88

3.3.3. Cyclic Voltammetry of complexes **2–8** 89

3.3.4. SQUID Magnetometry for complexes **3–8** 91

3.3.5. X-Ray Crystallography of complexes **5** and **7** 94

3.3.6. MALDI-ToF Mass Spectrometry for complexes **1–8** 96

3.3.7. Infrared Spectroscopy for complexes **1–8** 99

3.4. Polymerisation studies 102

3.4.1. ROCOP of CO_2 and CHO for complexes **1–8** 102

3.4.2. ROCOP of CO_2 and alternative epoxides using complexes **5** and **6** 111

3.4.3. Preliminary results – NA/CHO Copolymerisation 113

3.5. Synthesis and Characterisation of Homodinuclear systems 115

3.5.1. Synthesis of complexes **9** and **10** 115

3.5.2. Cyclic Voltammetry 117

3.5.3. Superconducting Quantum Interference Device (SQUID) Magnetometry 118

3.5.4. X-Ray Crystallography of complex **10** 120

3.5.5. Mass spectrometry 121

3.5.6. Infrared Spectroscopy 122

3.5.7. ROCOP of CO_2/CHO for complexes **9** and **10** 124

3.6. Conclusions and Outlook 125

3.7. References 127

Chapter 4 Investigations into backbone modifications in In-salan complexes for epoxide/CO_2 ROCOP 130

4.1. Introduction 131

4.2. Aims 133

4.3. Ligands syntheses and characterisation 135

4.3.1. Synthesis of salan C2 and C3 backbone 135

4.3.2. Synthesis of salen C3' and C4 backbone ($^{MePr\text{-}a/b}L_{tBu}H_2$ and $^{Bu\text{-}a/b}L_{tBu}H_2$) 136

4.3.3. Synthesis of salan C3' and C4 ($^{MePr\text{-}c}L_{tBu}H_2$ and $^{Bu\text{-}c}L_{tBu}H_2$) 138

4.4 Synthesis and Characterisation of In-salan complexes 141

4.4.1. Synthesis of complexes $^{Et}L_xInCl$ and $^{Pr}L_xInCl$ with X = ^{t}Bu, Me or OMe 141

4.4.2. Synthesis and characterisation of complexes $^{MePr\text{-}a/b}L_{tBu}InCl$ and $^{Bu\text{-}a/b}L_{tBu}InCl$ 145

4.4.3. Synthesis and characterisation of $^{Et}L_{tBu}In(O^tBu)$ and $^{Et}L_{tBu}ScCl$ 149

4.5. ROCOP of CO_2 and CHO 154

4.5.1. Experiments at 1 bar CO_2 154

4.5.2. Experiments at high CO_2 pressure 156

4.6. Conclusions and Outlook 158

4.7. References 159

Chapter 5 Conclusions and Outlook 161

5.1. General Conclusion 162

5.2. Future work 164

5.2.3. Heterodinuclear catalysts 164

5.2.2. Mononuclear Catalysts 167

5.4. References 170

Chapter 6 Experimental 171

6.1. General Comments 172

6.2. Instrumentation 172

6.2.1. Attenuated Total Reflection Infrared Spectroscopy (ATR-IR) 172

6.2.2. FT-IR 173

6.2.3. Matrix-Assisted Laser Desorption/Ionization – Time of Flight (MALDI-ToF) 173

6.2.4. Nuclear Magnetic Resonance (NMR) spectroscopy 173

6.2.5. Elemental Analysis 174

6.2.6. X-ray Diffraction 175

6.2.7. Cyclic Voltammetry 175

6.2.8. Superconducting Quantum Interference Device (SQUID) Magnetometry 175
6.2.9. Size Exclusion Chromatography (SEC) 176
6.3. Chapter 3 176
6.3.1. Polymerisation procedure 176
6.3.2. Synthesis of **LMgZn(OAc)$_2$** 178
6.3.3. General procedure 1 – Synthesis of **LMgM(OAc)$_2$** 180
6.3.4. Synthesis of complex **9**, LFeIIFeII(OAc)$_2$ 183
6.3.5. Synthesis of complex **10**, LFeIIFeIII(OAc)$_3$ 184
6.4. Chapter 4 185
6.4.1. Polymerisation 185
Polymerisation procedure (1bar) 185
Polymerisation procedure (high pressure) 185
6.4.2. Synthesis of ligands 186
6.4.3. Catalyst synthesis 193
6.4.4. Synthesis of *N,N'*-Dimethyl-2,2-dimethylpropane-1,3-diamine 200
6.4.5. Synthesis of *N*-Methyl-*N'*-[2-(methylamino)ethyl]-1,2-ethanediamine 201
6.5. References 203
Chapter 7 Appendices **205**
7.1. Chapter 3 206
7.1.1. SQUID Magnetometry 206
7.1.2. ROCOP of CO_2 and CHO 209
7.1.2. ROCOP of CO_2 and alternative epoxides 212
7.1.3. GPC 214
7.1.3. ROCOP of NA and CHO 215

7.1.4. X-Ray Crystallography 217

7.2. Chapter 4 223

7.2.1. X-Ray Crystallography 224

7.3. References 228

Chapter 1

Introduction

1.1. Polymers

Plastics are now a key part of our daily life with the first synthetic plastic, such as Bakelite, appearing in the early 20th century. Within a few decades they have become key materials for use in packaging, clothing, healthcare, automobiles components and electronics.[1-4] This scope of applicability is due to the wide range of mechanical properties obtained with a low synthetic cost.[1] Through the years the production of plastic has increased drastically and, in 2018, the global plastic production reached 359 million tonnes (61.8 Mt Europe production) with the largest proportion going to packaging (40 %) followed by construction (20 %) and automotive sectors, Figure 1.1.[3, 4]

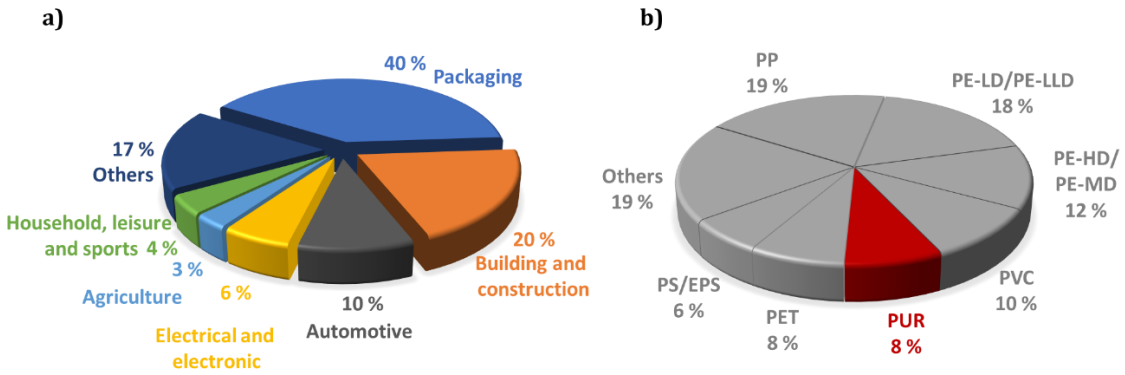


Figure 1.1. a) Distribution of European plastic converters demand by segment in 2018; b) Plastic relative demand by type in Europe.[3, 4]

Among the wide variety of plastic used today, polyurethanes consist of approximately 8 % of the European demand.[4] They are a class of polymer used in commercial applications such as rigid foams (insulation, automotive), solid elastomers (adhesives), flexible slab (furniture) and flexible moulded foams (automotive seating).[5, 6] The major raw materials used in polyurethane production are petrochemicals derived from crude oil, with only minor contributions from bio-based natural products, such as sugars, castor oil and bio-based glycerols.[7]

One of the key compounds used in polyurethane production are polyols, they are polyfunctional alcohols (containing at least one hydroxyl group), such as polycarbonate, polycaprolactone, poly(ethylene adipate) and poly(propylene oxide) glycol. Polyols can be divided into four main classes: Polyether polyols, amine-terminated polyethers, polyester polyols and polycarbonates. Polyether polyols represent the greatest proportion in terms of raw materials production and deliver flex-foam applications with low cost, however they can show lower thermal stability, modulus/strength and flammability when compared with other polyols.[5, 6] Polyester urethanes can alleviate these disadvantages, typically more hydrolytically resistant aliphatic polyesters are used such as polycaprolactone or hexamethylene polycarbonate, but the instability of polyesters to acids and hydrolysis remains an issue.[5]

Polycarbonate polyol can show resistance to hydrolysis, high modulus/strength and also improve flame retardant properties, therefore they typically serve high value markets.[6] The most common type of polycarbonate on the market is the aromatic polycarbonate currently made by bisphenol A and phosgene. They show desirable properties including good stability to UV, acids and water (when compared with polyether) and can be used in diverse industrial applications such as sunglasses, medical devices, bulletproof window and automotive interiors, so would be desirable targets to grow in the polyol sector.[8, 9]

Nowadays, an alternative economic way to produce polycarbonate is by the copolymerisation of CO_2 and an epoxide such as propylene oxide (PO) or cyclohexene oxide (CHO) (Figure 1.2).[10] The use of CO_2 is attractive due to the possibility to obtain high-value products derived from a low-cost, renewable and non-toxic source.[11]

Furthermore, when polycarbonate polyols with 20 wt% are compared to conventional polyether polyols can reduce by 11–19% greenhouse gas emission and save 13–16% of fossil resources.[8] Some polymers obtained from this process are already commercialized such as polypropylene carbonate (PPC) obtained from the copolymerisation of CO_2/PO.[8, 10]

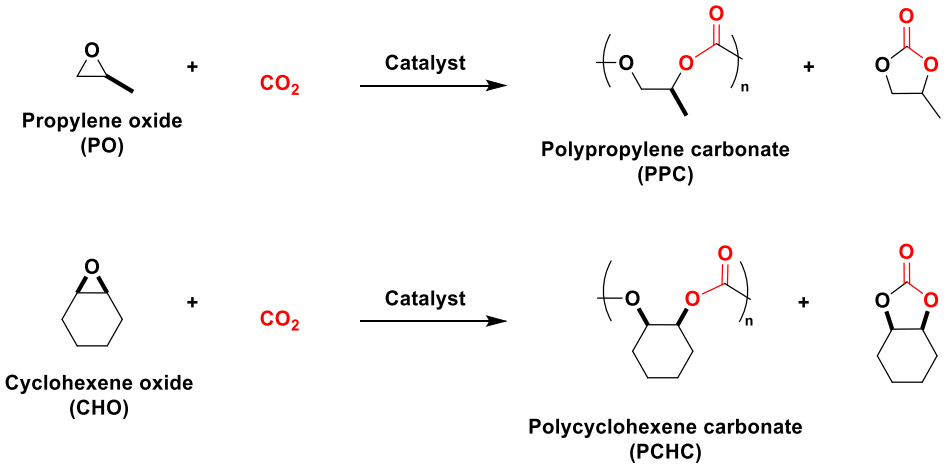


Figure 1.2. Ring-opening copolymerisation of epoxide (PO and CHO) and CO_2.

1.3. Ring-opening copolymerisation of CO_2/Epoxide

The general mechanism proposed to explain the copolymerisation of an epoxide with CO_2 can be divided into three main steps: Initiation, propagation and termination, illustrated in Figure 1.3 (for ROCOP of CO_2/CHO) and involves the use of a catalyst (such as a Lewis acid) as discussed below.[11-14]

Initiation: The first step of the mechanism consists of the coordination of the epoxide to the Lewis acid (often a metal centre) followed by the ring-opening of the epoxide through a nucleophilic attack by the initiating group (**X** = carboxylate, alkoxide or halide).[12, 13]

Propagation: Once a metal-alkoxide bond has been formed from the initiation process, rapid CO_2 insertion occurs forming a metal-carbonate species. This is followed by

coordination and ring-opening of an epoxide by the nucleophilic carbonate chain-end to regenerate the metal-alkoxide intermediate. The polymer propagates between these two intermediates resulting in polycarbonate chain-growth.

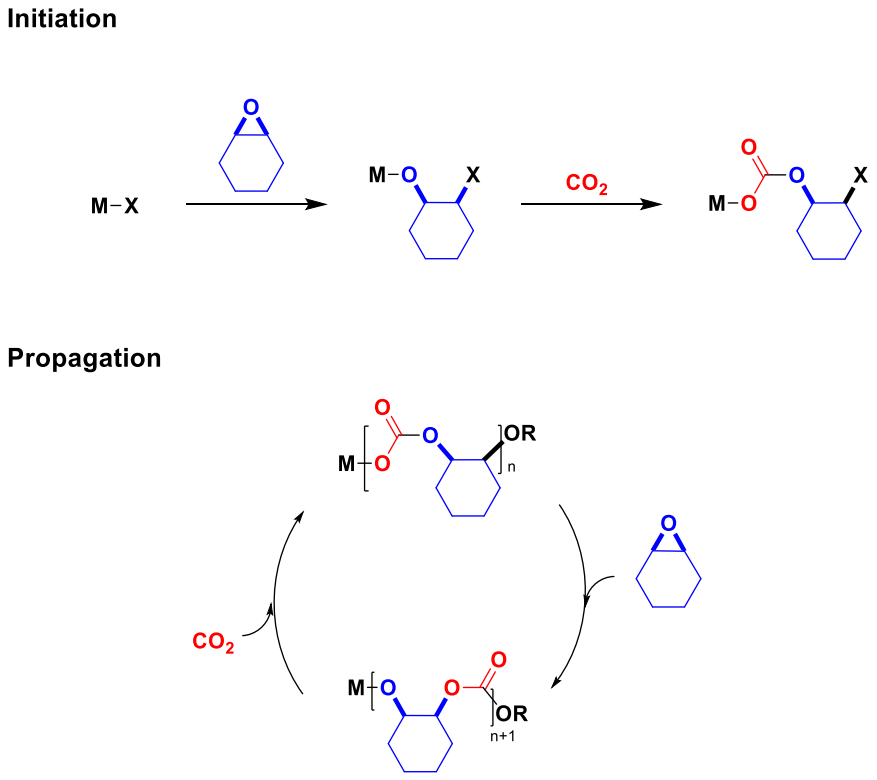


Figure 1.3. Initiation step for CO_2/CHO ROCOP and PCHC formation during propagation step for a ROCOP of CHO and CO_2 with excess of epoxide. Growing chain denoted as 'R'.

During the propagation step, side reaction may occur to generate polyether linkages or cyclic carbonates (Figure 1.4). The formation of polyether linkages can occur through sequential epoxide enchainment. A further possible side reaction is the formation of cyclic carbonates by chain backbiting from the attack of the metal–alkoxide (*trans*-cyclic product) or metal–carbonate (*cis*-cyclic product). This side-reaction is driven by the formation of a stable five-membered ring and is thermodynamically the most favoured product and thus favoured at elevated temperature.

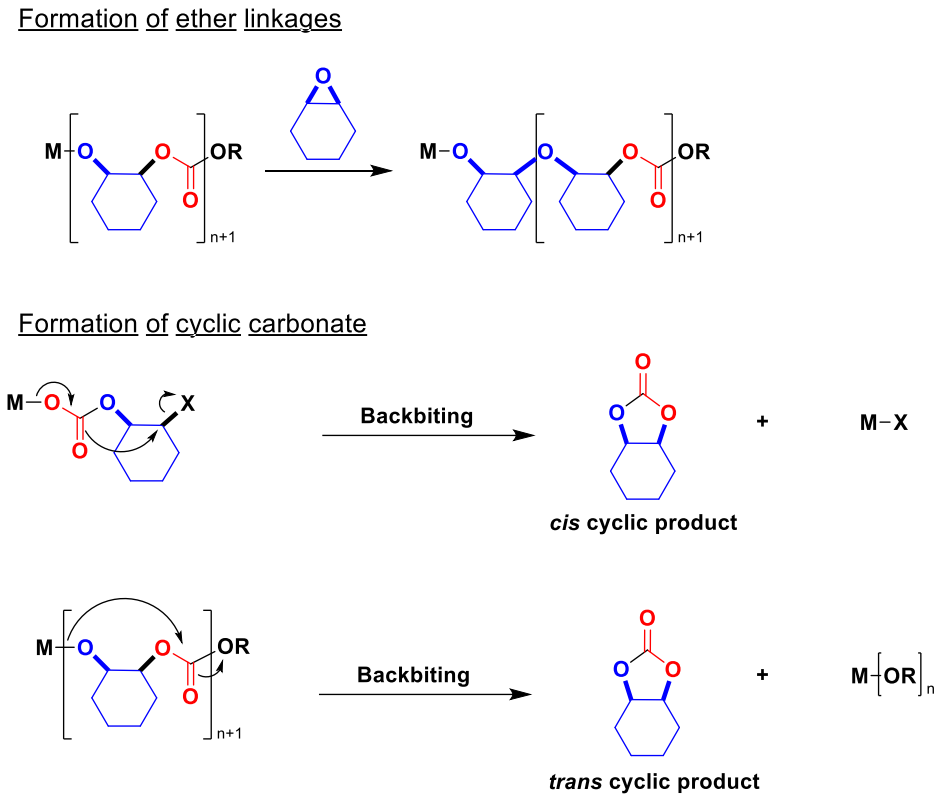


Figure 1.4. Possible side reactions during the propagation step of ROCOP CO_2/CHO. Formation of *cis* and *trans* cyclic product and polyether.

Termination: Polymerisation is suspended by the modification of the reaction medium (temperature, monomer removal, water, acid addition or polymer precipitation from reaction medium).

The concept of living polymerisation was introduced by Szwarc in 1956, where the term "living" was used to describe the capability of the polymer chain to incorporate more monomer even after the first batch of monomer has been consumed, and since then, the concept has been generalised and shown to apply to quite a range of catalysed polymerisations (although not all such reactions).[15, 16] In 2008, IUPAC determined living polymerisations as occurring without any chain termination or irreversible chain transfer reactions. In many cases of living polymerisation the rate of chain initiation is faster than the rate of chain propagation.[17-19]

When the polymerisation presents a faster chain initiation than propagation, this process leads to good polymerisation control and the number of polymer chains are consistent throughout the polymerisation, resulting in a proportional increase in molar mass (linear dependence of M_n to monomer conversion).[16] In some cases of living polymerisation, the reaction has slow initiation, followed by fast propagation, however, in these cases, the polymerisation is considered to lack control.[16, 19]

In some systems, such as the copolymerisation of epoxide/CO_2, a trace amount of moisture (often present in carbon dioxide gas, for example) can ring open the epoxide leading to the formation of a diol, which acts as a chain transfer agent (CTA).[20] In fact the majority of these polymerisation catalysis (conducted with just catalyst and without excess CTA) result in bimodal M_w distributions. Indeed, it is been shown that the upper distribution arises from chains initiated from the diol and show M_w values that are approximately double those of the lower M_w distribution, which arises due to initiation from the catalyst.[20] To avoid this bimodality, stringent monomer purification procedures and CO_2 drying can be performed but it should be noted that such conditions are somewhat unusual and would be very difficult to scale (i.e. use of an excess of trialkyl aluminium drying agent as a scrubber for CO_2 prior to each run).[21] The presence of water is only problematic for the production of narrow distribution, high molar mass polymers. It is also important to note that the production of multimodal/bimodal M_w distribution is not, in itself, a barrier to plastics being useful – many commercial plastic feature multiple M_w distributions or have deliberate addition of lower M_w chains as self-plasticizers.

When CO_2/epoxide ROCOP catalysis is conducted with the goal of delivering polycarbonate polyols then the presence of trace water is irrelevant because the

production of polyols requires catalysis to function in the presence of a large excess of diol/water/chain transfer agent. Thus, for polyol production the reactions and catalysts must tolerate the use of excess protic compound or chain-transfer agents (CTA). These are substances (such as alcohols) that exchange reversibly with the propagating metal-alkoxide species (faster than chain-propagation) during the polymerisation and result in the formation of telechelic polymer (essential for polyurethane productions) and monomodal GPC traces (due to the very rapid exchange with the propagating metal-alkoxide species).[19]

1.4 Catalysts for copolymerisation of CO_2 and epoxides

The possibility to access a copolymer from CO_2 and an epoxide was first reported in 1969 by Inoue et al. using $ZnEt_2$ made *in situ*. Their results inspired many researchers to explore this field.[22] In 1978, Takeda and Inoue reported a detailed work at the copolymerisation of CO_2 and 1,2-epoxypropane using as catalyst an aluminium tetraphenyl-porphyrin complex (Figure 1.5-a). The polymerisation was studied at 1 and 8 bar CO_2 and were observed to have low rates, taking an average of 24 days to obtain the polymer for a methoxide group (MeO^-) as an initiating, for X = Cl and Me just cyclic carbonate was obtained.[23] In 1995, Darensbourg started a series of papers about copolymerisation of CO_2/epoxide using variations of zinc bis(phenoxides), illustrated in Figure 1.5-b, where they explored different substituents at the *ortho*- and *para*-phenoxide. They noticed an increase in activity when electron-donating groups were added at *para*-position noticing that methyl > *tert*-butyl > phenyl > isopropyl, for copolymerisations of CHO/CO_2, (50 bar CO_2 pressure, 80 °C), however low rates still observed, taking almost 3 days at high pressure.[24-27]

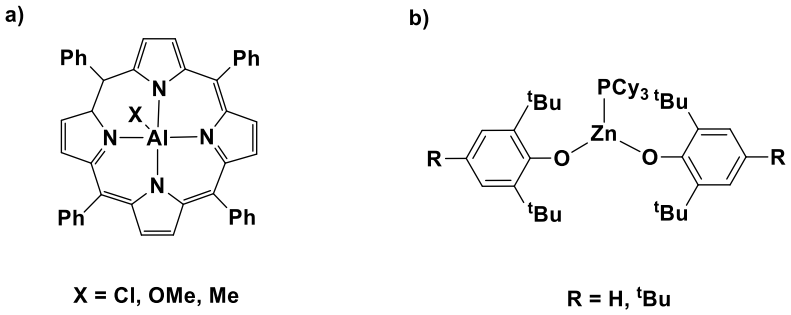


Figure 1.5. a) Aluminium tetraphenyl-porphyrin. b) Zinc bis(phenoxide).

Through the years a range of different catalysts have been developed and reported in the literature for the ROCOP of CO_2 and epoxides, some of them requiring the use of a co-catalyst. The reported catalysts can be divided into three main families varying the number of metal centres (mononuclear or dinuclear) and the presence or absence of a cocatalyst as shown in Figure 1.6.[28]

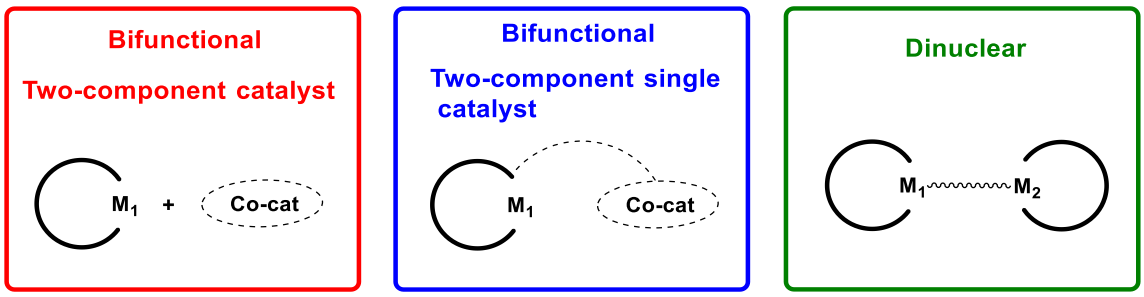


Figure 1.6. Three main families of catalysts discussed in this chapter. Figure adapted from Williams et al.[28]

1.5. Bifunctional/Two components catalysis

1.5.1 Examples of Bifunctional catalysts

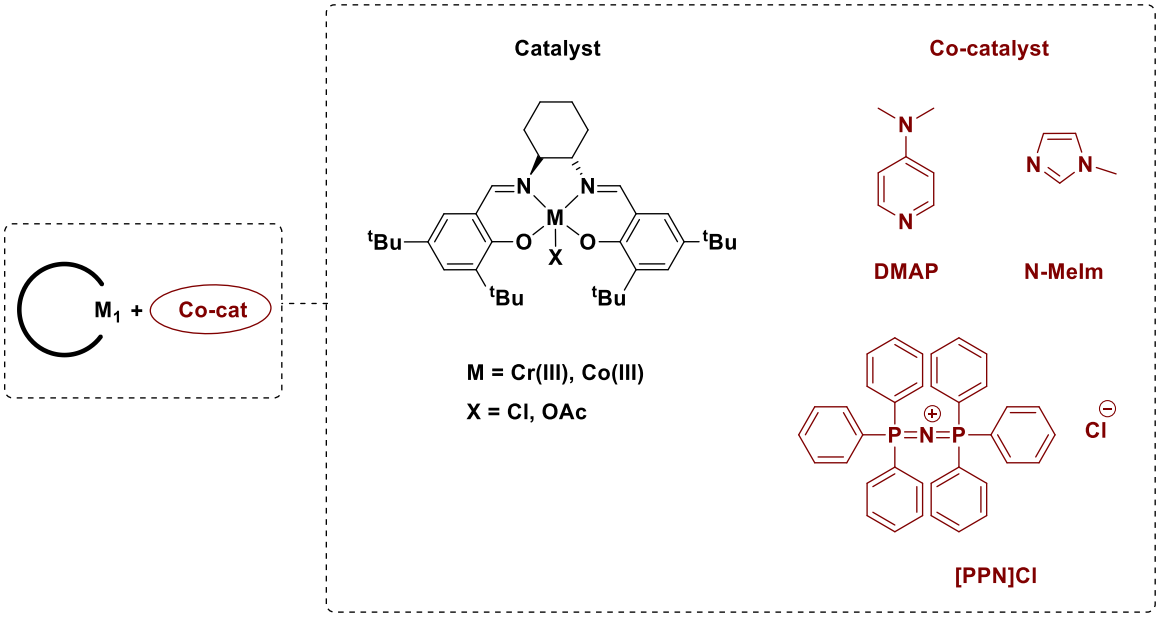


Figure 1.7. Examples of bifunctional/two components catalysts reported in the literature by Darenbourg; Lu and Coates with co-workers with bis(salicylaldimine) and co-catalysts: DMAP (4-dimethyl(amino)pyridine); *N*-MeIm (*N*-methylimidazole) and PPNCl (Bis(triphenylphosphoranylidene)ammonium chloride).

The bifunctional two components catalyst consists of a monometallic complex that acts in conjunction with a co-catalyst (ionic groups and/or nucleophiles).[28] The most widely studied example is based on the salen (*N*,*N*-bis(salicylaldimine)) ligand, first investigated in coordination complexes for asymmetric epoxidation of olefins during the 90s.[29, 30] The Cr(III) salen systems were also the first of these systems to be investigated for the ring-opening of different epoxides (Jacobsen, Paddock and Nguyen).[31-34] Inspired by this work (and Kruper's work on Cr(III) porphyrins used to achieve cyclic carbonates from CO_2/epoxide)[35], Darenbourg and co-workers, in 2002, explored (salen)Cr(III)Cl catalysts for the copolymerisation of CO_2/epoxide. The catalyst was used in combination with a neutral Lewis base *N*-methylimidazole (*N*-MeIm) and 4-dimethyl(amino)pyridine (DMAP) as co-catalyst showing a first-order

dependence in catalyst concentration with TOF = 32 h^{-1} for copolymerisation of CHO/CO_2 (5 Equiv. of N-MeIm, 80 °C, 58.5 bar CO_2).[36]

Improvement in activity was observed when the metal centre was changed to Co(III), exploring different initiating groups (such as OAc) and studied with a different co-catalyst, among them it was explored [PPN]Cl that achieved TOF = 110 h^{-1} for PO/CO_2 copolymerisation ([PO]:[Cat] = 2000:1, 14 bar CO_2, 22 °C).[37, 38] Despite (salen)Co(III)OAc being able to copolymerise CO_2/PO without the addition of a co-catalyst, the activity was lower and the complex did not show enough stability to perform polymerisation at high temperatures obtaining TOF = 81 and 17 h^{-1} for polymerisations at 25 and 40 °C, respectively ([PO]:[Cat] = 500:1, 55 bar CO_2).[39] The same behaviour was observed for (salen)Co(III) with other initiating groups, accredited to a reduction to Co(II) derivatives as an inactive red solid precipitate.[40]

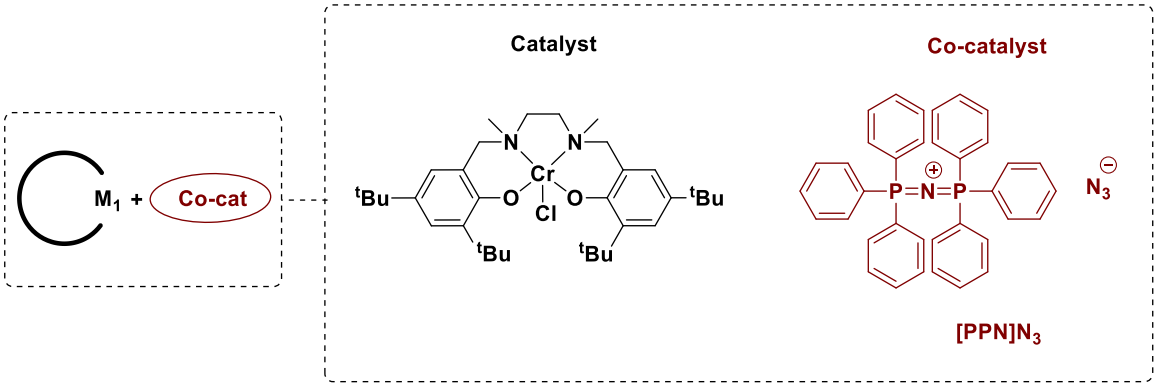


Figure 1.8. (salan)Cr(III)Cl catalysts developed by Darensbourg and co-workers.[41]

In 2009, Darensbourg and co-workers reported a Cr(III) complex synthesised with a derivative of the salen ligand named salan (N,N'-disubstituted bis(aminophenoxide) – Figure 1.8) with methyl substituents on the nitrogen presenting a greater donor character than the salen ligand (sp^3-hybridized amino donors).[41] Different from the (salen)Cr(III)Cl catalyst which showed a square-pyramidal geometry with an axial chloride,[36] the salan systems showed an increase in flexibility allowing the complex to

access a *cis*-coordination mode (one of a number of different conformations allowed by salan ligands as illustrated in Figure 1.9). [41, 42]

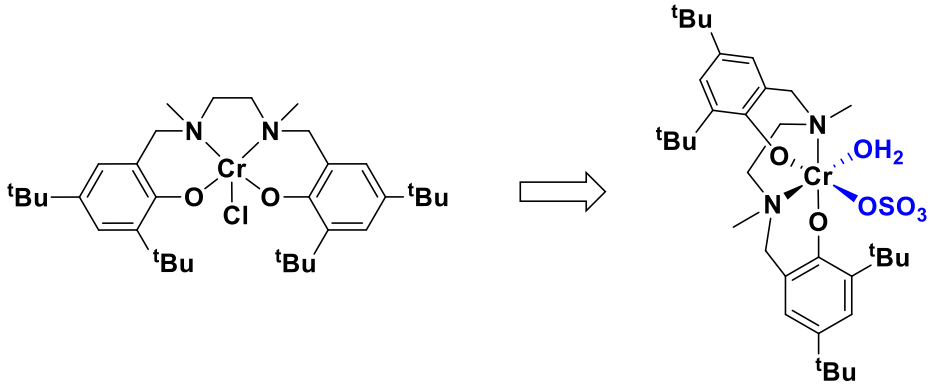


Figure 1.9. Figure adapted from Darensbourg et al., showing the *cis*-coordination conformation adopted by the salan-Cr catalyst.[41,42]

The (salan)Cr(III)Cl, with 1 equiv. of [PPN][N_3] as cocatalyst, showed activity for the ROCOP of CO_2 with cyclohexene oxide (CHO) and propylene oxide (PO) with TOF = 405 h^{-1} ([CHO]:[Cat] = 2500:1, 60 °C, 34 bar CO_2) and TOF = 21 h^{-1} (60 °C, 34 bar CO_2), respectively, and due to the possibility to polymerise both epoxides, the authors also explored block polymers.[41] The catalyst was also active for ROCOP of CO_2/CHO without the addition of a cocatalyst, however with lower activity (TOF = 14 h^{-1}, 60 °C, 34 bar CO_2). An interesting comparison made between (salen)/(salan)Cr(III)Cl concerns polymer purification. Due to the higher solubility of salan systems, the polymers obtained with using this catalyst were easier to purify.[41]

1.5.2. Mechanisms for two component catalysis

Through the years three main mechanisms were reported to describe the copolymerisation of CO_2 and epoxide using a monometallic catalyst. Dinuclear, bicomponent (described below) and mononuclear (described in the introduction of Chapter 4).

The initial step for dinuclear and bicomponent mechanisms involves the activation of a metal catalyst by a co-catalyst, both systems usually are sensitive to high dilution due to the requirement that two separate species come together / form an ion pair for effective catalysis.[11, 43, 44]

Bimetallic mechanism: With a second-order dependence in the catalyst concentration, this mechanism involves a cooperative interaction between two complexes, one activating the epoxide and the other one promoting the nucleophilic attack.[45]

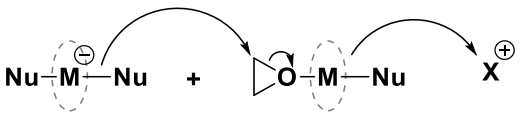


Figure 1.10. Epoxide ring-opening step at the bimetallic mechanism. Nu = anionic co-catalyst or growing carbonate polymer chain.

Bicomponent mechanism: This mechanism consists of a first-order dependence of the catalyst concentration, where the epoxide is coordinated at the metal centre and the attack is performed by a dissociated co-catalyst.[11, 45]



Figure 1.11. Epoxide ring-opening step at the bicomponent mechanism. Nu = anionic co-catalyst or carbonate polymer chain.

1.7. Bifunctional catalysts – Two-component single catalyst

When the metal complex and the co-catalyst are connected a two-component single catalyst is obtained, this strategy prevents the dissociation of the catalyst/cocatalyst pair when the polymerisation is performed at low catalytic loading, increasing the activity and selectivity.[28]

Nozaki and co-workers reported a derivative of (salcy)-Co with a piperidinium 'arm' connected to the complex, Figure 1.12-a.[46] When this catalyst was applied for copolymerisation of CO_2/PO they achieved TOF = 254 h^{-1} ([PO]:[Cat] = 2000:1, 14 bar CO_2) with high selectivity (>99 %) for poly(propylene carbonate). The authors were expecting an improvement in selectivity due to the control in the nucleophilicity of the propagating species provided by the piperidinium 'arms' by protonating the anionic propagating species. Therefore, the propagating species are not nucleophilic enough to backbite and form cyclic carbonate, but can react with CO_2 or activate the epoxide when deprotonated by one of the piperidyl groups.[46, 47] Due to the reduction in cyclic carbonate formation, this catalyst could be used at higher temperatures, accessing TOF = 602 h^{-1} at 60 °C and with 90 % PPC selectivity.[46]

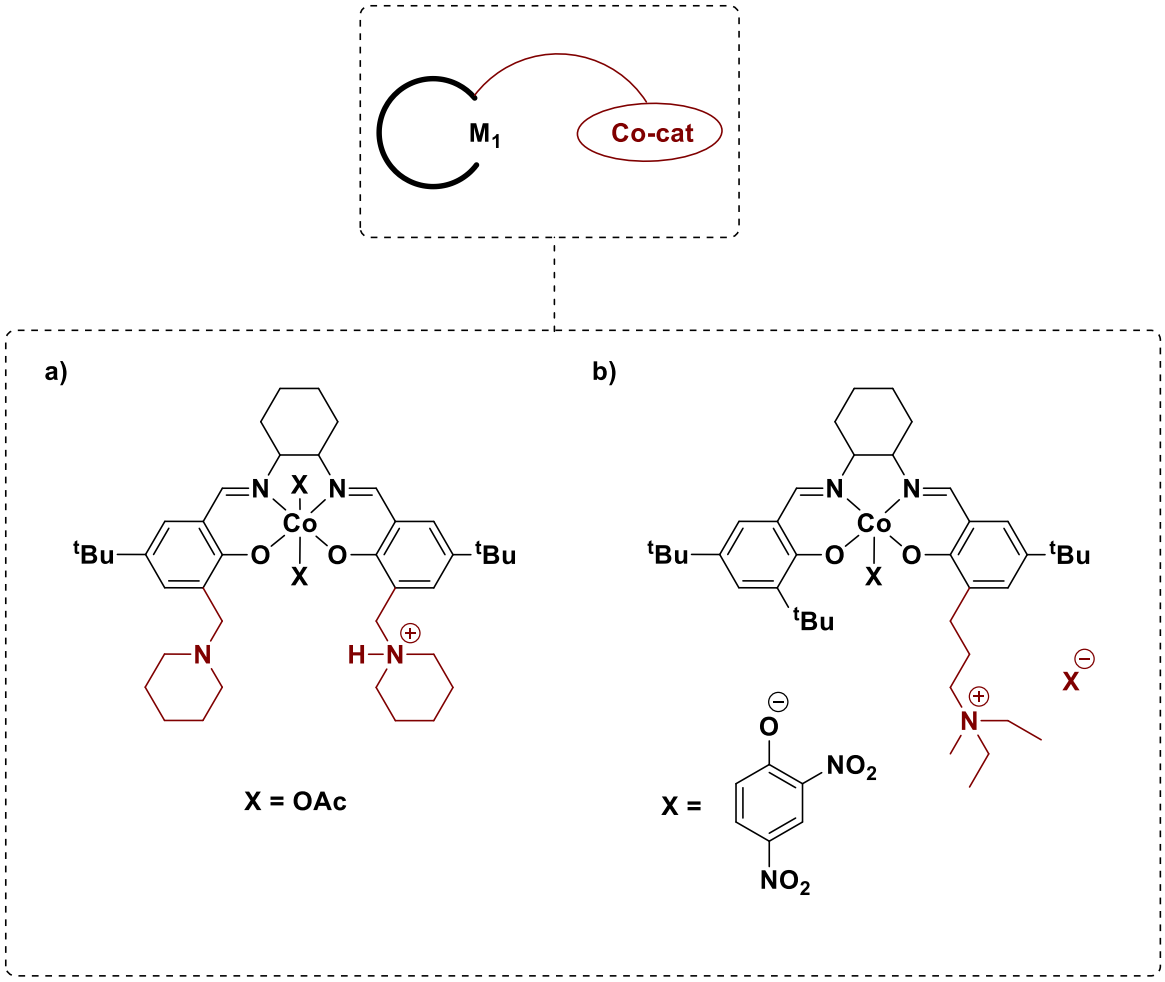


Figure 1.12. Two-component single catalyst derivative of (salcy)–Co with piperidinium 'arm'.

Another example of this strategy using a (salen)Co complexes was reported by Lu and co-workers, where the co-catalyst 'arm' was an ammonium salt, Figure 1.12-b.[48] The thermal stability was again improved, allowing copolymerisation of CO_2/CHO up to 120 °C, obtaining TOFs up to 6105 h^{-1} ([CHO]:[Cat] = 5000:1, 120 °C, 25 bar CO_2) with high PCHC selectivity (>99 %) over the range 25 °C to 120 °C. This catalyst was also active for copolymerisation of CO_2/CHO at 1 bar CO_2 pressure obtaining TOF = 68 h^{-1} and 263 h^{-1} for experiments performed at 25 °C and 50 °C with the same catalyst concentration. Due to the success achieved in the copolymerisation using CHO, the authors also explored the copolymerisation with CO_2/PO obtaining TOF = 497 h^{-1} ([PO]:[Cat] = 5000:1, 25 °C, 15 bar) with good selectivity (>99 %). When the pressure

and temperature were increased to 25 bar of CO_2 and 90 °C, TOF = 5160 h^{-1} was reported with only 6 % of cyclic carbonate formation.[48]

Another possibility to link the co-catalyst 'arm' to the main complex body is through the *para*-phenyl position. Examples of this type of catalyst were published by Lee and co-workers where they attached two ammonium groups at the (salen)Co catalyst, Figure 1.13-a and b.[49,50] Due to the thermostability showed by the complex, the authors were able to study the copolymerisation of CO_2/PO at a range of temperatures (from 50 to 90 °C), obtaining TOF = 3500 h^{-1} at 90 °C and low catalytic loading, ([PO]:[Cat] = 25000:1, 20 bar CO_2) with 90 % polycarbonate selectivity. The authors also showed the possibility to run these polymerisations at low catalytic loading, the authors managed to go as low as a ratio of [PO]:[Cat] = 50000:1, obtaining TOF = 3200 h^{-1} with 84 % PPC selectivity (80 °C, 20 bar CO_2).[49]

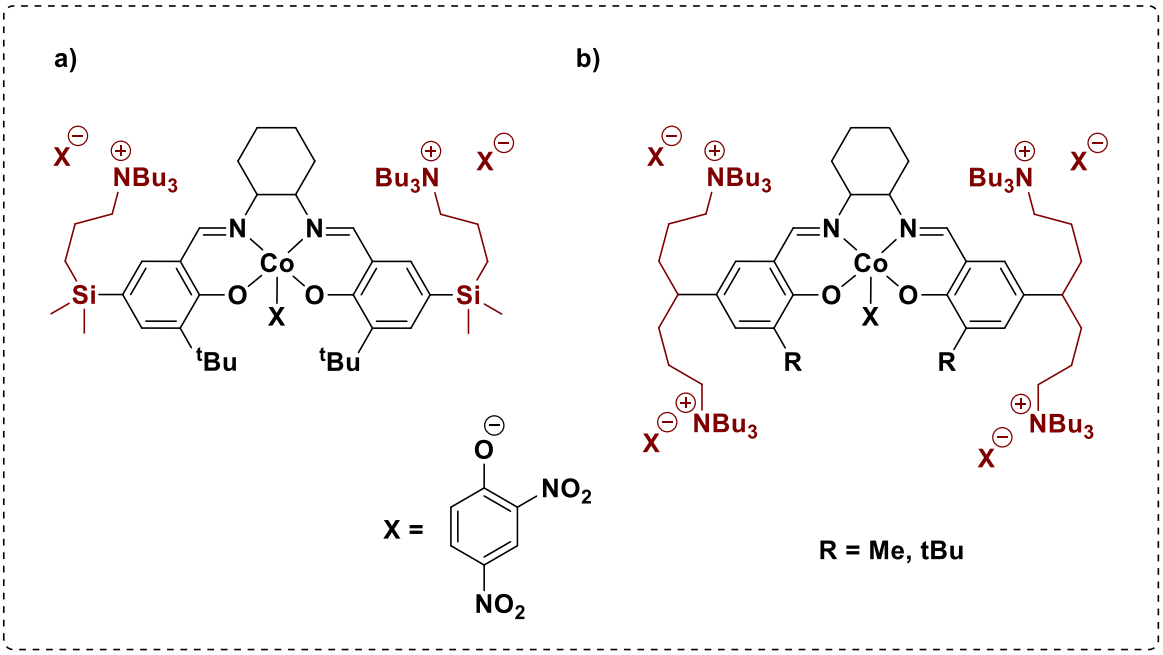


Figure 1.13. Examples of catalysts with two ammonium groups and (salen)Co reported in the literature.[49,50]

Lee and co-workers also studied the (salen)-Co with four onium 'arms' at the *para*-phenyl position and by varying the *ortho*-phenyl substituents (^{t}Bu, ^{i}Pr and Me).[50] Comparing the different *ortho*-substituents, the change from *tert*-butyl group to

methyl enhanced the activity from TOF = 1300 h^{-1} to 26000 h^{-1} ([PO]:[Cat] = 25000:1, 80 °C, 20 bar CO_2) with 99 % PPC selectivity. When the catalyst with Me *ortho*-substituent was tested, at low catalyst concentration, the same TOF and selectivity were obtained. PPC at larger scale was tested and the catalyst was able to show almost same performance with a [PO]:[Cat] = 100,000:1 (250 g PO: 0.095 g catalyst). Due to its quaternary ammonium salts the complex could be separated from the final polymer by filtration through a pad of silica gel and re-used (after being treated with some excess 2,4-dinitrophenol).[50]

Porphyrin catalysts are also used as bifunctional catalysts. A recent example (2020) is Ema, Nozaki, Hasegawa and co-workers' paper where a series of Al(III) porphyrins with quaternary ammonium halides arms (Figure 1.14) were tested for ROCOP of CO_2/CHO.[51]

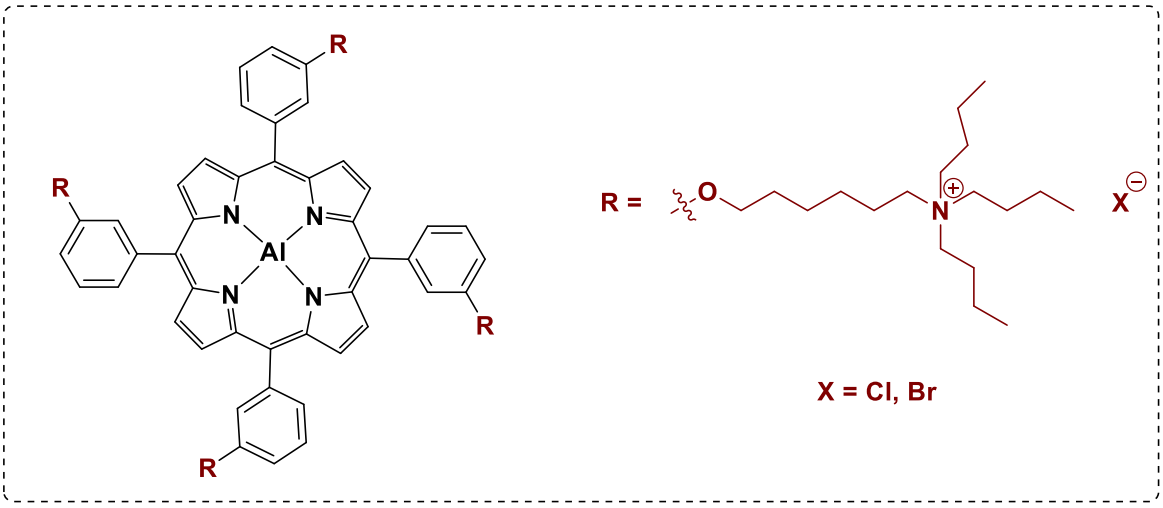


Figure 1.14. Al(III)porphyrin with quaternary ammonium halide as tethered co-catalyst.[51]

This porphyrin catalyst, already previously studied, with Mg(II) and Zn(II) as the metal centres and chloride, iodide and bromide as the counter anion of the ammonium 'arm', and applied for the synthesis of cyclic carbonates showing high activity, however, these prior complexes showed low activity for the formation of polycarbonate.[52, 53] Based on the previous work on cyclic carbonate synthesis, the metal centre of the optimized

structure was replaced to Al (III) achieving TOF = 10,000 h^{-1} ([CHO]:[Cat] = 40,000:1, 120 °C, 20 bar CO_2) for chloride and bromide with good PCHC selectivity (>99 %). The authors performed a kinetic investigation finding a first-order dependence in [CHO] and [Cat] and zero-order dependence in CO_2.[51]

Polymerisation and DFT studies were performed to compare the Mg(II) and Al(III) catalyst systems. The authors suggest that the higher Lewis acidity of Al(III), on one hand, disfavours the CO_2 insertion due to a reduction in the nucleophilicity of the carbonate anion, but, on the other hand, helps to stabilize the species generating in the epoxide ring-opening (rate-determining step). The quaternary ammonium cations not only avoid the diffusion of the anionic intermediates allowing copolymerisation at low catalyst concentration, as shown in Figure 1.15, but also help to stabilize and guide the carbonate anion during the epoxide ring-opening.[51]

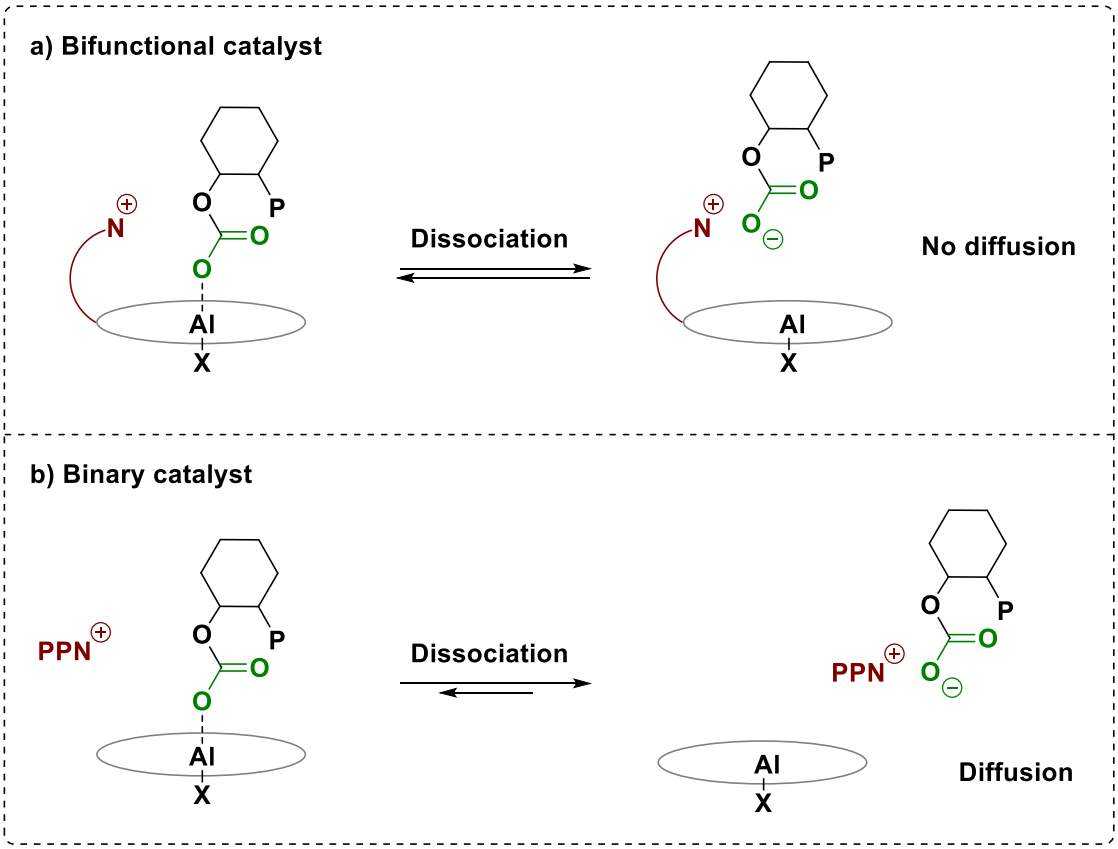


Figure 1.15. Representation of a) bifunctional catalyst; b) binary catalyst. Figure adapted from Ema et al.[51]

1.6. Dinuclear catalysts

In 2003, Coates and co-workers reported a zinc β-diiminate (BDI) catalyst (Figure 1.16) which was later shown to be present under conditions of catalysis as part of a monomer/dimer equilibrium.[54] Different versions of this catalyst were explored varying the initiating groups (OAc, OMe, OiPr, $N(SiMe_3)_2$) and the substitutions in the aniline rings (^{n}Pr, ^{i}Pr, Et, Me) attempting to influence the equilibrium.[54-56] A complex with OAc as the initiating group, varying the aniline ring substituents at the *ortho* position among ^{i}Pr, Et and Me led to three different scenarios. The less bulky substituent (Me) gave a dimer with strong interaction between the monomers (tight dimer), the medium substituent (Et) gave a dimer with a higher distance between Zn–Zn with less strong bonds. The most bulky system (^{i}Pr) gave a monomer/dimer equilibrium. When tested for ROCOP of CO_2/CHO, the tightest dimer was inactive while the equilibrium monomer/dimer showed TOF = 360 h^{-1}, the higher activity was observed for di-zinc with Et groups at *ortho* showing TOF = 431 h^{-1} ([CHO]:[Cat] = 1000:1, 50 °C, 7 bar CO_2). During kinetic studies, the authors found a zero-order dependence in CO_2, first-order dependence in CHO and the order in total zinc varied from 1.0 to 1.8, where the 1.8 order was found for the most active system proposing a bimetallic mechanism.[54] These studies inspired a lot of researchers to study dinuclear catalyst systems.

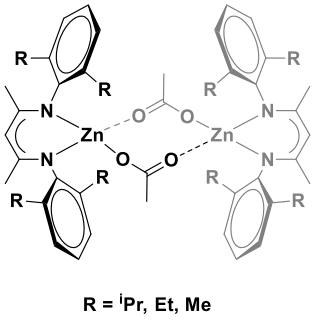


Figure 1.16. Zinc β-diiminate (BDI) catalyst.[54]

The family of dinuclear catalysts can be divided into three sub-groups, single ligand (2a), dimeric catalyst (2b) and tethered catalysts (2c), as shown in Figure 1.17. These systems are applied without the addition of a co-catalyst.[28]

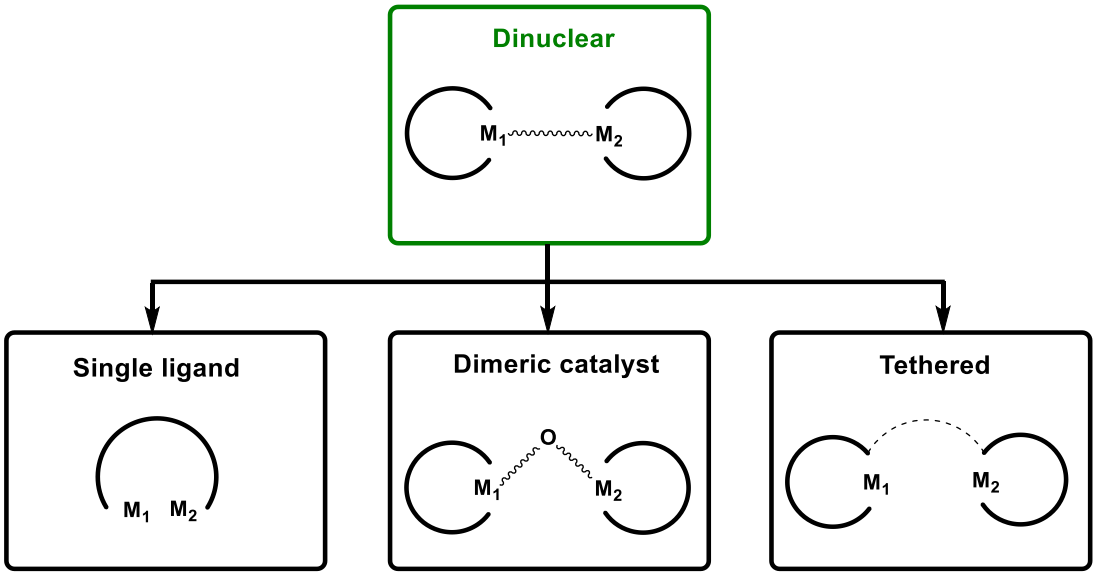


Figure 1.17. Representation of dinuclear catalysts: Singe ligand, dimeric and tethered catalysts. Figure adapted from Williams et al.[28]

1.6.1. Single ligand bimetallic catalysts

The bimetallic catalysts with a single ligand consist of a complex comprising two or more metal centres coordinated within a common ligand, as represented in Figure 1.17.[57]

One of the first examples of a catalyst active for copolymerisation of CO_2/epoxide at low CO_2 pressure (1 bar) was reported by Ding and co-workers where a series of di-zinc and di-magnesium complexes were investigated (Figure 1.18).[58, 59]

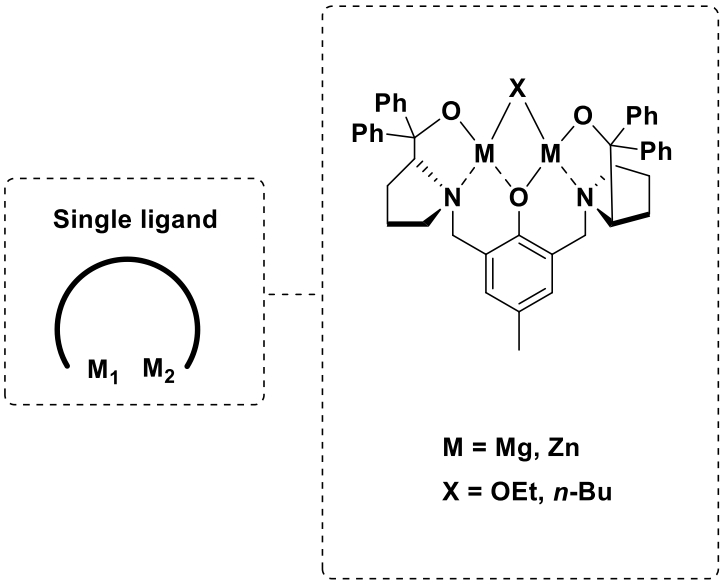


Figure 1.18. Dinuclear catalysts reported in the literature.[58, 59]

Lee and co-workers reported dinuclear zinc derived from an acyclic bis(anilido-aldimine) ligand, as shown in Figure 1.19. This catalyst was able to achieve TOF = 312 h^{-1} at low catalyst concentration ([CHO]:[Cat] = 5600:1, 80 °C, 12 bar CO_2). During this work, different *ortho*-substituents on the N-aryl ring were explored observing higher rates for the combination of isopropyl (R_1) and methyl (R_2) obtaining a TOF = 312 h^{-1}. When all *ortho*-substituents are the same (R_1 = R_2), methyl showed the best activity (TOF = 168 h^{-1}) when compared with ethyl (TOF = 106 h^{-1}) and isopropyl (negligible) under the same conditions ([CHO]:[Cat] = 5600:1, 80 °C, 12 bar CO_2), Figure 1.19-a.[60] When the authors try to achieve polymerisation at more diluted conditions the catalyst decomposed due to its sensitivity to protic impurities (water) present in the monomer. As a strategy to reduce this sensitivity, a fluorinated analogue of the di-zinc complex was prepared to reduce the basicity of the deprotonated anilido nitrogen atom. With this strategy, they managed to perform copolymerisation under dilute conditions ([CHO]:[Cat] = 50,000:1), reporting TOF = 2860 h^{-1} (80 °C, 14 bar CO_2).[61]

A macrocycle version of the di-zinc bis(anilido-aldimine) for ROCOP (Figure 1.19-b) under the same conditions did not show relevant activity due to the strong bond of the methylsulfinate not allowing the polymerisation to initiate.[60]

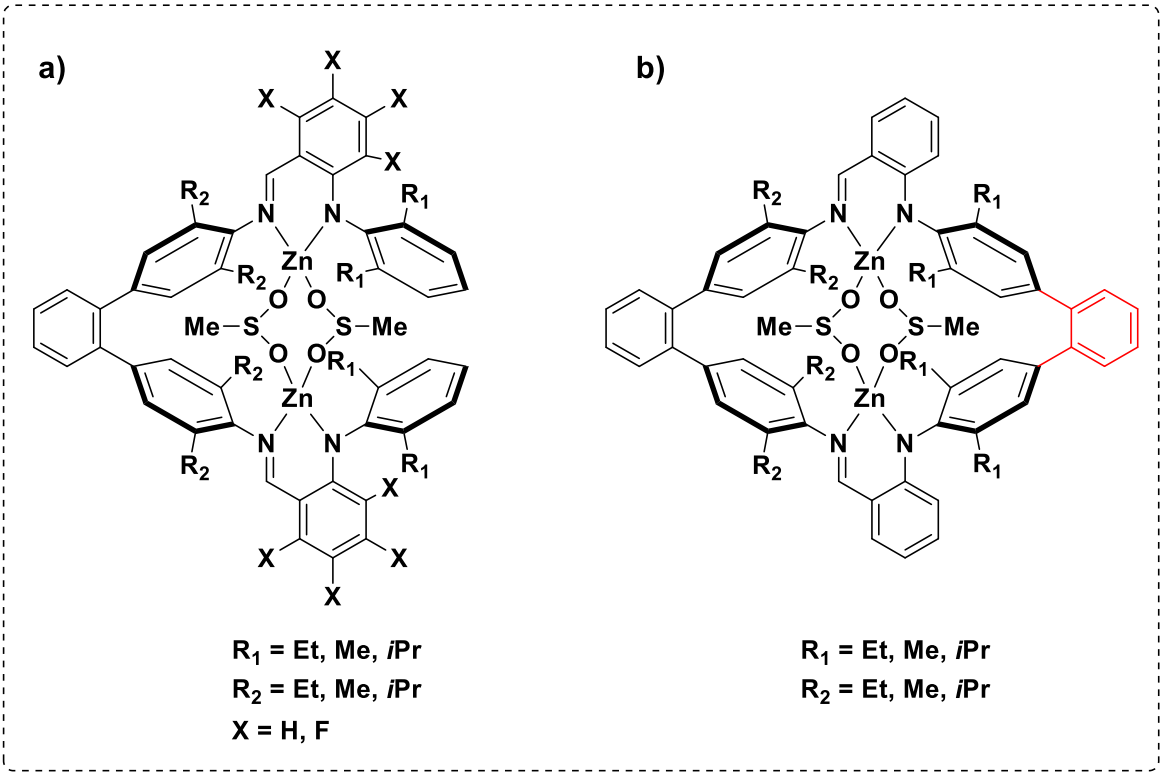


Figure 1.19. Range of single ligand bimetallic catalysts developed by Lee and co-workers. a) Di-zinc with acyclic bis(anilido-aldimine); b) Di-zinc macrocycle with bis(anilido-aldimine). [60, 61]

In 2009, Williams and co-workers published a di-zinc macrocycle (Figure 1.20) active for ROCOP of CO_2/CHO at 1 bar obtaining TOF = 18 h^{-1} ([CHO]:[Cat]=1000:1, 80 °C) with 96 % PCHC selectivity. This catalyst, when tested at a higher temperature, achieved TOF = 25 h^{-1} ([CHO]:[Cat] = 1000:1, 100 °C,) without loss of selectivity (94 %).[62, 63] These results inspired them to explore the effect of the metal centres such as Mg(II)Mg(II), Fe(III)Fe(III) and Co(II)Co(III) on the catalysis, Figure 1.20.

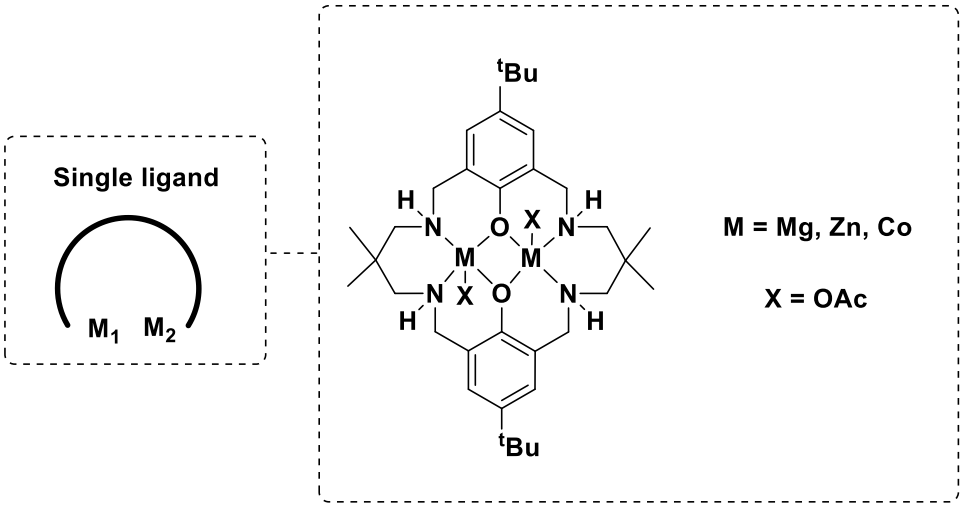


Figure 1.20. Dinuclear catalysts macrocycle explored for ROCOP of CO_2 and epoxide.

All complexes showed activity at 1 bar CO_2 even at low catalyst concentration and under unoptimized conditions showed TOF = 52 h^{-1} (di-magnesium), 6 h^{-1} (di-iron) and 160 h^{-1} (di-cobalt) at 80 °C and [CHO]:[Cat] = 1000:1.[64-67] The increase in activity of the di-cobalt complex can be associated with an increase in nucleophilicity of the intermediate cobalt carbonate.[64, 65] The di-iron catalyst showed the lowest activity when compared with the di-cobalt and di-magnesium complexes, this complex exhibits four chlorides initiating groups and no free coordinating sited to easy access the polymerisation, however, it is important to note it is the first iron catalyst reported for CHO/CO_2 ROCOP.[67] The study with di-cobalt complex at different temperatures showed the possibility to obtain TOF = 480 h^{-1} at 100 °C while retaining good selectivity.[64] The di-magnesium complex was also studied using carbon dioxide captured from a UK coal fired power station and using a model carbon dioxide impurity investigation (by adding progressively greater quantities of different 'impurities' to the CO_2 and measuring activity / productivity / product quality). The catalyst showed a good tolerance to all impurities and performed the polymerisation effectively in the presence of octadecanethiol, diethylamine and water representing the S–H, N–H and O–H functional groups, commonly found in captured carbon dioxide.[68]

Based on the kinetic and DFT studies for the di-zinc macrocycle, a mechanism was proposed, where each metal has a distinct role during the polymerisation and the polymer chain alternates between the metals during each CHO/CO_2 insertion.[69, 70] This mechanism is called "Chain shuttling" and will be discussed in more detail later in this chapter.

Inspired by the idea of each metal has a distinct role during the polymerisation process, Williams and co-workers explored a heterodinuclear macrocyclic complexes with Zn(II)Mg(II) and Br as co-ligand expecting to optimize the coordination and insertion process. The system was tested for ROCOP of CO_2/CHO at 1 bar CO_2 (unoptimized conditions) showing higher activity (TOF = 34 h^{-1}) when compared with the di-zinc (inactive), di-magnesium (TOF = 15 h^{-1}) and a mixture of 1:1 of Mg(II)Mg(II) and Zn(II)Zn(II) (TOF = 7 h^{-1}), under the same conditions ([CHO]:[Cat] = 1000:1, 80 °C). The copolymerisation of CHO/PA (phthalic anhydride) also showed the same trend where the heterodinuclear showed higher activity (TOF = 188 h^{-1}) then the homodinuclear and the mixture of 1:1 of di-zinc and di-magnesium (TOF = 5 h^{-1}), ([CHO]:[PA]:[Cat] = 800:100:1, 100 °C) suggesting an important synergy between the two metal centres. [71]

The heterodinuclear Zn(II)Mg(II) complex was further investigated with different co-ligands such as Br, CF_3, NO_2, NMe_2 and OAc obtaining TOF up to 8830 h^{-1} for CF_3 under optimised conditions ([CHO]:[Cat] = 1000:1, 120 °C, 20 bar CO_2). The different derivatives were also used to investigate the polymerisation mechanism and the individual role of each metal. A solid state structure obtained from a THF solution showed coordination of a molecule of THF at the Mg(II) centre, suggesting that in the

rate-limiting step the zinc provides the carbonate group which attacks the epoxide molecule coordinated at the magnesium centre.[72]

These first studies showing an increase in activity by combining different metals led to new strategies to improve other ROCOP catalysts and are explored in this work in Chapter 3.

The synergy between metals shown in bimetallic complexes can also be translated to multi-metallic complexes. In 2018, Mashima and co-workers reported a heterometallic catalyst with a macrocyclic ligand coordinating three Zn(II) and a Ln(III) centres and with the metals bridged by three acetates as co-ligands, Figure 1.21. By varying the backbones linkages (L^1–L^5, Figure 1.21), with Zn_3La metal centres, the researchers optimized complex solubility and the highest activity and selectivity (>99 %) for PCHC was observed with L^1, TOF = 230 h^{-1} ([CHO]:[Cat] = 2000:1, 100 °C, 10 bar CO_2). Due to the superior catalytic performance of L^1 backbone, this ligand was used to synthesise a series of Zn_3Ln (La, Ce, Pr, Nd, Sm, Eu, Gd, Dy) complexes. Among these complexes, the Ce(III) was able to show TOF = 370 h^{-1} with excellent PCHC selectivity (>99 %). The Zn_3Ce catalyst showed good performance even at low CO_2 pressure, TOF = 330 and 300 h^{-1} at 6 and 3 bar.[73]

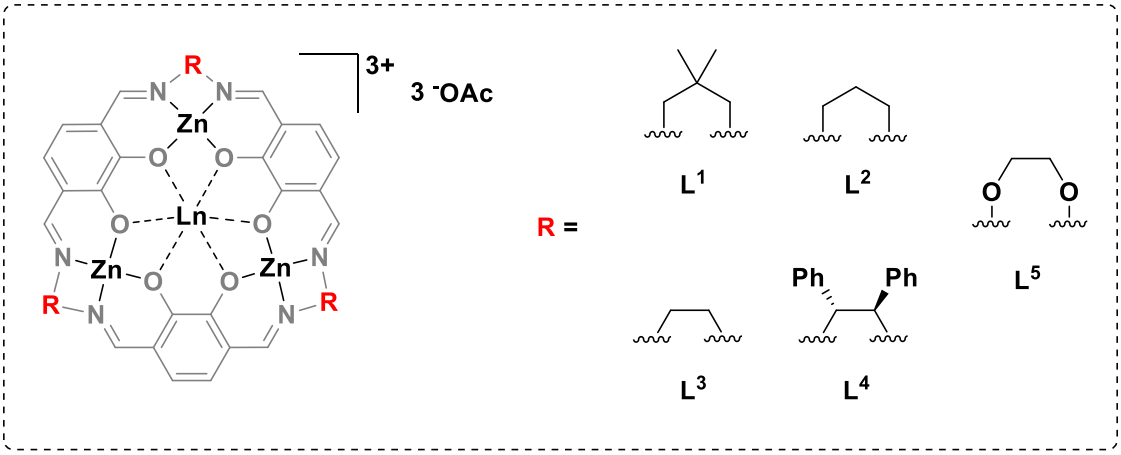


Figure 1.21. Heterometallic catalysts with a macrocyclic tris(salen)-based ligand with three Zn(II) and a Ln(III).[73]

More recently (2020) Nozaki and Mashima reported a four metal complex with three Co(II) and one Ln(III) (Ln = La, Ce, Pr, Nd, Eu and Gd) using the tris(N_2O_2) hexaoxime macrocycle, as shown in Figure 1.22-a. They also synthesised the monomeric version for comparison, Figure 1.22-b.[74-76]

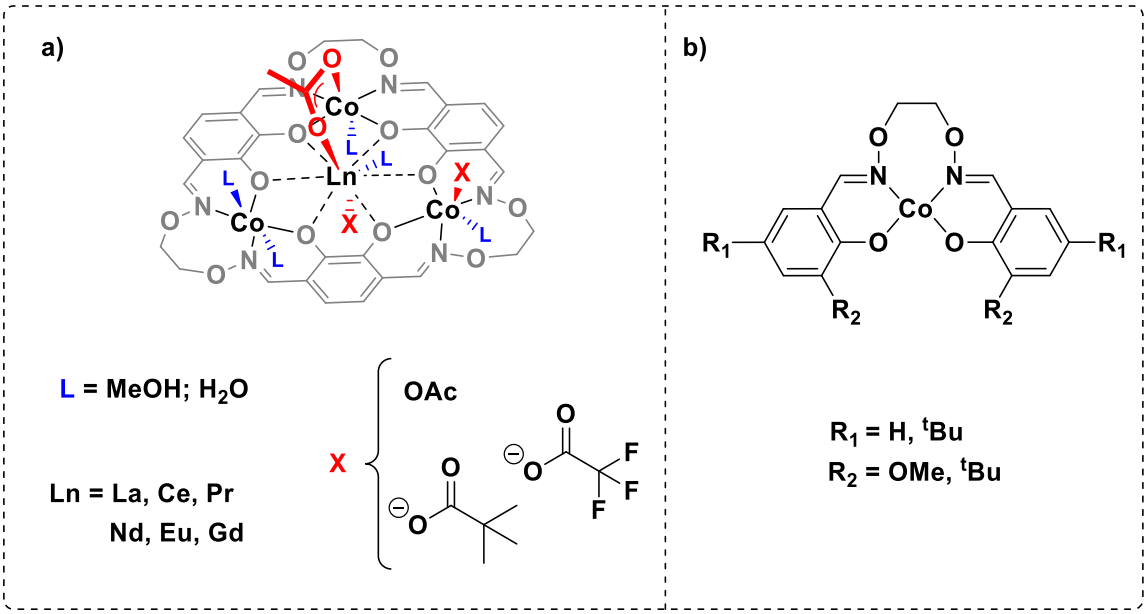


Figure 1.22. a) Tetranuclear complex with tris(N_2O_2) hexaoxime macrocycle. b) (salen)Co(II) mononuclear catalyst.

The $Co(II)_3La(III)$ complex was synthesised with three different initiating groups (acetate, pivalate and trifluoroacetate) and the acetate version showed the best activity among them for ROCOP of CO_2/CHO obtaining TOFs = 1375, 162 and 62 h^{-1} respectively for acetate, pivalate and trifluoroacetate ([CHO]:[Cat] = 20,000:1, 130 °C, 20 bar CO_2). The mononuclear catalyst was tested under the same conditions and showed only a trace amount of polymer formation, even when it was combined with $La(OAc)_3$, this result highlights the importance of the La(III) and Co(II) centres being coordinated together in the macrocyclic environment. The authors also reported a range of $Co(II)_3Ln(III)$ catalysts (Ln(III) = La, Ce, Pr, Nd, Eu, Gd): all of them were able to copolymerise CO_2 and CHO and the highest active catalyst was $Co(II)_3Nd(III)$ with TOF = 1625 h^{-1} ([CHO]:[Cat] = 20,000:1, 130 °C, 20 bar CO_2) with 98 % PCHC selectivity

and $Co(II)_3Sm(III)$ the least active with TOF = 290 h^{-1}. They compared the activity order found to the series of lanthanides complexes with different parameters, such as bond dissociation energy of Ln–O, water-exchange rate constant, ionic radii and hydrolysis constant. However, no obvious correlation could be observed.[74]

1.6.2. Dimeric catalyst

The dimeric catalysts are compounds with more than one metal centres resulted from dimerization of monometallic complexes. An example of this class of catalyst is the zinc β-diiminate (BDI) presented previously. Another example of this class of catalysts was reported by Li and co-workers based on NNO-tridentate Schiff-base ligand coordinated to copper (Figure 1.23-a). The different substituents were explored with the aim of obtaining a mono-, di- and trinuclear complex and test them for copolymerisation of CO_2/CHO. The highest activity was obtained for the bimetallic species with TOF = 18 h^{-1} (20 bar CO_2 and 120 °C).[77]

More recently, Meyer and co-workers, inspired by previous work from Nozaki et al., reported a di-zinc catalyst with a proline-derived ligand, Figure 1.23-b.[78-80] This catalyst was reported as a tetranuclear species in solid-sate (X-ray diffraction) that, based on mass spectrometry and NMR studies, split into an active dimeric species in solution under catalytic conditions. This catalyst obtained good activity TOF = 149 h^{-1} and 99 % selectivity for PCHC under 1 bar CO_2 when tested for ROCOP of CO_2/CHO.[80]

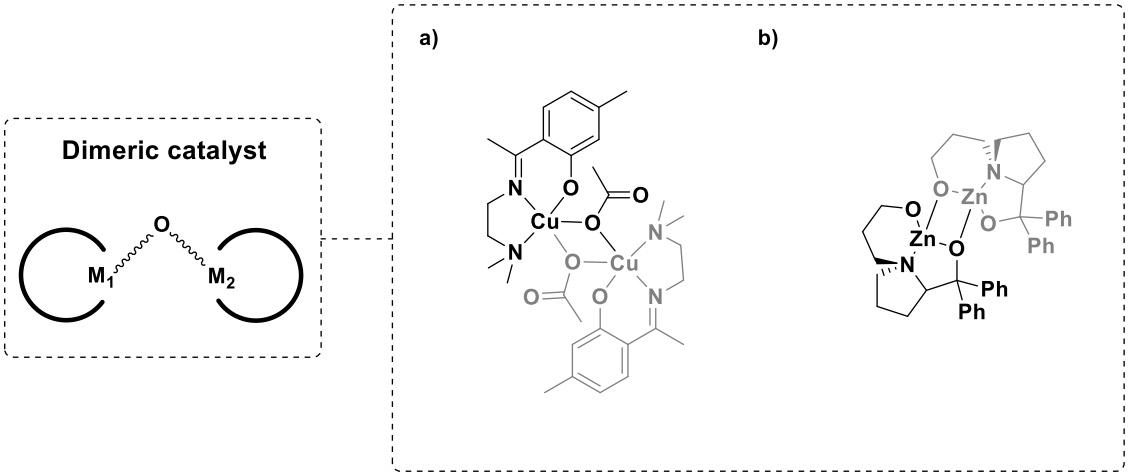


Figure 1.23. Examples of selected other dimeric catalysts reported in the literature.[77, 79]

1.6.3. Tethered Catalysts

This class of catalysts consists of two mononuclear species tethered together obtaining a dinuclear catalyst. Inspired by the previous work of Darensbourg et al.[24, 25] and Coates et al.[55, 56, 81] on zinc phenoxides or zinc BDI complexes, Rieger and co-workers reported an example of this latter class of catalysts, exploring a range of di-zinc complexes with two BDI ligands linked through the phenyl rings (Figure 1.24-a and b).[82-84] Other bridges with different flexibilities were explored (Figure 1.24-a – more flexible example and Figure b – more rigid type ligand).

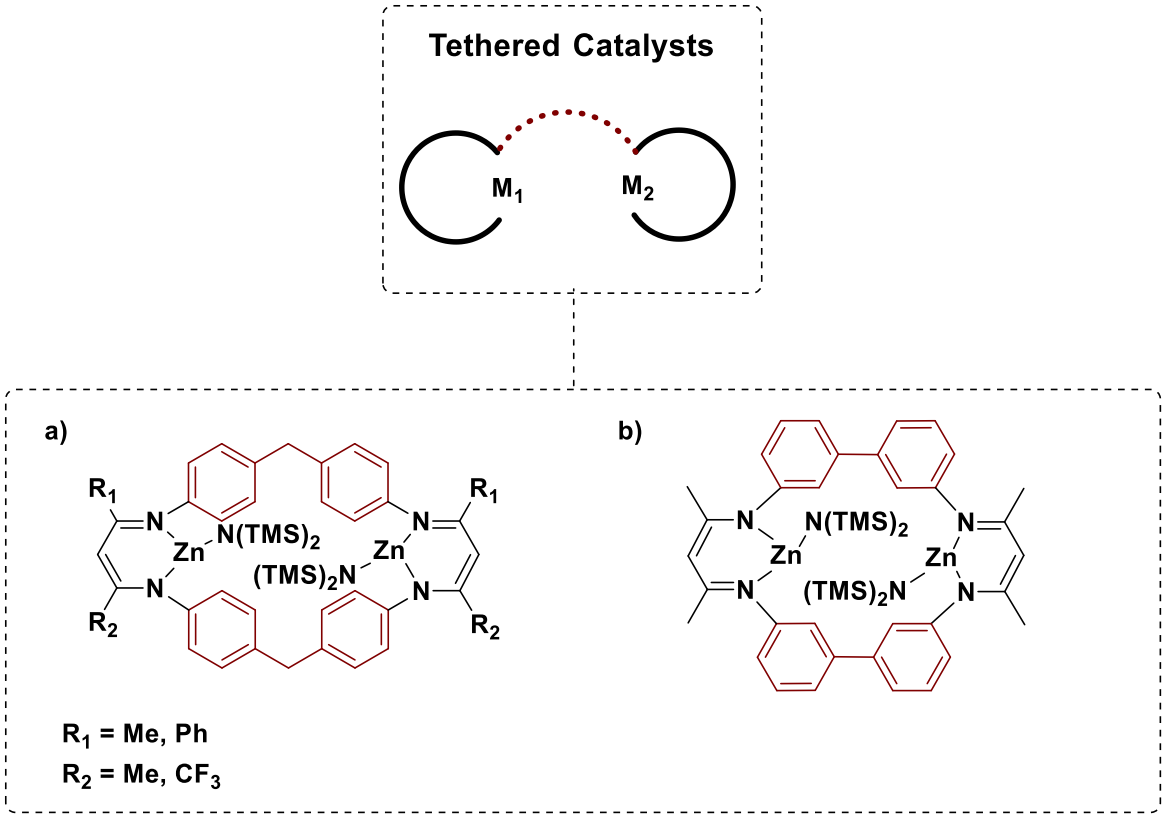


Figure 1.24. Examples of tethered catalysts with different bridges flexibility.[82-84]

They observed that the greater flexibility complex resulted in TOFs up to 9130 h^{-1} (40 bar, 100 °C) for ROCOP of CO_2/CHO with good selectivity, however, this catalyst was inactive for ROCOP of CO_2/PO.[83] Through DFT studies they predicted that the more flexible ligand accelerates the epoxide ring-opening step, allowing the transition states to adopt an optimal structure, shifting the rate-determining step to carbon dioxide insertion.[82, 83] When electron-withdrawing groups were added to the flexible di-zinc catalyst (Figure 1.24-a, with R_1 = Ph and R_2 = CF_3) higher activity was achieved, with TOF up to 155,000 h^{-1} and 88 % PCHC selectivity ([CHO]:[Cat] = 8000:1, 30 bar CO_2, 100 °C). These polymerisations were followed by *in situ* IR spectroscopy, and the activity was calculated considering the initial linear reaction time.[84]

In 2010, Nozaki and Rieger published a series of Co- and Cr-salen based tethered catalysts with a range of different linker lengths (Figure 1.25-a and b)[85, 86].

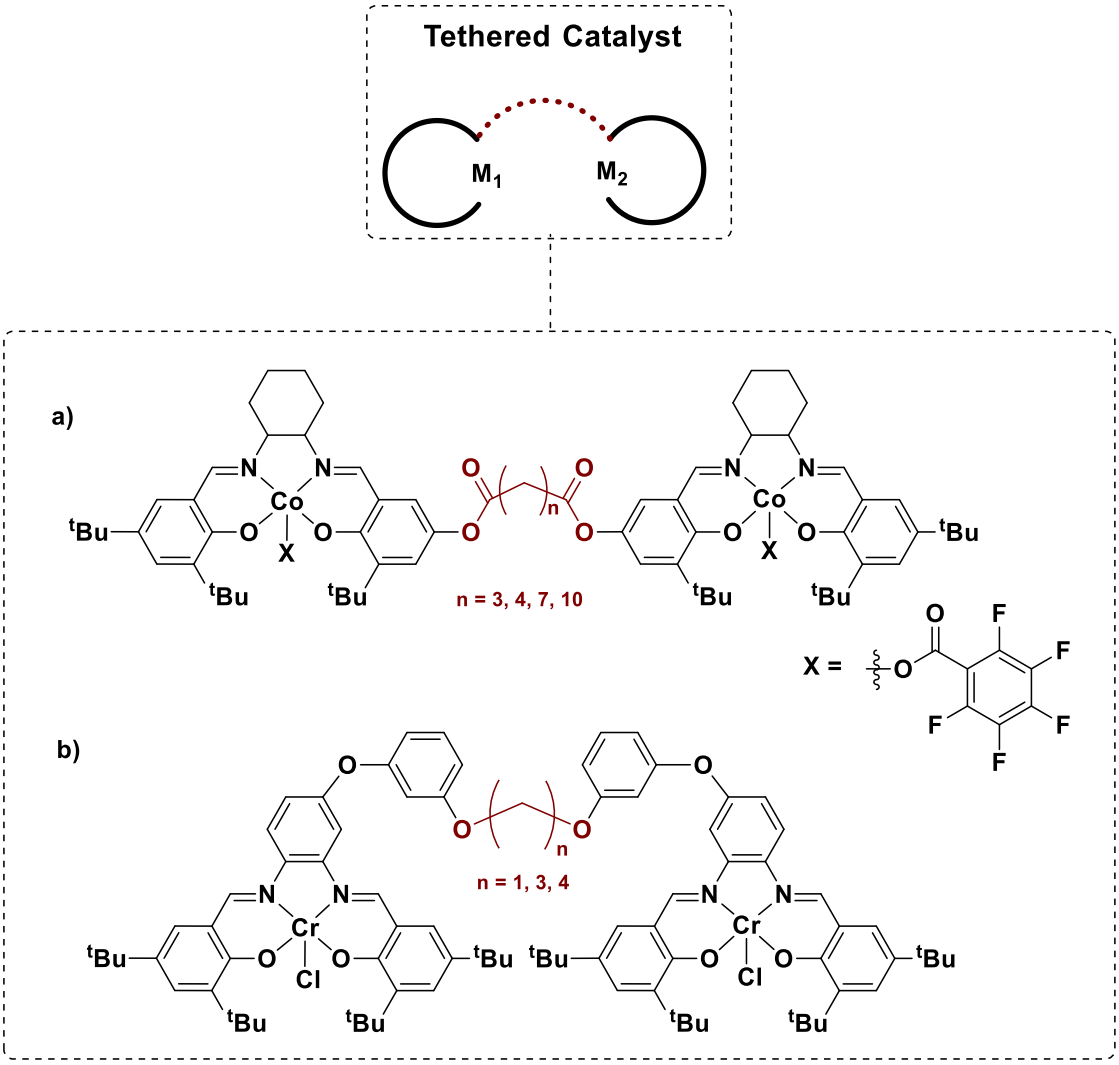


Figure 1.25. Examples of tethered catalysts with different linker lengths.[85, 86]

For the Co-salen system, the best catalyst for copolymerisation of CO_2/PO (without the addition of a co-catalyst) was the complex with four methylene linkers bridging the two Co-salen units, achieving TOF = 180 h^{-1} ([PO]:[Cat] = 1000:1, 50 bar CO_2, 22 °C). This complex was also able to maintain catalytic activity under dilute conditions (TOF = 120 h^{-1}, [PO]:[Cat] = 10,000:1). The catalyst with four-methylene linkers, despite presenting the highest activity, showed lowest selectivity, accelerating the formation of polyether/ether linkages. The authors tested the system capacity to perform copolymerisation with and without the addition of a co-catalyst, inducing the system to propagate *via* a monometallic (with cocatalyst) or bimetallic (without cocatalyst) mechanism.[85]

The complex derived from Cr-salen systems was also active for copolymerisation of CO_2/PO, without the addition of a co-catalyst even at low catalytic loading, and it showed higher activity compared with the monometallic analogue with TOF = 82 h^{-1} and 7 h^{-1}, respectively ([PO]:[Cat] = 2000:1). This system also follows either a bimetallic or bicomponent mechanisms, when tested in the absence and presence of a co-catalyst.[86, 87]

1.6.4. Dinuclear catalyst mechanism – Polymer chain shuttling mechanism

Mechanistic studies using a di-zinc macrocycle showed a first-order dependence on catalyst and epoxide concentrations and a zero-order dependence on CO_2 pressure (1–40 bar) (Figure 1.26). The catalyst presented an overall second-order rate law.[69] During the polymerisation, one metal centre is responsible for activating the epoxide while the other one provides the nucleophile.[69, 70]

The macrocycle can assume two conformations in the solid state: "bowl" and "S" – shape. Based on DFT, X-ray crystallography and *in situ* spectroscopy studies, the structure where all NH substituents are on the same side of the molecule (bowl-shape conformation) has the lowest energy and it is proposed that initiation occurs from the acetate group coordinated on the convex face of the catalyst.[70]

During the initiation step, the epoxide is activated by one of the metal centres and then during initiation, the acetate performs a nucleophilic attack at the epoxide, leading to the formation of a metal-alkoxide species. This metal alkoxide undergoes the fast insertion of CO_2. The second acetate coordinated on the concave face is proposed to remain coordinated to both metal centres (κ^2) throughout the polymerisations. It's function appears to be to maintain metallic octahedral coordination environments and to provide charge balance during the polymerisation. The rate-determining step is

nucleophilic attack of the zinc-carbonate group at the epoxide and during the sequence of ring-opening and CO_2 insertion, the growing polymer chain shuttles between the metal centres.[69]

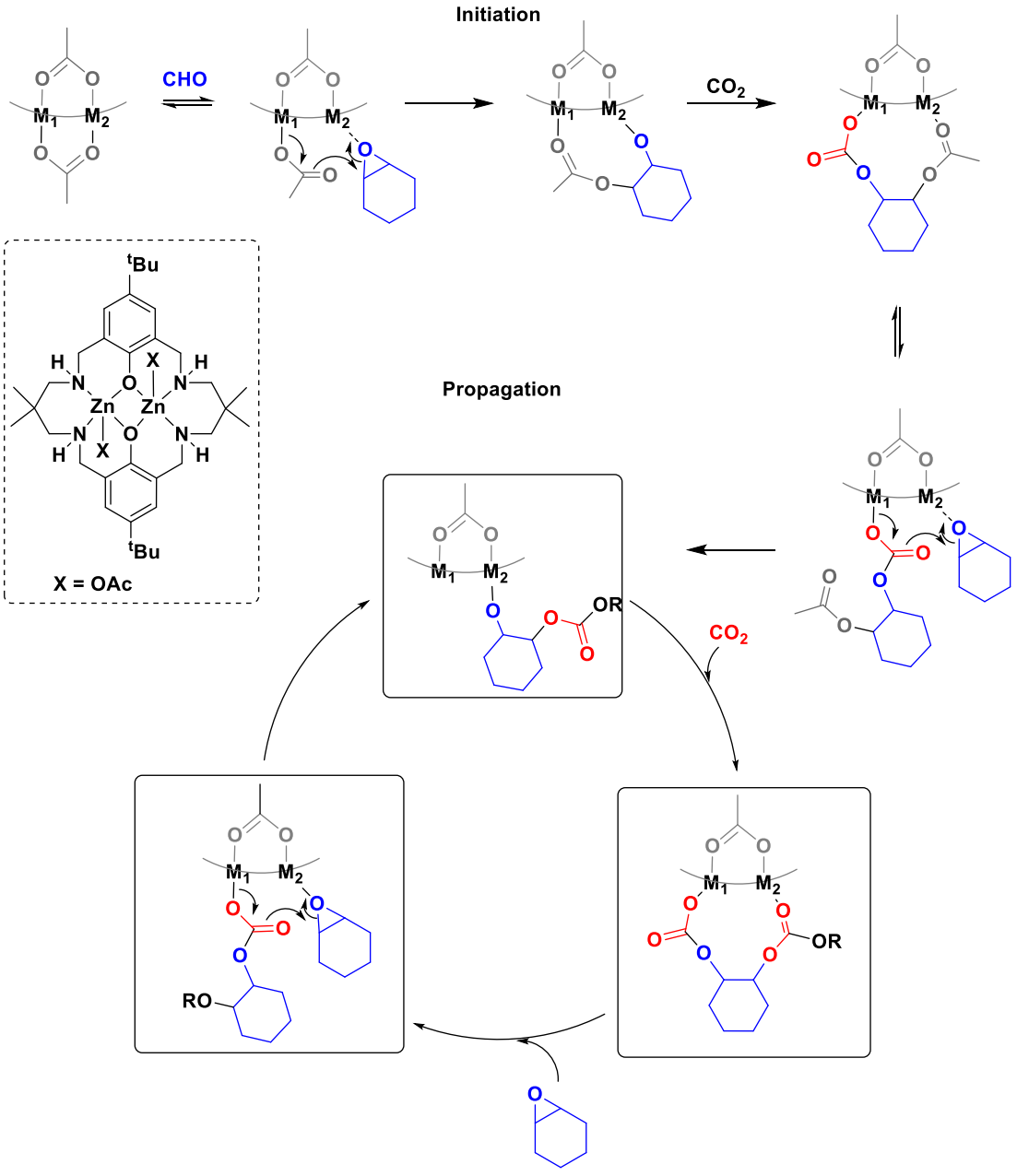


Figure 1.26. Chain-shuttling mechanism. The ligand scaffold is depicted as a curve line and the growing chain denoted as 'R'. Figure adapted from Williams et al.[69, 71]

1.8. Aims

This thesis will explore two different catalytic systems for the ring-opening copolymerisation of CO_2/epoxides (mainly CHO), using a range of monometallic (bifunctional–Two components) and bimetallic (single ligand bimetallic) catalysts.[71, 88, 89]

Heterodunuclear Catalysts: The goals are to undertake the following experiments:

- To synthesise and explore combinations of Mg(II) and the first-row transition metals (M(II) where M = Cr, Mn, Fe, Co, Ni, Cu and Zn) to produce heterobimetallic complexes. The key question is to understand whether the synthesis developed for Mg/Co is generalizable to the other metals. These new complexes will all need to be characterized, including using techniques suitable for paramagnetic complexes.
- To test these heterodinuclear catalysts in terms of the rate and selectivity for the ROCOP of CO_2/CHO. The goal is to understand the differences between the different transition metal centres. To ensure this is reproducible and reliable it is preferable to use detailed kinetic analysis (rate coefficients) rather than point kinetics measures (turn-over frequency). The reason for this was already established in the study from Trott et al. using ZnMg catalysts where they showed that simply analysing rates using TOF can lead to misinterpretations of actual rates of propagation because the TOF value include initiation and propagation rates. Thus, to properly understand the influences of the second metal, if any, over polymerisation will require analysis of propagation rate coefficients. In parallel with analysis to the rates of polymerisation, it will be

necessary also to evaluate the polymerisation selectivity and polymer molar mass/dispersity values.

- To evaluate the rate data (propagation) and to understand whether these data fit the chain shuttling mechanism and whether trends can be interpreted/predicted. This is a very challenging objective as most previous research fails to address why a particular metal centre is optimal for catalysis, yet it remains a key need to the field. It is also worth emphasis that the study of Trott et al. showed that there was not a clear relationship between rate and co-ligand hammet parameter, implying a more complex interdependence of physical-chemical phenome over rate.
- To explore the activity with the most active catalyst for a range of monomers, including vCHO, CPO and E-THE. The goal being to understand the scope for more general use of these catalysts and the influence of catalysts upon rates/selectivity.

Monometallic catalysts will also be examined with the following objectives and key research questions:

- To access a variety of salan and salen complexes with In(III), with different ligand backbone flexibility. The goal is to build upon the earlier work of Thevenon et al. using phosphasalen indium catalysts and to try to improve upon the rates observed using these *cis*-mononuclear catalysts.
- To understand whether the use of more flexible backbones does allow access the *cis*-coordination of epoxide and initiating group. This work will be conducted through analysis of the ground-state structures of the metal complexes, through temperature dependent studies and through studies to

understand any structural changes which may occur upon donor binding (e. g. THF or epoxide).

- To modify the nitrogen-substituents to salan, altering the electronic density at the In(III) active site, to understand the influences on low pressure copolymerisation of CHO/CO_2
- To investigate the influence of electron-withdrawing groups at the *para*-phenolate site on (salan)-In systems. This section was developed in collaboration with Mr Sebastian Morton (Williams group part II student).

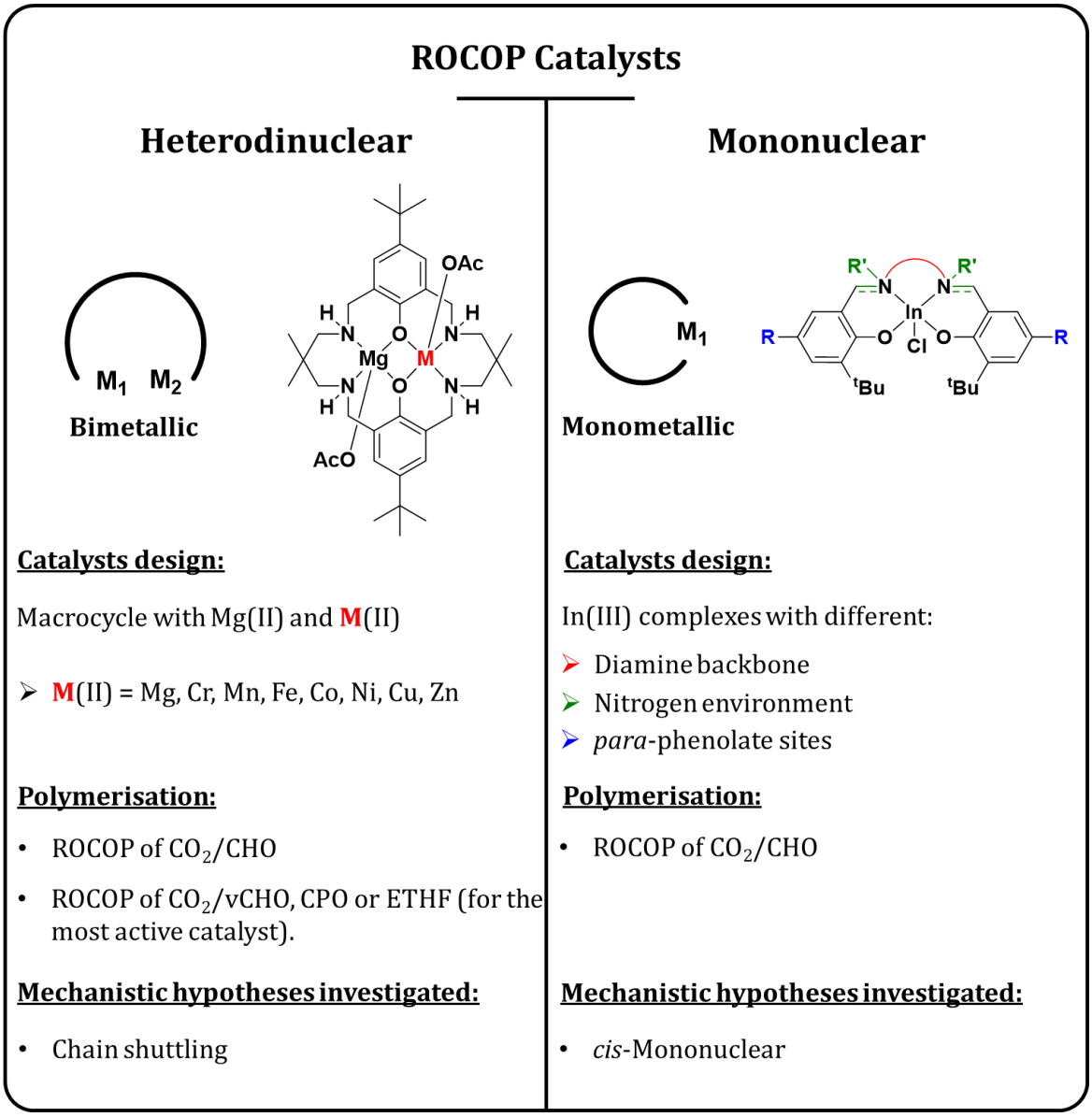


Figure 1.27. Systems explored in this thesis.

1.9. References

1. Zhang, X.; Fevre, M.; Jones, G. O.; Waymouth, R. M., Catalysis as an Enabling Science for Sustainable Polymers. *Chem. Rev.* **2018,** *118* (2), 839-885.
2. Geyer, R.; Jambeck, J. R.; Law, K. L., Production, use, and fate of all plastics ever made. *Sci. Adv.* **2017,** *3* (7), e1700782.
3. *Science to enable sustainable plastics - A white paper from the 8th Chemical Sciences and Society Summit (CS3)* Royal Society of Chemistry, 2020.
4. *An analysis of European plastic production, demand and waste data*; PlasticsEurope, 2019.
5. Szycher, M., *Szycher's Handbook of Polyurethanes*. Second Edition ed.; CRC Press, 2013.
6. Akindoyo, J. O.; Beg, M. D. H.; Ghazali, S.; Islam, M. R.; Jeyaratnam, N.; Yuvaraj, A. R., Polyurethane types, synthesis and applications – a review. *RSC Advances* **2016,** *6* (115), 114453-114482.
7. Avar, G.; Meier-Westhues, U.; Casselmann, H.; Achten, D., 10.24 - Polyurethanes. In *Polymer Science: A Comprehensive Reference*, Matyjaszewski, K.; Möller, M., Eds. Elsevier: Amsterdam, 2012; pp 411-441.
8. von der Assen, N.; Bardow, A., Life cycle assessment of polyols for polyurethane production using CO_2 as feedstock: insights from an industrial case study. *Green Chem.* **2014,** *16* (6), 3272-3280.
9. Wang, Y.; Darensbourg, D. J., Carbon dioxide-based functional polycarbonates: Metal catalyzed copolymerization of CO_2 and epoxides. *Coord. Chem. Rev.* **2018,** *372*, 85-100.
10. Darensbourg, D. J.; Wilson, S. J., What's new with CO_2? Recent advances in its copolymerization with oxiranes. *Green Chem.* **2012,** *14* (10), 2665-2671.
11. Klaus, S.; Lehenmeier, M. W.; Anderson, C. E.; Rieger, B., Recent advances in CO_2/epoxide copolymerization—New strategies and cooperative mechanisms. *Coord. Chem. Rev.* **2011,** *255* (13), 1460-1479.
12. Paul, S.; Zhu, Y.; Romain, C.; Brooks, R.; Saini, P. K.; Williams, C. K., Ring-opening copolymerization (ROCOP): synthesis and properties of polyesters and polycarbonates. *Chem. Comm.* **2015,** *51* (30), 6459-6479.
13. Kember, M. R.; Buchard, A.; Williams, C. K., Catalysts for CO_2/epoxide copolymerisation. *Chem. Comm.* **2011,** *47* (1), 141-163.
14. Trott, G.; Saini, P. K.; Williams, C. K., Catalysts for CO_2/epoxide ring-opening copolymerization. *Philos. Trans. R. Soc. A* **2016,** *374* (2061), 20150085.
15. Szwarc, M., 'Living' Polymers. *Nature* **1956,** *178* (4543), 1168-1169.
16. Penczek, S.; Pretula, J.; Lewiński, P., Dormant Polymers and Their Role in Living and Controlled Polymerizations; Influence on Polymer Chemistry, Particularly on the Ring Opening Polymerization. *Polymers (Basel)* **2017,** *9* (12), 646.
17. Jenkins, A. D.; Kratochvíl, P.; Stepto, R. F. T.; Suter, U. W., Glossary of basic terms in polymer science (IUPAC Recommendations 1996). *Pure App. Chem.* **1996,** *68* (12), 2287-2311.
18. Stanisław, P.; Graeme, M., Glossary of terms related to kinetics, thermodynamics, and mechanisms of polymerization (IUPAC Recommendations 2008). *Pure Appl. Chem.* **2008,** *80* (10), 2163-2193.
19. Müller, A. H.; Matyjaszewski, K., *Controlled and living polymerizations*. Wiley-VCH: 2009.

20. Wu, G.-P.; Darensbourg, D. J., Mechanistic Insights into Water-Mediated Tandem Catalysis of Metal-Coordination CO_2/Epoxide Copolymerization and Organocatalytic Ring-Opening Polymerization: One-Pot, Two Steps, and Three Catalysis Cycles for Triblock Copolymers Synthesis. *Macromolecules* **2016,** *49* (3), 807-814.
21. Darensbourg, D. J., Chain transfer agents utilized in epoxide and CO_2 copolymerization processes. *Green Chem.* **2019,** *21* (9), 2214-2223.
22. Inoue, S.; Koinuma, H.; Tsuruta, T., Copolymerization of carbon dioxide and epoxide. *J. Polym. Sci. B Polym. Lett.* **1969,** *7* (4), 287-292.
23. Takeda, N.; Inoue, S., Polymerization of 1,2-epoxypropane and copolymerization with carbon dioxide catalyzed by metalloporphyrins. *Die Makromolekulare Chemie* **1978,** *179* (5), 1377-1381.
24. Darensbourg, D. J.; Holtcamp, M. W., Catalytic Activity of Zinc(II) Phenoxides Which Possess Readily Accessible Coordination Sites. Copolymerization and Terpolymerization of Epoxides and Carbon Dioxide. *Macromolecules* **1995,** *28* (22), 7577-7579.
25. Darensbourg, D. J.; Holtcamp, M. W.; Struck, G. E.; Zimmer, M. S.; Niezgoda, S. A.; Rainey, P.; Robertson, J. B.; Draper, J. D.; Reibenspies, J. H., Catalytic Activity of a Series of Zn(II) Phenoxides for the Copolymerization of Epoxides and Carbon Dioxide. *J. Am. Chem. Soc.* **1999,** *121* (1), 107-116.
26. Darensbourg, D. J.; Wildeson, J. R.; Yarbrough, J. C.; Reibenspies, J. H., Bis 2,6-difluorophenoxide Dimeric Complexes of Zinc and Cadmium and Their Phosphine Adducts: Lessons Learned Relative to Carbon Dioxide/Cyclohexene Oxide Alternating Copolymerization Processes Catalyzed by Zinc Phenoxides. *J. Am. Chem. Soc.* **2000,** *122* (50), 12487-12496.
27. Darensbourg, D. J., Making Plastics from Carbon Dioxide: Salen Metal Complexes as Catalysts for the Production of Polycarbonates from Epoxides and CO_2. *Chem. Rev.* **2007,** *107* (6), 2388-2410.
28. Romain, C.; Thevenon, A.; Saini, P. K.; Williams, C. K., Dinuclear Metal Complex-Mediated Formation of CO_2-Based Polycarbonates. In *Carbon Dioxide and Organometallics. Topics in Organomet. Chem.*, Lu, X., Ed. Springer, Cham: 2015; Vol. 53.
29. Jacobsen, E. N.; Zhang, W.; Muci, A. R.; Ecker, J. R.; Deng, L., Highly enantioselective epoxidation catalysts derived from 1,2-diaminocyclohexane. *J. Am. Chem. Soc.* **1991,** *113* (18), 7063-7064.
30. Brandes, B. D.; Jacobsen, E. N., Highly Enantioselective, Catalytic Epoxidation of Trisubstituted Olefins. *J. Org. Chem.* **1994,** *59* (16), 4378-4380.
31. Paddock, R. L.; Nguyen, S. T., Chemical CO_2 Fixation: Cr(III) Salen Complexes as Highly Efficient Catalysts for the Coupling of CO_2 and Epoxides. *J. Am. Chem. Soc.* **2001,** *123* (46), 11498-11499.
32. Jacobsen, E. N., Asymmetric Catalysis of Epoxide Ring-Opening Reactions. *Acc. Chem. Res.* **2000,** *33* (6), 421-431.
33. Hansen, K. B.; Leighton, J. L.; Jacobsen, E. N., On the Mechanism of Asymmetric Nucleophilic Ring-Opening of Epoxides Catalyzed by (Salen)CrIII Complexes. *J. Am. Chem. Soc.* **1996,** *118* (44), 10924-10925.
34. Martinez, L. E.; Leighton, J. L.; Carsten, D. H.; Jacobsen, E. N., Highly Enantioselective Ring Opening of Epoxides Catalyzed by (salen)Cr(III) Complexes. *J. Am. Chem. Soc.* **1995,** *117* (21), 5897-5898.
35. Kruper, W. J.; Dellar, D. D., Catalytic Formation of Cyclic Carbonates from Epoxides and CO_2 with Chromium Metalloporphyrinates. *J. Org. Chem.* **1995,** *60* (3), 725-727.

36. Darensbourg, D. J.; Yarbrough, J. C., Mechanistic Aspects of the Copolymerization Reaction of Carbon Dioxide and Epoxides, Using a Chiral Salen Chromium Chloride Catalyst. *J. Am. Chem. Soc.* **2002,** *124* (22), 6335-6342.
37. Cohen, C. T.; Chu, T.; Coates, G. W., Cobalt Catalysts for the Alternating Copolymerization of Propylene Oxide and Carbon Dioxide: Combining High Activity and Selectivity. *J. Am. Chem. Soc.* **2005,** *127* (31), 10869-10878.
38. Lu, X.-B.; Wang, Y., Highly Active, Binary Catalyst Systems for the Alternating Copolymerization of CO_2 and Epoxides under Mild Conditions. *Angew. Chem. Int. Ed.* **2004,** *43* (27), 3574-3577.
39. Qin, Z.; Thomas, C. M.; Lee, S.; Coates, G. W., Cobalt-Based Complexes for the Copolymerization of Propylene Oxide and CO_2: Active and Selective Catalysts for Polycarbonate Synthesis. *Angew. Chem. Int. Ed.* **2003,** *42* (44), 5484-5487.
40. Lu, X.-B.; Shi, L.; Wang, Y.-M.; Zhang, R.; Zhang, Y.-J.; Peng, X.-J.; Zhang, Z.-C.; Li, B., Design of Highly Active Binary Catalyst Systems for CO_2/Epoxide Copolymerization: Polymer Selectivity, Enantioselectivity, and Stereochemistry Control. *J. Am. Chem. Soc.* **2006,** *128* (5), 1664-1674.
41. Darensbourg, D. J.; Ulusoy, M.; Karroonnirum, O.; Poland, R. R.; Reibenspies, J. H.; Çetinkaya, B., Highly Selective and Reactive (salan)CrCl Catalyst for the Copolymerization and Block Copolymerization of Epoxides with Carbon Dioxide. *Macromolecules* **2009,** *42* (18), 6992-6998.
42. Balsells, J.; Carroll, P. J.; Walsh, P. J., Achiral Tetrahydrosalen Ligands for the Synthesis of C2-Symmetric Titanium Complexes: A Structure and Diastereoselectivity Study. *Inorg. Chem.* **2001,** *40* (22), 5568-5574.
43. Thevenon, A.; Cyriac, A.; Myers, D.; White, A. J. P.; Durr, C. B.; Williams, C. K., Indium Catalysts for Low-Pressure CO_2/Epoxide Ring-Opening Copolymerization: Evidence for a Mononuclear Mechanism? *J. Am. Chem. Soc.* **2018,** *140*, 6893-6903.
44. Darensbourg, D. J.; Mackiewicz, R. M., Role of the Cocatalyst in the Copolymerization of CO_2 and Cyclohexene Oxide Utilizing Chromium Salen Complexes. *J. Am. Chem. Soc.* **2005,** *127* (40), 14026-14038.
45. Ohkawara, T.; Suzuki, K.; Nakano, K.; Mori, S.; Nozaki, K., Facile Estimation of Catalytic Activity and Selectivities in Copolymerization of Propylene Oxide with Carbon Dioxide Mediated by Metal Complexes with Planar Tetradentate Ligand. *J. Am. Chem. Soc.* **2014,** *136* (30), 10728-10735.
46. Nakano, K.; Kamada, T.; Nozaki, K., Selective Formation of Polycarbonate over Cyclic Carbonate: Copolymerization of Epoxides with Carbon Dioxide Catalyzed by a Cobalt(III) Complex with a Piperidinium End-Capping Arm. *Angew. Chem. Int. Ed.* **2006,** *45* (43), 7274-7277.
47. Luinstra, G. A.; Haas, G. R.; Molnar, F.; Bernhart, V.; Eberhardt, R.; Rieger, B., On the Formation of Aliphatic Polycarbonates from Epoxides with Chromium(III) and Aluminum(III) Metal–Salen Complexes. *Chem. Eur. J.* **2005,** *11* (21), 6298-6314.
48. Ren, W.-M.; Zhang, X.; Liu, Y.; Li, J.-F.; Wang, H.; Lu, X.-B., Highly Active, Bifunctional Co(III)-Salen Catalyst for Alternating Copolymerization of CO_2 with Cyclohexene Oxide and Terpolymerization with Aliphatic Epoxides. *Macromolecules* **2010,** *43* (3), 1396-1402.
49. Noh, E. K.; Na, S. J.; S, S.; Kim, S.-W.; Lee, B. Y., Two Components in a Molecule: Highly Efficient and Thermally Robust Catalytic System for CO_2/Epoxide Copolymerization. *J. Am. Chem. Soc.* **2007,** *129* (26), 8082-8083.

50. Sujith, S.; Min, J. K.; Seong, J. E.; Na, S. J.; Lee, B. Y., A highly active and recyclable catalytic system for CO_2/propylene oxide copolymerization. *Angew. Chem. Int. Ed. Engl.* **2008,** *47* (38), 7306-9.
51. Deng, J.; Ratanasak, M.; Sako, Y.; Tokuda, H.; Maeda, C.; Hasegawa, J.-y.; Nozaki, K.; Ema, T., Aluminum porphyrins with quaternary ammonium halides as catalysts for copolymerization of cyclohexene oxide and CO_2: metal–ligand cooperative catalysis. *Chem. Sci.* **2020,** *11* (22), 5669-5675.
52. Ema, T.; Miyazaki, Y.; Koyama, S.; Yano, Y.; Sakai, T., A bifunctional catalyst for carbon dioxide fixation: cooperative double activation of epoxides for the synthesis of cyclic carbonates. *Chem. Comm.* **2012,** *48* (37), 4489-4491.
53. Ema, T.; Miyazaki, Y.; Shimonishi, J.; Maeda, C.; Hasegawa, J.-y., Bifunctional Porphyrin Catalysts for the Synthesis of Cyclic Carbonates from Epoxides and CO_2: Structural Optimization and Mechanistic Study. *J. Am. Chem. Soc.* **2014,** *136* (43), 15270-15279.
54. Moore, D. R.; Cheng, M.; Lobkovsky, E. B.; Coates, G. W., Mechanism of the Alternating Copolymerization of Epoxides and CO_2 Using β-Diiminate Zinc Catalysts: Evidence for a Bimetallic Epoxide Enchainment. *J. Am. Chem. Soc.* **2003,** *125* (39), 11911-11924.
55. Cheng, M.; Lobkovsky, E. B.; Coates, G. W., Catalytic Reactions Involving C1 Feedstocks: New High-Activity Zn(II)-Based Catalysts for the Alternating Copolymerization of Carbon Dioxide and Epoxides. *J. Am. Chem. Soc.* **1998,** *120* (42), 11018-11019.
56. Cheng, M.; Moore, D. R.; Reczek, J. J.; Chamberlain, B. M.; Lobkovsky, E. B.; Coates, G. W., Single-Site β-Diiminate Zinc Catalysts for the Alternating Copolymerization of CO_2 and Epoxides: Catalyst Synthesis and Unprecedented Polymerization Activity. *J. Am. Chem. Soc.* **2001,** *123* (36), 8738-8749.
57. Park, J.; Hong, S., Cooperative bimetallic catalysis in asymmetric transformations. *Chem. Soc. Rev.* **2012,** *41* (21), 6931-6943.
58. Xiao, Y.; Wang, Z.; Ding, K., Intramolecularly Dinuclear Magnesium Complex Catalyzed Copolymerization of Cyclohexene Oxide with CO_2 under Ambient CO_2 Pressure: Kinetics and Mechanism. *Macromolecules* **2006,** *39* (1), 128-137.
59. Xiao, Y.; Wang, Z.; Ding, K., Copolymerization of Cyclohexene Oxide with CO_2 by Using Intramolecular Dinuclear Zinc Catalysts. *Chem. Eur. J.* **2005,** *11* (12), 3668-3678.
60. Lee, B. Y.; Kwon, H. Y.; Lee, S. Y.; Na, S. J.; Han, S.-i.; Yun, H.; Lee, H.; Park, Y.-W., Bimetallic Anilido-Aldimine Zinc Complexes for Epoxide/CO_2 Copolymerization. *J. Am. Chem. Soc.* **2005,** *127* (9), 3031-3037.
61. Bok, T.; Yun, H.; Lee, B. Y., Bimetallic Fluorine-Substituted Anilido–Aldimine Zinc Complexes for CO_2/(Cyclohexene Oxide) Copolymerization. *Inorg. Chem.* **2006,** *45* (10), 4228-4237.
62. Kember, M. R.; White, A. J. P.; Williams, C. K., Di- and Tri-Zinc Catalysts for the Low-Pressure Copolymerization of CO_2 and Cyclohexene Oxide. *Inorg. Chem.* **2009,** *48* (19), 9535-9542.
63. Kember, M. R.; Knight, P. D.; Reung, P. T.; Williams, C. K., Highly active dizinc catalyst for the copolymerization of carbon dioxide and cyclohexene oxide at one atmosphere pressure. *Angew. Chem. Int. Ed.* **2009,** *48* (5), 931-933.
64. Kember, M. R.; White, A. J. P.; Williams, C. K., Highly Active Di- and Trimetallic Cobalt Catalysts for the Copolymerization of CHO and CO_2 at Atmospheric Pressure. *Macromolecules* **2010,** *43* (5), 2291-2298.

65. Kember, M. R.; Jutz, F.; Buchard, A.; White, A. J.; Williams, C. K., Di-cobalt (ii) catalysts for the copolymerisation of CO_2 and cyclohexene oxide: support for a dinuclear mechanism? *Chem. Sci.* **2012,** *3* (4), 1245-1255.
66. Saini, P. K.; Romain, C.; Williams, C. K., Dinuclear metal catalysts: improved performance of heterodinuclear mixed catalysts for CO_2–epoxide copolymerization. *Chem. Comm.* **2014,** *50* (32), 4164-4167.
67. Buchard, A.; Kember, M. R.; Sandeman, K. G.; Williams, C. K., A bimetallic iron(iii) catalyst for CO_2/epoxide coupling. *Chem. Comm.* **2011,** *47* (1), 212-214.
68. Chapman, A. M.; Keyworth, C.; Kember, M. R.; Lennox, A. J. J.; Williams, C. K., Adding Value to Power Station Captured CO_2: Tolerant Zn and Mg Homogeneous Catalysts for Polycarbonate Polyol Production. *ACS Catalysis* **2015,** *5* (3), 1581-1588.
69. Jutz, F.; Buchard, A.; Kember, M. R.; Fredriksen, S. B.; Williams, C. K., Mechanistic Investigation and Reaction Kinetics of the Low-Pressure Copolymerization of Cyclohexene Oxide and Carbon Dioxide Catalyzed by a Dizinc Complex. *J. Am. Chem. Soc.* **2011,** *133* (43), 17395-17405.
70. Buchard, A.; Jutz, F.; Kember, M. R.; White, A. J. P.; Rzepa, H. S.; Williams, C. K., Experimental and Computational Investigation of the Mechanism of Carbon Dioxide/Cyclohexene Oxide Copolymerization Using a Dizinc Catalyst. *Macromolecules* **2012,** *45* (17), 6781-6795.
71. Garden, J. A.; Saini, P. K.; Williams, C. K., Greater than the Sum of Its Parts: A Heterodinuclear Polymerization Catalyst. *J. Am. Chem. Soc.* **2015,** *137* (48), 15078-15081.
72. Trott, G.; Garden, J. A.; Williams, C. K., Heterodinuclear zinc and magnesium catalysts for epoxide/CO_2 ring opening copolymerizations. *Chem. Sci.* **2019,** *10* (17), 4618-4627.
73. Nagae, H.; Aoki, R.; Akutagawa, S.-n.; Kleemann, J.; Tagawa, R.; Schindler, T.; Choi, G.; Spaniol, T. P.; Tsurugi, H.; Okuda, J.; Mashima, K., Lanthanide Complexes Supported by a Trizinc Crown Ether as Catalysts for Alternating Copolymerization of Epoxide and CO_2: Telomerization Controlled by Carboxylate Anions. *Angew. Chem. Int. Ed.* **2018,** *57* (9), 2492-2496.
74. Asaba, H.; Iwasaki, T.; Hatazawa, M.; Deng, J.; Nagae, H.; Mashima, K.; Nozaki, K., Alternating Copolymerization of CO_2 and Cyclohexene Oxide Catalyzed by Cobalt–Lanthanide Mixed Multinuclear Complexes. *Inorg. Chem.* **2020,** *59* (12), 7928-7933.
75. Akine, S.; Sunaga, S.; Nabeshima, T., Multistep Oligometal Complexation of the Macrocyclic Tris(N_2O_2) Hexaoxime Ligand. *Chem. Eur. J.* **2011,** *17* (24), 6853-6861.
76. Feltham, H. L. C.; Klöwer, F.; Cameron, S. A.; Larsen, D. S.; Lan, Y.; Tropiano, M.; Faulkner, S.; Powell, A. K.; Brooker, S., A family of 13 tetranuclear zinc(ii)-lanthanide(iii) complexes of a [3 + 3] Schiff-base macrocycle derived from 1,4-diformyl-2,3-dihydroxybenzene. *Dalton Trans.* **2011,** *40* (43), 11425-11432.
77. Tsai, C.-Y.; Huang, B.-H.; Hsiao, M.-W.; Lin, C.-C.; Ko, B.-T., Structurally Diverse Copper Complexes Bearing NNO-Tridentate Schiff-Base Derivatives as Efficient Catalysts for Copolymerization of Carbon Dioxide and Cyclohexene Oxide. *Inorg. Chem.* **2014,** *53* (10), 5109-5116.
78. Nozaki, K.; Nakano, K.; Hiyama, T., Optically Active Polycarbonates: Asymmetric Alternating Copolymerization of Cyclohexene Oxide and Carbon Dioxide. *J. Am. Chem. Soc.* **1999,** *121* (47), 11008-11009.
79. Nakano, K.; Nozaki, K.; Hiyama, T., Asymmetric Alternating Copolymerization of Cyclohexene Oxide and CO_2 with Dimeric Zinc Complexes. *J. Am. Chem. Soc.* **2003,** *125* (18), 5501-5510.

80. Schütze, M.; Dechert, S.; Meyer, F., Highly Active and Readily Accessible Proline-Based Dizinc Catalyst for CO_2/Epoxide Copolymerization. *Chem. Eur. J.* **2017,** *23* (65), 16472-16475.
81. Moore, D. R.; Cheng, M.; Lobkovsky, E. B.; Coates, G. W., Electronic and Steric Effects on Catalysts for CO_2/Epoxide Polymerization: Subtle Modifications Resulting in Superior Activities. *Angew. Chem. Int. Ed.* **2002,** *41* (14), 2599-2602.
82. Kissling, S.; Altenbuchner, P. T.; Lehenmeier, M. W.; Herdtweck, E.; Deglmann, P.; Seemann, U. B.; Rieger, B., Mechanistic Aspects of a Highly Active Dinuclear Zinc Catalyst for the Co-polymerization of Epoxides and CO_2. *Chem. Eur. J.* **2015,** *21* (22), 8148-8157.
83. Lehenmeier, M. W.; Kissling, S.; Altenbuchner, P. T.; Bruckmeier, C.; Deglmann, P.; Brym, A.-K.; Rieger, B., Flexibly Tethered Dinuclear Zinc Complexes: A Solution to the Entropy Problem in CO_2/Epoxide Copolymerization Catalysis? *Angew. Chem. Int. Ed.* **2013,** *52* (37), 9821-9826.
84. Kissling, S.; Lehenmeier, M. W.; Altenbuchner, P. T.; Kronast, A.; Reiter, M.; Deglmann, P.; Seemann, U. B.; Rieger, B., Dinuclear zinc catalysts with unprecedented activities for the copolymerization of cyclohexene oxide and CO_2. *Chem. Comm.* **2015,** *51* (22), 4579-4582.
85. Nakano, K.; Hashimoto, S.; Nozaki, K., Bimetallic mechanism operating in the copolymerization of propylene oxide with carbon dioxide catalyzed by cobalt–salen complexes. *Chem. Sci.* **2010,** *1* (3), 369-373.
86. Vagin, S. I.; Reichardt, R.; Klaus, S.; Rieger, B., Conformationally Flexible Dimeric Salphen Complexes for Bifunctional Catalysis. *J. Am. Chem. Soc.* **2010,** *132* (41), 14367-14369.
87. Klaus, S.; Vagin, S. I.; Lehenmeier, M. W.; Deglmann, P.; Brym, A. K.; Rieger, B., Kinetic and Mechanistic Investigation of Mononuclear and Flexibly Linked Dinuclear Complexes for Copolymerization of CO_2 and Epoxides. *Macromolecules* **2011,** *44* (24), 9508-9516.
88. Trott, G.; Garden, J. A.; Williams, C. K., Heterodinuclear zinc and magnesium catalysts for epoxide/CO_2 ring opening copolymerizations. *Chem. Sci.* **2019**, 10, 4618-4627.
89. Deacy, A. C.; Kilpatrick, A. F. R.; Regoutz, A.; Williams, C. K., Understanding metal synergy in heterodinuclear catalysts for the copolymerization of CO_2 and epoxides. *Nat. Chem.* **2020,** *12* (4), 372-380.

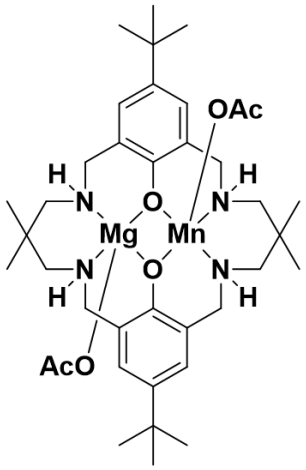
Chapter 2

Methodology

This chapter will describe the underpinning principles and utility of magnetochemistry, electrochemistry and infrared spectroscopy. These characterisation techniques are used in this thesis for the characterisation of complexes and polymerisation studies.

2.1. Superconducting Quantum Interference Device Magnetometry

To obtain information about the metal centre in a paramagnetic system a measurement of magnetic susceptibility (χ) – the ability of a substance to be attracted or repelled by an external magnetic field – can be analysed. The values of susceptibility for diamagnetic materials are generally independent of field strength and temperature, with experimental values being negative and small ($\simeq$ -1 to 100 x10^{-6} cm^3 mol^{-1}). On the other hand, the values of χ for paramagnetic materials are also generally independent of field strength but are temperature dependent, with experimental values being positive and significantly larger than those of diamagnetic material ($\simeq 10^2$ to 10^4 cm^3 mol^{-1}).[1-3] As the species with unpaired electrons also carry a number of filled electron shells, and in the specific case of coordination compounds with ligands that are generally closed shell species, these molecular systems (including the one reported in this thesis) should have a diamagnetic contribution correction calculated. This correction can be made using the Pascal constants, where a diamagnetic susceptibility value is attributed to each atom as shown in Figure 2.1.[4]



$C_{38}H_{60}MgMnN_4O_6$

	$\chi_{diamagnetic}$		Total
Mg(II)	-5×10^{-6}	=	-5×10^{-6}
Mn(II)	-14×10^{-6}	=	-14×10^{-6}
2 O	$2 \times (-4.60\times10^{-6})$	=	-9.2×10^{-6}
4 N	$4 \times (-4.61\times10^{-6})$	=	-18.44×10^{-6}
12 C_{ring}	$12 \times (-6.24\times10^{-6})$	=	-74.88×10^{-6}
22 C	$22 \times (-6.00\times10^{-6})$	=	-132×10^{-6}
60 H	$60 \times (-2.93\times10^{-6})$	=	-175.8×10^{-6}
2 Benzene	$2 \times (-1.4\times10^{-6})$	=	-2.8×10^{-6}
2 ($^-$OAc)	$2 \times (-31.5\times10^{-6})$	=	-63.0×10^{-6}
Total			**-495.12×10^{-6} emu mol^{-1}**

Figure 2.1. Diamagnetic correction calculated for a Mg(II)Mn(II) macrocycle. The values for the Pascal's constants for the diamagnetic susceptibility for each atom were taken from Gordon A. Bain et al.[4]

A typical experiment to obtain information about the susceptibility consists of measuring susceptibility under constant applied field and varying the temperature. When the magnetic centres are isolated in the sample and so have no interaction between them, the susceptibility is inversely proportional to the temperature (Curie's law) and the graph of χ versus T is a straight line passing through the origin.[2] Deviations from the Curie law can occur due to a change in the energy level population resulting from a change in temperature or from magnetic interactions. These magnetic interactions can happen when the distance between paramagnetic centres in a sample is small enough or they are connected by a species able to transmit magnetic interactions, leading to two types of magnetic interaction: Ferromagnetic and antiferromagnetic, explained below.[2] This behaviour can be expressed by a modification in the Curie Law, by adding a correction term (θ) leading to the Curie-Weiss Law, where θ is the Curie-Weiss constant, Equation 2.1.[3]

$$\chi = \frac{C}{T-\theta} \qquad \text{Equation 2.1}$$

Ferromagnetic interaction: When the large domains of magnetic dipoles in a sample are aligned in the same direction, this promotes an increase in the susceptibility values when compared with the normal paramagnetic (magnetically isolated) materials.[5]

Antiferromagnetic interaction: When neighbouring magnetic dipoles with the same intensity are aligned in opposite directions, the value of χ will be lower than the magnetic isolated material.[5]

The graph of χ^{-1} vs. T for a system that follows the Curie-Weiss law is a straight line where the slope gives C^{-1} and the intercept with the T axis gives the Curie-Weiss constant. For antiferromagnetic systems, the value of θ is negative, and for ferromagnetic systems, it is positive as shown in Figure 2.2. When no interactions between the spins are observed, $\theta = 0$, reverting to the Curie Law equation.[1, 2]

Another way to represent the magnetic data is through a $\chi_M T$ vs. T graph allowing easier identification since a positive θ leads to an increase of $\chi_M T$ and a negative velue leads to a decrease. The magnetic measurements of paramagnetic materials are frequently expressed as effective magnetic moment (μ_{eff}) obtained from the molar magnetic susceptibility (χ_M) following Equation 2.2.[1]

$$\mu_{eff} = 2.828\sqrt{\chi_m T} \qquad \text{Equation 2.2}$$

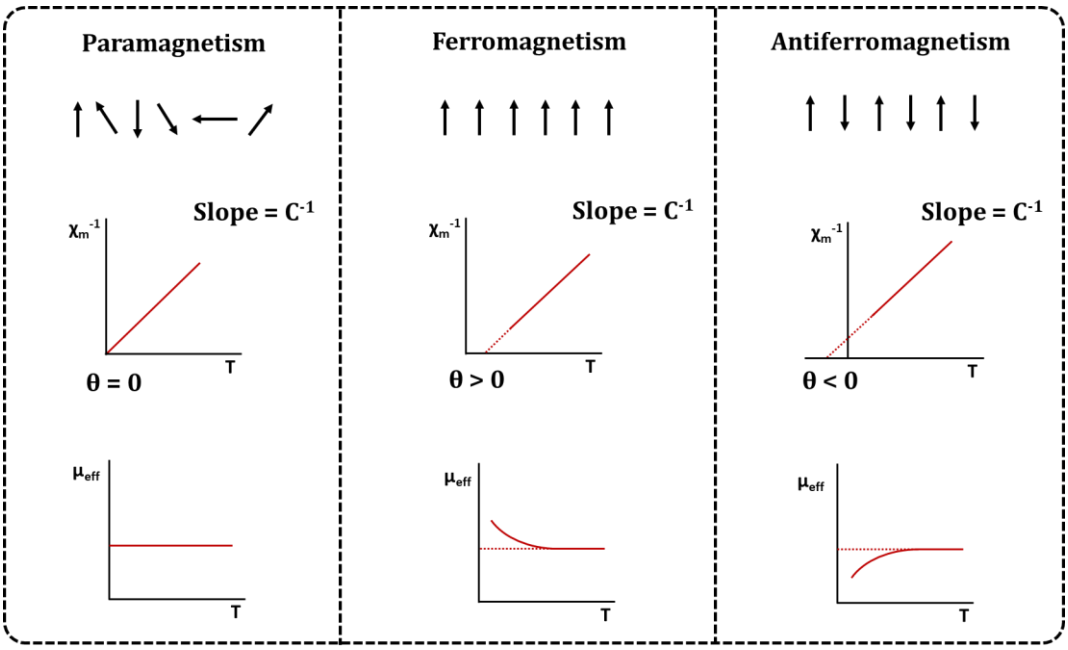


Figure 2.2. Representation of χ^{-1} *vs.* T and μ_{eff} *vs.* T graphs and large domains of magnetic dipoles for paramagnetic, ferromagnetic and antiferromagnetic materials.

The theoretical value for μ_{eff} can be predicted by the spin-only equation, using the number of unpaired electrons (n) or the spin momentum (represented by the quantum number S), Equation 2.3 and 2.4. This value provides information about the sample, such as the number of unpaired electrons, therefore, the oxidation state of the metal and if the complex is low- or high-spin. In this thesis, the magnetic susceptibility experiments were used to obtain information about interactions between the metal centres and the oxidation state of the transition metal; these data were obtained by comparing the μ_{eff} obtained experimentally with the calculated values.[5]

$$\mu_{(spin-only)} = \sqrt{n(n+2)} \qquad \text{Equation 2.3}$$

As $S = \frac{n}{2}$

$$\mu = 2\sqrt{(S(S+1)} \qquad \text{Equation 2.4}$$

As an example the magnetic susceptibility experiment for the macrocycle with Mg(II) and Mn(II) metal centres is represented in Figure 2.3. The antiferromagnetic

interaction, indicated by the negative Curie-Weiss constant, is most clearly observed in the μ_{eff} *vs*. temperature plot by the decrease in the μ_{eff} values at low temperatures, Figure 2.3-b.

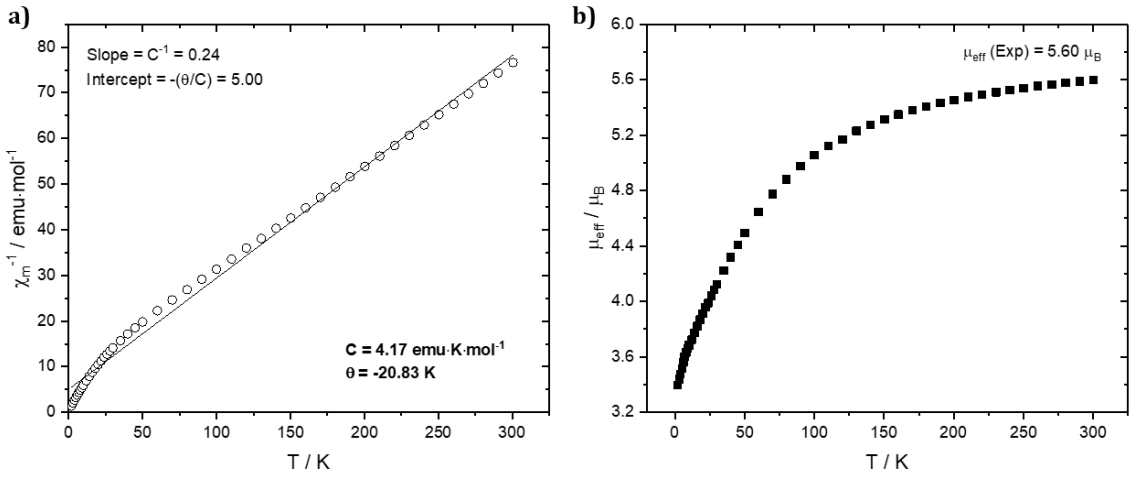


Figure 2.3. Example of magnetic susceptibility experiment for a Mg(II)Mn(II) macrocycle system. a) Inverse of molar susceptibility *vs*. temperature. ∘ experimental data, – fitting of the curve. b) Effective magnetic moment *vs.* temperature calculated from susceptibility experiment.

Comparing the value obtained for the μ_{eff} at room temperature with the theoretical values, obtained from the spin-only equation for different oxidation states of Mn (II, III or IV), shows that the value fit occurs for high spin Mn(II), Table 2.1.

Table 2.1. Theoretical values obtained using spin-only equation for different oxidation states of manganese.

		Number of unpaired electrons	S	μ_{eff} (SO) / μ_B
Mn(II)	**High spin**	**5**	**5/2**	**5.92**
	Low spin	1	1/2	1.73
Mn(III)	High spin	4	2	4.90
	Low spin	2	1	2.83
Mn(IV)	–	3	3/2	3.87

Not all paramagnetic complexes follow the spin-only formula and in some cases the magnetic moment arises from both spin and orbital angular momenta, leading to μ_{eff} values greater than those calculated from the spin-only equation. For high-spin octahedral complexes, the orbital contribution to the magnetic moment are important

for configurations t_{2g}^1, t_{2g}^2, t_{2g}^4 e_g^2 and t_{2g}^5 e_g^2. The orbital angular moment is represented by the quantum number L and the μ_{eff} can be calculated by Equation 2.5.[1, 5] In this thesis, the orbital contribution will need to be considered for Fe(II) and Co(II) complexes.

$$\mu_{(eff)} = 2\sqrt{(S(S+1) + L(L+1)} \qquad \text{Equation 2.5}$$

2.2. Cyclic Voltammetry

Cyclic voltammetry (CV) is used to determine the oxidation and reduction processes occurring in a species. During a CV experiment, heterogeneous electron transfer from/to an electrode reduces/oxides the species.[6] A typical CV experiment occurs with a three-electrode setup, consisting of an electrical conductor, called the working electrode (typically it is comprised of platinum, gold, mercury or glass carbon), connected to an external power source; a counter electrode (platinum), a reference electrode (calomel or silver chloride/silver electrode) and an electrochemical cell (vessel) where the experiment is performed, represented in Figure 2.4-a. All electrodes are immersed in the sample solution with the sample dissolved in a suitable solvent. For non-aqueous solvents, a supporting electrolyte, such as $NaClO_4$ or $[^nBu_4N][BF_3]$, are added to increase the solution conductivity and minimize ohmic drop. During the cyclic voltammetry experiment, as the electron transfer occurs at the electrodes, the supporting electrolyte will migrate to balance the charge and complete the electrical circuit.[5, 6]

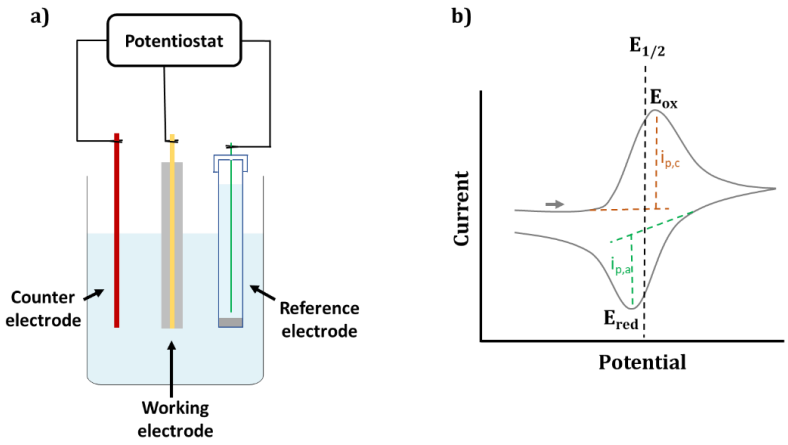


Figure 2.4. a) Representation of the three electrodes in a cell for cyclic voltammetry.[6, 7] b) Generic voltammogram experiments with formal potential ($E_{1/2}$), peak cathodic and anodic currents ($i_{p,c}$,$i_{p,a}$) and potential for oxidation and reduction. Figures adapted from Dempsey et al. and Skoog (*Principles of Instrumental Analysis*).[6, 8]

Nowadays, many reports add ferrocene as an internal standard and its common to report the redox potential referenced against the ferrocene/ferrocenium redox couple (i.e. *vs* Fc^+/Fc = 0 V).[5, 6] The calibration is performed after the cyclic voltammetry experiment, to avoid interferences in the measurement, and it is done by adding a small amount of ferrocene into the same system already measured and recording the voltammogram again. The signal of ferrocene is clear and the value of $E_{1/2}$ (Fc^+/Fc potential) is used to calibrate the voltammogram recorded for the sample, as illustrated in Figure 2.5.

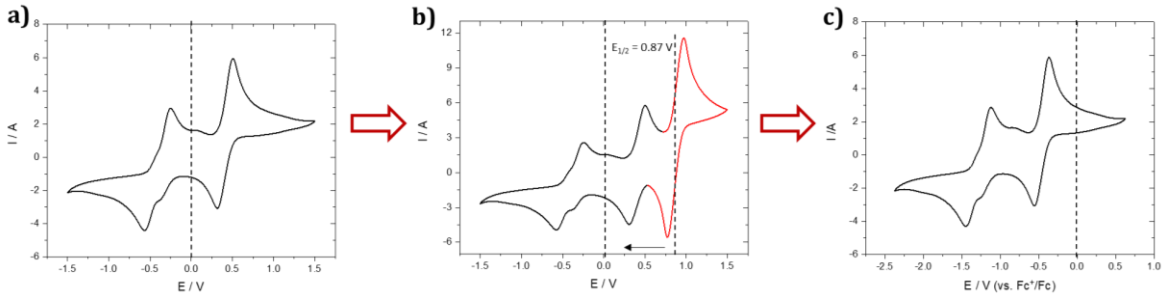


Figure 2.5. Example of cyclic voltammogram calibration with ferrocene. a) Cyclic voltammogram before calibration. b) Cyclic voltammogram with the Fc^+/Fc signal. c) Cyclic voltammogram after calibration.

The peak-to-peak separation (ΔE_p) follows Equation 2.6. In a reversible voltammogram, oxidation and reduction waves are symmetric and ΔE_p is lower than 0.059 V.[5, 9] When the electron transfer reaction between electrode and the analyte is

slow (high barrier), the reduction/oxidation of the compound analysed will require more negative/positive potential, increasing the value of ΔE_p, characteristic of an irreversible system.

$$\Delta E_p = E_{ox} - E_{red} \qquad \text{Equation 2.6}$$

In this thesis, the redox potential values obtained were referenced against Fc^+/Fc and compared with similar systems in the literature.

2.3. Reaction monitoring – *in situ* Attenuated Total Reflectance – Infrared spectroscopy (ATR–IR)

Among the techniques used to measure the molecular vibrations, the attenuated total reflection (ATR) is a popular one in Fourier transform infrared spectroscopy. In an ATR-IR experiment, the sample is in contact with the ATR crystal. The IR radiation travels through the crystal and interacts with the sample on the surface, so the result is based on total internal reflections.[10, 11] The reflections form a wave, and the reflections that occur at the interface sample/crystal penetrate a short distance into the sample, called the "evanescent wave". The IR light absorbed when this wave interacts with the sample produces an slightly attenuated total reflection and by repeating such reflections, the signal is amplified enabling reasonable signal:noise ratios, Figure 2.6-a.[11-15]

ATR-IR spectroscopy can be applied *in situ*, when the probe is immersed into a reaction solution and this allows continual monitoring of absorbance over time obtaining kinetic data as explained bellow (Figure 2.6-b and c).[11]

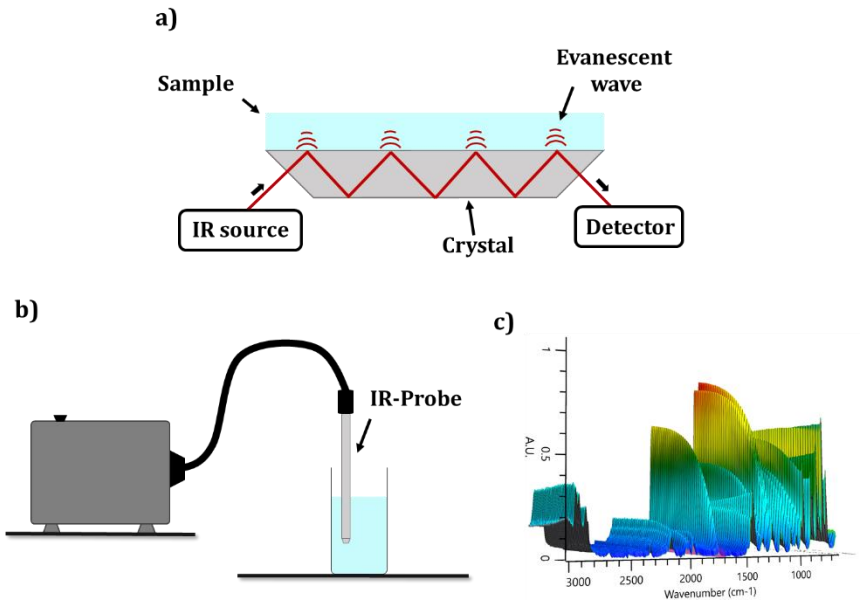


Figure 2.6. a) Illustration of a ATR set up with a representation of the evanescent wave (Figure adapted from literature).[11, 14] b) Representation of a ReactIR equipment with a probe for *in situ* IR studies. c) Example of a 3D graph obtained in the experiment.

- Monitoring copolymerisation reactions

ATR-IR spectroscopy can be applied *in situ*, when the probe is immersed into a reaction solution and this allows continual monitoring of absorbance, obtaining information of the reaction progress. For example, for a copolymerisation of cyclohexene oxide and CO_2, the absorbance intensity used to monitor the formation of poly(cyclohexene carbonate) is first normalised to zero at T_0, as showing in Figure 2.7-a. The final conversion of CHO to PCHC ($\%_f$) can be accessed by ^{1}H NMR spectroscopy of an aliquot obtained at the end of the experiment (T_f), and used to calibrate the normalised intensity to CHO conversion, following Equation 2.7 and Figure 2.7-b.

$$\%\ CHO_{conversion} = I \times \left(\frac{\%_f}{I_f}\right) \qquad \text{Equation 2.7}$$

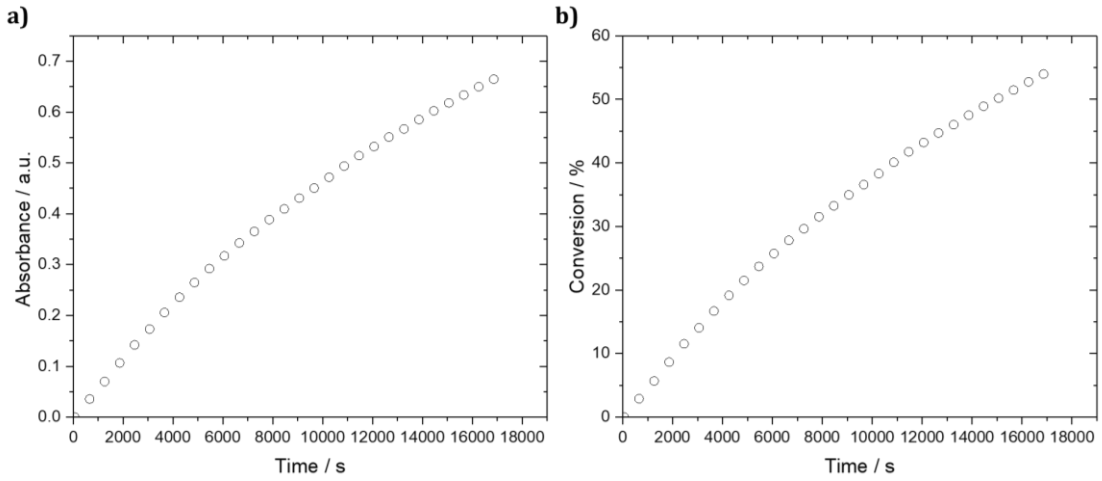


Figure 2.7. a) Example of absorbance vs. time plot for PCHC (every 10th point displayed). b) Normalised conversion vs. time plot for PHCH (every 10th point displayed), total conversion of 55 % calculated by ^{1}H NMR.

The percentage of CHO conversion can be directly correlated to the concentration of CHO as shown in Equation 2.8.

$$[CHO]_t = \left(\frac{\%CHO_{conversion}}{100}\right) \times [CHO]_0 \qquad \text{Equation 2.8}$$

For polymerisations performed in neat CHO, $[CHO]_0$ = 9.9 M.

As the copolymerisation of CHO and CO_2 is first order depended to [CHO], the k_{obs} can be obtained from the plot $\ln([CHO]/[CHO]_0)$ *vs* time, following Equations 2.9, as illustrated in Figure 2.8.

$$\ln[CHO] = \ln[CHO]_0 - k_{obs}t \qquad \text{Equation 2.9}$$

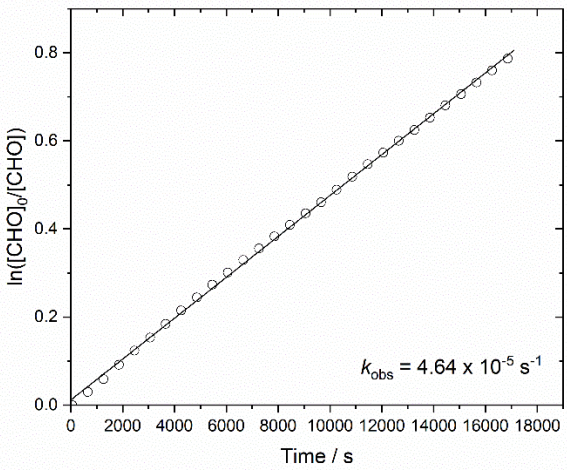


Figure 2.8. Example of logarithm of epoxide concentration vs. time plot and k_{obs} obtained from the linear fit of the curve.

- Standard error

When a polymerisation system is analysed it's important to perform the experiment carefully to minimise the error, for example, the polymerisations reported in this thesis were performed in glassware of the same size, using similar stirrer bars and stirring plates. Before the experiment starts, the oil bath was allowed to equilibrate for at least 1 h to the desired temperature and at least 5 vacuum/CO_2 refill cycles were conducted to ensure the gas mixture was pure. In order to minimize errors in the conversion, the aliquots (used to calculate the conversion by ^{1}H NMR) were taken immediately after the polymerisation stopped and quenched by exposure to air.

The errors quoted in this thesis for polymerisation systems were obtained by repeating the polymerisation three times and the standard error and standard deviation (S) were calculated following Equations 2.10 and 2.11.

$$S = \sqrt{\frac{\sum_{i=1}^{n}(x_i-\mu_x)^2}{n-1}} \qquad \text{Equation 2.10}$$

Where, $\mu_x = \frac{\sum_{i=1}^{n} x_i}{n}$, x_i is each scope in the distribution, n is the number of systems analysed.

$$Standard\ error = \frac{S}{\sqrt{n}} \qquad \text{Equation 2.11}$$

2.4. References

1. Kahn, O., *Molecular Magnetism*. VCH: 1993.
2. Earnshaw, A., *Introduction to Magnetochemistry*. Academic Press: 1968.
3. Carlin, R. L., *Magnetochemistry*. Spring-Verlag Berlin Heidelberg: 1986.
4. Bain, G. A.; Berry, J. F., Diamagnetic Corrections and Pascal's Constants. *J. Chem. Ed.* **2008,** *85* (4), 532.
5. Housecroft, C. E.; Sharpe, A. G., *Inorg. Chem.* Pearson: 2008.
6. Elgrishi, N.; Rountree, K. J.; McCarthy, B. D.; Rountree, E. S.; Eisenhart, T. T.; Dempsey, J. L., A Practical Beginner's Guide to Cyclic Voltammetry. *J. Chem. Educ.* **2018,** *95* (2), 197-206.
7. Marken, F.; Neudeck, A.; Bond, A. M., Cyclic Voltammetry. In *Electroanalytical Methods: Guide to Experiments and Applications*, Scholz, F.; Bond, A. M.; Compton, R. G.; Fiedler, D. A.; Inzelt, G.; Kahlert, H.; Komorsky-Lovrić, Š.; Lohse, H.; Lovrić, M.; Marken, F.; Neudeck, A.; Retter, U.; Scholz, F.; Stojek, Z., Eds. Springer Berlin Heidelberg: Berlin, Heidelberg, 2010; pp 57-106.
8. Skoog, D. A.; Holler, F. J.; Crouch, S. R., *Principles of Instrumental Analysis*. Sixth ed.; Thomson Brooks/Cole: 2007.
9. Mabbott, G. A., An introduction to cyclic voltammetry. *J. Chem. Educ.* **1983,** *60* (9), 697.
10. Nakamoto, K., Infrared and Raman Spectra of Inorganic and Coordination Compounds. *Handbook of Vibrational Spectroscopy* **2006**.
11. Lumpi, D.; Braunshier, C., Effective Reaction Monitoring of Intermediates by ATR-IR Spectroscopy Utilizing Fibre Optic Probes. In *Infrared Spectroscopy: Materials Science, Engineering and Technology*, Theophanides, T., Ed. InTech: 2012.
12. Li, H.; Rahimi, F.; Sinha, S.; Maiti, P.; Bitan, G.; Murakami, K., Amyloids and Protein Aggregation—Analytical Methods. In *Encyclopedia of Analytical Chemistry*, 2009.
13. Wartewig, S.; Neubert, R. H. H., Pharmaceutical applications of Mid-IR and Raman spectroscopy. *Adv. Drug Deliv. Rev.* **2005,** *57* (8), 1144-1170.
14. Atital, M. F.; Belhadj, H.; Dillert, R.; Bahnemann, D. W., The Relevance of ATR-FTIR Spectroscopy in Semiconductor Photocatalysis. In *Emerging Pollutants in the Environment: Current and Further Implications*, Larramendy, M. L.; Soloneski, S., Eds. InTech: 2015.
15. Ruysschaert, J.-M.; Raussens, V., *ATR-FTIR analysis of amyloid proteins.* 2018; Vol. 1777, pp 69-81.

Chapter 3

Heterodinuclear Catalysts for the Ring-Opening Copolymerisation of CO_2/Epoxide

3.1. Introduction

As discussed in chapter 1, Williams and co-workers reported a study comparing the activities of heterodinuclear macrocycle [LMgZnBr$_2$] with the homodinuclear analogue [LMg$_2$Br$_2$] and [LZn$_2$Br$_2$], giving TOFs = 34, 15 and 7 h^{-1} respectively, under unoptimized conditions.[1]

The increased activity of the heterodinuclear system inspired further work investigating different metal combinations for ROCOP of CHO/CO_2.[2, 3] Synthesising the di-zinc complex and also combining Zn(II) with metals from Groups 1 and 2, allowed preparation of a series of LZnM(X)$_2$ complexes where M = Na(I), Li(I), K(I), Mg(II), Zn(II) or Ca(II) for X = I and M = Li(I), K(I) or Zn(II) for X = OBz*p*CF$_3$ (4-trifluoromethyl)benzoate). When these catalysts were tested in the ROCOP of CO_2 with CHO at 1 bar CO_2, the Mg(II)Zn(II) metal combination still showing the best activity and selectivity.[2] Subsequently, complexes with Zn(II) and Group 13 elements were investigated.[3] The series of complexes LZnM(X)$_2$ or LZnM(X)$_3$ where M = Zn(II), Al(III), Ga(III) or In (III) and X = Cl. were tested for ROCOP of CO_2 with CHO at 1 bar CO_2 pressure; all systems showed lower activity and selectivity than the di-zinc complex, and consequently, lower activity than the Mg(II)Zn(II) catalyst systems. These results were interpreted as resulting from the enhanced Lewis acidity and higher M–O strengths of Group 13 elements slowing the critical metal carbonate attack step in the catalytic cycle.[3]

Inspired by these previous work, the Mg(II) metal centre was kept in the catalyst structure and Zn(II) replaced for Co(II) to increase the carbonate nucleophilicity.[4] When tested for ROCOP of CO_2 and CHO, this catalyst showed an increase in the activity and selectivity with TOFs up to 1,205 h^{-1} and 12,400 h^{-1} at 1 and 40 bar CO_2 pressure,

respectively. The LMgCo(OAc)$_2$ catalyst was also more active when compared with the homodinuclear versions, i.e. di-cobalt and di-magnesium complexes, under the same polymerisation conditions ([CHO]:[CHD]:[Cat] = 4000:20:1, 120 °C, 1 bar CO_2). Based on kinetic studies, the authors attributed the higher catalytic activity to synergy between the metals and, further, proposed different roles for the two metals (based on Eyring analysis). The kinetic analysis suggests that the magnesium centre reduces the barriers to epoxide coordination and the cobalt centre shows an enhanced nucleophilicity of the cobalt-carbonate; by acting together the magnesium reduces the transition state entropy whilst the cobalt reduces the transition state enthalpy compared to either homodinuclear variant.[4] Such insight into catalytic synergy is extremely rare but could be relevant to other metal combinations and catalysts.

3.2. Aims

Given the recent insights into how synergy operates for the LMgCo(OAc)$_2$ catalyst, this chapter will explore a series of first-row transition metals Mg(II)M(II), complexes where M(II) = Mn, Cr, Ni, Co, Fe, Cu, Zn, with the aim of understanding which systems, if any, also show enhanced activity and selectivity.

After the set of catalysts are explored for the ROCOP of CO_2/CHO, the complex with the best activity and selectivity will be compared with the homodinuclear variant to understand whether there is any metal synergy in catalysis. The most active catalyst will also be tested for the ROCOP of CO_2 and a range of other epoxides, all conducted under low pressure conditions (i.e. at 1 bar CO_2).

After the set of catalysts are explored for the ROCOP of CO_2/CHO, they will also be investigated for the ROCOP of CHO and norbornene anhydride to compare the order of catalyst activity between the two mechanistically related, but distinct, reactions.

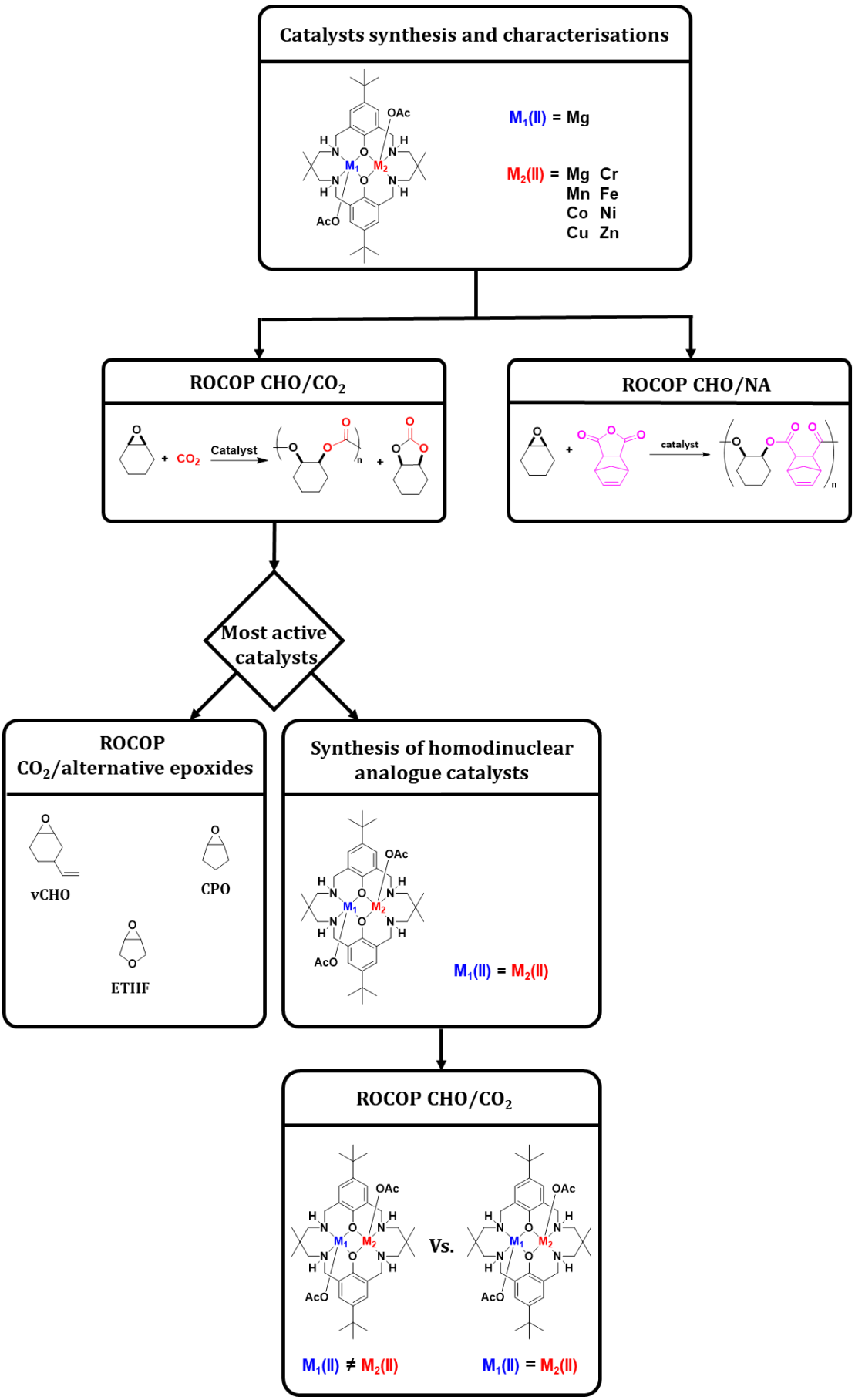
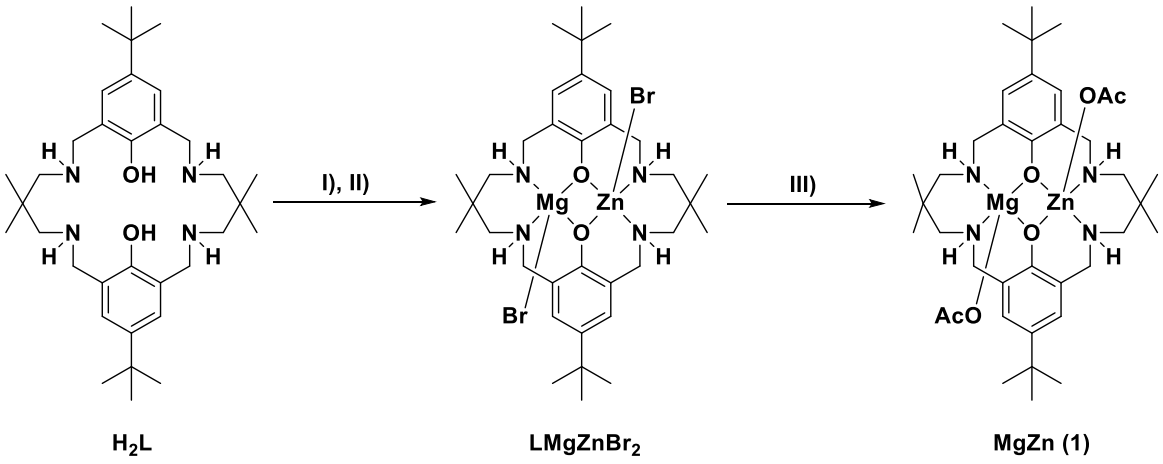


Figure 3.1. Chapter 3 summary.

3.3. Synthesis and Characterisation of Heterometallic LMgM(OAc)$_2$ complexes (where M = Cr, Mn, Fe, Co, Ni, Cu, Zn)

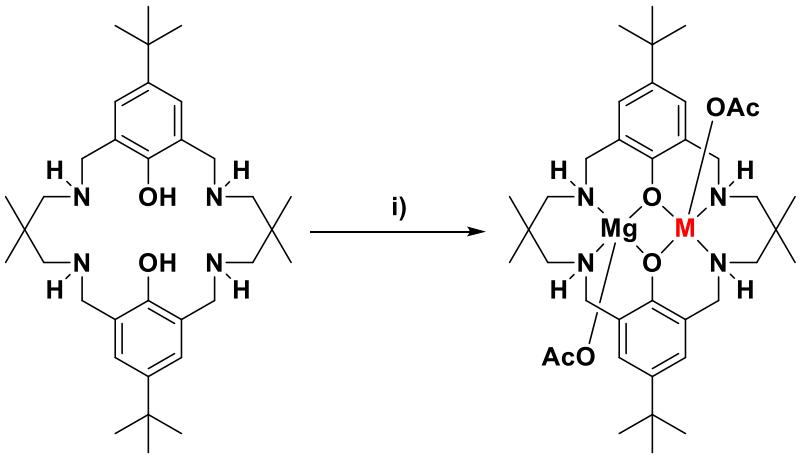
3.3.1. Synthesis of complex 1

Complex **1** was synthesised according to its literature procedure (Scheme 3.1). The initial step is the monometalation of the pro-ligand (**H$_2$L**) by diethylzinc, followed by the addition of MgBr$_2$ under cryogenic conditions to form a heterodinuclear bromide complex (LMgZnBr$_2$). The acetate catalyst was obtained through a salt metathesis of this species via the addition of potassium acetate. The potassium bromide by-product was removed by product extraction into DCM followed by pentane washes.[1, 5] Complex **1** was isolated as a white powder in 50 % yield and characterised by mass spectrometry, NMR- and IR- spectroscopy and purity was assessed by elemental analysis. All characterisation data are in agreement with literature.[1, 5, 6]



Scheme 3.1. Synthesis of complex **1**. I) ZnEt$_2$, THF, RT, 16 h; II) MgBr$_2$, THF, –78 °C → RT, 1 h; III) KOAc, THF, RT, 16h.

3.3.2. Synthesis of complexes 2–8



M		Yield
MgII	(2)	70 %
CrII*	(3)	50 %
MnII	(4)	68 %
FeII	(5)	75 %
CoII	(6)	75 %
NiII	(7)	78 %
CuII	(8)	65 %

Scheme 3.2. Synthesis of di-magnesium complex **2** and heterodinuclear catalysts **3–8**. i) $Mg(N(SiMe_3)_2)_2$, $M(OAc)_2$, THF, 100 °C, 16 h.*MgCr complex was synthesised at room temperature, 72h, due to decomposition.

The synthesis of complexes **2–8** was carried out using an adapted procedure described by Williams and co-workers, where complexes **2** and **6** are reported.[4] Monometallation of the pro-ligand was achieved by reaction with $Mg(N(SiMe_3)_2)_2$ in THF at 25 °C to generate the mono-magnesium species. After 2 h the appropriate metal acetate salt, $M(OAc)_2$ (M = Mg, Cr, Mn, Fe, Co, Ni and Cu) was added and the system was heated at 100 °C, for 16 h, to access the heterodinuclear catalysts in good yield (50 – 78 %).

Complex **2** was characterised by NMR spectroscopy and was in good agreement with literature.[4, 5, 7a] Due to the paramagnetic nature of most of the transition metals in the second oxidation state, complexes **3–8** were characterised by cyclic voltammetry (CV), Superconducting Quantum Interference Device (SQUID), mass spectrometry, IR Spectroscopy, X-Ray crystallography when appropriate and complex purity was assessed by elemental analysis.

3.3.3. Cyclic Voltammetry of complexes 2–8

Cyclic voltammetry investigations of complexes **2–8** were performed in a 0.1 M solution of the complex in THF (10 mL) with [^{n}Bu$_4$N][PF$_6$] as the supporting electrolyte. All measurements were performed in a glovebox, under a N_2 atmosphere, and the reference electrode was calibrated to the ferrocinium/ferrocene redox couple (at 0.00 V).

The cyclic voltammogram of complex **2** (redox inactive Mg(II) centres) displays a series of oxidations above +0.39 V. This is proposed to be oxidation of the ligand phenolates to phenoxyl radicals, as has been observed in similar ligand systems.[8, 9] Similarly for heteronuclear complexes **7** and **8**, no oxidation or reduction of the proposed Ni(II) and Cu(II) ions is observed in the analysed potential range (Figure 3.2), therefore no further data on the metal oxidation state was available.

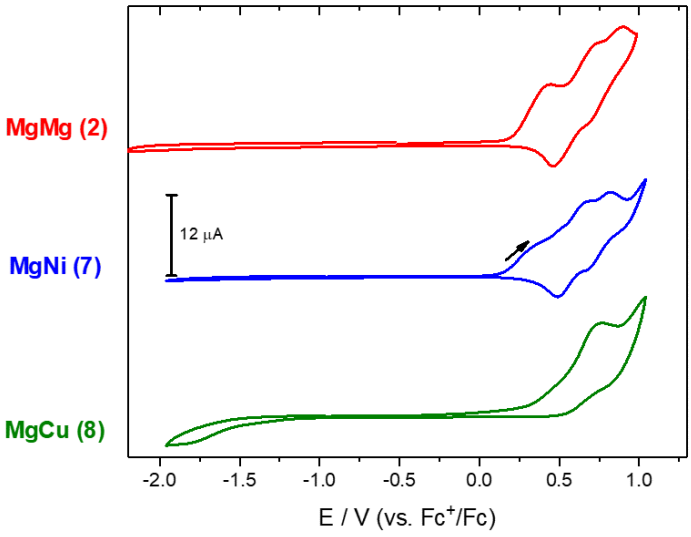


Figure 3.2. Cyclic voltammograms of complexes **2**, **7** and **8** showing only oxidations of the ligand phenolate to phenoxyl radicals.

Analysis of the cyclic voltammograms of MgCr, complex **3**, revealed two semi-reversible redox processes with peaks observed at -0.33 V and -2.20 V, consistent to

[MgIICrII]/[MgIICrIII]$^{+}$ and [MgIICrIII]$^{+}$/[MgIICrIV]$^{2+}$ oxidation, respectively (Figure 3.3). Additionally, a third reduction wave for [MgIICrII]/[MgIICrI]$^{-}$ was also observed.

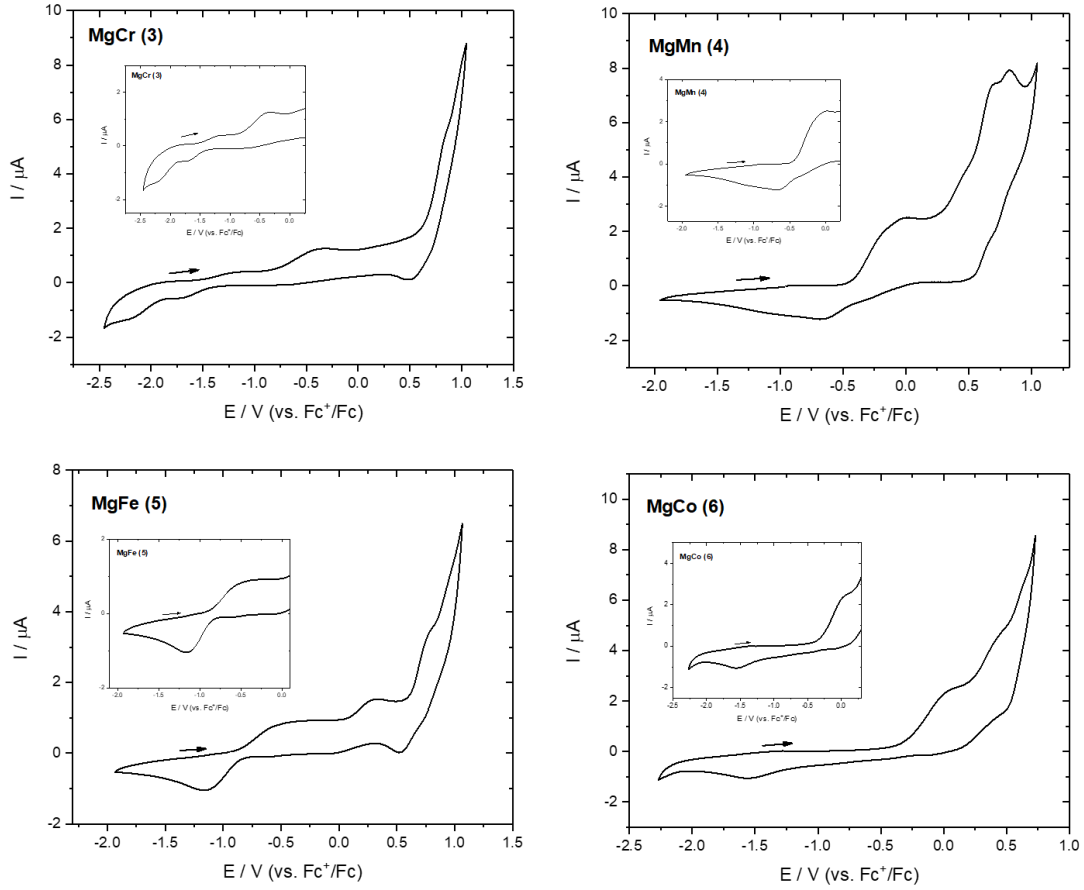


Figure 3.3. Cyclic voltammograms for complexes **3**–**6**, performed in THF.

The cyclic voltammograms of complexes **4**–**6** (Figure 3.3) each showed oxidation consistent with [MgIIMII]/[MgIIMIII]$^{+}$ (with M = Mn, Fe and Co), Figure 3.3. The values for oxidation and reduction of complexes **4**–**6** are displayed in Table 3.1. In comparison to literature, the obtained voltammograms are in good agreement with other reported mono-Co(II) and mono-Fe(II) complexes. For example, a Co(II)– bipyridine complex, a Co(II)–salen and the MgCo macrocycle have reported $E_{1/2}$ between -0.01 and 0.01 V assigned to the [CoII]/[CoIII]$^{+}$ oxidation.[4, 10-12] Furthermore, mono-Fe(II) porphyrins and macrocycle complexes gave $E_{1/2}$ values between -0.40 V and -0.51 V (E_{pa} = -0.36

and -0.47 V) assigned to [FeII]/[FeIII]$^{+}$.[13, 14] All values were converted to Fc^{+}/Fc reference when appropriate.[15, 16]

Table 3.1. Redox values of the complexes **3–6**.[a]

Complex	Metal Centre	Transition	$E_{p,a}$ / V	$E_{p,c}$/ V
3	Cr(II)	$Cr^{II/III}$	-1.16	–
		$Cr^{III/IV}$	-0.33	–
		$Cr^{IV/III}$	–	-0.75
		$Cr^{III/II}$	–	-1.71
		$Cr^{II/I}$	–	-2.20
4	Mn (II)	$Mn^{II/III}$	-0.02	–
		$Mn^{III/II}$	–	-0.66
5	Fe(II)	$Fe^{II/III}$	-0.37	–
		$Fe^{II/I}$	–	-1.15
6	Co(II)	$Co^{II/III}$	-0.06	–
		$Co^{II/I}$	–	-1.55

[a] Potential values are given in V *vs*. the Fc^{+}/Fc.

3.3.4. SQUID Magnetometry for complexes 3–8

Variable-temperature magnetic susceptibility (χ) measurements, using solid samples of complexes **3–8**, were performed on a Superconducting Quantum Interference Device (SQUID) magnetometer (external field 1000 Oe). The magnetic susceptibility was corrected for the underlying diamagnetic contribution, using Pascal constants (Appendix, Table A1–A3).[17] As an example the data for MgFe, complex **5**, is presented. The temperature dependence of the inverse of molar susceptibility (χ_m^{-1}) (Figure 3.4) follows the Curie-Weiss law given by Equation 3.1. The value for the Currie constant (C) obtained was 3.82 emu·K·mol^{-1} and a Curie-Weiss constant (θ) 1.40 K, the positive signal of θ indicates an intermolecular ferromagnetic interaction between the metal centres from different macrocycles.

$$\chi_m = \frac{C}{T-\theta}$$ Equation 3.1

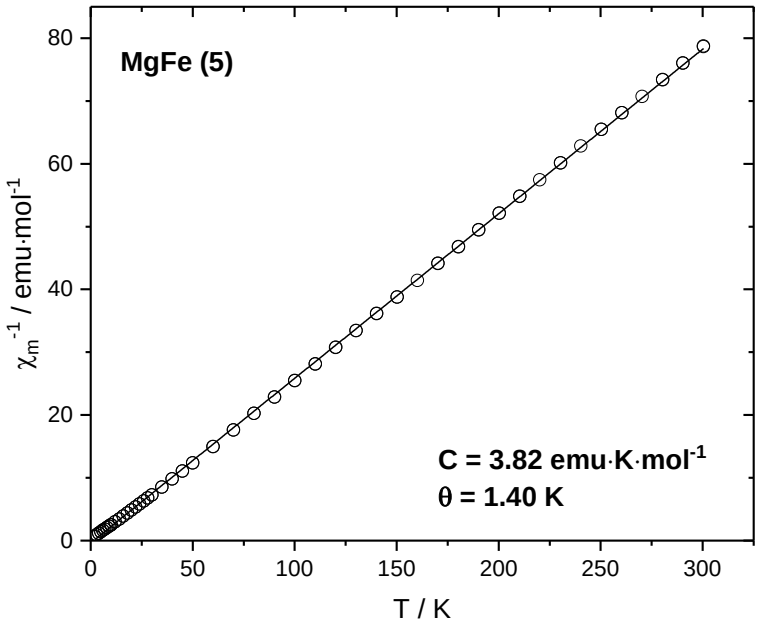


Figure 3.4. Inverse of molar susceptibility *vs*. temperature for MgFe complex **5**.

Related data was acquired for complexes **3–8** and the values of Curie and Curie-Weiss constants obtained from the linear fitting of the graphs of the inverse of molar susceptibility (χ_m^{-1}) against temperature (Figure A1–A6) are shown in Table 3.2. Complexes **3**, **4** and **6–8** presented an antiferromagnetic interaction between the metal centres, indicated by the negative values of the Curie-Weiss constants.

Table 3.2. Values of Curie constant (C) and Curie-Weiss constant (θ) for complexes **3–8.**

Complex	Metal Centre	C / emu·K·mol^{-1}	θ / K
3	Cr(II)	2.56	-81.30
4	Mn (II)	4.10	-20.48
5	Fe(II)	3.82	1.40
6	Co(II)	2.89	-9.75
7	Ni(II)	2.11	-6.97
8	Cu(II)	0.22	-8.13

The weak ferromagnetic interaction between two Fe(II) centres from neighbouring molecules in complex **5** can be easily visualised by the increase in values of effective magnetic moment (μ_{eff}) when the system is cooled (Figure 3.5). The effective magnetic

moment observed experimentally at room temperature (5.5 μ_B) was greater than the theoretical value obtained from the spin-only equation (Equation 3.2) for a high spin iron(II) centre (μ_{SO}=4.90 μ_B , for S=2, g=2).

$$\mu_{eff}(SO) = \sqrt{4S(S+1)} \qquad \text{Equation 3.2}$$

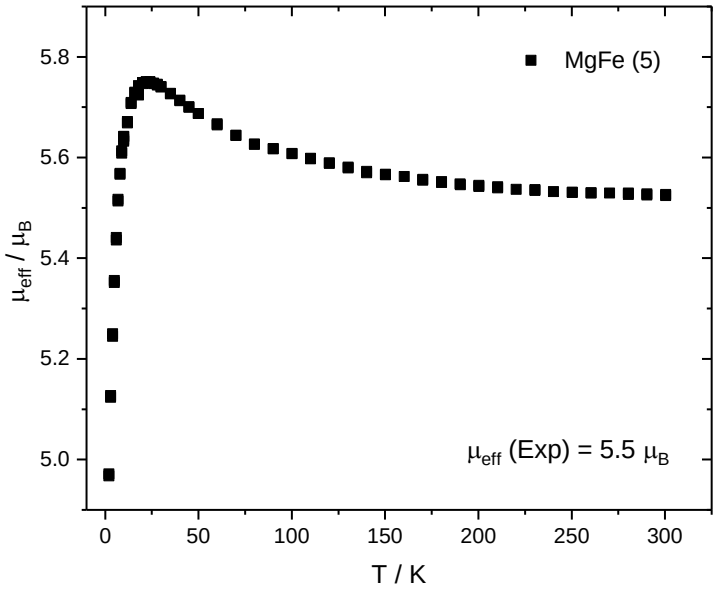


Figure 3.5. Effective magnetic moment *vs.* temperature graph for complex **5**.

The difference between the theoretical and experimental values for the effective magnetic moment at room temperature can be explained due to a spin-orbit coupling observed in some high spin Fe(II) complexes.[14, 18] The effective magnetic moment at room temperature considering a spin-orbit coupling is given by Equation 3.3, where μ_{s+L}=5.48 μ_B (for S=2, L=2, g=2), this value is closer to the experimental obtained and it is in accordance with μ_{eff} reported for Fe(II) porphyrin complexes with spin-orbit coupling ($\mu_{eff_reported}$=5.5 μ_B)[14, 18].

$$\mu_{S+L} = \sqrt{4S(S+1) + L(L+1)} \qquad \text{Equation 3.3}$$

The theoretical values for the effective magnetic moment at room temperature for metal ions with 2+ oxidation states were also calculated for each complex and

compared with the experimental data showed in Figures A1–A6. The experimental and theoretical μ_{eff} (calculated using the spin-only equation, Equation 3.2) and μ_{S+L} (Equation 3.3), when applicable, are shown in Table 3.3. The values obtained for complexes **3–8** are in agreement with the theoretical values and they are close to the values reported in the literature for different complexes using these metal centres.

Table 3.3. Theoretical and experimental values obtained for magnetic susceptibility for complexes **3–8** and some values reported in the literature for the same metal centres in different complex environment.[18-20]

Complex	Metal Centre	S	μ_{eff}(SO)	μ_{S+L}	μ_{eff}(Exp)	μ_{eff}(Lit.)	Ref.
3	Cr(II)	2*	4.9	–	4.0	4.8 – 5.0	19, 20
4	Mn (II)	5/2*	5.9	–	5.6	5.8 – 6.0	19-22
5	Fe(II)	2*	4.9	5.5	5.5	4.9 – 5.5	18-20, 23, 24
6	Co(II)	3/2*	3.9	5.2	4.8	4.3 – 5.2	19, 20
7	Ni(II)	1	2.8	–	3.3	2.9 – 3.9	19, 20, 23
8	Cu(II)	½	1.7	–	1.4	1.7 – 2.2	19, 20, 23

* S values for high spin systems

3.3.5. X-Ray Crystallography of complexes 5 and 7

Single crystals, suitable for X-ray diffraction of complex **5** and **7** were obtained from a saturated solution of the complex in toluene, held at –40 °C over 15 days under a nitrogen atmosphere. The elucidated molecular structure (Figure 3.6 and 3.7 – a) shows the macrocycle adopts a "bowl-shape" conformation, where all the NH are on the same face of the molecule. The structure is dimeric with two molecules of **5** or **7** connected by a bridging acetate ligand represented in Figure 3.6-b and Figure 3.7-b. In both structures, both metal centres are in a distorted octahedral configuration and the intermolecular distance between the two metal centres are 3.008(2) Å for complex **5** and 3.036(5) Å for complex **7** (in this case it was reported the average of the M–M distance for both MgNi showed in the structure). The angle formed between different macrocycles are 43.69° (complex **5**) and 50.96° (complex **7**), as illustrated in Figure

3.6-c and Figure 3.7-c. The structure of complex **7** also shows the coordination of adventitious water to one of the metal centres, presumably arising from the crystallisation process. The specific metals [magnesium (II), iron (II) and nickel (II)] could not be assigned due to positional uncertainty and the similarities in electron density within each biding pocket.

A similar structure was observed for reported MgCo complex **6**.[25] The solid-state structures for **5**, **6** and **7** possess similar metal–nitrogen, metal–oxygen and metal–metal distances. Additionally, complex **6** is also dimeric, features an additional molecule of coordinated water, and similar bond angles (compared with complex **7**) formed between the planes from two macrocycles connected by a bridging acetate.

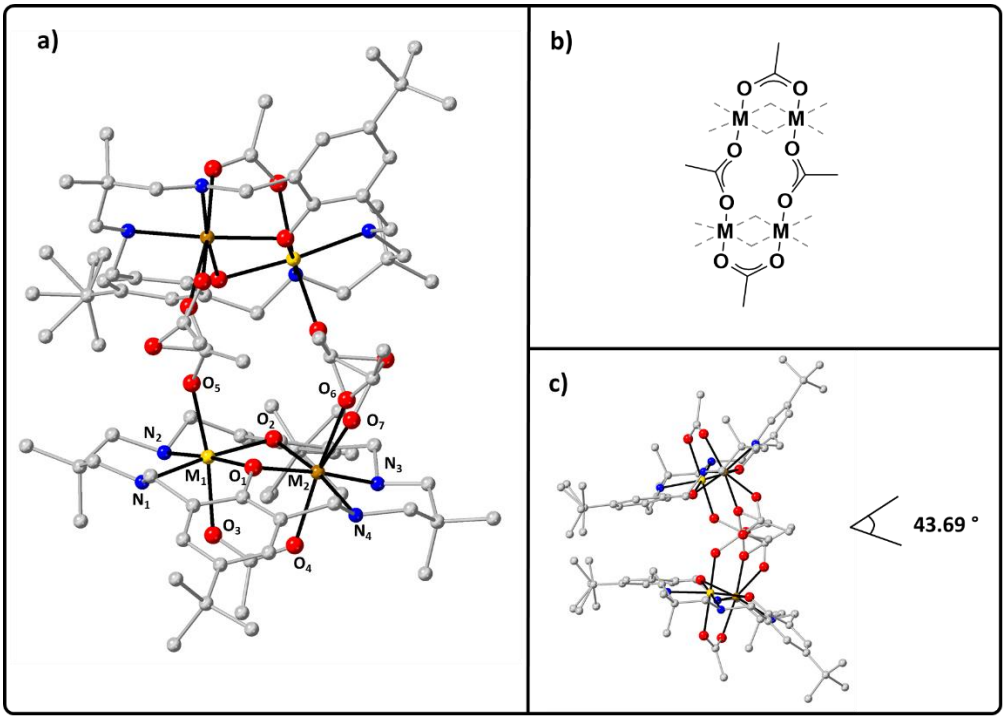


Figure 3.6. a) Molecular structures of the complex MgFe (**5**) represented as ball & stick to clarify due to disorder. (b) Representation of acetate bridging two macrocycles. (c) Angle between the planes from different macrocycle. H-atoms and crystallisation solvent (toluene) were omitted to clarify.

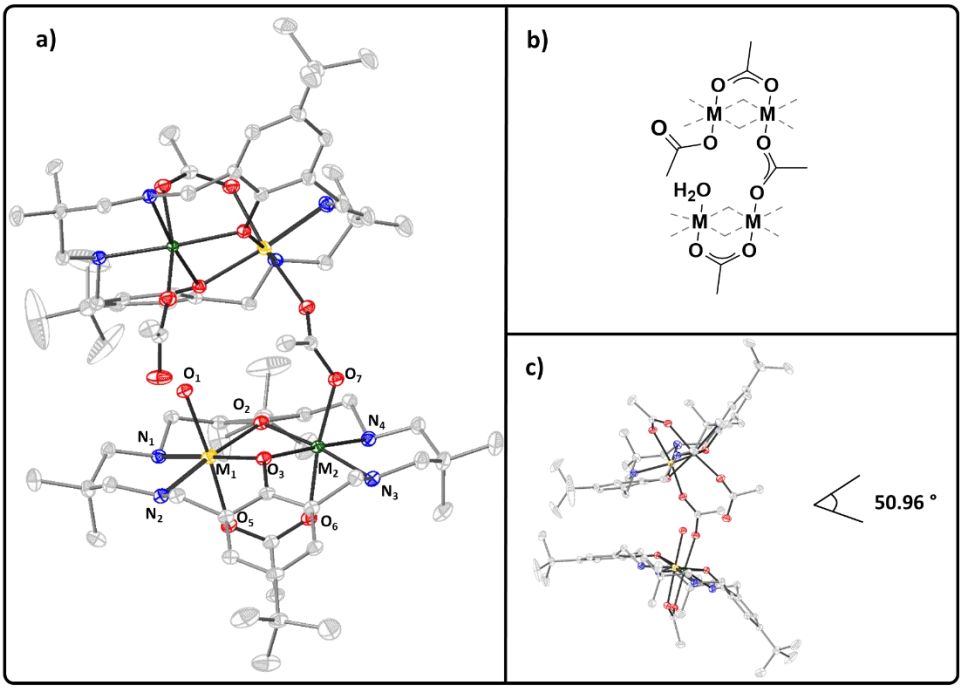


Figure 3.7. a) Molecular structures of the complex MgNi (**7**) (b) Representation of acetate bridging two macrocycles. (c) Angle between the planes from different macrocycle. Thermal ellipsoids represented at 40 % probability. H-atoms and crystallisation solvent (toluene) were omitted to clarify.

Table 3.4. Selected bond distances, for complexes **5** and **7.**

Complex	Bond	Distance / Å	Bond	Distance / Å
MgFe	M_1–M_2	3.0083(17)	M_2–O_1	2.137(3)
	M_1–O_1	2.048(5)	M_2–O_2	2.069(5)
	M_1–O_2	2.087(3)	M_2–O_4	2.137(3)
	M_1–O_3	2.144(3)	M_2–O_7	2.034(7)
MgNi	M_1–M_2	3.0317(6) 3.0413(5)	M_2–O_2	2.1082(13)
	M_1–O_1	2.0293(15)	M_2–O_3	2.0892(13)
	M_1–O_2	2.0954(12)	M_2–O_6	2.0934(14)
	M_1–O_3	2.0559(13)	M_2–O_7	2.0690(13)
	M_1–O_5	2.1075(14)		

3.3.6. MALDI-ToF Mass Spectrometry for complexes 1–8

Complexes **1–8** were characterised by MALDI-ToF mass spectrometry. Heterodinuclear, complexes **1**, **3–7**, revealed signals corresponding to the molecular ion peak, with the loss of an acetate group $[LMgM(OAc)]^+$ (M = Zn: 697.18 *m/z*, Cr: 685.19 *m/z*, Mn: 688.19 *m/z*, Fe: 689.28 *m/z*, Co: 692.26 *m/z*, Ni: 691.36 *m/z* and Cu:

696.35 *m/z*) (Figure 3.8). Additional signals for the homodinuclear $[LMg_2(OAc)]^+$ (657.41 *m/z*) and $[LM_2(OAc)]^+$ (M = Zn: 737.18 *m/z*, Cr: 713.15 *m/z*, Mn: 719.14 *m/z*, Fe: 721.26 *m/z*, Co: 727.22 *m/z* and Ni: 725.18 *m/z*) were also observed in each case. For complex **2** only a single signal corresponding to $[LMgMg(OAc)]^+$ (657 *m/z*) was detected.

Complexes **7** and **8** also show an additional peak at 677.66 *m/z* and 676.17 *m/z* which may be a water adduct of the homodinuclear magnesium ion ($[LMg_2(OAc)(OH_2)]^+$, 675.42 *m/z*). Finally, the ionisation of complex **3** gave a signal at 696.75 *m/z* that could be attributed to ($[LMg_2(OAc)]^+$ with potassium contamination from the MALDI spectrometer.

The presence of homodinuclear species may indicate possible contamination within the heterodinuclear samples or scrambling of the metal centres under ionisation conditions. This is expected as previous synthesis of heterodinuclear complexes on the same ligand system with NMR silent metals show contaminations of homodinuclear species of up to 8 % by NMR.[1, 3, 5, 25, 26]

Furthermore, the isotopic distribution patterns obtained for complexes **1, 2** and **6** are in agreement with the results for $LMgZn(OAc)_2$, $LMgMg(OAc)_2$ and $LMgCo(OAc)_2$ previously published in the literature.[25, 26]

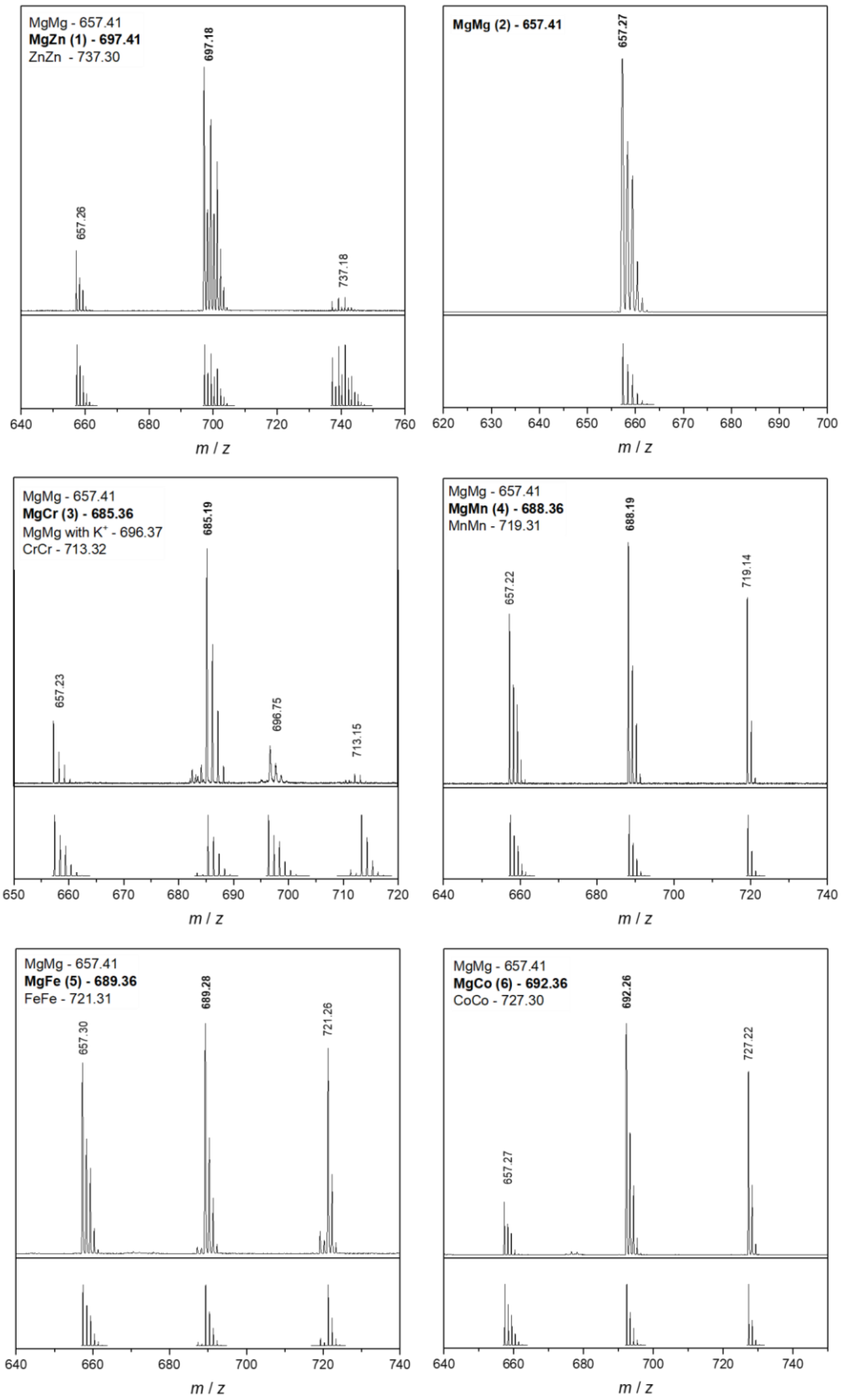


Figure 3.8. MALDI-ToF spectra of MgZn, MgMg, MgCr, MgMn, MgFe and MgCo with the experimental (above peak) and theoretical (top left of each graph) values. The simulated isotopic distribution is also represented on the bottom of each graph.

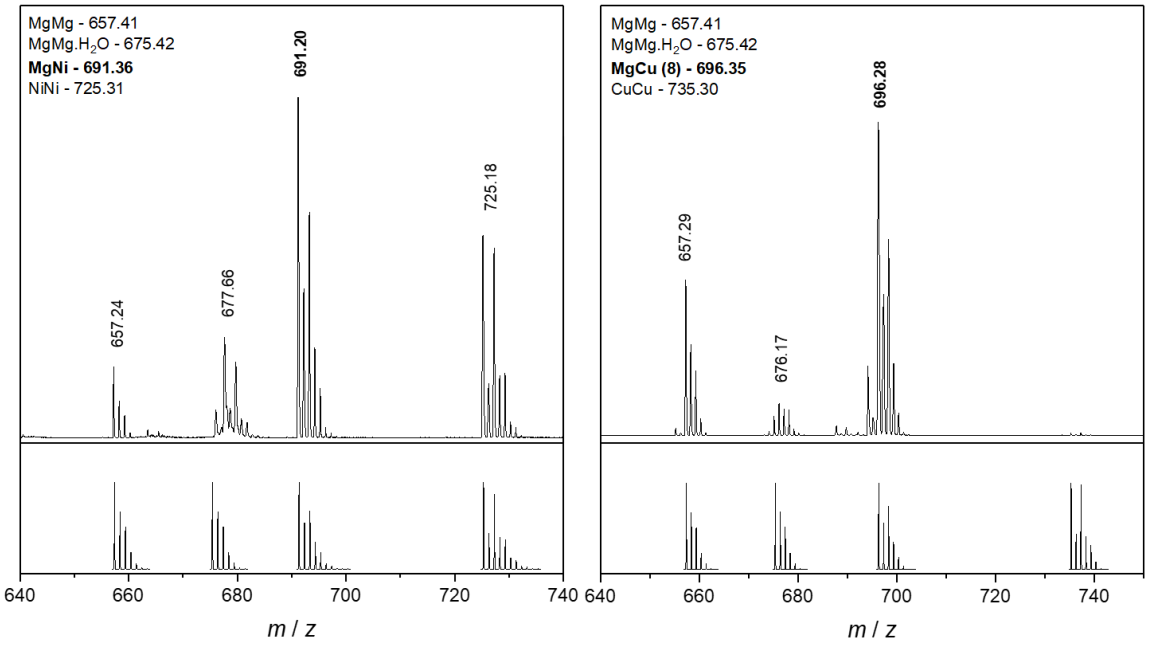


Figure 3.9. MALDI-ToF spectra of MgNi and MgCu, complexes **7** and **8** showing the water adduct $[LMg_2(OAc)(OH_2)]^+$, with the experimental (written on top of the peak) and theoretical (top left of each graph) values. The simulated isotopic distribution is also represented on the bottom of each graph.

3.3.7. Infrared Spectroscopy for complexes 1–8

Complexes **1–8** were further analysed by Fourier transform infrared (FT-IR) spectroscopy in solid-state and compared against the pro-ligand H_2L. Compared to the pro-ligand, the complexes show a loss of the characteristic out-of-plane phenol OH deformation ($\delta_{Ar\text{-}OH}$) at 707 cm^{-1}. Furthermore, additional signals corresponding to the asymmetric stretch and bending modes of the acetate co-ligand (stretching: 1590 and 1440 cm^{-1}, bending 924 cm^{-1}) are observed.[27] The signal at 3298 cm^{-1} corresponds to an NH stretching mode are both sharper and more intense than in the pro-ligand. The comparison between the pro-ligand and complex **5** is illustrated in Figure 3.10 and spectrum of complexes **1–8** with the main bands' values are shown in Figure 3.11 and Table 3.5. When the IR for complexes **1–8** are compared, there is no particular trend in the wavenumbers for specific bonds.

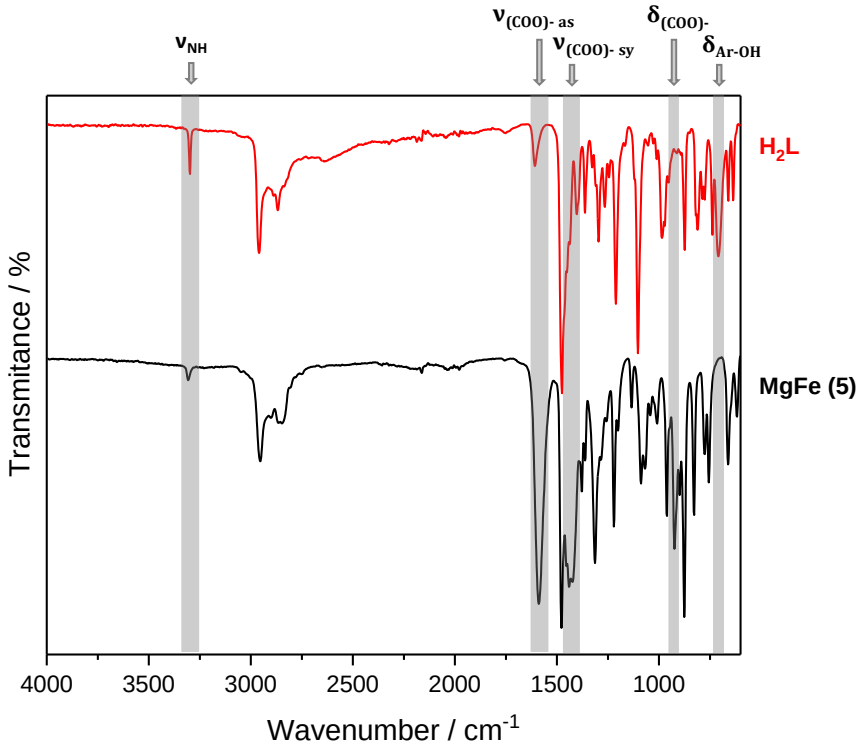


Figure 3.10. Comparison between infrared spectra of pro-free ligand H_2L and complex **5**. Highlighted bands are discussed in the text; 3298 cm^{-1}, 1590 cm^{-1}, 1440 cm^{-1}, 924 cm^{-1}, 707 cm^{-1}.

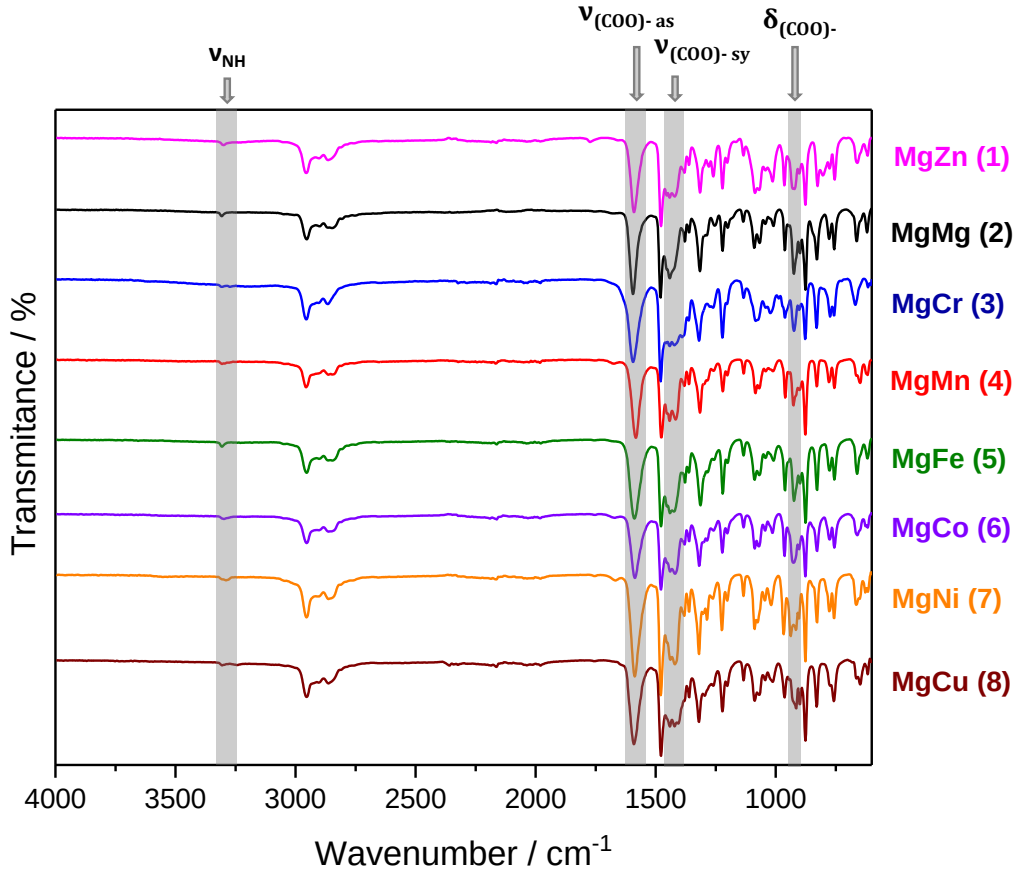


Figure 3.11. Comparison of the infrared spectra for complexes **1**–**8** obtained in solid-state.

Table 3.5. The resonance frequencies (cm^{-1}) obtained from the solid-state infrared spectra for complexes **1**–**8**.

Catalyst	Metal	ν_{NH} / cm^{-1}	$\nu_{(COO)-as}$ / cm^{-1}	$\nu_{(COO)-sy}$ / cm^{-1}	$\delta_{(COO)-}$ / cm^{-1}
1	Zn	3300	1591	1419	922
2	Mg	3308	1595	1423	924
3	Cr	3307	1593	1421	924
4	Mn	3308	1583	1415	926
5	Fe	3308	1587	1421	924
6	Co	3300	1587	1419	925
7	Ni	3290	1587	1419	937
8	Cu	3306	1591	1421	914

3.4. Polymerisation studies

3.4.1. ROCOP of CO_2 and CHO for complexes 1–8

With complexes **1–8** fully characterised, the effect of the transition metals in the ROCOP of CO_2/CHO was investigated. The reactions were conducted at 100 °C, under an atmosphere (1 bar) of CO_2, in neat epoxide (9.9 M) and with 20 equiv. of cyclohexene-1,2-diol (CHD), as similar conditions have resulted in good rates and selectivity with related catalysts.[4] In previous studies, a significant rate increase was observed between 60 °C and 100 °C, without any compromise in polymer selectivity (>99 %). However, the selectivity decreased at temperatures higher than 100 °C, resulting in cyclic carbonate formation. This was attributed to a reduction in CO_2 concentration at elevated temperatures. The addition of chain transfer agent (CTA) is necessary both to make polyols and it helps to provide uniform activity values by maintaining reduced solution viscosity throughout polymerisation (i.e. preventing reaction-diffusion control).

Catalyst activities are typically reported in terms of TOF values, however, the catalysts are often measured under different catalytic conditions and the single point kinetic measure is a composite of both initiation and propagation rates, making the comparison among different systems somewhat subjective. A much more informative and better means to compare catalytic performances is to compare initiation and propagation rate coefficients. For polymerisations performed under the same conditions, TOFs can be used for comparative studies, however, they should be calculated for the same time intervals and ideally only over the propagation regime.

The polymerisations performed in this chapter were monitored *in situ* by an ATR spectroscopy which provided data from which k_{obs} and TOFs were obtained. The k_{obs}

values were obtained from the linear fit of $\ln([CHO]_t/[CHO]_0)$ *vs.* time. The concentration of epoxide was obtained from the conversion *vs.* time plot, calibrated externally with ^1H NMR spectroscopy, for monomer conversion from the change in intensity (absorbance) of the signal at 1749 cm^{-1}, Figure 3.12-a. All polymerisations were performed three times to obtain the errors and prove good reproducibility, one example is shown in Figure 3.12-d (The other polymerisation systems are shown in Appendix, Figure A.9 to A.12) .

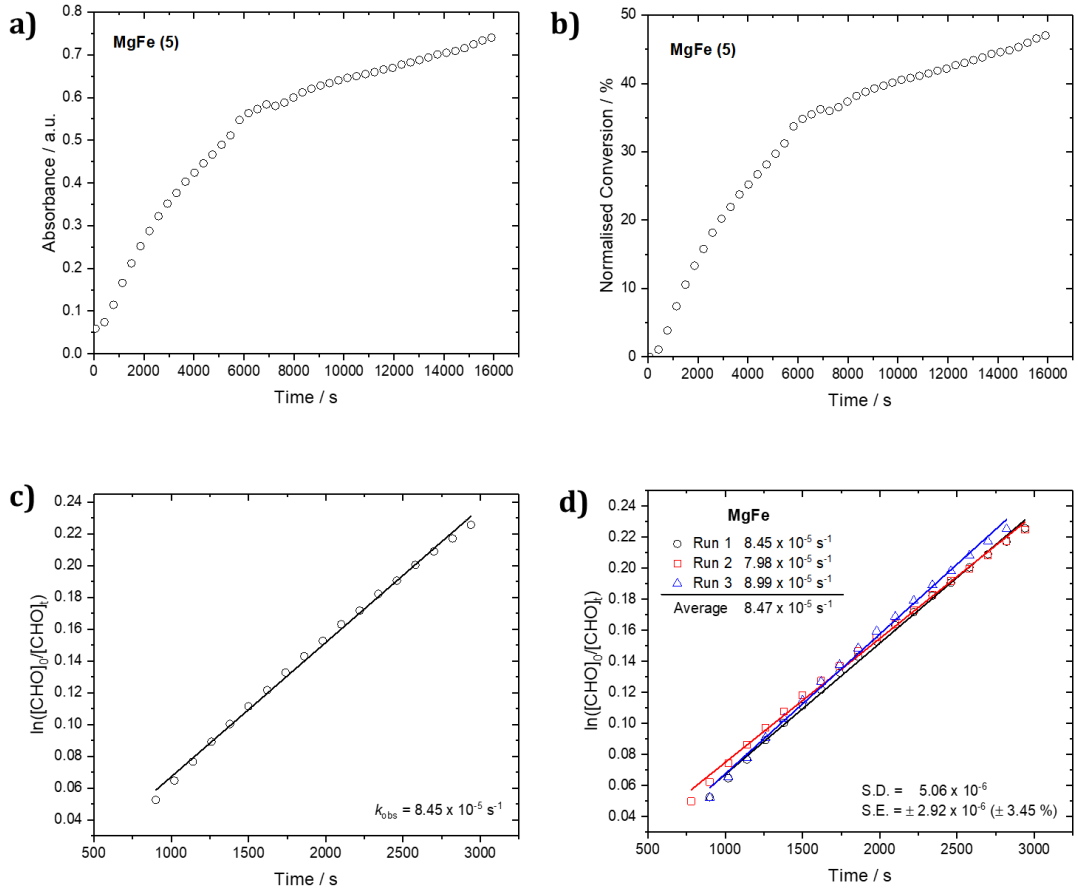


Figure 3.12. a) Absorbance vs. time plot for PCHC (every 4th point displayed). b) Normalised conversion vs. time plot for PCHC (every 4th point displayed). c) Logarithm of epoxide concentration vs. time for PCHC. d) Logarithm of epoxide concentration vs. time for three ROCOP runs with MgFe, complex **5**.

Due to the increase in solution viscosity, the maximum conversions over which data were analysed are for values up to 60 %. Catalytic turn over frequencies were compared based on initial rates (5–20 % conversion). Rates below 5 % conversion were not considered due to initiation influences on the data.

All ROCOP, using catalysts **1–8**, displayed excellent CO_2 selectivity, (> 99 %), with no ether linkages observed by ^{1}H NMR spectroscopy (Table 3.6). Excellent polymer selectivity was measured (>99 %), except for complexes **4** and **8** that resulted in 10 % and 6 % selectivity for *trans*-cyclic carbonate, respectively. All polymerisation systems plots for complexes **1–8** with errors are shown in Figure 3.13. Some values for copolymerisation for similar homodinuclear macrocycle systems using Co(II), Zn(II) and Fe(III) reported in the literature are shown in the Table 3.6. These systems show lower TOF values, however, as the polymerisation conditions are different, a direct comparison among these systems is difficult.

Table 3.6. CO_2/CHO copolymerisation at 1 bar CO_2 with catalysts **1–8**[a] and literature reported complexes ZnZn, CoCo and LFe_2Cl_4.[7]

Catalyst	Conv. (%)	CO_2 (%)[b]	Polym. (%)[c]	TOF (h^{-1})[d]	k_{obs} (x 10^{-5} s^{-1})[f]	M_n (g mol^{-1}) [$Đ$] [g]
MgMg	57	>99	>99	402 ± 11	3.24 ± 0.07	9200 [1.15]
MgCr	40	>99	>99	103 ± 5	0.82 ± 0.04	4000 [1.15]
MgMn	76	>99	90	362 ± 32	2.90 ± 0.2	4100 [1.23]
MgFe	59	>99	>99	1071 ± 33	8.47 ±0.3	8400 [1.11]
MgCo	59	>99	>99	1056 ± 18	8.39 ±0.1	8000 [1.25]
MgNi	60	>99	>99	632 ± 34	5.05 ±0.3	6300 [1.16]
MgCu	47	>99	94	136 ± 3	1.09 ± 0.03	6500 [1.15]
MgZn	37	>99	>99	506 ± 16	3.81 ±0.3	5000 [1.17]
ZnZn[h]	53	>99	94	25	Not reported	7400 [1.21]
CoCo[i]	34	>99	>99	86	Not reported	5100 [1.26]
LFe_2Cl_4[j]	29	66	93	6	Not reported	2000 [1.55]

[a]Copolymerisation conditions: CHO:CHD:Cat 4000:20:1 ([Cat] = 2.44 mM , [CHO] = 9.9 M), 1 bar CO_2, 100 °C. [b]Expressed as a percentage of CO_2 uptake *vs* the theoretical maximum (100 %), determined by comparison of the relative integrals of the ^{1}H NMR resonances due to carbonate (δ 4.65 ppm) and ether (δ 3.45 ppm)

linkages in the polymer backbone. [c]Expressed as a percentage of polymer formation vs. the theoretical maximum (100 %), determined by comparison of the relative integrals of the ^{1}H NMR proton resonances due to polymer (4.65 ppm), *cis*-cyclic carbonate (4.68 ppm) and *trans*-cyclic carbonate (4.00 ppm). [d]Turnover frequency (TOF) = Turnover number (TON) / Time (h) calculated for 5–20 % conversion, TON = Number of moles of CHO consumed / number of moles of catalyst. [e]k_{obs} calculated from the gradient of the semilogarithmic plot of $\ln([CHO]_0/[CHO]_t)$ *vs.* time. [g]Determined by SEC, in THF, using narrow-M_n polystyrene standards as the calibrant; dispersity is given in brackets. [h]This literature catalyst was tested at 0.1mol% catalyst loading, 1 bar CO_2, 100 °C[7a]; [i]This literature catalyst was tested at 0.05mol% catalyst loading, 1 bar CO_2, 120 °C[7b]; [j]This literature catalyst was tested at 0.1mol% catalyst loading, 1 bar CO_2, 80 °C[7c].

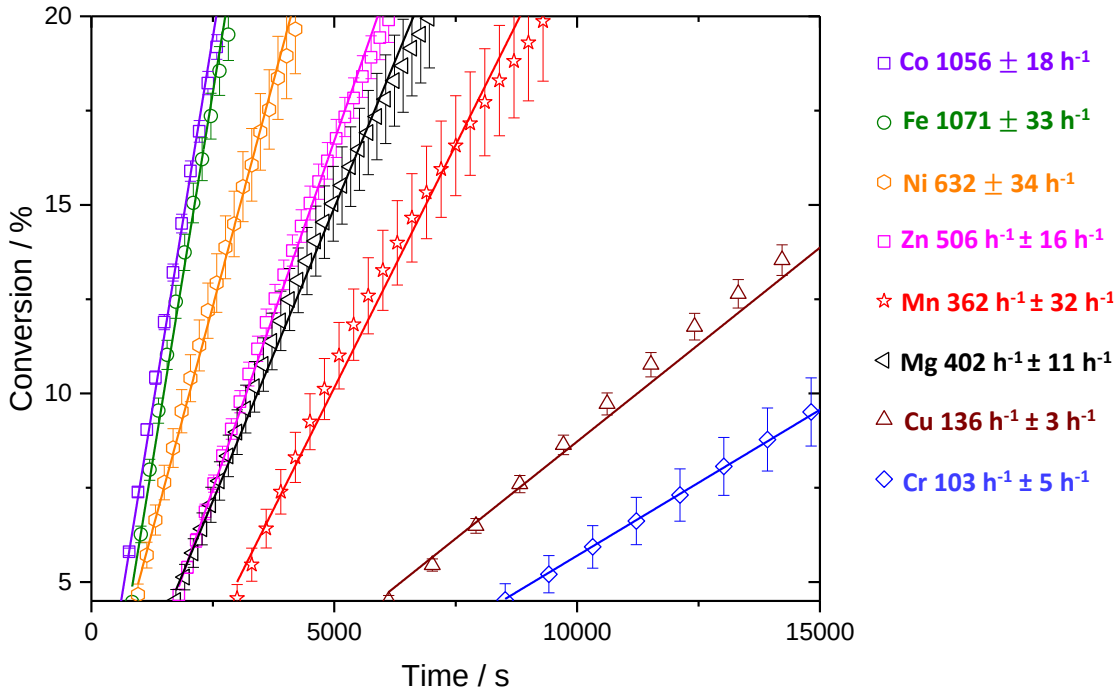


Figure 3.13. Graph of CHO conversion against Time for CO_2/CHO copolymerisation using complexes **1–8**.

The most active catalysts were MgCo (**6**) (already reported)[4] and MgFe (**5**), with TOFs of 1056 ± 18 h^{-1} and 1071 ± 33 h^{-1}, respectively. In both cases, high polymer and CO_2 selectivity (>99 %) and good polymerization control, with Đ = 1.25 and 1.11, were observed. Comparing catalysts **1–8**, the reactivity order obtained was Fe ~ Co > Ni > Zn > Mg > Mn > Cu > Cr. All rates show good molar mass control and monomodal, narrow dispersity distributions (1.11 < Đ < 1.23), Figure 3.14. The low activity of complex **3** (MgCr) may potentially be explained by its high sensitivity to both oxygen and moisture, as a rapid colour change from blue to brown was observed during polymerisation which also happens when the complex is exposed to air. This shows

that even working under inert atmosphere and with dry solvents, a trace of moisture can still be found in these systems.

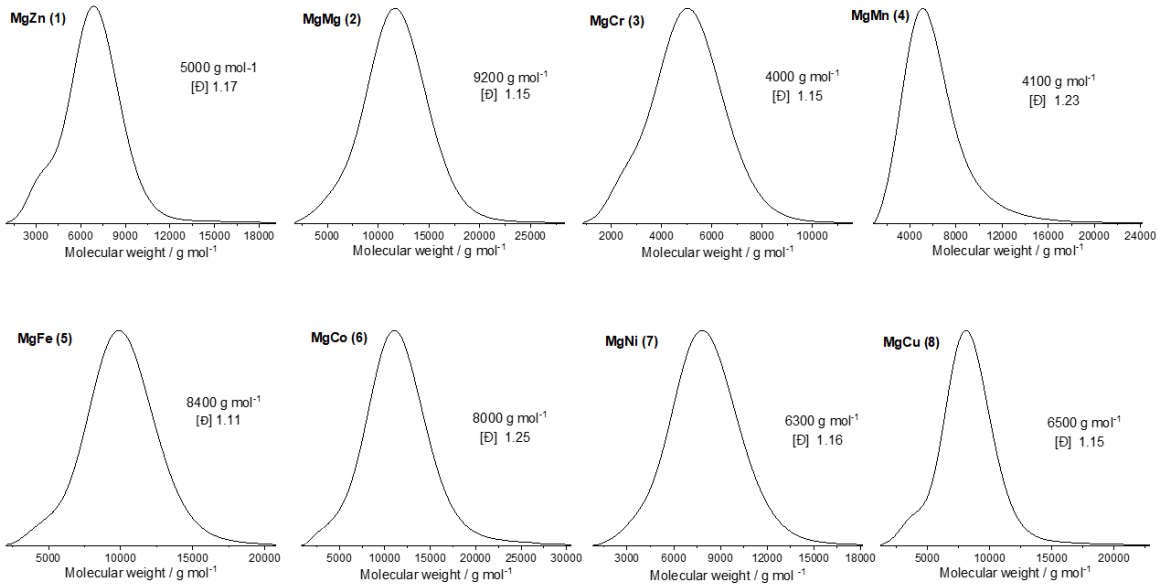


Figure 3.14. GPC traces for complexes **1**–**8**.

When the order of reactivity is analysed through the first-row for transition metals, the activity data form a volcano plot, where the most effective metals are in the middle of the period and like in a mirror, when you go far from this middle point, the reactivity decreases to a minimum before increasing slightly again, Figure 3.15. This trend shows that the reactivity does not follow a specific metal property and cannot be explained using just one physical-chemical parameter, but could be influenced by a combination of aspects such as bond dissociation energy, monomer or ligand exchange rate, explored below.

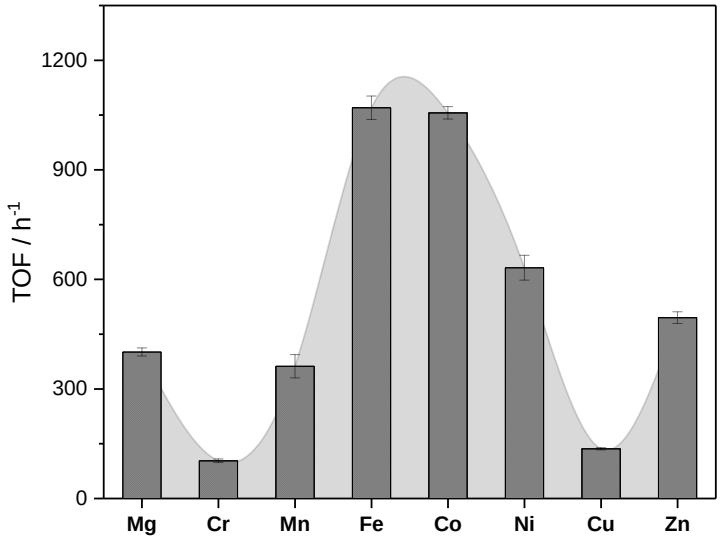


Figure 3.15. TOFs values obtained from ROCOP of CO_2/CHO for complexes **1–8** represented in following MgMg and the first-row of transition metals MgM(II) (M(II) = Cr, Mn, Fe, Co, Ni, Cu, Zn).

- Bond dissociation enthalpies (BDEs)

Kepp and co-workers recently reported a theoretical study of bond dissociation enthalpies for transition metals.[28] In this study, calculated and experimental values (reported in the literature) follow a trend where the early transition metals show the strongest metal-oxygen bonds interactions, decreasing towards the right, with two humps, due to a combination of oxophilicity and orbital effects, explained bellow.[28] This trend was already predicted by DFT by Van Santen et al.[29]

Oxophilicity and electronegativity: This effect is dominated by the difference in electronegativity between the metal and oxygen, which determines the bond strength of a polar covalent bond. In the transition-metal series, the values in electronegativity increase from the left to right, resulting in decreasing M–O bond strengths. Therefore, metals with higher electronegativity values show lower oxophilicity and consequently lower values of BDEs. This trend can be most easily observed when oxophilicity, electronegativity and BDEs are plotted together for the first-row of transition metals (Figure 3.16).

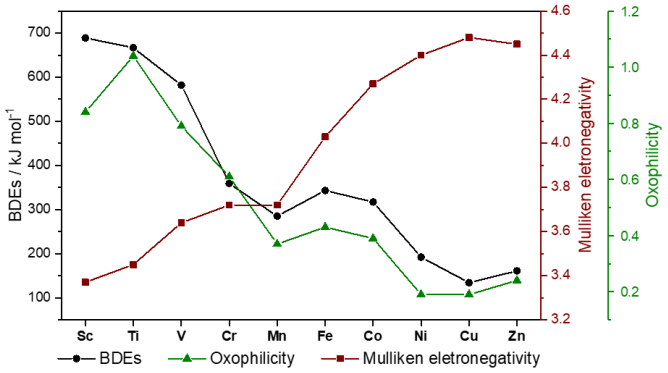


Figure 3.16. Comparison of BDEs (M–O), Mulliken electronegativity and oxophilicity through the fist-row transition metals. Graph adapted from Moltved et al.[28]

d-Orbital occupation and effective nuclear charge: The second effect that influences the BDEs trend is the antibonding d-orbital occupation (e_g orbitals in O_h symmetry) in high-spin complexes, explaining the humps, whereas the linear trend is caused by the effective nuclear charge, which correlates with the filling of the d-orbitals.[28]

When the BDEs values for M–O (M = Mg, Cr, Mn, Fe, Co, Ni, Cu and Zn), based on the CRC *Comprehensive Handbook of Chemical Bond Energies*,[30] are compared with the TOFs obtained for complexes **1**–**8**, although the general shape of the curves are similar, TOFs and BDEs do not directly correlate, Figure 3.17. Despite low activity was obtained for complexes with metals that presented the highest and the lowest BDEs values (Cr(II) and Cu(II)), the other transition metals do not follow any clear BDE pattern. To test whether the activity correlates with the extremes of BDEs, the complex with Sc(II), Ti(II) and V(II) could be synthesized and probed. Based on Figure 3.16, the BDEs values reported for these metals are much higher than the values of the metals studied in this chapter.

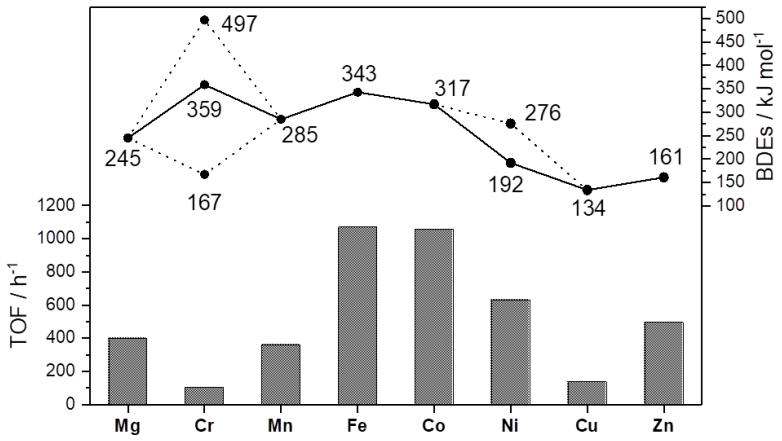


Figure 3.17. Graph comparing the catalyst activity with BDEs (M–O) values reported in the literature. Due to a non-agreement in the Cr and Ni BDEs values, both values found in the literature (---) were reported in the graph, and the values suggested by Keep and co-workers are connected by a full line (–).[28, 30]

- Water exchange rate constant and hydrolysis constant

Water exchange rate constant (WERC): Other characteristics to be considered are monomer or ligand exchange rate constants. As a first attempt at understanding these, values for water exchange rates for homoleptic metal complexes were taken from the literature (WERC).[31-34] The ligand exchange rate constants for TM(II) (TM = first-row transition metal ions) in aqueous solution fall between 3 x 10^4 and 8 x 10^9 M^{-1} s^{-1}. Traditionally, metal ions are grouped into different classes according to the rates of water exchange.[35] When the WERC values are compared with the polymerisation TOFs, the highest WERC values correlated with TM showing lower activity Cr(II) (7 x 10^9 M^{-1} s^{-1}) and Cu(II) (8 x 10^9 M^{-1} s^{-1}) while intermediate values, 3–1 x 10^6 s^{-1}, were reported for Fe(II) and Co(II) respectively, which comprise the most active catalysts.[35] Plotting the catalyst activity against conventional WERC values (logarithmic scale) shows the lack of obvious trend, Figure 3.18.[31, 34]

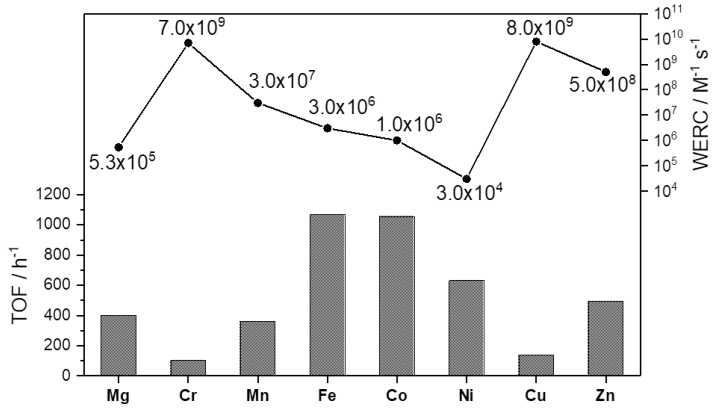


Figure 3.18. Graph comparing the catalyst activity with WERC values, plotted on a log scale.[31-34]

Hydrolysis constant (pK_a): The pK_a values are correlated to the Lewis acidity of the cation and are related to hydration energy.[31, 34] Comparing the pK_a values for magnesium and the first-row of transition metals with the activity also fails to show a strong correlation, Figure 3.19. Although Cr(II) shows a low pK_a, indicating feasible cation hydrolysis. High pKa values (≥ 10.08), for example, Mg(II) and Mn(II), usually indicates that the cations have a small hydration energy and the cations are highly stable. The other metals show intermediate pK_a values.[31, 34]

It was reported by Kobayashi et al., that comparing WERC and pK_a for transition metals and lanthanides allowed some correlation with catalytic activity in the Aldol reaction. In that study, metals with intermediate pK_a values showed the best results – similar to the performance in polymerization catalysis of this series of complexes.[31-33]

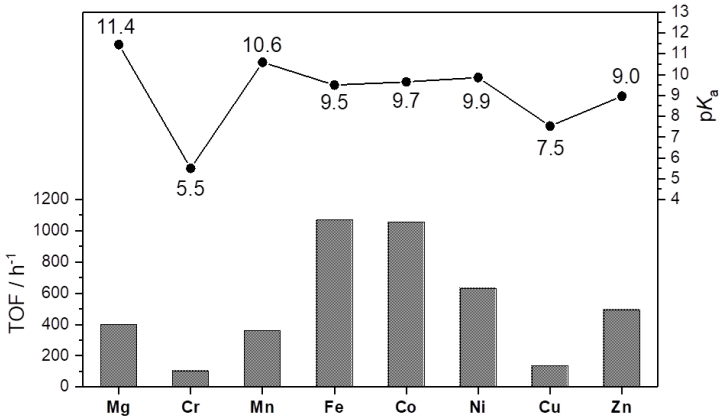


Figure 3.19. Comparison between pK_a values reported in the literature and TOFs for the series of metal ions.[31, 34]

Overall, none of these specific physical phenomena correlate directly or obviously with the catalytic activity, but perhaps that is unsurprising given most measures relate to different phases or solvents. In general, complexes showing higher activity (MgFe(II) and MgCo(II)) show intermediate values for all the parameters analyzed. On the other hand, the catalysts that showed low activity (MgCr(II) and MgCu(II)) show maxima or minima for most parameters, either interacting weakly (allowing the monomer to coordinate and dissociate in a time scale faster than the polymerization) or too strongly with monomers. One future option to better understand the influence of metal could be to conduct a computational study.

3.4.2. ROCOP of CO_2 and alternative epoxides using complexes 5 and 6

To have a better understanding of the two most active catalysts (MgFe and MgCo), they were tested for ROCOP at 1 bar CO_2 and different epoxides, including vinyl cyclohexene oxide (vCHO) that contains an external double bond that can be further reacted with thiols to install different functionality to the polymer, Figure 3.20.

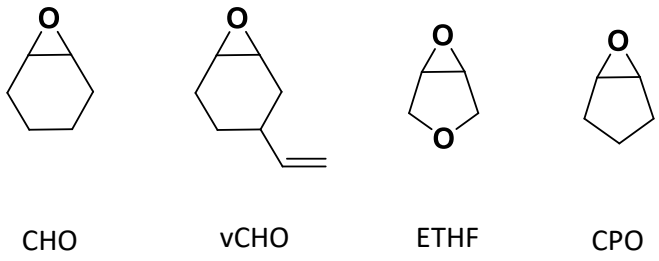


Figure 3.20. Structures of different epoxides investigated for ROCOP. Cyclohexene oxide (CHO); vinyl cyclohexene oxide (vCHO); 3,4-epoxytetrahydrofuran (ETHF); cyclopentene oxide (CPO).

To test the reactivity with each epoxide, catalyst **6** was used in the ROCOP for vCHO, CPO and ETHF with CO_2. As all polymerisations were performed in neat epoxide, due to the difference in their molecular weight and density, the polymerizations were performed in different catalysts : monomer ratio, to keep the catalyst concentration the same through all the systems (2.44 mM). In all systems, the epoxide was

successfully converted to polycarbonate with excellent selectivity (>99%), and monomodal narrow dispersity distribution for vCHO and CPO (Table 3.7 and Figure A.15), however, the copolymerisation of CO_2 with CHO still showing the higher rate.

Table 3.7. CO_2/Epoxides ROCOP with MgCo (**6**). For individual polymerisation plots (conversion *vs.* time), see Appendix Figure A.15 and for GPC see Figure A.17.

Epoxide	Temp. (°C)	Conv. (%)	CO_2 (%)	Polym. (%)	TOF (h^{-1})	k_{obs} (x 10^{-5} s^{-1})	M_n (g mol^{-1}) [$Đ$]
CHO[a]	100	59	>99	>99	1056	8.39	8000 [1.25]
vCHO[b]	100	37	>99	>99	778	7.87	9580 [1.14]
CPO[c]	80	30	>99	>99	112	0.76	7060 [1.17]
ETHF[d]	80	15	>99	94	120	0.25	–

[a]Copolymerisation conditions: CHO:CHD:Cat 4000:20:1 ([Cat] = 2.44 mM , neat [CHO] = 9.9 M), 100 °C. [b]vCHO:CHD:Cat 3100:20:1 ([Cat] = 2.44 mM , neat [vCHO] = 7.7 M), 100 °C.[c]CPO:CHD:Cat 4600:20:1 ([Cat] = 2.44 mM , neat [CPO] = 11.5 M), 80 °C. [d]Copolymerisation conditions: ETHF:CHD:Cat 5800:20:1 ([Cat] = 2.44 mM , neat [CHO] = 14.4 M), 80 °C.

Furthermore, the ROCOP was also performed for vCHO, CPO and ETHF using MgFe (**5**) (Table 3.8). Vinyl cyclohexene oxide (vCHO) showed reasonable conversion to poly(vinyl cyclohexene carbonate) (TOF = 240 h^{-1}) with excellent selectivity. However, limited reactivity was observed for CPO (conv. 12 %) and ETHF (conv. ≤ 3%) both featuring a 5-membered ring moiety. It is important to point it out that due to the lower boiling point, CPO and ETHF polymerisations were performed at 80 °C, lower temperature when compared with the polymerisation of CHO and vCHO (100 °C), also contributing to the low rates. The ROCOP of CO_2/CHO still show the best result for this catalytic system.

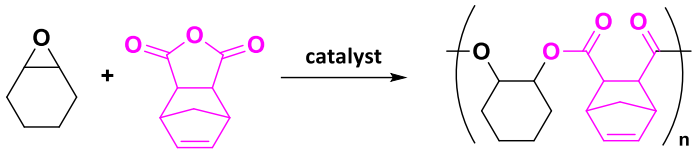
Table 3.8. CO_2/Epoxides ROCOP with MgFe (**5**). For individual polymerisation plots (conversion *vs.* time), see Appendix Figure A.16 and for GPC see Figure A.18.

Epoxide	Temp. (°C)	Conv. (%)	CO_2 (%)	Polym. (%)	TOF (h^{-1})	k_{obs} (x 10^{-5} s^{-1})	M_n (g mol^{-1}) [$Đ$]
CHO[a]	100	59	>99	>99	1071	8.47	8400 [1.11]
vCHO[b]	100	40	>99	>99	240	2.45	5700 [1.19]
CPO[c]	80	12	>99	>99	15	0.1	8080 [1.35]
ETHF[d]	80	2	–	–	–	–	–

[a]Copolymerisation conditions: CHO:CHD:Cat 4000:20:1 ([Cat] = 2.44 mM , neat [CHO] = 9.9 M), 100 °C. [b]vCHO:CHD:Cat 3100:20:1 ([Cat] = 2.44 mM , neat [vCHO] = 7.7 M), 100 °C.[c]CPO:CHD:Cat 4600:20:1 ([Cat] = 2.44 mM , neat [CPO] = 11.5 M), 80 °C. [d]Copolymerisation conditions: ETHF:CHD:Cat 5800:20:1 ([Cat] = 2.44 mM , neat [CHO] = 14.4 M), 80°C.

3.4.3. Preliminary results – NA/CHO Copolymerisation

A further investigation into the ROCOP of CHO and 5-norbonene-2,3-dicarboxylic anhydride (NA), was conducted (Scheme 3.3).



Scheme 3.3. Ring-opening co-polymerisation of CHO and NA.

The reactions were conducted at 100 °C, under nitrogen atmosphere, in neat epoxide (9.9 M), with 20 equiv. of CHD and 100 equiv. of NA compared to catalyst, similar conditions as the polymerisations performed for CO_2/CHO ROCOP. The polymerisations were performed with MgM(II) (M(II) = Mg, Mn, Fe, Co, Ni and Cu) catalysts. Polymerisations were monitored by *in situ* ATR-IR spectroscopy by following the anhydride resonance (1784 cm^{-1}) until complete consumption, as confirmed by ^1H NMR spectroscopy. As the raw conversion vs. time data show sigmoidal fits (consistent with slow initiation and/or reagent dissolution issues), for a preliminary comparison of catalytic activity, k_{obs} and TOFs data were analysed from 30–80% conversion, Figure

A-19 to A-21 and Table 3.9. However, a full fitting with different initiation models should be undertaken in the future.

Table 3.9. CHO/NA ROCOP data for MgM(II) (M(II) = Mg, Cr, Mn, Fe, Co, Ni, Cu).[a]

MgM	Polym. (%)[b]	TOF (h^{-1})[c]	k_{obs}(x 10^{-4} s^{-1})[d]
Mg	>99	190	1.37
Cr	>99	11	0.06
Mn	>99	140	1.01
Fe	>99	115	0.78
Co	>99	435	3.04
Ni	>99	118	0.82
Cu	>99	70	0.48

[a]Copolymerisation conditions: CHO:NA:CHD:Cat 4000:100:20:1 ([Cat] = 2.44 mM , [CHO] = 9.9 M), 100 °C. [b]Expressed as a percentage of anhydride conversion against the theoretical maximum (100 %). [c]Turnover frequency (TOF) = Turnover number (TON) / Time (h) calculated for 30-80 % conversion, TON = Number of moles of CHO consumed / number of moles of catalyst. [e]k_{obs} calculated from the gradient of the plot of $[NA]_t$ *vs*. time.

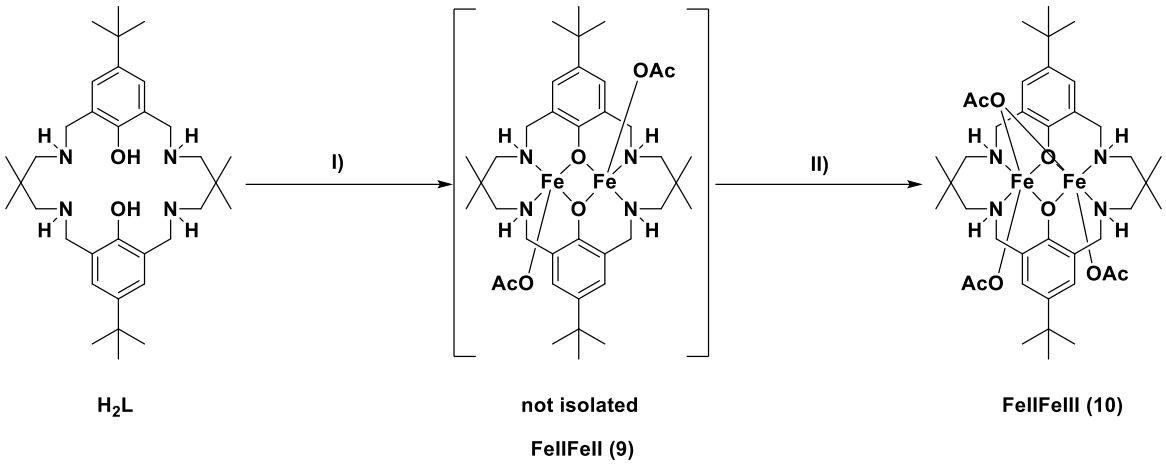
The preliminary data showed that the MgCo catalyst is the most active and MgCr and MgCu as the least active, following the same trend obtained for the ROCOP of CHO and CO_2 systems. Nonetheless, there are some differences, for example MgFe did not perform as well as in the CHO/CO_2 system. As mentioned before, these are preliminary results, and in order to obtain a fair comparison among the series, each polymerisation should be repeated at least three times and different fits to incorporate data from the entire polymerisation run used. These preliminary results also indicate an activity order that depends on synergy between the two metals.

3.5. Synthesis and Characterisation of Homodinuclear systems

With a range of heterodinuclear complexes suitable for the ROCOP of CO_2/CHO, MgFe (**5**) was of particular interest due to its comparable activity with the most active catalyst in the series reported MgCo (**6**).[4] The use of an iron-based catalyst over the related cobalt system has several advantageous, including, the greater natural abundance of iron, its relatively lower cost and inherently lower toxicity. For example in rats, the LD_{50}s (Median lethal dose) for soluble cobalt compounds was reported in a range from 42.4 to 317 mg/kg body weight, depending on the compound and species.[36] On the other hand, for iron complexes, the values reported were between 500 to 3,800 mg/kg body weight (reported for rats).[37-39] Therefore, an investigation comparing the relative performance of MgFe against its homodinuclear analogues were warranted.

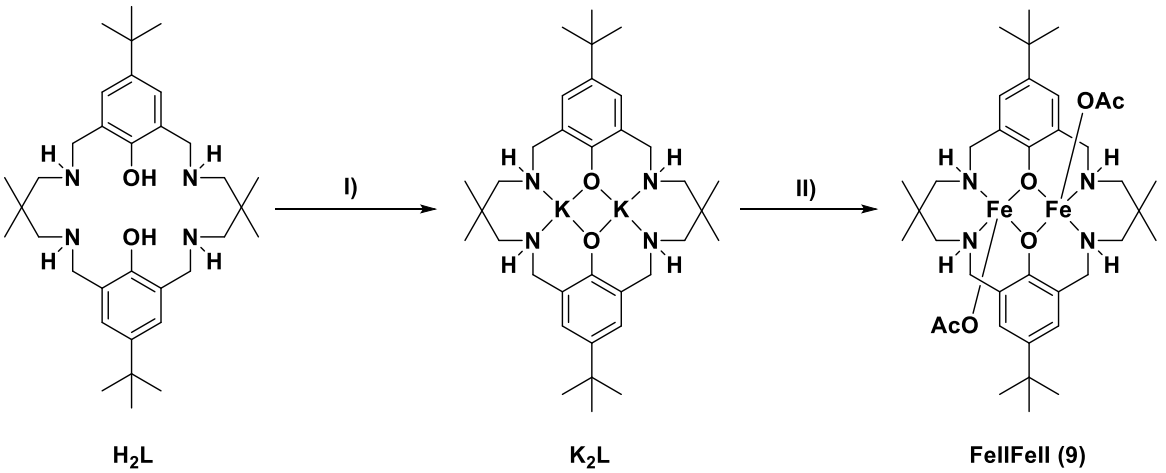
3.5.1. Synthesis of complexes 9 and 10

Initially, the synthesis of complex **9** was targeted using a similar procedure used for complexes **2–8**, by the reaction of H_2L with $Fe(OAc)_2$, in THF and with heating to 100 °C for 16 h, obtaining a purple powder with 60 % yield (Scheme 3.4.). However, due to the *in situ* formation of acetic acid, oxidation of a single Fe(II) centre to Fe(III) was observed (Scheme 3.4, complex **10**). Confirmation of this undesired reaction was resolved by cyclic voltammetry (Figure 3.21), magnetometry (Figure 3.23) and X-ray crystallography (Figure 3.24). Therefore, a different approach was needed to access complex **9**, with both Fe ions in the 2+ oxidation state.



Scheme 3.4. Synthesis of FeIIFeIII complex **10** with unisolable complex **9** intermediate. I) 2 $Fe(OAc)_2$ in THF at 100 °C for 16 h with the formation of HOAc. II) Excess of HOAc formed from the first reaction.

To access the desired complex FeIIFeII a new synthetic strategy was necessary. First a bis-potassium complex (LK_2) was synthesised following a procedure previously reported in the literature, where the pro-ligand H_2L is reacted with 2 Equiv. of $K(N(SiMe_3)_2)$.[2] The bis-potassium product was than reacted with 2 Equiv. of $Fe(OAc)_2$ in THF and heated to 100 °C for 16 h. After purification, FeIIFeII was obtained as a red powder which was successfully characterized by CV, SQUID magnetometry and MALDI-ToF.



Scheme 3.5. Synthesis of $Fe^{II}Fe^{II}$ complex **9**. I) $K(N(SiMe_3)_2)$ in THF at 100 °C for 16 h. II) $Fe(OAc)_2$ in THF at 100 °C for 16h.

3.5.2. Cyclic Voltammetry

The cyclic voltammograms of complexes **9** and **10** showed in Figure 3.21, were obtained following the same procedure as complexes **1**–**8**. The cyclic voltammogram of complex **9** displays two quasi-reversible redox events with $E_{½}$= -1.29 and -0.46 V, which correspond to [FeIIFeII]/[FeIIFeIII]$^{+}$ and [FeIIFeIII]$^{+}$/[FeIIIFeIII]$^{2+}$. In contrast, the cyclic voltammogram for complex **10** showed a single redox event at $E_{½}$= -0.48 V, consistent to [FeIIFeIII]/[FeIIIFeIII]$^{+}$ and an irreversible reduction FeIIFeII/FeIIFeI at E_{pa} = -1.67 V. A summary of the redox potentials are in Table 3.10. The series of redox events above +0.59 V attributed to the ligand are not clear in the homodinuclear cyclic voltammograms probably due to the strong signals obtained for their redox events.

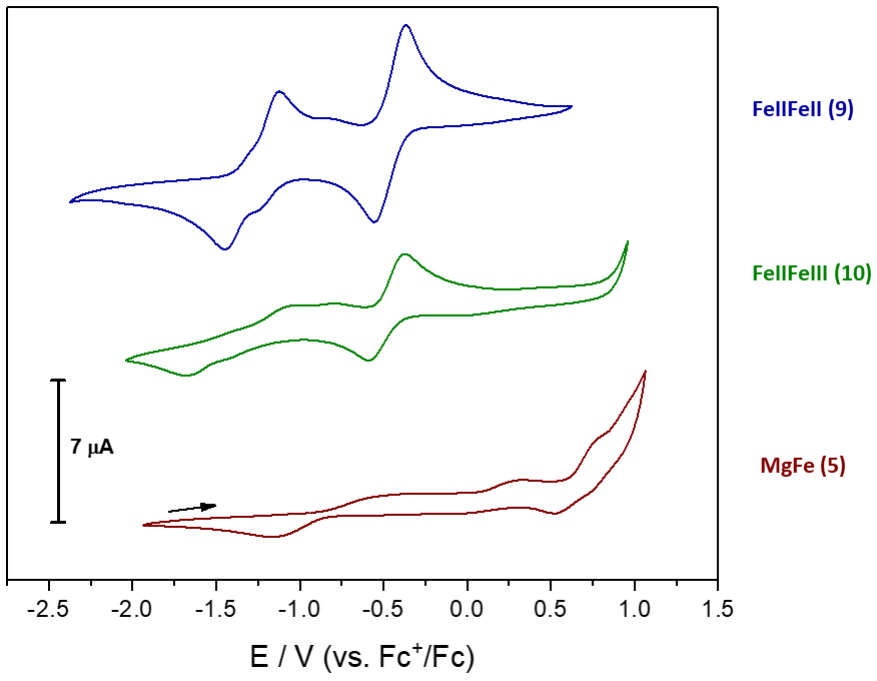


Figure 3.21. Cyclic voltammograms of complexes **5**, **9** and **10** in THF at scan rate 0.1 V, calibrated against Fc^{+}/Fc.

Table 3.10. Redox values of the complexes **9** and **10**.

Complex	Transition	E_{pa}	E_{pc}
FeIIFeII (9)	$[FeIIFeII]/[FeIIFeIII]^{+}$	-1.13	–
	$[FeIIFeIII]^{+}/[FeIIIFeIII]^{2+}$	-0.37	–
	$[FeIIIFeIII]^{2+}/[FeIIFeIII]^{+}$	–	-0.545
	$[FeIIFeIII]^{+}/[FeIIFeII]$	–	-1.45
FeIIFeIII (10)	$[FeIIFeIII]/[FeIIIFeIII]^{+}$	-0.38	–
	$[FeIIIFeIII]^{+}/[FeIIFeIII]$	–	-0.58
	FeIIFeII/FeIIFeI	–	-1.67

3.5.3. Superconducting Quantum Interference Device (SQUID) Magnetometry

The magnetic susceptibility (χ) measured at different temperatures was studied for complexes **9** and **10**. As previously shown, the magnetic susceptibility was corrected for the underlying diamagnetic contribution, using Pascal constants, (Table A.3).[17] The temperature dependence of the inverse of molar susceptibility (χ_m^{-1}) (Figure 3.22-a and 3.23-a) also follows the Curie-Weiss law showing Currie constant (C) of 9.82 and 7.70 emu·K·mol^{-1} for complexes **9** and **10** respectively with a Curie-Weiss constant (θ) 2.64 and 2.34 K. The positive signal of θ, and the increase in the μ_{eff} values when the system is cooled (Figure 3.22-b and Figure 3.23-b), indicate a ferromagnetic interaction between the two irons.

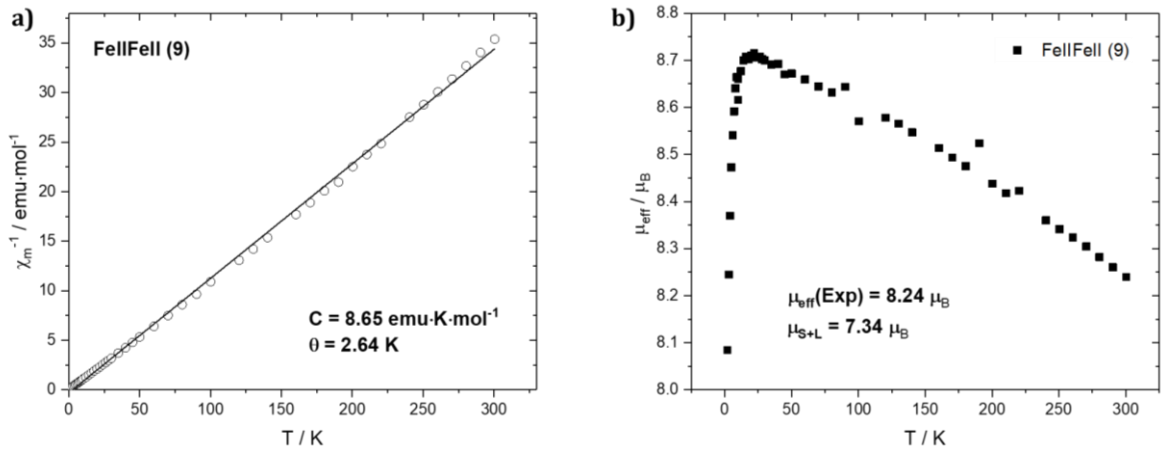


Figure 3.22. a) Inverse of molar susceptibility *vs*. temperature for complex **9**. ∘ experimental data, – fitting of the curve. b) Effective magnetic moment *vs.* temperature plot for complex **9**.

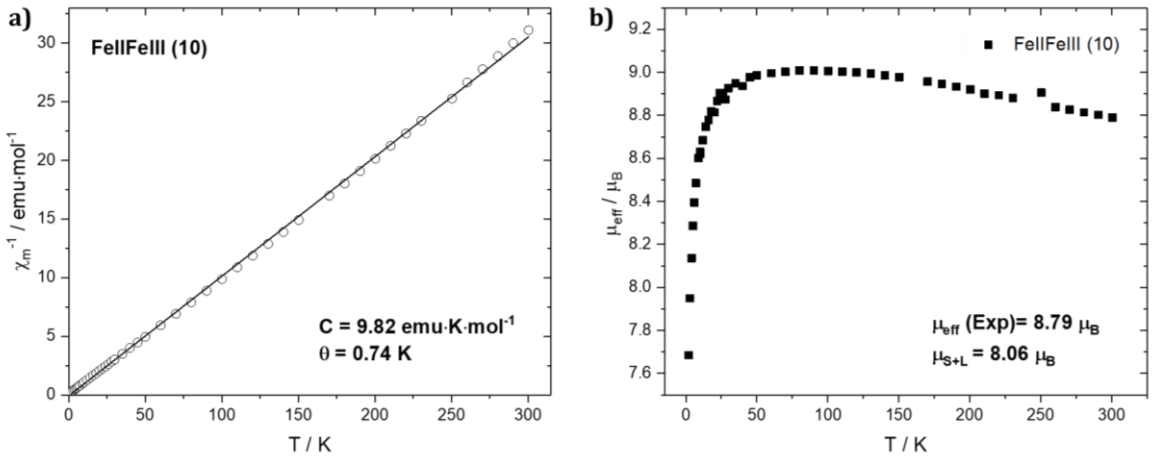


Figure 3.23. a) Inverse of molar susceptibility *vs*. temperature for complex **10**. ∘ experimental data, – fitting of the curve. b) Effective magnetic moment *vs.* temperature plot for complex **10**.

The theoretical values for the effective magnetic moment at room temperature were calculated considering the spin-orbit coupling following equation 3.2 as explained previously in this chapter. The Fe ions were considered magnetically isolated with S = 2 and 5/2 for Fe(II) and Fe(III) and L = 2, giving a μ_{S+L} = 7.34 and 8.06 μ_B for complex **9** and **10** respectively.

The experimental magnetic moment values are higher than the calculated ones, μ_{eff}(Exp) = 8.24 and 8.79 μ_B for complex **9** and **10**, indicating that the metal centres are not perfectly isolated and some interaction is already happening at room temperature, however, the interaction is not strong enough to consider a valence-delocalized diiron once the theoretical μ_{S+L} should be 9.28 μ_B (S = 4 and L = 2) and 10.25 μ_B (S = 9/2 and

L = 2) for complex **9** and **10**. Previous diiron complexes with tetraaminodiphenol macrocyclic ligands reported in the literature also presented as valence-trapped with a weak electron coupling at room temperature.[40]

3.5.4. X-Ray Crystallography of complex 10

Single crystals, suitable for X-ray diffraction, of complex **10** were obtained by Arron Deacy (University of Oxford), from a saturated solution of the complex in THF, held at -40 °C over 10 days under nitrogen atmosphere. The elucidated molecular structure (Figure 3.24) shows the macrocycle adopts a "bowl-shape" as obtained for the MgFe, MgNi and MgCo complexes. The structure shows three coordinated acetates, where one of them is bridging across both iron centres. The metal–metal distance is 2.90 Å, similar to the distance found in the MgFe and MgNi system (3.0083 and 3.036 Å), selected atom distances are shown in Table 3.11.

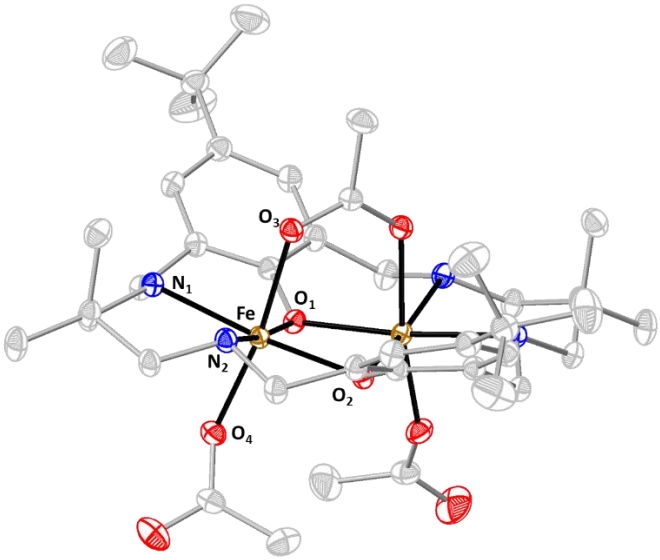


Figure 3.24. Crystal structure obtained for the complex FeIIFeIII (**10**) by Dr. Arron Deacy (University of Oxford). Thermal ellipsoids represented at 40 % probability. H-atoms and THF crystallization solvent were omitted to clarify.

Table 3.11. Selected distances for complex **10**.

Bond	Distance / Å	Bond	Distance / Å
Fe–Fe	2.8999(5)	Fe–O_4	1.9644(14)
Fe–O_1	2.0602(13)	Fe_1–N_1	2.1964(15)
Fe–O_2	2.0640(13)	Fe_1–N_2	2.1912(15)
Fe–O_3	2.0946(13)		

3.5.5. Mass spectrometry

The MALDI-ToF mass spectrum for complexes **9** and **10** each display a single molecular mass at 721.31 *m/z*, correspondent to $[LFe(II)Fe(II)(OAc)]^+$, Figure 3.25. Only the loss of a single acetate group during ionisation, to form $[LFe(II)Fe(II)(OAc)]^+$ (721.31 *m/z*) and $[LFe(II)Fe(III)(OAc)_2]^+$ (780.32 *m/z*), was expected. This may indicate the further reduction of Fe(III) to Fe(II), and the loss of an additional acetate group, occurred during ionisation of complex **10**.

As cyclic voltammetry and SQUID results showed that two distinct products where obtained, the presence of the same signal indicates that complex **9** lost one acetate during the ionization process while complex **10** lost two acetates during the analysis. These MALDI-ToF results indicate that this type of spectrometry is not suitable to distinguish between homodinuclear complexes **9** and **10**, therefore, a softer ionization technique would be required to analyse these compounds such as electrospray ionization mass spectrometry.

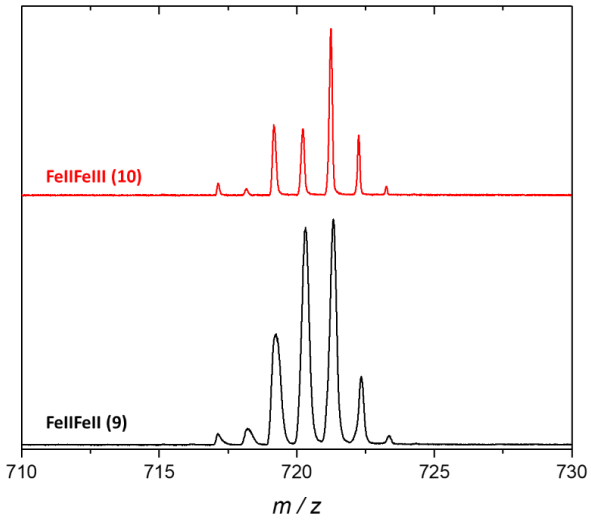


Figure 3.25. MALDI-ToF spectra of complexes **9** and **10** with signals at 721.3 *m/z*.

3.5.6. Infrared Spectroscopy

The FT-IR spectra for complexes **9** and **10** were obtained following the same procedure as described previously for complexes **1–8**. Comparing spectra for **9** and **10** with complex MgFe (**5**) and pro-ligand H_2L, the set of signals correspondently to acetate and the NH stretching are presented in all spectra, as showed in Figure 3.26. All spectra also showed the absence of a signal at 707 cm^{-1} characteristic out-of-plane phenol OH deformation, indicating the absence of pro-ligand contamination. For the spectrum of FeIIFeIII, complex **10**, the signal at 1562 cm^{-1} corresponds to $\nu_{(COO)\text{-}as}$ it is broader than the same signal for complexes **5** and **9**, showing a shoulder from signals overlapping at 1597 cm^{-1}. This signal together with the appearance of several signals in the $\nu_{(COO)\text{-}sy}$ region (1425, 1382 and 1363 cm^{-1}) is in agreement with the multiple acetate environments shown in the single-crystal structure for this compound (Figure 3.24), exhibiting the Δ values [$\nu_{(COO)\text{-}as}-\nu_{(COO)\text{-}sy}$] varying from 139 to 242, indicating the presence of unidentate and bridging acetate complexes.[41] In the same spectrum (complex **10**) a signal at 1710 cm^{-1} can also be observed, corresponding to the $\nu_{(C=O)st}$ of acetic acid,[42] suggesting that there may also be some free acid due to an exchange

with other protic species. A summary of the wavenumber of the main signals is represented in Table 3.12.

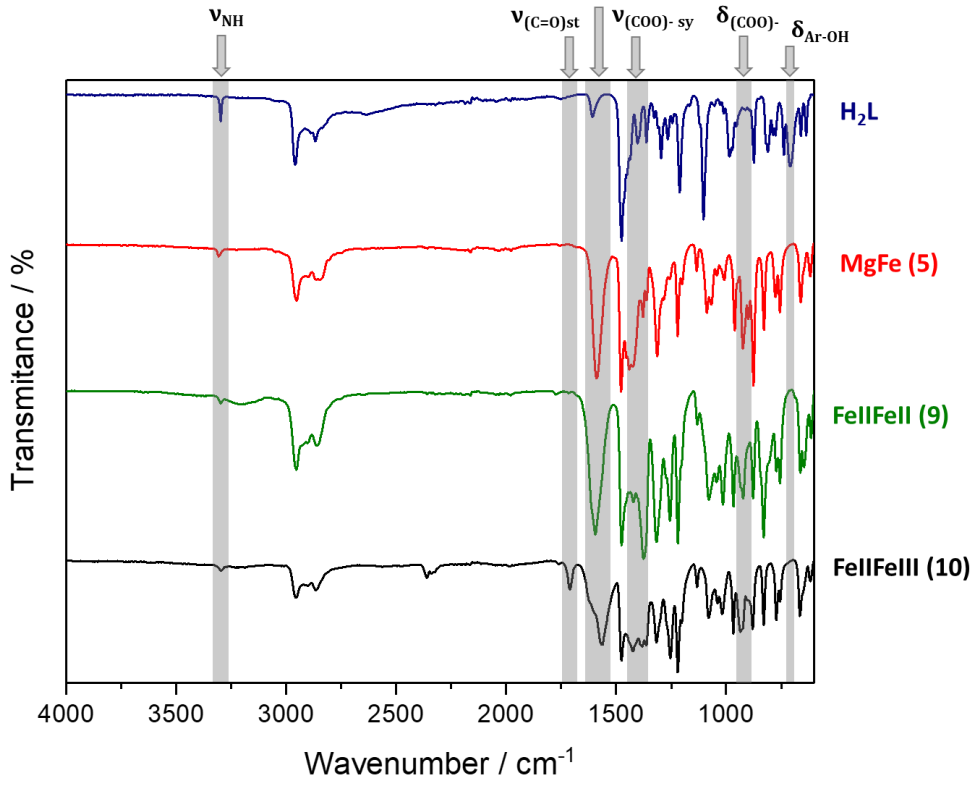


Figure 3.26. Comparison among infrared spectrum for complexes **5, 9**,**10** and pro-ligand H_2L.

Table 3.12. Main bands of infrared spectrum for complexes **5, 9** and **10.**

Catalyst	Metal	ν_{NH}	$\nu_{(COO)-as}$	$\nu_{(COO)-sy}$	$\delta_{(COO)-}$
5	MgFe	3308	1587	1452–1421	924
9	FeIIFeII	3298	1595	1421, 1375	921
10	FeIIFeIII	3296	1596,1564	1425–1363	925

3.5.7. ROCOP of CO_2/CHO for complexes 9 and 10

Following the same polymerisation conditions used for complexes **1–8**, complexes **9** and **10** were tested for the ROCOP of CO_2/CHO at 1 bar CO_2, [CHO]:[CHD]:[Cat] = 4000:20:1. The polymerisations were followed by *in situ* ATR-IR for 18 h, however, only trace conversions were observed.

The heterometallic MgFe, complex **5**, shows better polymerisation activity than the homodinuclear MgMg, FeIIFeII and FeIIFeIII. The performance of the heterodinuclear catalyst is in accordance with previous studies reported comparing the reactivity of MgCo and MgZn with their respective homodinuclear systems, MgMg, CoCo or ZnZn, where the heterodinuclear catalysts showed higher activity, when compared in the same polymerisation conditions.[1, 4]

These results reaffirm previously published studies where, in the "chain-shuttling mechanism", the growing polymer chain alternates between the two metal centres, and the two metals cooperate to ring-open the epoxide, with one binding the epoxide and the other providing the nucleophile.[43, 44] This highlights the importance of the heteronuclear systems, where the cooperative effect of the ions support the idea of each metal ion playing a different role in the polymerisation catalytic cycle.

3.6. Conclusions and Outlook

A series of heterodinuclear catalysts with Mg(II) and transition metals M(II) (M(II) = Cr, Mn, Fe, Co, Ni, Cu, Zn) and the homodinuclear di-magnesium were synthesised, characterised and tested in ROCOP reactions with CHO and CO_2 at 1 bar CO_2 pressure. The copolymerisation results showed MgFe and MgCo as the most active catalysts, with TOFs = 1071 ± 33 and 1056 ± 18 h^{-1}, respectively. On the other hand, MgCr and MgCu showed the lowest rates, with TOFs = 103 ± 5 and 136 ± 3 h^{-1}. There was no obvious correlation between catalytic activity and published data for the second metal ion, including bond dissociation enthalpies (M–O), water exchange rate constant or pK_a. The only tentative correlation was that the most active complexes (Co(II) and Fe(II)), show intermediary values for these phenomena whilst the least actives complexes (Cr(II) and Cu(II)) tend to show values at the extremes.

The two most active catalysts (MgFe and MgCo) were also tested for the copolymerisation of CO_2 and different epoxides (vCHO, ETHF and CPO) at 1 bar CO_2 pressure. The complex MgCo was able to copolymerise all three monomers tested with CO_2, while the MgFe catalyst was able to copolymerise vCHO and CPO with CO_2, failing in the ROCOP of ETHF and CO_2.

The same series of catalysts was used for copolymerisation of CHO and NA as part of a preliminary study. MgCo showed the highest activity (TOF = 435 h^{-1}) and MgCu/MgCr showed the lowest rates (TOFs = 70 and 11 h^{-1}). For a better comparison among the CHO/anhydride systems, each polymerisation should be repeated and conversion *vs*. time data more carefully analysed. The experiment with MgZn should also be performed.

As MgFe was one of the most active catalyst, the di-iron (FeIIFeIII and FeIIFeII) catalysts were also synthesised and tested under the same conditions. Both di-iron species were inactive for the ROCOP, confirming the importance of the synergic interactions between Mg(II) and the transition metal ions M(II).

3.7. References

1. Garden, J. A.; Saini, P. K.; Williams, C. K., Greater than the Sum of Its Parts: A Heterodinuclear Polymerization Catalyst. *J. Am. Chem. Soc.* **2015,** *137* (48), 15078-15081.
2. Deacy, A. C.; Durr, C. B.; Garden, J. A.; White, A. J. P.; Williams, C. K., Groups 1, 2 and Zn(II) Heterodinuclear Catalysts for Epoxide/CO_2 Ring-Opening Copolymerization. *Inorg. Chem.* **2018,** *57* (24), 15575-15583.
3. Deacy, A. C.; Durr, C. B.; Williams, C. K., Heterodinuclear complexes featuring Zn(ii) and M = Al(iii), Ga(iii) or In(iii) for cyclohexene oxide and CO_2 copolymerisation. *Dalton Tran.* **2020,** *49* (1), 223-231.
4. Deacy, A. C.; Kilpatrick, A. F. R.; Regoutz, A.; Williams, C. K., Understanding metal synergy in heterodinuclear catalysts for the copolymerization of CO_2 and epoxides. *Nat. Chem.* **2020,** *12* (4), 372-380.
5. Trott, G.; Garden, J. A.; Williams, C. K., Heterodinuclear zinc and magnesium catalysts for epoxide/CO_2 ring opening copolymerizations. *Chem. Sci.* **2019,** *10* (17), 4618-4627.
6. Saini, P. K.; Romain, C.; Williams, C. K., Dinuclear metal catalysts: improved performance of heterodinuclear mixed catalysts for CO_2–epoxide copolymerization. *Chem. Comm.* **2014,** *50* (32), 4164-4167.
7. a) Kember, M. R.; Williams, C. K., Efficient Magnesium Catalysts for the Copolymerization of Epoxides and CO_2; Using Water to Synthesize Polycarbonate Polyols. *J. Am. Chem. Soc.* **2012,** *134* (38), 15676-15679. b) Kember, M. R.; White, A. J. P.; Williams, C. K., Highly Active Di- and Trimetallic Cobalt Catalysts for the Copolymerization of CHO and CO_2 at Atmospheric Pressure. *Macromolecules* **2010,** *43* (5), 2291-2298. c) Buchard, A.; Kember, M. R.; Sandeman, K. G.; Williams, C. K., A bimetallic iron(iii) catalyst for CO_2/epoxide coupling. *Chem. Comm.* **2011,** *47* (1), 212-214.
8. Mukherjee, A.; Lloret, F.; Mukherjee, R., Synthesis and Properties of Diphenoxo-Bridged CoII, NiII, CuII, and ZnII Complexes of a New Tripodal Ligand: Generation and Properties of MII-Coordinated Phenoxyl Radical Species. *Inorg. Chem.* **2008,** *47* (11), 4471-4480.
9. DiCiccio, A. M.; Longo, J. M.; Rodríguez-Calero, G. G.; Coates, G. W., Development of Highly Active and Regioselective Catalysts for the Copolymerization of Epoxides with Cyclic Anhydrides: An Unanticipated Effect of Electronic Variation. *J. Am. Chem. Soc.* **2016,** *138* (22), 7107-7113.
10. Arora, H.; Philouze, C.; Jarjayes, O.; Thomas, F., CoII, NiII, CuII and ZnII complexes of a bipyridine bis-phenol conjugate: Generation and properties of coordinated radical species. *Dalton Trans.* **2010,** *39* (42), 10088-10098.
11. Kanso, H.; Clarke, R. M.; Kochem, A.; Arora, H.; Philouze, C.; Jarjayes, O.; Storr, T.; Thomas, F., Effect of Distortions on the Geometric and Electronic Structures of One-Electron Oxidized Vanadium(IV), Copper(II), and Cobalt(II)/(III) Salen Complexes. *Inorg. Chem.* **2020,** *59* (7), 5133-5148.
12. Kochem, A.; Kanso, H.; Baptiste, B.; Arora, H.; Philouze, C.; Jarjayes, O.; Vezin, H.; Luneau, D.; Orio, M.; Thomas, F., Ligand Contributions to the Electronic Structures of the Oxidized Cobalt(II) salen Complexes. *Inorg. Chem.* **2012,** *51* (20), 10557-10571.

13. McCollum, D. G.; Yap, G. P.; Liable-Sands, L.; Rheingold, A. L.; Bosnich, B., Bimetallic Reactivity. Oxo Transfer Reactions with a Heterobimetallic Complex of Iron (II) and Vanadium (III). *Inorg. Chem.* **1997,** *36* (10), 2230-2235.
14. Fitzgerald, J. P.; Haggerty, B. S.; Rheingold, A. L.; May, L.; Brewer, G. A., Iron octaethyltetraazaporphyrins: synthesis, characterization, coordination chemistry, and comparisons to related iron porphyrins and phthalocyanines. *Inorg. Chem.* **1992,** *31* (11), 2006-2013.
15. Pavlishchuk, V. V.; Addison, A. W., Conversion constants for redox potentials measured versus different reference electrodes in acetonitrile solutions at 25°C. *Inorg. Chim. Acta* **2000,** *298* (1), 97-102.
16. Connelly, N. G.; Geiger, W. E., Chemical Redox Agents for Organometallic Chemistry. *Chemical Reviews* **1996,** *96* (2), 877-910.
17. Bain, G. A.; Berry, J. F., Diamagnetic Corrections and Pascal's Constants. *J. Chem. Edu.* **2008,** *85* (4), 532.
18. Walker, F. A.; Simonis, U., Iron Porphyrin Chemistry. In *Encyclopedia of Inorganic Chemistry*, King, R. B.; Crabtree, R. H.; Lukehart, C. M.; Atwood, D. A.; Scott, R. A., Eds. 2006.
19. Kahn, O., *Molecular Magnetism*. VCH: 1993.
20. Carlin, R. L., *Magnetochemistry*. Spring-Verlag Berlin Heidelberg: 1986.
21. Kumar, R.; Chnadra, S.; Mishra, P., Spectroscopic and electrochemical investigation with coordination stabilities: Mononuclear manganese(II) complexes derived from different constituents macrocyclic ligands. *Spectrochim. Acta A Mol. Biomol. Spectrosc.* **2007,** *68* (5), 1250-1255.
22. Bermejo, M. R.; Castiñeiras, A.; Garcia-Monteagudo, J. C.; Rey, M.; Sousa, A.; Watkinson, M.; McAuliffe, C. A.; Pritchard, R. G.; Beddoes, R. L., Electronic and steric effects in manganese Schiff-base complexes as models for the water oxidation complex in photosystem II. The isolation of manganese-(II) and -(III) complexes of 3- and 3,5-substituted N,N′-bis(salicylidene)ethane-1,2-diamine (H2salen) ligands. *Dalton Trans.* **1996,** (14), 2935-2944.
23. Fraser, C.; Bosnich, B., Bimetallic reactivity. Investigation of metal-metal interaction in complexes of a chiral macrocyclic binucleating ligand bearing 6-and 4-coordinate sites. *Inorg. Chem.* **1994,** *33* (2), 338-346.
24. Klose, A.; Solari, E.; Floriani, C.; Chiesi-Villa, A.; Rizzoli, C.; Re, N., Magnetic Properties Diagnostic for the Existence of Iron(II)-Iron(II) Bonds in Dinuclear Complexes Which Derive from Stepwise Insertion Reactions on Unsupported Iron-Aryl Bonds. *J. Am. Chem. Soc.* **1994,** *116* (20), 9123-9135.
25. Deacy, A. Heterodinuclar Cooperativity in Oxygenated Polymer Catalysis. University of Oxford, 2019.
26. Trott, G. Heterodinuclear Catalysts for CO_2/Epoxide Copolymerisations. University of Oxford, 2018.
27. Badertscher, M.; Buhlmann, P.; Pretsch, E., *Structure Determination of Organic Compounds*. Springer, 2009.
28. Moltved, K. A.; Kepp, K. P., The Chemical Bond between Transition Metals and Oxygen: Electronegativity, d-Orbital Effects, and Oxophilicity as Descriptors of Metal–Oxygen Interactions. *The Journal of Physical Chemistry C* **2019,** *123* (30), 18432-18444.
29. van Santen, R. A.; Tranca, I., How molecular is the chemisorptive bond? *Physical Chemistry Chemical Physics* **2016,** *18* (31), 20868-20894.
30. Luo, Y.-R., *Comprehensive handbook of chemical bond energies*. CRC press: 2007.

31. Kobayashi, S.; Nagayama, S.; Busujima, T., Lewis Acid Catalysts Stable in Water. Correlation between Catalytic Activity in Water and Hydrolysis Constants and Exchange Rate Constants for Substitution of Inner-Sphere Water Ligands. *J. Am. Chem. Soc.* **1998,** *120* (32), 8287-8288.
32. Hawkes, S. J., All Positive Ions Give Acid Solutions in Water. *J. Chem. Edu.* **1996,** *73* (6), 516-517.
33. Jackson, V. E.; Felmy, A. R.; Dixon, D. A., Prediction of the pKa's of Aqueous Metal Ion +2 Complexes. *J. Phys. Chem. A* **2015,** *119* (12), 2926-2939.
34. Takafumi, M.; Iwao, W.; Shigero, I., Amplitude in EXAFS and Ligand Exchange Reaction of Hydrated 3d Transition Metal Complexes. *Chem. Lett.* **1988,** *17* (6), 1073-1076.
35. Pfennig, B. W., *Principles of inorganic chemistry*. John Wiley & Sons: 2015.
36. Kim, J. H.; Gibb, H. J.; Howe, P. D., Cobalt and Inorganic Cobalt compounds. In *Concise International Chemical Assessment Document 69*, WHO Press: World Health Organization, 2006.
37. Somers, G. F., Relative Oral Toxicity Of Some Therapeutic Iron Preparations. *Br. Med. J.* **1947,** *2* (4518), 201-203.
38. Li, Z.; Lu, J.; Wu, C.; Pang, Q.; Zhu, Z.; Nan, R.; Du, R.; Chen, J., Toxicity Studies of Ethyl Maltol and Iron Complexes in Mice. *BioMed Res. Int.* **2017,** *2017*, 2640619.
39. Egorova, K. S.; Ananikov, V. P., Which Metals are Green for Catalysis? Comparison of the Toxicities of Ni, Cu, Fe, Pd, Pt, Rh, and Au Salts. *Angew. Chem. Int. Ed.* **2016,** *55* (40), 12150-12162.
40. Dutta, S. K.; Ensling, J.; Werner, R.; Flörke, U.; Haase, W.; Gütlich, P.; Nag, K., Valence-Delocalized and Valence-Trapped FeIIFeIII Complexes: Drastic Influence of the Ligands. *Angew. Chem. Int. Ed. in English* **1997,** *36* (1-2), 152-155.
41. Nakamoto, K., Infrared and Raman Spectra of Inorganic and Coordination Compounds. *Handbook of Vibrational Spectroscopy* **2006**.
42. Pavia, D. L.; Lampman, G. M.; Kriz, G. S.; Vyvyan, J. A., *Introduction to spectroscopy*. Cengage Learning: 2008.
43. Jutz, F.; Buchard, A.; Kember, M. R.; Fredriksen, S. B.; Williams, C. K., Mechanistic Investigation and Reaction Kinetics of the Low-Pressure Copolymerization of Cyclohexene Oxide and Carbon Dioxide Catalyzed by a Dizinc Complex. *J. Am. Chem. Soc.* **2011,** *133* (43), 17395-17405.
44. Buchard, A.; Jutz, F.; Kember, M. R.; White, A. J. P.; Rzepa, H. S.; Williams, C. K., Experimental and Computational Investigation of the Mechanism of Carbon Dioxide/Cyclohexene Oxide Copolymerization Using a Dizinc Catalyst. *Macromolecules* **2012,** *45* (17), 6781-6795.

Chapter 4

Investigations into backbone modifications in In-salan complexes for epoxide/CO_2 ROCOP

4.1. Introduction

During the mechanistic studies of the catalytic cycle for the copolymerisation of CO_2 and epoxides researchers have reported two main pathways: a dinuclear/dimeric or a bicomponent mechanism; both involve the addition of an ionic or Lewis basic co-catalyst, and were explored in Chapter 1.[1]

Among all the catalysts reported for the copolymerisation of CO_2/epoxide, metal salen complexes are significant due to their capacity to perform polymerisations with high selectivity, control and activity and have been extensively studied and reported in the literature.[1-3] However, when applied for ROCOP of CO_2/epoxide, these catalysts usually require high CO_2 pressure and co-catalyst. [4-6]

Recently, Williams and co-workers reported an indium catalyst, with a series of phosphasalen ligands that are hypothesised to operate by a mononuclear polymerization mechanism (Figure 4.1-a).[7] Based on crystallographic data, the propagating species had an octahedral coordination geometry at the indium core.[7] In contrast to most previously reported metal salen catalysts, that showed the ligand in a *trans*-configuration,[8-10] this system reveals a chelating (κ^2) carbonate and the ligand in a *cis-β* configuration (N.B. Configurations of tetradentate Schiff base ligands are illustrated in Figure 4.1-b).[11, 12] So far, the influence of the ligand conformation over the catalyst activity remains unclear.[7]

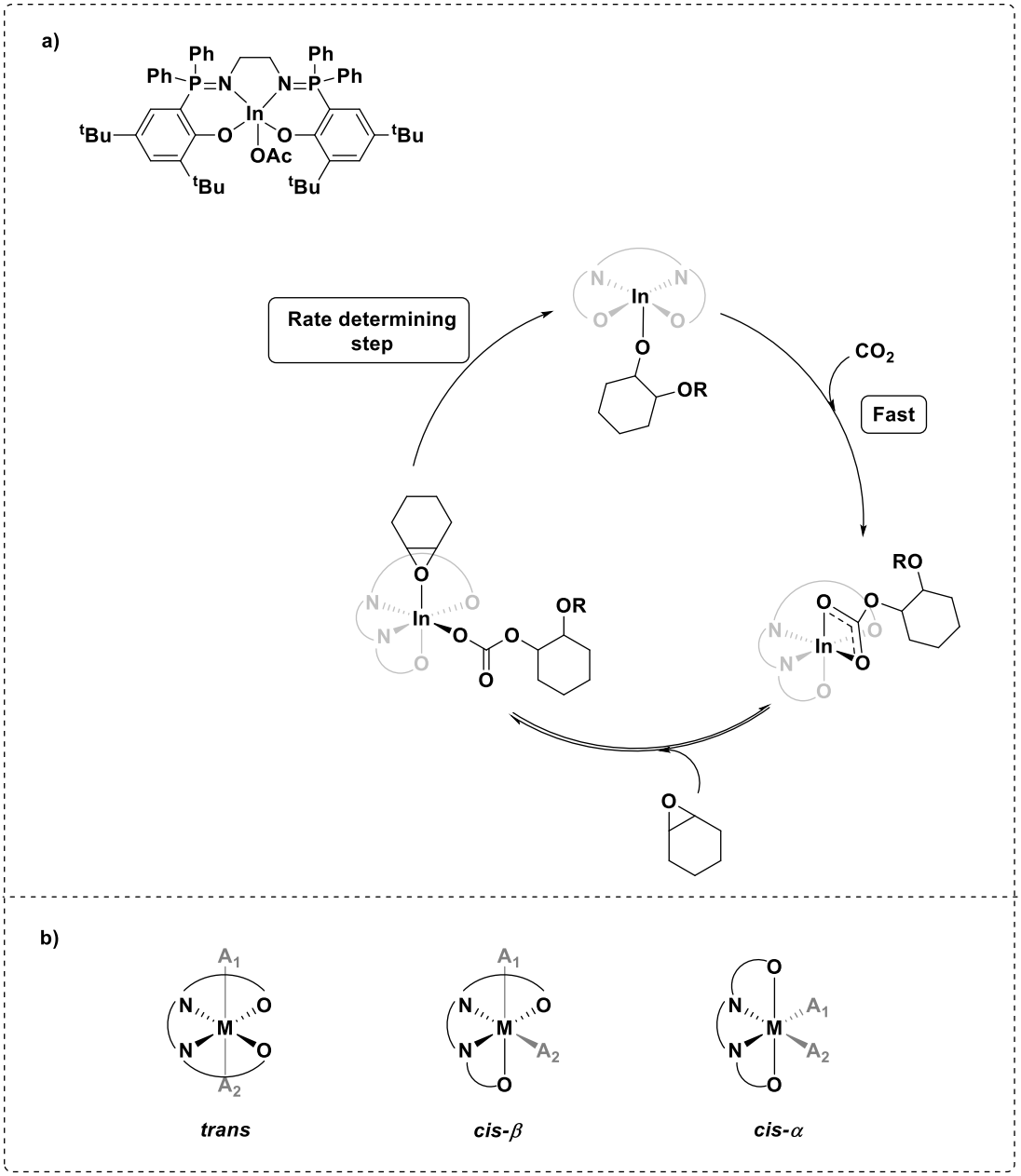


Figure 4.1. a) Structure of the In-phosphasalen and mononuclear mechanism for CO_2/epoxide ROCOP using indium catalyst. R = Growing polymer chain. Figure based on C. K. Williams, 2018.[7] b) Three possible configurations (*trans*, *cis*-β and *cis*-α) for tetradentate Schiff base ligand in an octahedral complex.

In the ROCOP of CO_2/CHO, the indium phosphasalen catalyst performed with better activity and selectivity than indium salen analogous catalyst.[7] These results could suggest some influence from the ligand, particularly considering that the phosphasalen ligand is more electron-donating (strong σ and π donor) and so may reduce the Lewis acidity of the metal centre compared with the In-salen complexes.[13, 14]

It was also reported that the reduction of the Lewis acidity in yttrium-phosphasalen complexes increased activity in ring-opening polymerisation of lactide, perhaps due to the increase in the lability of metal–alkoxide bonds.[15]

4.2. Aims

While most metal-salen complexes give good activity only when used with co-catalyst at high CO_2 pressure (20/30 bar), the In-phospasalens operated at 1 bar pressure, without co-catalyst and showed moderate activity and first order dependence on catalyst concentration. [7]

One of the hypotheses supporting this mononuclear mechanism was that the larger ionic radius of In(III), compared with other metals commonly used in these catalysts (r_{ionic} (pm) In(III) = 80, Cr(III) = 62, Co(III) = 55 and Al(III) = 54 pm),[16] allows the epoxide and carbonate to coordinate in a *cis*-position and to undergo back-side attack from these *cis*-sites during propagation. [7]

Another important aspect to consider are the influences, if any, of the substituents on the phenolate sites of the ligands. Previous studies explored the significance of *ortho*- and *para*-phenolate and showed that catalysts with bulky groups at *ortho* positions, such as *tert*-butyl groups, performed polymerisation with higher selectivity than those without. The preliminary studies on the *para*-phenolate substituents showed an increase in activity when electron withdrawing groups were added.[17, 18]

In this way, the influences of electron donating groups, metal size and ligand flexibility should be explored finding a balance to improve the catalysts activity and selectivity.

Considering all aspects discussed in this section, a range of In-salen complexes will be investigated to understand how different characteristics of the catalyst can influence the ROCOP and the possibility to access the new mononuclear mechanism:

1. Different backbones with 2, 3 and 4 carbons will be explored, to investigate flexibility and In(III) coordination chemistry (and for future work, other large ions such as La(III) and Y(III)).
2. Modifications of the nitrogen-substituents, specifically changing from salens to salans, will alter the electronic density at In(III) as well as increase the ligand flexibility and may accommodate the *cis*-coordinate transition state.
3. Electron withdrawing groups in the *para*-phenolate sites will also be examined using ^{t}Bu, OMe and Me groups. This part of the work was developed through the co-supervision of Mr. Sebastian Morton (part II student, Oxford Chemistry 2019).

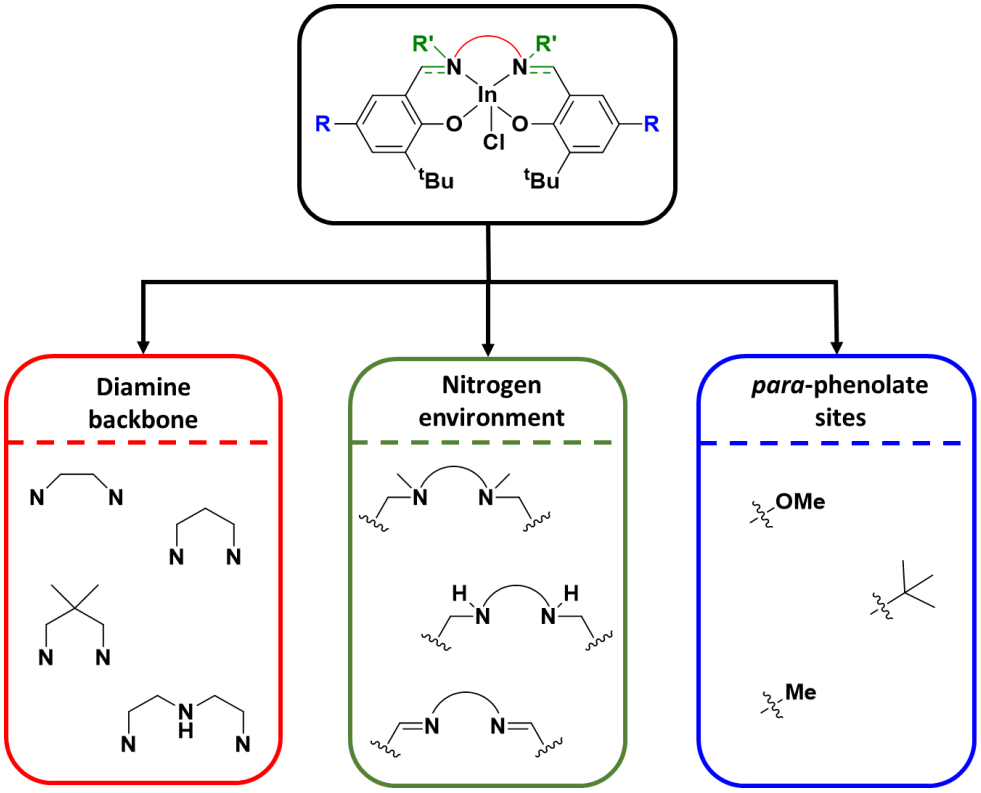
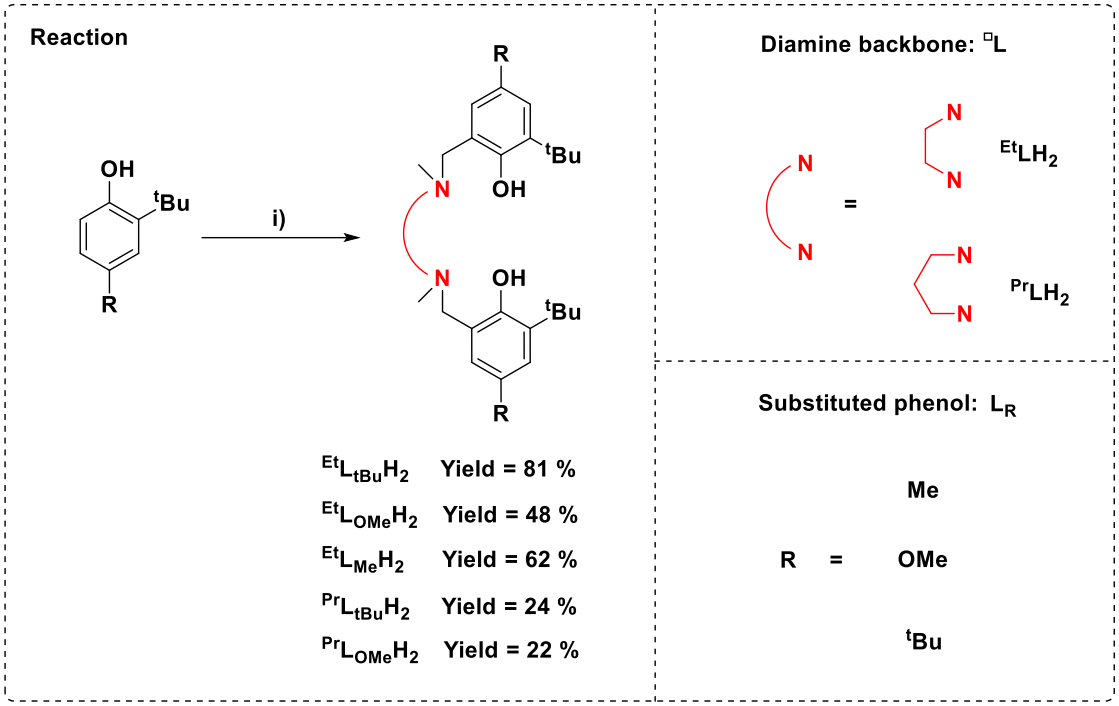


Figure 4.2. Catalyst designing explored in this chapter.

4.3. Ligands syntheses and characterisation

4.3.1. Synthesis of salan C2 and C3 backbone

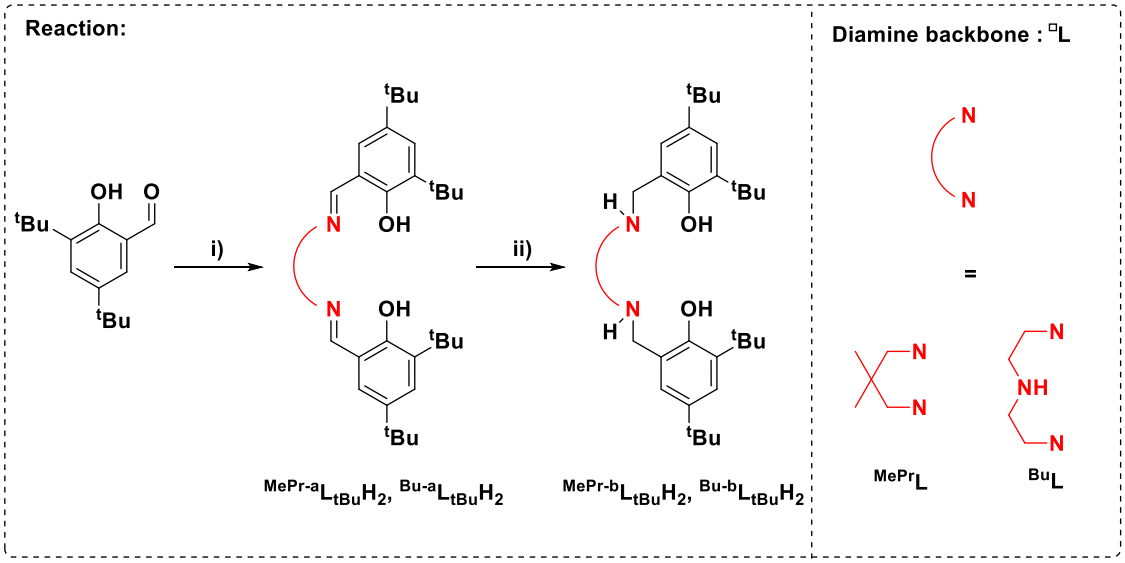


Scheme 4.1. Synthesis of ligands $^{Et}L_RH_2$ and $^{Pr}L_RH_2$, R = tBu, Me or OMe. i) formaldehyde and the correspondent amine, reflux in methanol for 17 h.

The appropriate phenol was used as a starting point for the synthesis of five salan ligands by a Mannich condensation, following an adapted procedure reported in the literature.[19] Amination of the commercially available phenol was carried out in the presence of formaldehyde, in methanol, by reaction with either *N,N*-dimethylethane-1,2-diamine ($^{Et}LH_2$) or *N,N*-dimethyl-1,3-propanediamine ($^{Pr}LH_2$), Scheme 4.1. The ligands differ according to the diamine 'linker' group, where C2 and C3 likers gave $^{Et}L_{tBu}H_2$ and $^{Pr}L_{tBu}H_2$, respectively, with 81 and 24 % yield. These backbones were also explored with different *para*-phenol substituents giving $^{Et}L_XH_2$ (X = OMe and Me) and $^{Pr}L_XH_2$ (X = OMe), with yields between 20 and 60 %.

4.3.2. Synthesis of salen C3' and C4 backbone ($^{MePr\text{-}a/b}L_{tBu}H_2$ and $^{Bu\text{-}a/b}L_{tBu}H_2$)

To access the C3 and C4 backbone ligand with N–CH_3 groups, an alternative synthesis was required as the necessary amines are not commercially available.



Scheme 4.2. Synthesis of ligands $^{MePr\text{-}a/b}L_{tBu}H_2$ and $^{Bu\text{-}a/b}L_{tBu}H_2$. i) Correspondent amine, reflux in ethanol for 2 h. ii) $NaBH_4$ in methanol for 16 h.

To access the desired ligands three step synthesis were required and all ligands were isolated, purified and reacted with indium precursors to give different complexes, as shown in the following sections. In the first step, 3,5-di-*tert*-butyl-2-hydroxibenzaldehyde was reacted with the correspondent amine [2,2-dimethyl-1,3-propanediamine (^{MePr}**L**) or 2,2'-diaminodiethylamine (^{Bu}**L**)] in ethanol.[20, 21] The product formation was monitored by ^{1}H NMR spectroscopy ($CDCl_3$) by the disappearance of the aldehyde singlet resonance at 9.82 ppm and the appearance of the imine singlet resonance, at 8.29 ppm for $^{MePr\text{-}a}L_{tBu}H_2$ or 7.83 ppm for $^{Bu\text{-}a}L_{tBu}H_2$. Overall, these ligands were isolated at 90 and 80 % yield.

Next, the two salan ligands ($^{MePr\text{-}b}L_{tBu}H_2$ and $^{Bu\text{-}b}L_{tBu}H_2$) were obtained by reducing the salens $^{MePr\text{-}a}L_{tBu}H_2$ and $^{Bu\text{-}a}L_{tBu}H_2$, with $NaBH_4$ in methanol.[22, 23] The reduction was followed by ^{1}H NMR spectroscopy ($CDCl_3$) with the disappearance of the imine singlet

resonances at 8.29 ppm (for $^{MePr\text{-}b}L_{tBu}H_2$) or 7.83 ppm (for $^{Bu\text{-}b}L_{tBu}H_2$), and the appearance of the benzylic resonances, at 3.94 and 5.58 ppm for $^{MePr\text{-}b}L_{tBu}H_2$ or $^{Bu\text{-}b}L_{tBu}H_2$, confirmed the reaction was complete.

The success of the protonation was also evidenced by FT-IR spectroscopy, showing the appearance of signals at 3321 and 3319 cm^{-1} for $^{MePr\text{-}b}L_{tBu}H_2$ or $^{Bu\text{-}b}L_{tBu}H_2$ characteristic of υ_{NH}, and the absence of C=N signal at 1630 cm^{-1} as shown in Figure 4.3, some selected wavenumbers are represented in Table 4.1.[24, 25]

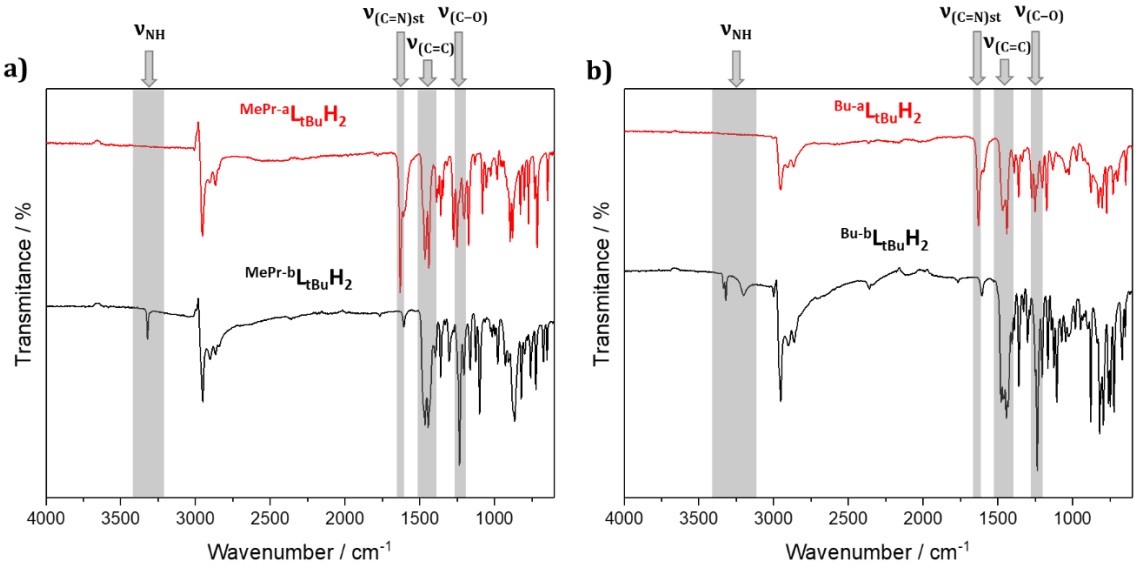


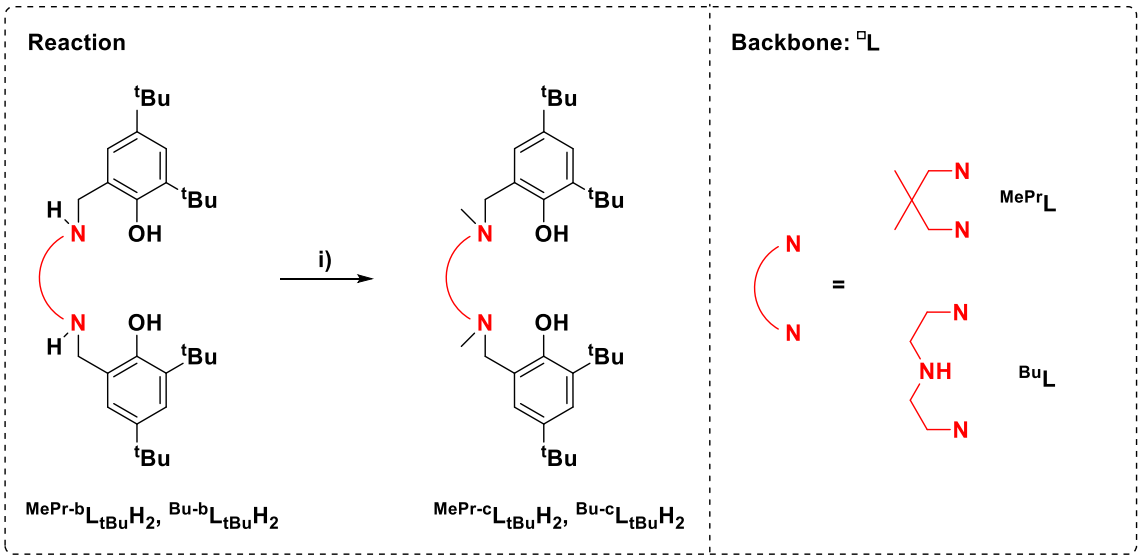
Figure 4.3. Infrared spectra for a) $^{MePr\text{-}a/b}L_{tBu}H_2$ and b) $^{Bu\text{-}a/b}L_{tBu}H_2$.

Table 4.1. Selected resonance frequencies (cm^{-1}) obtained from the solid state infrared spectra for ligands $^{MePr\text{-}a/b}L_{tBu}H_2$ and $^{Bu\text{-}a/b}L_{tBu}H_2$

Ligand	ν_{NH} cm^{-1}	$\nu_{(C=N)}$ cm^{-1}	$\nu_{(C=C)}$ cm^{-1}	$\nu_{(C-O)}$ cm^{-1}
$^{MePr\text{-}a}L_{tBu}H_2$	–	1631	1608; 1465; 1438	1234
$^{MePr\text{-}b}L_{tBu}H_2$	3321	–	1604; 1465; 1443	1234
$^{Bu\text{-}a}L_{tBu}H_2$	–	1630	1595; 1468; 1439	136
$^{Bu\text{-}b}L_{tBu}H_2$	3335; 3319; 3202	–	1606; 1477 – 1443	1236

To access the final ligands $^{MePr\text{-}c}L_{tBu}H_2$ or $^{Bu\text{-}c}L_{tBu}H_2$, the methylation of $^{MePr\text{-}b}L_{tBu}H_2$ or $^{Bu\text{-}b}L_{tBu}H_2$ was attempted by reaction with acetic acid and formaldehyde, in acetonitrile, followed by reduction with $NaBH_4$ and hydrolysis with 2M NaOH, Scheme

4.3. The reaction was performed on a small scale (0.1 g), however, $NaBH_4$ was not a strong enough reductant to methylate the secondary amine. One potential way to solve this would be to use a stronger methylating agent, such as MeI, however this would require protection of all the OH groups, adding two extra steps to the ligand synthesis. In an attempt to simplify the overall ligand synthesis (now with 5 steps), another approach was explored, as reported below.

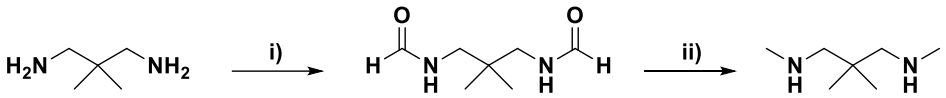


Scheme 4.3. Attempted methylation of $^{MePr\text{-}b}L_{tBu}H_2$ and $^{Bu\text{-}b}L_{tBu}H_2$. i) Acetic acid, formaldehyde and $NaBH_4$.

4.3.3. Synthesis of salan C3' and C4 ($^{MePr\text{-}c}L_{tBu}H_2$ and $^{Bu\text{-}c}L_{tBu}H_2$)

The new synthetic approach requires formation of the methylated secondary amine, followed by condensation with the corresponding benzaldehyde.[19, 26] The advantages of this method are the overall salan synthesis will have fewer steps and once the methylated amine is synthesised, it can be used to access the backbone of other ligands, such as the macrocycles.

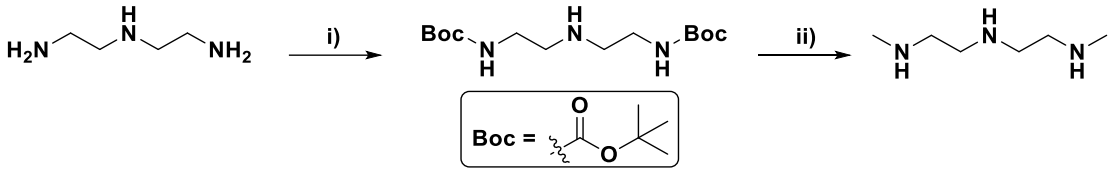
- **Synthesis of *N,N'*-Dimethyl-2,2-dimethylpropane-1,3-diamine**



Scheme 4.4. Synthesis of C3 backbone amine. i) HCOOMe, neat amine, reflux for 12 h. ii) $LiAlH_4$ in Et_2O, 0 °C → RT, 20 h.

Synthetic procedures adapted from the literature were followed.[26] During the first step, methyl formate (HCOOMe) was reacted with 2,2-dimethylpropane, in neat amine, leading to the formation of *N,N'*-diformyl-2,2-dimethylpropane-1,3-diamine, as a yellow solid, with 89 % yield. The synthesis was confirmed by the appearance of the aldehyde proton signal in the ^{1}H NMR spectrum (MeOD-d_4) at 8.14 ppm.[26, 27] The diamine was then reacted with $LiAlH_4$ to afford the desired product as a pale yellow oil with 25 % yield (density = 0.82 g mL^{-1}). Isolation of the diamine was confirmed by the ^{1}H NMR (C_6D_6) spectrum, where two methyl groups were observed as two singlets. The data obtained is in accordance with the results reported in the literature.[26]

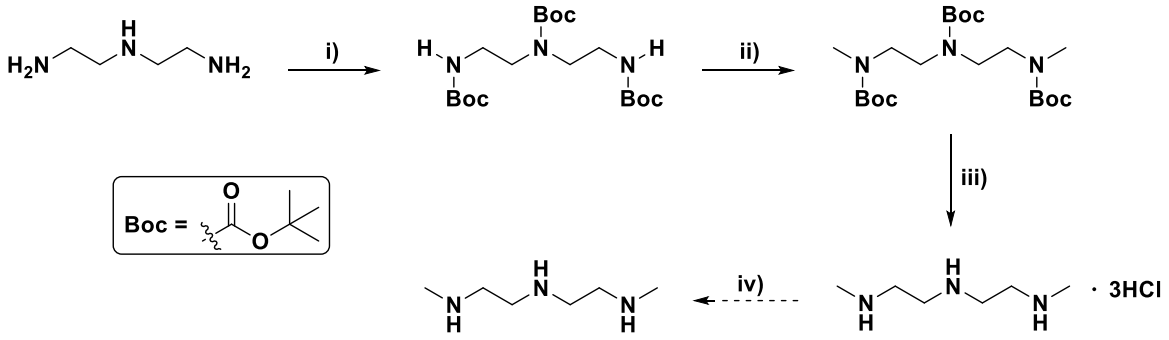
- **Synthesis of *N*-Methyl-*N'*-[2-(methylamino)ethyl]-1,2-ethanediamine**



Scheme 4.5. Synthesis of C4 backbone amine. i) $(CH_3)_3COCOOC_6H_5$, in DMF with a catalytic amount of Et_3N during 16h. ii) $LiAlH_4$ in THF, reflux 18h.

To access the Boc-protected diethylenetriamine, a literature procedure was followed, where *tert*-butyl phenyl carbonate was treated with diethylenetriamine and a catalytic amount of trimethylamine in DMF.[28] The compound was obtained as a white solid and isolated with a 60 % yield. In an attempt to obtain the desired amine, $LiAlH_4$ was added to a suspension of Boc-protected diethylenetriamine, in THF. The product was

obtained in low yield and was difficult to purify, also the last step showed the necessity to protect the NH group in the backbone of the amine. Therefore, the synthesis was adjusted to protect all three NH groups and proceed *via* a triamine hydrochloride salt to simplify the purification process, before accessing the amine, following a procedure adapted from the literature.[29]

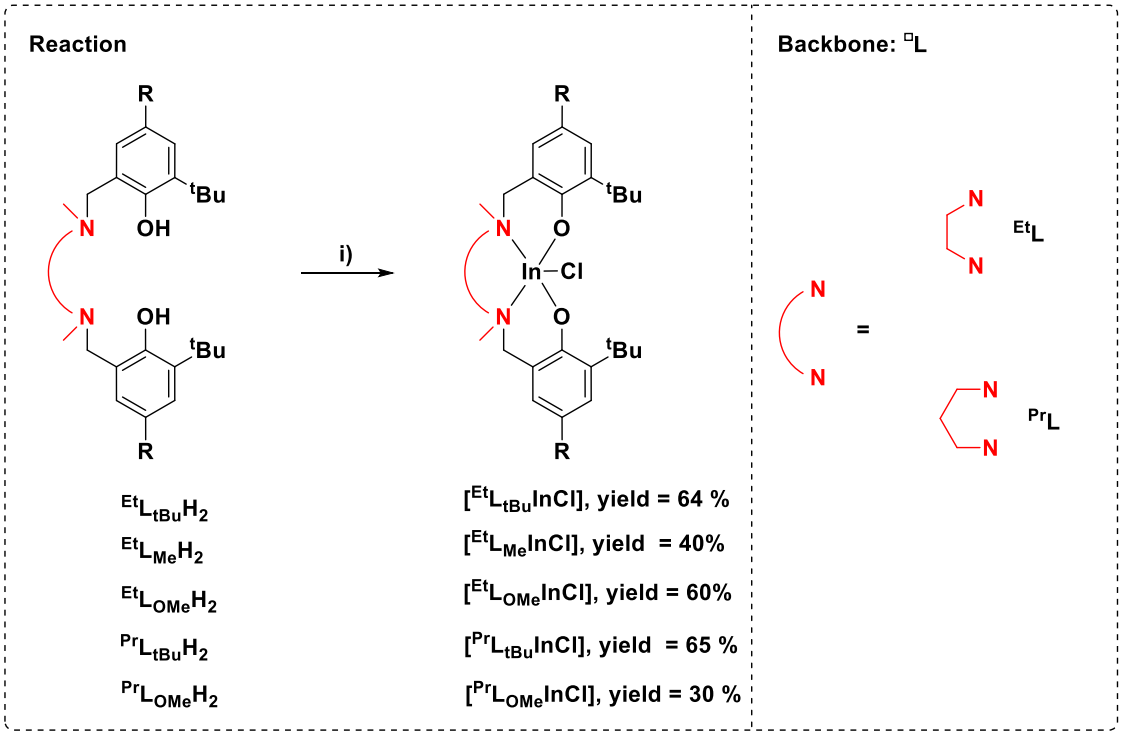


Scheme 4.6. Synthesis of amine. i) Di-tert-butyl decarbonate, methanol 48 h. ii) NaH, MeI in DMF, 12h. iii) 2 M HCl in ether, 5h.

The protected amine was accessed by reaction of di-*tert*-butyl dicarbonate with diethylenetriamine, in methanol, giving a white powder, with 87 % yield. The isolated product was then reacted with NaH and MeI, in DMF, giving a viscous pale yellow oil, after purification of the crude product by column chromatography (20 % yield). The oil was reacted with 2 M HCl, in ether, obtaining a white powder, in 90 % yield. The deprotection of all amines was confirmed by ^{1}H NMR spectroscopy (D_2O).[29] Free-basing of the amine and subsequent reaction with benzaldehyde will be done as a future work.

4.4 Synthesis and Characterisation of In-salan complexes

4.4.1. Synthesis of complexes $^{Et}L_xInCl$ and $^{Pr}L_xInCl$ with X = ^{t}Bu, Me or OMe



Scheme 4.7. Synthesis of $^{Et}L_RInCl$ and $^{Pr}L_RInCl$ (R = ^{t}Bu, Me or OMe) complexes. i) $KN[Si(CH_3)_3]_2$, $InCl_3$, THF.

The indium chloride complexes were synthesised following the deprotonation of the pro-ligand with bis(trimethylsilyl)amide [$KN(SiMe_3)_2$] and then reaction with $InCl_3$ (adapted from the literature).[7] The series of complexes were characterised by NMR spectroscopy and elemental analysis. Comparison of the ^{1}H NMR spectra of the complex with that of the pro-ligand reveals the disappearance of the phenolic OH signal, at 10.78 and 11.08 ppm for $^{Et}L_{tBu}InCl$. The signal correspondent to the benzylic protons splits into two doublets at 4.26 (J = 12.1 Hz) and 2.50 (J = 12.1 Hz). This arises as the benzylic protons are diastereotopic upon ligand coordination to In(III), as an example, the ^{1}H NMR spectra of $^{Et}L_{tBu}H_2$ and $^{Et}L_{tBu}InCl$ are represented in Figure 4.4. The same pattern was observed for the other systems.

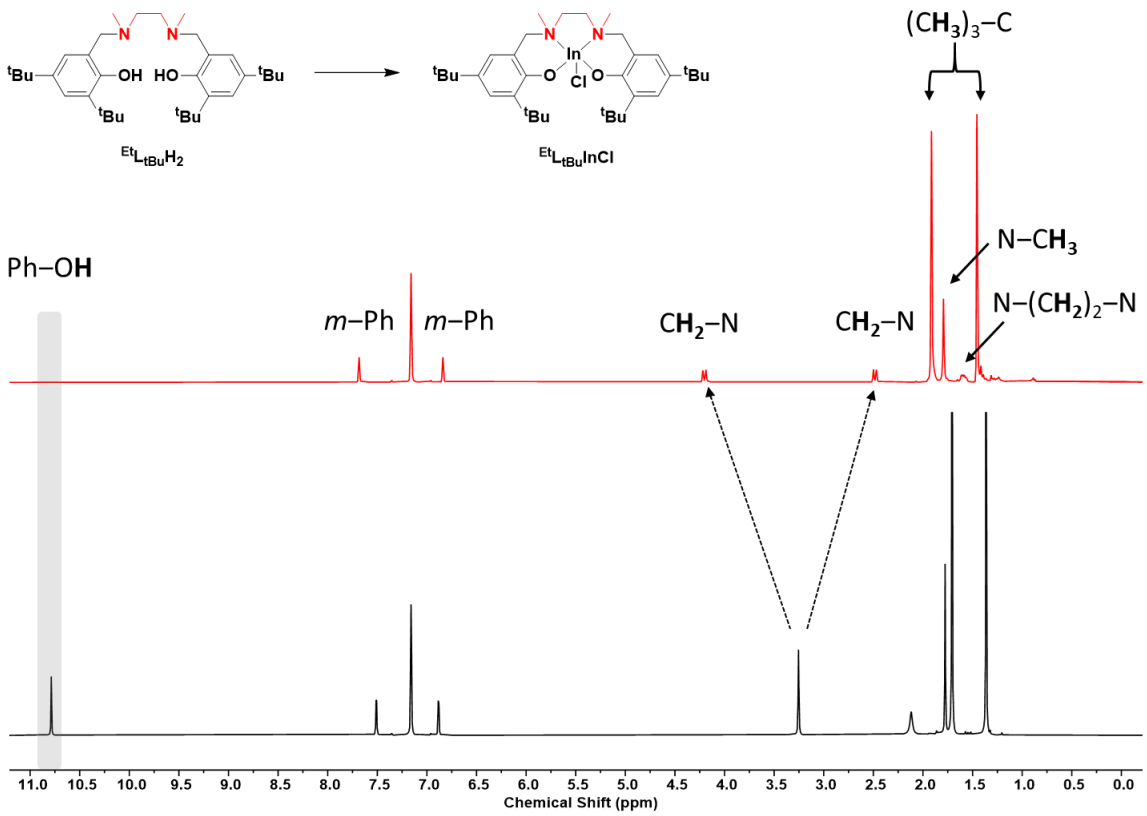


Figure 4.4. Comparison between ^{1}H NMR spectrum (C_6D_6, 298 K) for $^{Et}L_{tBu}H_2$ (bottom spectrum) and $^{Et}L_{tBu}InCl$ (top spectrum).

Single crystals suitable for X-ray diffraction were obtained for complexes $^{Pr}L_{tBu}InCl$ or $^{Et}L_{Me}InCl$ from a saturated solution dissolved in THF and hexane, held at -40 °C over 5 days, under a nitrogen atmosphere, for $^{Pr}L_{tBu}InCl$ and the crystals of $^{Et}L_{Me}InCl$ were obtained from a saturated benzene solution stored at room temperature.

The crystal structure of $^{Pr}L_{tBu}InCl$ shows an In(III) ion in a distorted octahedral conformation with a chloride and THF coordinated in *cis* position, Figure 4.5. This coordination mode is feasible due to the increased flexibility obtained with the C3 backbone. The N–Me groups are disposed *cis* to each other, similar to the structure of $^{Et}L_{tBu}InCl$.[30] The list of main bond distances and angles for $^{Pr}L_{tBu}InCl$ are in Table 4.2.

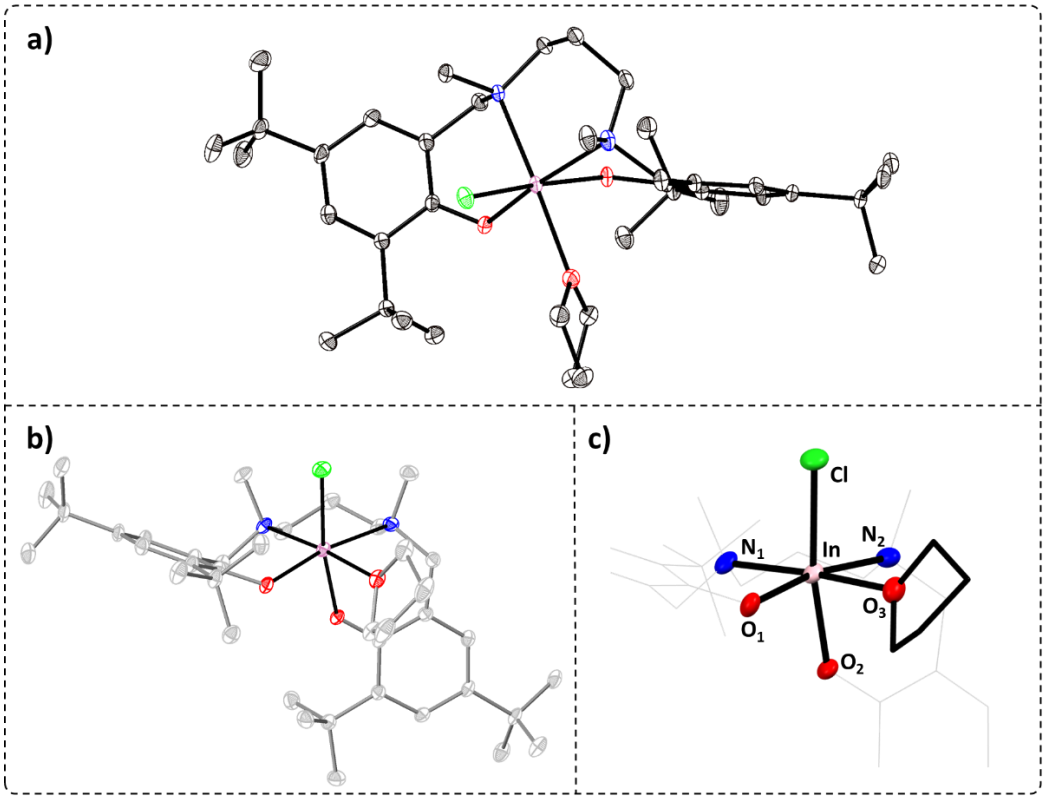


Figure 4.5. a) and b) Molecular structures of $^{Pr}L_{tBu}InCl$. c) In(III) environment and atom labels for complex $^{Pr}L_{tBu}InCl$. Thermal ellipsoids represented at 40 % probability. H–atoms and crystallisation solvent (THF) were omitted to clarity.

Table 4.2. Selected bond distances and angles for $^{Pr}L_{tBu}InCl$.

Bond	Bond Length (Å)	Bond	Bond Angle (°)	Bond	Bond Angle (°)
In–N1	2.308 (3)	**Cl–In–N1**	94.03 (9)	**O3–In–O1**	89.55 (11)
In–N2	2.369 (3)	**Cl–In–N2**	92.54 (9)	**O3–In–O2**	86.26 (11)
In–O1	2.097 (3)	**Cl–In–O1**	97.49 (9)		
In–O2	2.086 (3)	**Cl–In–O2**	88.51(9)		
In–O3	2.292 (3)	**O3–In–N1**	91.80 (12)		
In–Cl	2.4259 (10)	**O3–In–N2**	80.24 (11)		

The X-ray diffraction experiment for complex $^{Et}L_{Me}InCl$ (Figure 4.6-a) reveals a distorted square pyramidal geometry at indium, with the ligand coordinated in the equatorial positions and the chloride coordinated in the axial position, with a $\tau = 0.34$ (Figure 4.6-b). The methyl groups at the nitrogen atoms are in *cis* positions, similar to $^{Pr}L_{tBu}InCl$. Selected bond distances and angles are shown in Table 4.3.

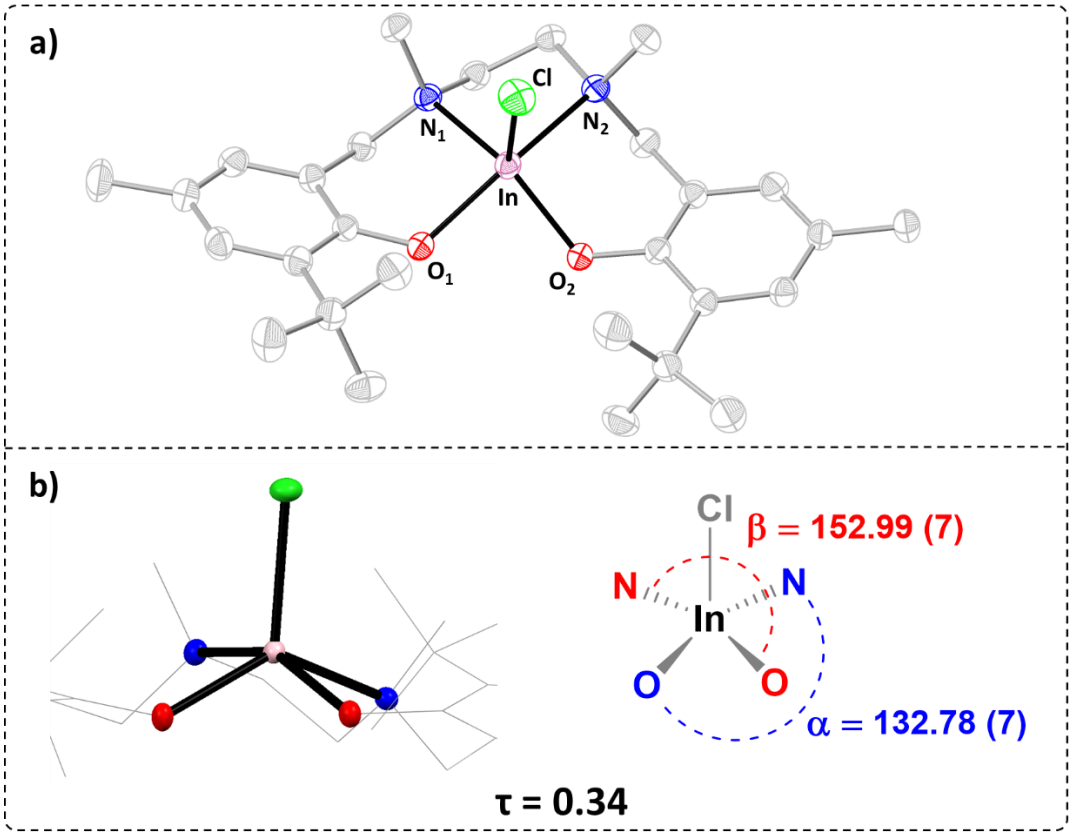
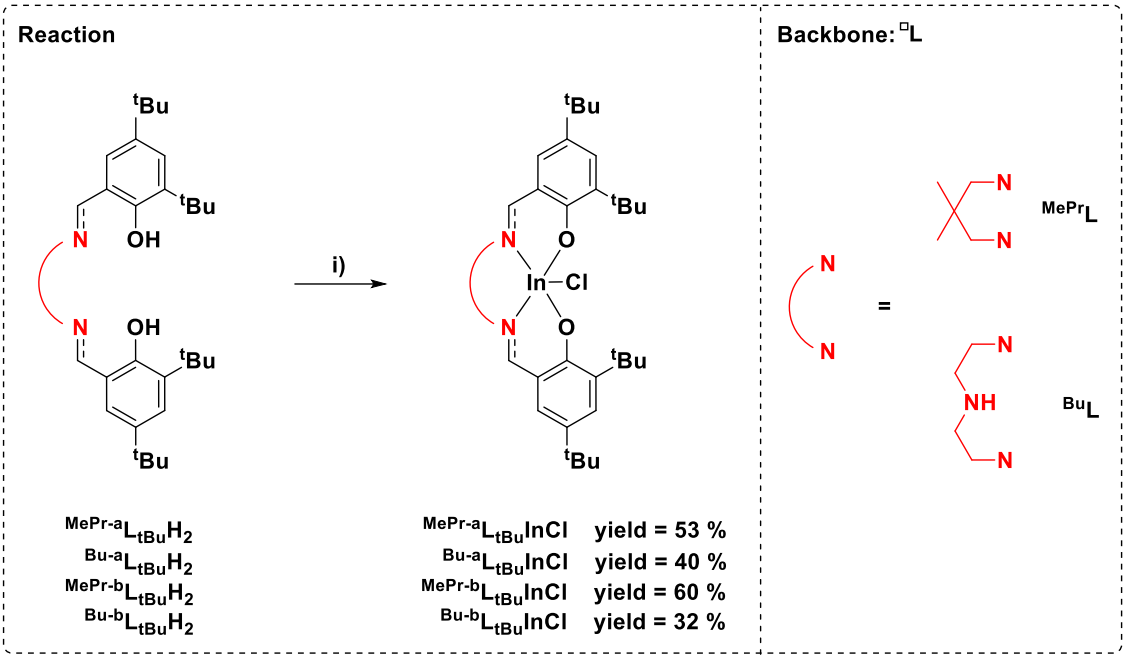


Figure 4.6. a) Molecular structures of $^{Et}L_{Me}InCl$. b) In(III) environment and bond angles used to calculate τ factor. Thermal ellipsoids represented at 40 % probability. H–atoms and crystallisation solvent (benzene) were omitted to clarity.

Table 4.3. Selected bond distances and angles for $^{Et}L_{Me}InCl$.

Bond	Bond Length (Å)	Bond	Bond Angle (°)
In–N1	2.349 (2)	**N2–In–O2**	86.79 (7)
In–N2	2.2743 (19)	**N1–In–O1**	87.76 (7)
In–O1	2.0447 (16)		
In–O2	2.0672 (17)		
In–Cl	2.3661 (6)		

4.4.2. Synthesis and characterisation of complexes $^{MePr-a/b}L_{tBu}InCl$ and $^{Bu-a/b}L_{tBu}InCl$



Scheme 4.8. Synthesis of $^{MePr-a/b}L_{tBu}InCl$ and $^{Bu-a/b}L_{tBu}InCl$ complexes. i) $KN[Si(CH_3)_3]_2$, $InCl_3$, THF.

The indium complexes with C3 and C4 backbones were synthesised by deprotonation of the ligand, using $[KN(SiMe_3)_2]$, and reaction with $InCl_3$. For $^{MePr-a}L_{tBu}InCl$ or $^{Bu-a}L_{tBu}InCl$, the ^1H NMR spectra showed the disappearance of signals at 14.28 and 14.00 Hz respectively, which correspond to the deprotonation of the OH groups. The reduced flexibility caused by the coordination to In(III) leads to splitting of the backbone -CH_2- signals as illustrated for $^{MePr-a}L_{tBu}InCl$ in Figure 4.7. For this complex, THF resonances could also be observed, even after drying the compound, under high vacuum, for 24 h, suggesting THF is coordinated both solution and solid state, confirmed by the crystal structure (discussed below).

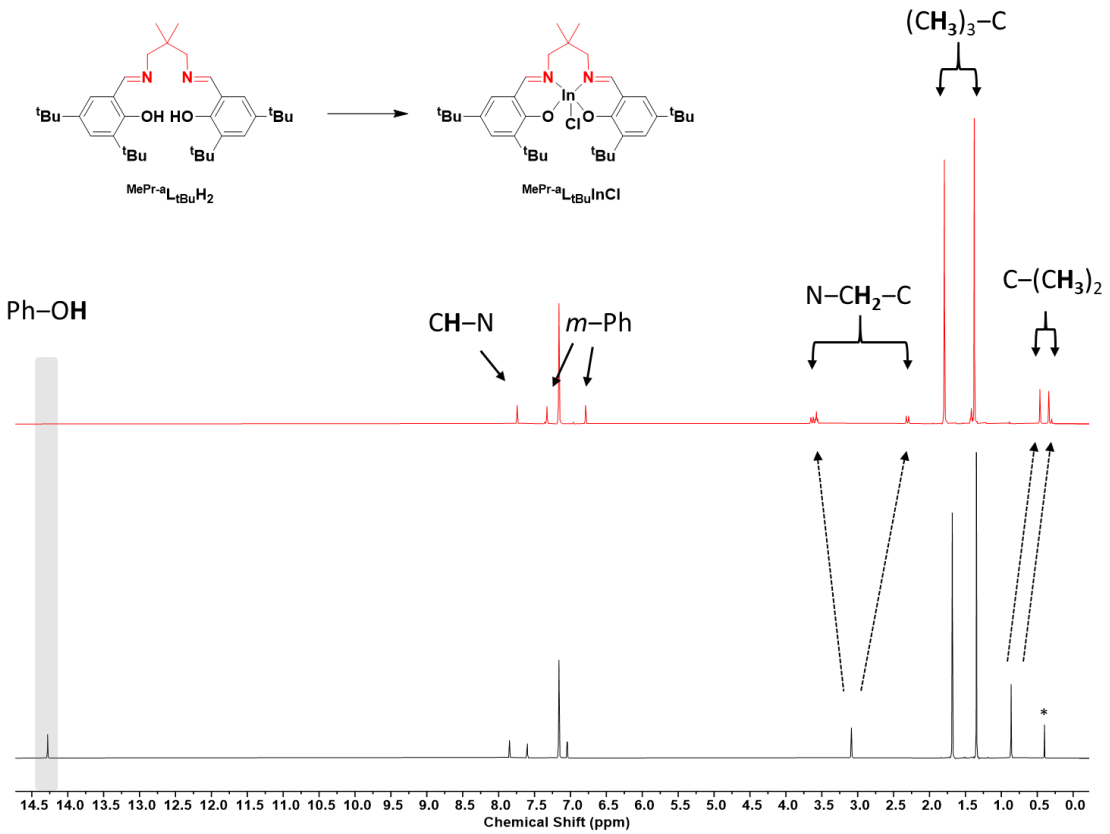


Figure 4.7. Comparison between ^{1}H NMR spectrum (C_6D_6, 298 K) for $^{MePr\text{-}a}L_{tBu}H_2$ (bottom spectrum) and $^{MePr\text{-}a}L_{tBu}InCl$ (top spectrum). * Residual water from C_6D_6.

Single crystals suitable for X-ray diffraction of $^{MePr\text{-}a}L_{tBu}InCl$ were obtained from a saturated solution of a mixture of THF/hexane, held at -40 °C over 3 days, under a nitrogen atmosphere. The In(III) metal centre is in an octahedral conformation, with a THF and chloride coordinated in the axial position, with the oxygens and nitrogen from the ligand in the equatorial sites as shown in Figure 4.8-a. Comparing the crystal structure obtained for $^{MePr\text{-}a}L_{tBu}InCl$ and $^{Pr}L_{tBu}InCl$, Figure 4.8-b, the rigidity of the double bond between nitrogen and carbon does not allow the complex to access the conformation with THF and chloride coordinated in *cis* position. This information is important as the mechanistic study, published by Williams et al.,[7] proposed that the propagating species and the epoxide must be *cis* coordinated for the mononuclear pathway.[7] Selected bond distances and angles are listed in Table 4.4.

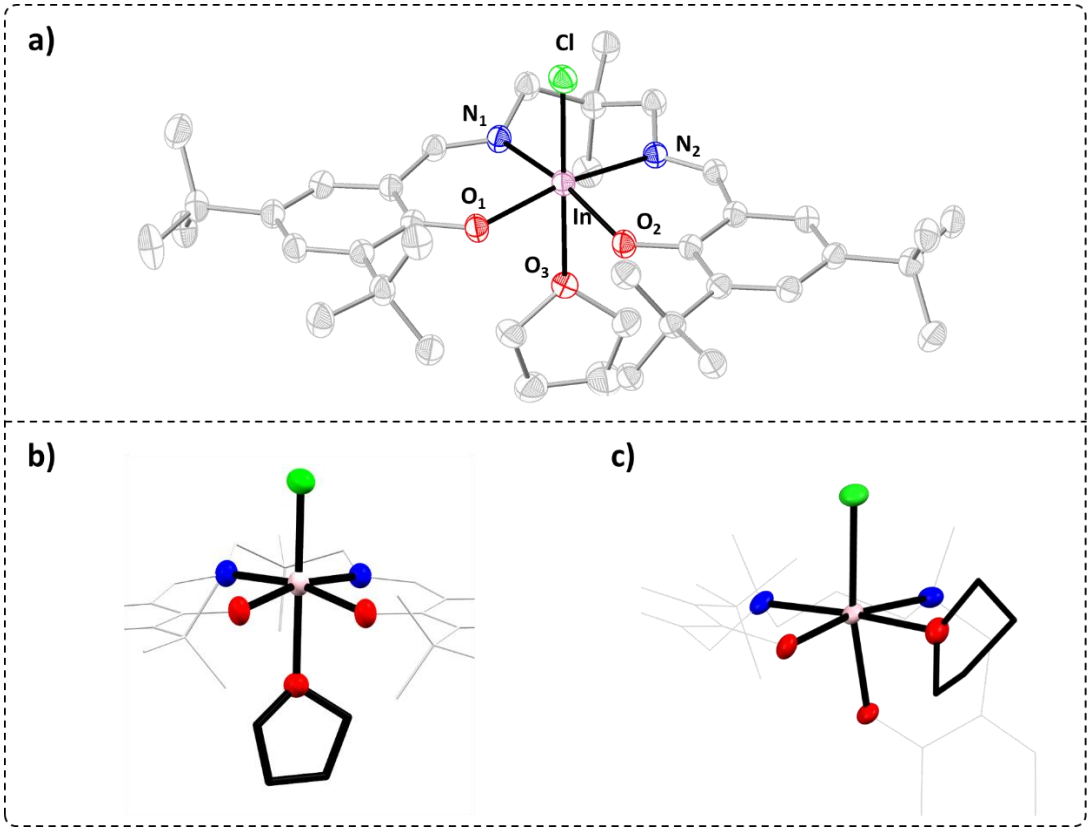


Figure 4.8. a) Molecular structures of $^{MePr\text{-}a}L_{tBu}InCl$. b) In(III) environment for complex $^{MePr\text{-}a}L_{tBu}InCl$ (left) and $^{Pr}L_{tBu}InCl$ (right). Thermal ellipsoids represented at 40 % probability. H–atoms and crystallisation solvent (THF) were omitted to clarity.

Table 4.4. Selected bond distances and angles for $^{MePr\text{-}a}L_{tBu}InCl$.

Bond	Bond Length (Å)	Bond	Bond Angle (°)	Bond	Bond Angle (°)
In–N1	2.197 (3)	**Cl–In–N1**	93.35 (9)	**O3–In–O1**	81.74 (11)
In–N2	2.210 (3)	**Cl–In–N2**	94.52 (8)	**O3–In–O2**	80.16 (11)
In–O1	2.069 (2)	**Cl–In–O1**	99.25 (9)		
In–O2	2.059 (3)	**Cl–In–O2**	100.72 (9)		
In–O3	2.449 (3)	**O3–In–N1**	85.76 (11)		
In–Cl	2.4427 (11)	**O3–In–N2**	84.46 (11)		

Complexes $^{MePr\text{-}b}L_{tBu}InCl$ and $^{Bu\text{-}b}L_{tBu}InCl$ are more flexible compared with complexes obtained with $^{MePr\text{-}a}L_{tBu}H_2$ and $^{Bu\text{-}a}L_{tBu}H_2$ ligands, this allows them to access different conformations. When the ^{1}H NMR spectrum of complex $^{MePr\text{-}b}L_{tBu}InCl$ is analysed, all signals are duplicated as shown in Figure 4.9; this could be due to a formation of

different isomers or to the formation of a dimer species. To understand the fluxionality of the complexes, VT-NMR experiments were performed, however, the same spectrum was obtained at all temperatures, as shown in Figure 4.10.

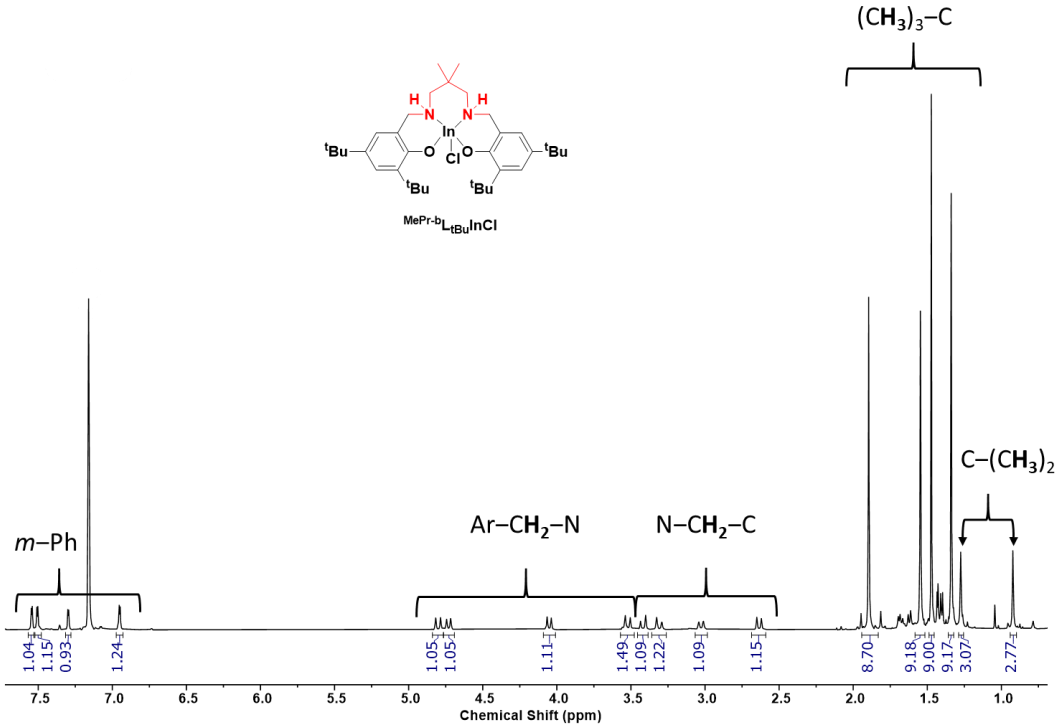


Figure 4.9. ^{1}H NMR spectrum for **$^{MePr\text{-}b}L_{tBu}InCl$**, ($C_6D_6$, 500 Hz, 298 K). The signal at 7.16 ppm is from C_6D_6 solvent.

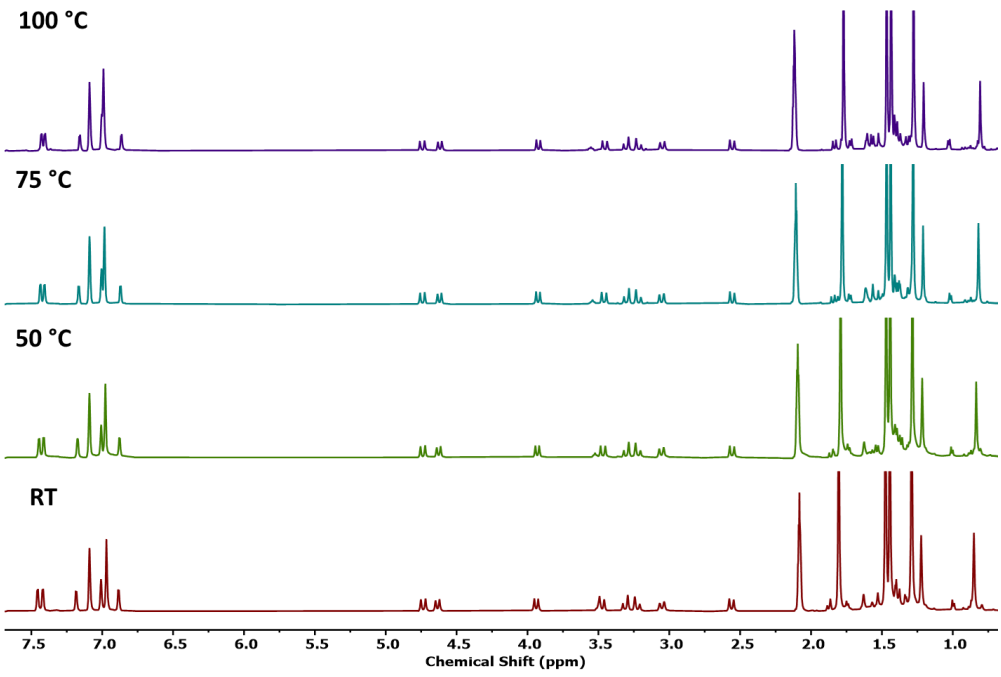


Figure 4.10. Variable temperature ^{1}H NMR spectrum for **$^{MePr\text{-}b}L_{tBu}InCl$**, (Toluene-$d_8$, 500 Hz, 298; 273 and 248 K). Signals at 7.09; 7.01; 6.95 and 2.05 ppm are solvent residual signal from Toluene-d_8 solvent.

The ^{1}H NMR spectrum for complex $^{Bu\text{-}b}\mathbf{L_{tBu}InCl}$ revealed broad peaks and so the system was cooled to -25 °C to reduce any bond rotation or solvent exchange; temperatures below - 25 °C were not possible due to poor complex solubility, Figure 4.11. In the spectrum at -25 °C, the signals from the backbone and benzylic protons are doublets and a THF signal is observed, possibly coordinated to In(III).

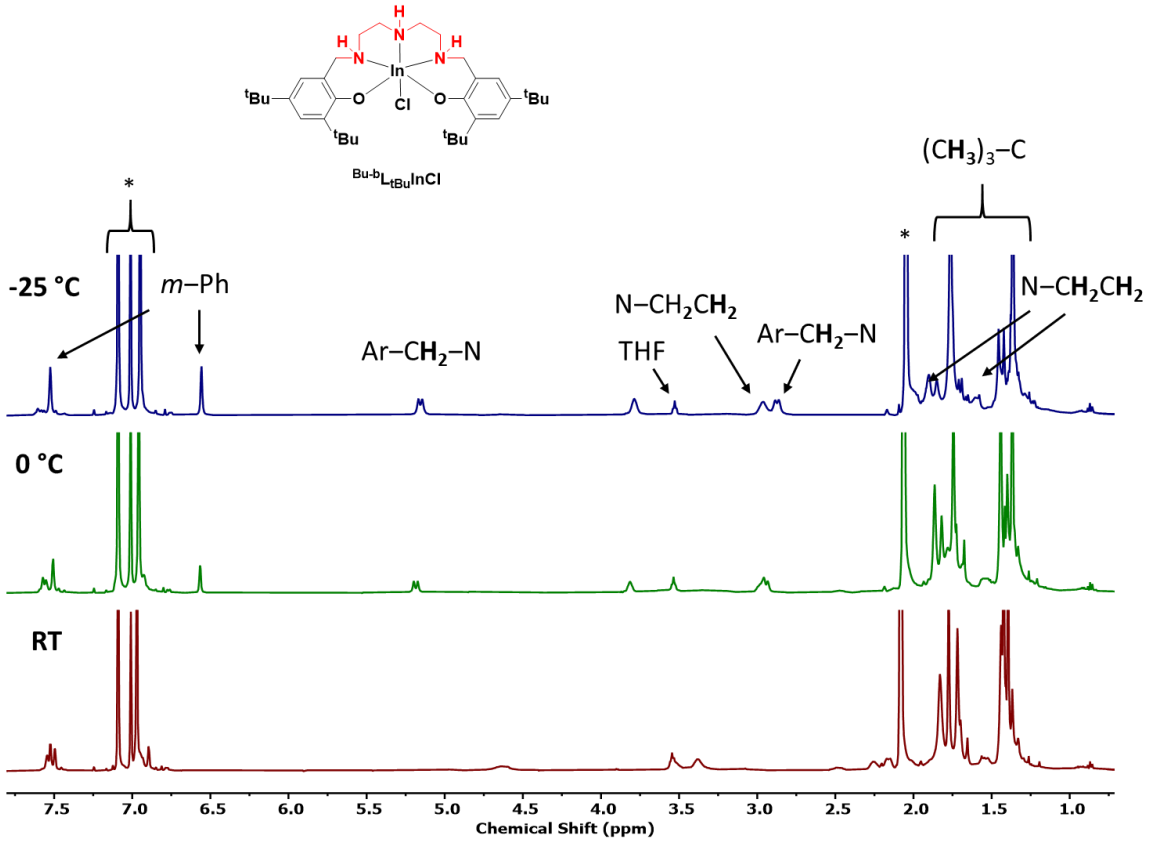
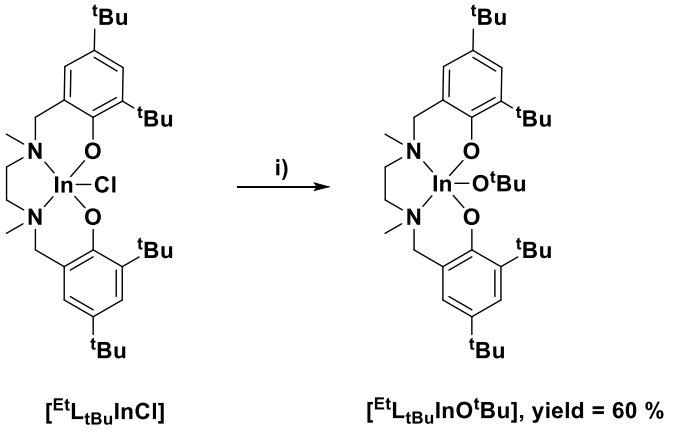


Figure 4.11. Variable temperature ^{1}H NMR spectrum for $^{Bu\text{-}b}\mathbf{L_{tBu}InCl}$, (Toluene-$d_8$, 500 Hz, 298; 273 and 248 K). Signals at 7.09; 7.01; 6.95 and 2.05 ppm (*) are from Toluene-d_8 solvent.

4.4.3. Synthesis and characterisation of $^{Et}\mathbf{L_{tBu}In(O^tBu)}$ and $^{Et}\mathbf{L_{tBu}ScCl}$

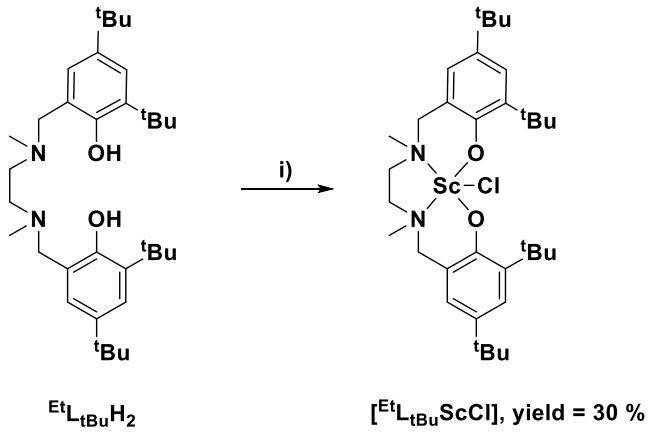
For the purpose of studying the influence of the metal centre in the ROCOP of CHO/CO_2 using the $^{Et}\mathbf{L_{tBu}H_2}$ ligand, the related Sc(III) complex, $^{Et}\mathbf{L_{tBu}ScCl}$ was investigated. Additionally, to study the influence of the initiating group, an In(III) complex was obtained with an alkoxide co-ligand, $^{Et}\mathbf{L_{tBu}InO^tBu}$.

To access $^{Et}L_{tBu}InO^tBu$, the corresponding indium chloride complex, $^{Et}L_{tBu}InCl$ was treated with KO^{t}Bu, in THF, to give the desired complex with 60 % yield. As expected, the ^{1}H NMR spectrum of $^{Et}L_{tBu}InO^tBu$ was similar to $^{Et}L_{tBu}InCl$, and doublets at 4.26 and 2.50 ppm from the benzylic protons were shifted to 3.97 and 2.62 ppm, respectively. The protons signal for N–CH_3 also shifted from 1.79 to 2.05 ppm. The new signal at 1.40 ppm is attributed to O^{t}Bu.



Scheme 4.9. Synthesis of $^{Et}L_{tBu}InO^tBu$ complex. i) KO^{t}Bu, THF, RT, 4 h.

To access the complex $^{Et}L_{tBu}ScCl$ a similar procedure as for $^{Et}L_{tBu}InCl$ was followed, using the adduct $ScCl_3(THF)_3$ (due to the low solubility of $ScCl_3$), obtaining the product with 30 % yield. The ^{1}H NMR spectrum of the complex, in THF-d_8, shows ambiguous resonances at room temperature, therefore, a low temperature ^{1}H NMR experiment was performed and the spectra at -75 °C showed a clear set of doublets attributed to -CH_2- resonances, Figure 4.12.



Scheme 4.10. Synthesis of $^{Et}L_{tBu}ScCl$. i) $KN[Si(CH_3)_3]_2$, $ScCl_3(THF)_3$, THF.

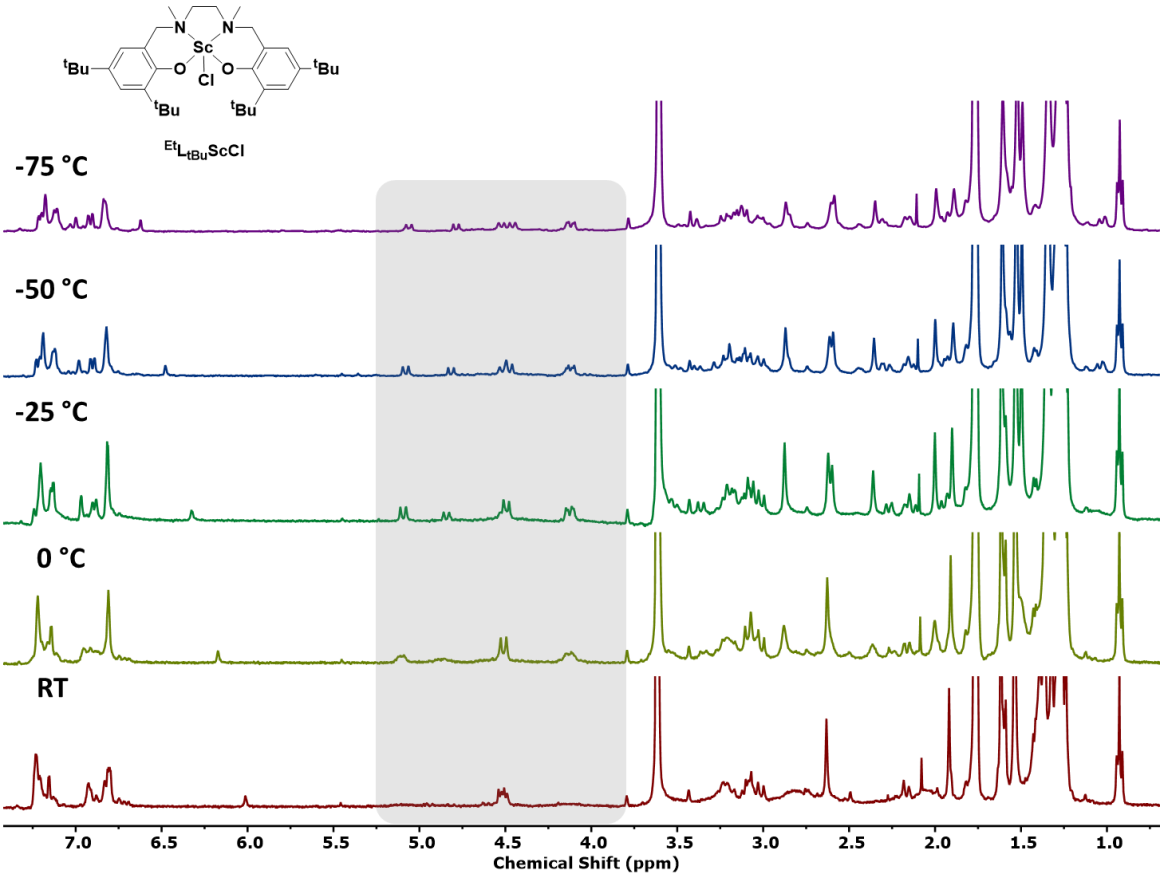


Figure 4.12. Variable temperature ^1H NMR spectrum in THF-d_8, 400 Hz of $^{Et}L_{tBu}ScCl$. Temperatures: 298, 273, 248, 223 and 198 K.

When the ^1H NMR spectrum of $^{Et}L_{tBu}ScCl$ is analysed, in toluene-d_8 at room temperature, a sharp assignable spectra is obtained, Figure 4.13. When the same sample is dried and redissolved in a sequence of toluene-THF-toluene, the final spectra obtained in toluene-d_8 remains clear, suggesting a strong solvent exchange when dissolved in THF, Figure 4.13. The ^1H NMR spectrum in toluene was analysed at high

temperature (50, 80, 90 and 100 °C) to average any conformation and bond rotation limitation, Figure 4.14.

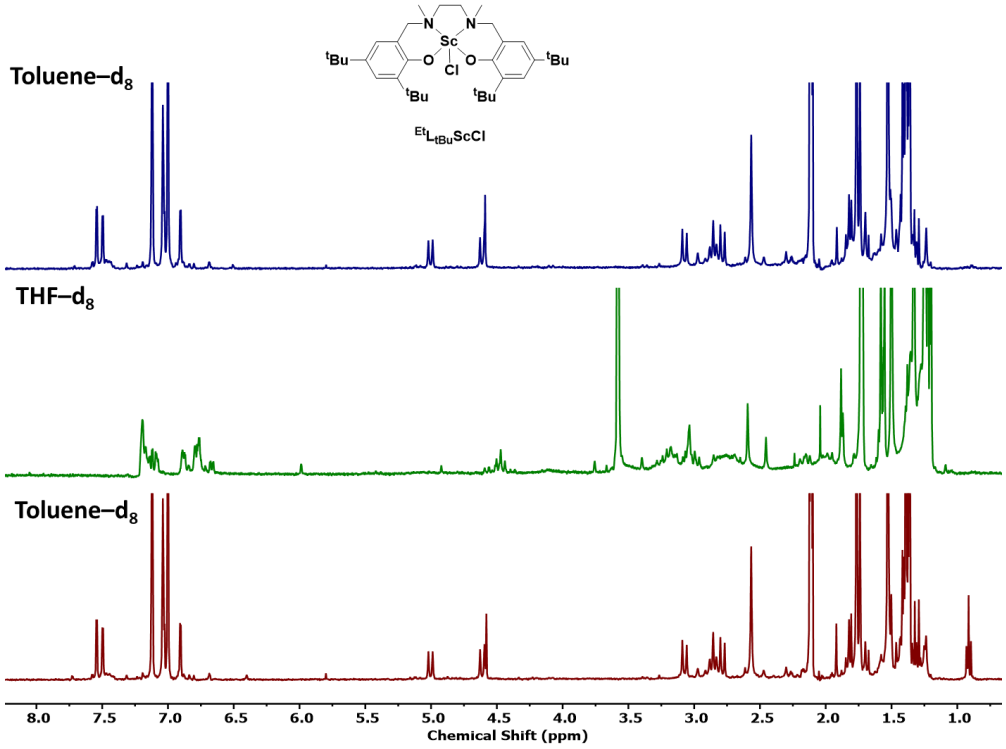


Figure 4.13. ^{1}H NMR spectrum of $^{Et}L_{tBu}ScCl$ in toluene-d$_8$ and THF-d_8. Toluene-d_8 (bottom) fist sample run. Toluene-d$_8$ (top) second sample run (after dry the sample used in THF-d_8 and re-dissolve in toluene-d_8).

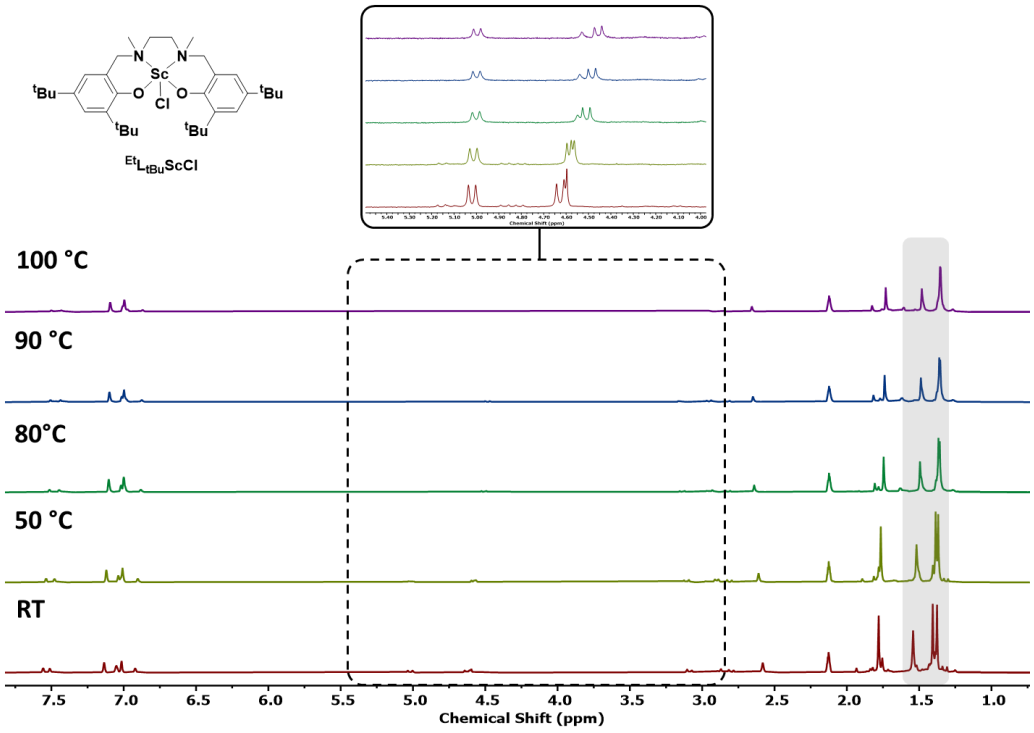


Figure 4.14. Variable temperature ^{1}H NMR spectrum in toluene-d$_8$, 400 Hz of $^{Et}L_{tBu}ScCl$. Temperatures: 298, 323, 353, 363 and 373 K.

To investigate the species that was forming in toluene-d_8 and THF-d_8, DOSY NMR experiments were performed in both solvents. The spectra collected for toluene-d_8 at room temperature (Figure A.22) showed one diffusion species with an estimated molecular weight of 913 g mol^{-1}, this value is in between the values expected for a monomer (603 g mol^{-1}) and a dimer (1207 g mol^{-1}), indicating a potential equilibrium between both species. When DOSY NMR is performed in THF-d_8 (Figure A.23) three diffusion coefficients were obtained with an estimated molecular weight of 1127; 860 and 681 g mol^{-1}, showing the presence of monomer and dimer in solution. This indicates that in non-coordinating solvents the exchange between dimer and monomer is fast and just the average can be seen, however, in coordinating solvents, this coordination of THF into the monomer allows the monomer and the dimer be detected in solution. The MALDI-ToF spectrum reveals signals just at 567.41 m/z, corresponding to the molecular ion peak of the monomer with the loss of a chloride $[^{Et}L_{tBu}Sc]^+$.

4.5. ROCOP of CO_2 and CHO

4.5.1. Experiments at 1 bar CO_2

The new series of indium complexes were tested for ROCOP of CO_2/CHO, at 1 bar CO_2 pressure and 60 °C. The results were compared with other salen complexes reported in the literature, which were tested under the same conditions.[7] As presented in Table 4.5, all catalysts gave some activity, however, the all corresponding TOFs are lower than 4 h^{-1}. $^{MePr\text{-}a}$**L$_{tBu}$InCl** presented less than 5 % conversion in 48 h and it was not possible to integrate the polymer signal in the ^{1}H NMR spectrum to obtain reliable data (Table 4.5, entry 3). The data obtained were compared with similar compounds reported in the literature by Williams et al (Figure 4.15).[7]

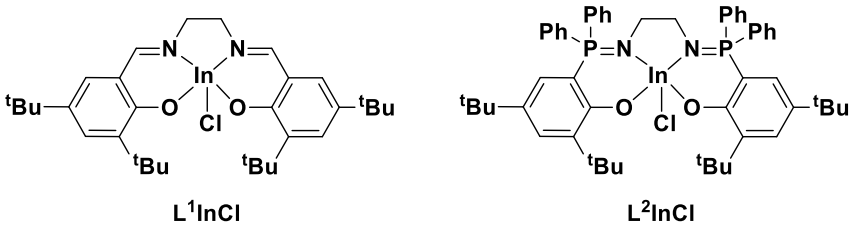


Figure 4.15. Complexes reported in the literature by Williams et al.[7]

All complexes, apart from ^{Et}**L$_{tBu}$InCl**, exclusively formed polyether with no CO_2 insertion during the time that the polymerisation was studied (48 h) and with TOFs between 1.6 to 3 h^{-1}, entries 2–5 (Table 4.5). The polymerisation performed with the C2 backbone complex, ^{Et}**L$_{tBu}$InCl**, made a mixture of PCHC, polyether and cyclic carbonate (entries 7 and 8, Table 4.5).

To simplify the discussion, the polymerisations from Table 4.5 will be divided into significant outcomes:

- **Entries 1 and 2:** Complexes containing a C2 and C3 backbone with N–Me groups, where **$^{Pr}L_{tBu}InCl$** could not achieve PCHC formation, giving only polyether.
- **Entries 3 and 4:** Of the complexes containing a C3 backbone, the salen showed lower activity than the analogous with NH group.
- **Entries 4 and 5:** Complexes featuring a C3 and C4 amine backbone showed almost no difference in catalyst performance.
- **Entries 1 and 6:** Changing the initiating group from Cl to O^{t}Bu for a C2 backbone system lowered the activity, however, an increase in PCHC formation was observed.

Table 4.5. CO_2/CHO ROCOP catalysed by **$^{Y}L_{tBu}InCl$** (Y = Et, Pr, MePr-a/b or Bu-a/b) at 1 bar CO_2, without the addition of co-catalyst.[a]

Entry	Catalyst	Conv. (%)	% PCHC	% Carbonate linkages[b]	% Polymer selectivity[b]	TOF (h^{-1})[c]
1	**$^{Et}L_{tBu}InCl$**	16	16	18	98	3.4
2	**$^{Pr}L_{tBu}InCl$**	8	<1	<1	>99	1.6
3	**$^{MePr\text{-}a}L_{tBu}InCl$**	–	–	–	–	–
4	**$^{MePr\text{-}b}L_{tBu}InCl$**	11	<1	<1	>99	2.2
5	**$^{Bu\text{-}b}L_{tBu}InCl$**	15	<1	<1	>99	3
6	**$^{Et}L_{tBu}InO^tBu$**	9	20	20	>99	1.9
7	**L^1InCl**[d]	21	<1	<1	>99	4.4
8	**L^2InCl**[d]	14	62	66	94	3

[a]Copolymerisation conditions: CHO : cat = 1000:1 , 60 °C, 48 h. [b]Determined by comparison of the integrals of signals arising from the methylene protons in the ^{1}H NMR spectrum due to copolymer carbonate linkages (δ = 4.65 ppm) and copolymer ether linkages (only for the % polymer selectivity, δ = 3.45 ppm) against *trans*-cyclic carbonate (δ = 4.00 ppm), and *cis*-cyclic carbonate (δ = 4.67 ppm). [c]Turnover frequency (TOF) = Turnover number (TON) / Time (h). TON = Number of moles of CHO consumed / number of moles of catalyst. [d]Values reported by Williams et al.[7]

Comparing the ROCOP results for the different *para*-phenol substitution, the C2 catalysts systems when the *para*-substituent was changed from ^{t}Bu to Me and OMe a decrease in the activity was observed, Table 4.6., entry 1–3. For the C3 backbone, when

the *para*-substituent was changed from ^{t}Bu to OMe, TOFs had almost no change and the system still showed just polyether formation.

Table 4.6. CO_2/CHO ROCOP catalysed by a series of $^{Et}L_{R}InCl$ (R = ^{t}Bu, Me or OMe) complexes at 1 bar CO_2, without the addition of co-catalyst.[a]

Entry	Catalyst	Conv. (%)	% PCHC[b]	% Carbonate linkages[b]	% Polymer selectivity[b]	TOF (h^{-1})[c]
1	$^{Et}L_{tBu}InCl$	16	16	18	98	3.4
2	$^{Et}L_{Me}InCl$	7	6	7	99	1.4
3	$^{Et}L_{OMe}InCl$	8	16	20	97	1.8
4	$^{Pr}L_{tBu}InCl$	8	<1	<1	>99	1.6
5	$^{Pr}L_{OMe}InCl$	14	<1	<1	>99	2.9

[a]Copolymerization conditions: CHO : cat = 1000:1 , 60 °C, 48 h. [b]Determined by comparison of the integrals of signals arising from the methylene protons in the ^{1}H NMR spectrum due to copolymer carbonate linkages (δ = 4.65 ppm) and copolymer ether linkages (only for the % polymer selectivity, δ = 3.45 ppm) against *trans*-cyclic carbonate (δ = 4.00 ppm), and *cis*-cyclic carbonate (δ = 4.67 ppm). [c]Turnover frequency (TOF) = Turnover number (TON) / Time (h). TON = Number of moles of CHO consumed / number of moles of catalyst.

The systems studied have modest TOFs, however, $^{Et}L_{tBu}InCl$, $^{Et}L_{tBu}InO^{t}Bu$, $^{Et}L_{Me}InCl$ and $^{Et}L_{OMe}InCl$ are active for the formation of PCHC at 1 bar CO_2 at 60 °C without the addition of any co-catalyst.

4.5.2. Experiments at high CO_2 pressure

The catalysts $^{Et}L_{tBu}InCl$ and $^{Et}L_{OMe}InCl$ were tested for ROCOP of CO_2/CHO at high pressure (40 bar CO_2) without co-catalyst and negligible improvement in selectivity was observed, but the TOF increased from 3.4 to 6 h^{-1} ($^{Et}L_{tBu}InCl$) and 1.4 to 9 h^{-1} ($^{Et}L_{OMe}InCl$), entries 2 and 4 – Table 4.7. Changing the initiating group from chloride to O^{t}Bu, complex $^{Et}L_{tBu}InO^{t}Bu$, showed an increase in TOF from 2 to 12 h^{-1} with a slight increase in polymer selectivity (Entry 3 – Table 4.7).

When complexes $^{Et}L_{tBu}InCl$ and $^{Et}L_{OMe}InCl$ were studied with the addition of 1 equiv. of PPNCl an improvement in TOF (from 6 to 17 h^{-1} and 9 to 30 h^{-1}) and selectivity were

observed, Table 4.7, entries 1 and 5. For complex $^{Et}L_{tBu}InCl$ there was no formation of polyether, just PCHC and cyclic carbonate.

When comparing the *para*-phenolate substituents ^{t}Bu, Me and OMe for the C2 backbone systems, with addition of 1 equiv. of PPNCl (Table 4.7 – Entries 1, 5 and 6), the best catalyst is $^{Et}L_{Me}InCl$ with selectivity similar to $^{Et}L_{tBu}InCl$. The selectivity of OMe systems was improved when the C2 backbone was changed to the more flexible C3 linker, $^{Pr}L_{OMe}InCl$, with only PCHC detected (no presence of polyether or cyclic carbonate) (Entry 7, Table 4.7).

Table 4.7. CO_2/CHO ROCOP catalysed by $^{Y}L_{R}InCl$ (Y = Et or Pr; R = tBu, Me or OMe), at 40 Bar CO_2.[a]

Catalyst	Entry	Cocat.	Conv. (%)	% PCHC	% Carbonate linkages[c]	% Pol. Select.[c]	TOF (h^{-1})[d]
$^{Et}L_{tBu}InCl$	**1**[b]	PPNCl	20	93	>99	93	17
	2[b]	–	7	18	26	92	6
$^{Et}L_{tBu}InO^{t}Bu$	**3**[b]	–	14	33	38	95	11
$^{Et}L_{OMe}InCl$	**4**	–	4	21	26	95	9
	5	PPNCl	12	84	91	93	30
$^{Et}L_{Me}InCl$	**6**	PPNCl	15	92	>99	92	38
$^{Pr}L_{OMe}InCl$	**7**	PPNCl	7	>99	>99	>99	18

[a]Copolymerization conditions: CHO : PPNCl : cat = 2000:0(1):1 , 80 °C, 8 h. [b]Reaction time = 23 h. [c]Determined by comparison of the integrals of signals arising from the methylene protons in the ^{1}H NMR spectrum due to copolymer carbonate linkages (δ = 4.65 ppm) and copolymer ether linkages (only for the % polymer selectivity, δ = 3.45 ppm) against *trans*-cyclic carbonate (δ = 4.00 ppm), and *cis*-cyclic carbonate (δ = 4.67 ppm). [d]Turnover frequency (TOF) = Turnover number (TON) / Time (h). TON = Number of moles of CHO consumed / number of moles of catalyst.

4.6. Conclusions and Outlook

This chapter describes a series of In(III) complexes with different backbones and *para*-phenolate substituents. Among these complexes, a crystal structure of a C3 backbone In-salan system revealed the *cis* coordination of chloride and THF co-ligand on the metal centre, allowed by the increased flexibility of the system. Two diamine starting materials were also synthesised for future exploration of salan ligand backbones to explore the N–Me group influence in the catalyst activity.

The isolated indium catalysts were explored for ROCOP of CO_2 and CHO at 1 and 40 bar CO_2 pressure. At 1 bar CO_2 all complexes presented low activity with TOFs up to 3.4 h^{-1}. For the C2 backbone featuring the *para*- OMe and ^{t}Bu groups, a slightly higher PCHC selectivity was observed over Me.

The experiments performed at 40 bar CO_2 showed low activity and the systems were explored with the addition of a co-catalyst PPNCl. The catalyst with C2 backbone and Me substitution gave higher activity (among the catalysts tested) and C3 backbone with OMe group yielded the higher selectivity.

To obtain a good range of comparisons to determine a trend among the backbone and the phenolate substituents, the other complexes synthesised in this chapter should be explored for ROCOP. Also the ligands and complexes using the diamines with the synthesis presented here should be synthesised and tested.

4.7. References

1. Darensbourg, D. J., Making Plastics from Carbon Dioxide: Salen Metal Complexes as Catalysts for the Production of Polycarbonates from Epoxides and CO_2. *Chem. Rev.* **2007,** *107* (6), 2388-2410.
2. Paul, S.; Zhu, Y.; Romain, C.; Brooks, R.; Saini, P. K.; Williams, C. K., Ring-opening copolymerization (ROCOP): synthesis and properties of polyesters and polycarbonates. *Chem. Comm.* **2015,** *51* (30), 6459-6479.
3. Darensbourg, D. J.; Mackiewicz, R. M.; Phelps, A. L.; Billodeaux, D. R., Copolymerization of CO_2 and Epoxides Catalyzed by Metal Salen Complexes. *Acc. Chem. Res.* **2004,** *37* (11), 836-844.
4. Cohen, C. T.; Coates, G. W., Alternating copolymerization of propylene oxide and carbon dioxide with highly efficient and selective (salen)Co(III) catalysts: Effect of ligand and cocatalyst variation. *J. Polym. Sci. A Polym. Chem.* **2006,** *44* (17), 5182-5191.
5. Cohen, C. T.; Thomas, C. M.; Peretti, K. L.; Lobkovsky, E. B.; Coates, G. W., Copolymerization of cyclohexene oxide and carbon dioxide using (salen)Co(iii) complexes: synthesis and characterization of syndiotactic poly(cyclohexene carbonate). *Dalton Trans.* **2006,** (1), 237-249.
6. Nakano, K.; Nakamura, M.; Nozaki, K., Alternating Copolymerization of Cyclohexene Oxide with Carbon Dioxide Catalyzed by (salalen)CrCl Complexes. *Macromolecules* **2009,** *42* (18), 6972-6980.
7. Thevenon, A.; Cyriac, A.; Myers, D.; White, A. J. P.; Durr, C. B.; Williams, C. K., Indium Catalysts for Low-Pressure CO_2/Epoxide Ring-Opening Copolymerization: Evidence for a Mononuclear Mechanism? *J. Am. Chem. Soc.* **2018,** *140*, 6893-6903.
8. Hansen, K. B.; Leighton, J. L.; Jacobsen, E. N., On the Mechanism of Asymmetric Nucleophilic Ring-Opening of Epoxides Catalyzed by (Salen)CrIII Complexes. *J. Am. Chem. Soc.* **1996,** *118* (44), 10924-10925.
9. Jacobsen, E. N., Asymmetric Catalysis of Epoxide Ring-Opening Reactions. *Acc. Chem. Res.* **2000,** *33* (6), 421-431.
10. Darensbourg, D. J.; Yarbrough, J. C., Mechanistic Aspects of the Copolymerization Reaction of Carbon Dioxide and Epoxides, Using a Chiral Salen Chromium Chloride Catalyst. *J. Am. Chem. Soc.* **2002,** *124* (22), 6335-6342.
11. Cyriac, A.; Jeon, J. Y.; Varghese, J. K.; Park, J. H.; Choi, S. Y.; Chung, Y. K.; Lee, B. Y., Unusual coordination mode of tetradentate Schiff base cobalt(iii) complexes. *Dalton Trans.* **2012,** *41* (5), 1444-1447.
12. Katsuki, T., Unique asymmetric catalysis of cis-β metal complexes of salen and its related Schiff-base ligands. *Chem. Soc. Rev.* **2004,** *33* (7), 437-444.
13. Bakewell, C.; Cao, T.-P.-A.; Le Goff, X. F.; Long, N. J.; Auffrant, A.; Williams, C. K., Yttrium Phosphasalen Initiators for rac-Lactide Polymerization. *Organometallics* **2013,** *32* (5), 1475-1483.
14. Cao, T.-P.-A.; Labouille, S.; Auffrant, A.; Jean, Y.; Le Goff, X. F.; Le Floch, P., Pd(ii) and Ni(ii) complexes featuring a "phosphasalen" ligand: synthesis and DFT study. *Dalton Trans.* **2011,** *40* (39), 10029-10037.
15. Bakewell, C.; Cao, T. P.; Long, N.; Le Goff, X. F.; Auffrant, A.; Williams, C. K., Yttrium phosphasalen initiators for rac-lactide polymerization: excellent rates and high iso-selectivities. *J. Am. Chem. Soc.* **2012,** *134* (51), 20577-80.
16. Bakewell, C.; White, A. J. P.; Long, N. J.; Williams, C. K., Metal-Size Influence in Iso-Selective Lactide Polymerization. *Angew. Chem. Int. Ed.* **2014,** *53* (35), 9226-9230.

17. Hormnirun, P.; Marshall, E. L.; Gibson, V. C.; Pugh, R. I.; White, A. J. P., Study of ligand substituent effects on the rate and stereoselectivity of lactide polymerization using aluminum salen-type initiators. *Proc. Natl. Acad. Sci.* **2006,** *103* (42), 15343-15348.
18. Romain, C.; Thevenon, A.; Saini, P. K.; Williams, C. K., Dinuclear Metal Complex-Mediated Formation of CO_2-Based Polycarbonates. In *Carbon Dioxide and Organometallics. Topics in Organometallic Chemistry*, Lu, X., Ed. Springer, Cham: 2015; Vol. 53.
19. Schneider, F.; Zhao, T.; Huhn, T., Cytotoxic heteroleptic heptacoordinate salan zirconium(IV)-bis-chelates-synthesis, aqueous stability and X-ray structure analysis. *Chemical Comm.* **2016,** *52*, 10151-10154.
20. Morris, G. A.; Zhou, H.; Stern, C. L.; Nguyen, S. T., A General High-Yield Route to Bis(salicylaldimine) Zinc(II) Complexes: Application to the Synthesis of Pyridine-Modified Salen-Type Zinc(II) Complexes. *Inorg. Chem.* **2001,** *40* (13), 3222-3227.
21. Herrmann, W. A.; Rauch, M. U.; Artus, G. R. J., Multiple Bonds between Main Group Elements and Transition Metals. 153.1 Rhenium(V) Oxo Complexes with Tetradentate Schiff Bases: Structural Considerations. *Inorg. Chem.* **1996,** *35* (7), 1988-1991.
22. Thevenon, A.; Garden, J. A.; White, A. J. P.; Williams, C. K., Dinuclear Zinc Salen Catalysts for the Ring Opening Copolymerization of Epoxides and Carbon Dioxide or Anhydrides. *Inorg. Chem.* **2015,** *54* (24), 11906-11915.
23. Yeori, A.; Goldberg, I.; Shuster, M.; Kol, M., Diastereomerically-Specific Zirconium Complexes of Chiral Salan Ligands: Isospecific Polymerization of 1-Hexene and 4-Methyl-1-pentene and Cyclopolymerization of 1,5-Hexadiene. *J. Am. Chem. Soc.* **2006,** *128* (40), 13062-13063.
24. Khanmohammadi, H.; Salehifard, M.; Abnosi, M. H., Synthesis, characterization, biological and thermal studies of Cu(II) complexes of salen and tetrahedrosalen ligands. *J. Iran. Chem. Soc.* **2009,** *6* (2), 300-309.
25. Nakamoto, K., Infrared and Raman Spectra of Inorganic and Coordination Compounds. *Handbook of Vibrational Spectroscopy* **2006**.
26. Qian, F.; McCusker, J. E.; Zhang, Y.; Main, A. D.; Chlebowski, M.; Kokka, M.; McElwee-White, L., Catalytic Oxidative Carbonylation of Primary and Secondary Diamines to Cyclic Ureas. Optimization and Substituent Studies. *J. Org. Chem.* **2002,** *67* (12), 4086-4092.
27. Betschart, C.; Schmidt, B.; Seebach, D., Anwendungsbreite der reduktiven Kupplung aromatischer Aldimin-Derivate mit niedervalenten Titan-Reagenzien zu 1,2-Diarylethylendiaminen. *Helv. Chim. Acta* **1988,** *71* (8), 1999-2021.
28. Pittelkow, M.; Lewinsky, R.; Christensen, J. B., Selective Synthesis of Carbamate Protected Polyamines Using Alkyl Phenyl Carbonates. *Synthesis* **2002,** *2002* (15), 2195-2202.
29. Truong, T.-T.; Coates, G. W.; Abruña, H. D., High power organic cathodes using thin films of electropolymerized benzidine polymers. *Chemical Comm.* **2015,** *51* (78), 14674-14677.
30. Beament, J.; Mahon, M. F.; Buchard, A.; Jones, M. D., Salan group 13 complexes – structural study and lactide polymerisation. *New J. Chem.* **2017,** *41* (5), 2198-2203.

Chapter 5

Conclusions and Outlook

5.1. General Conclusion

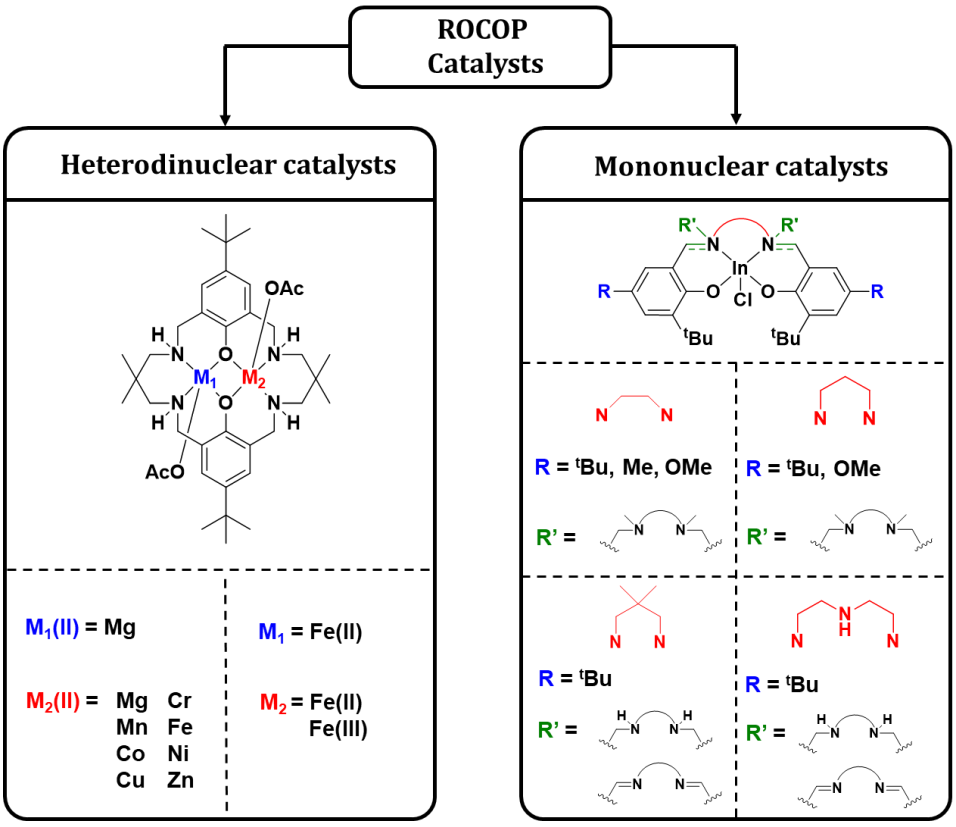


Figure 5.1. Summary of the catalysts reported in this thesis.

This thesis details two families of catalysts, both mono- and di-nuclear systems, for the ROCOP of cyclohexene oxide and CO_2. Investigation of the heterodinuclear macrocyclic complexes revealed all metal combinations were active using carbon dioxide at 1 bar. The most active catalysts were MgCo (TOF = 1056 ± 18 h^{-1}) and MgFe (TOF = 1071 ± 33 h^{-1}) and the least active was MgCr (TOF = 103 ± 5 h^{-1}). These findings highlight the importance of the second metal in controlling catalytic rate and selectivity. Reaction monitoring, using *in situ* ATR-IR spectroscopy, also confirmed point kinetic analyses and resulted in a volcano plot when activity was correlated with the metal group – i.e. factors influencing polymerisation activity are complex and subject to subtle changes. The MgCo catalyst was also highly active for the ROCOP of CO_2 and various other epoxides.

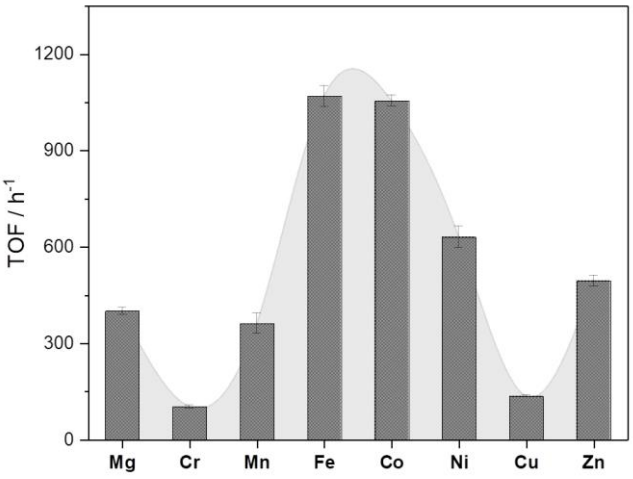


Figure 5.2. TOFs *vs.* heterodinuclear complexes Mg(II)M(II) with M = Mg, Cr, Mn, Fe, Co, Ni, Cu and Zn, ordered by atomic number.

Mononuclear In(III) salen and salan type complexes, with different backbones and *para*-phenol substituents, were also investigated. When tested in ROCOP of CHO/CO_2 the complexes showed low activity and required co-catalyst addition (PPNCl) to improve rate and selectivity. The results are comparable with the activity values reported by Thevenon et al. for an In(III)-phosphasalen catalyst, however, with lower selectivity.[1]

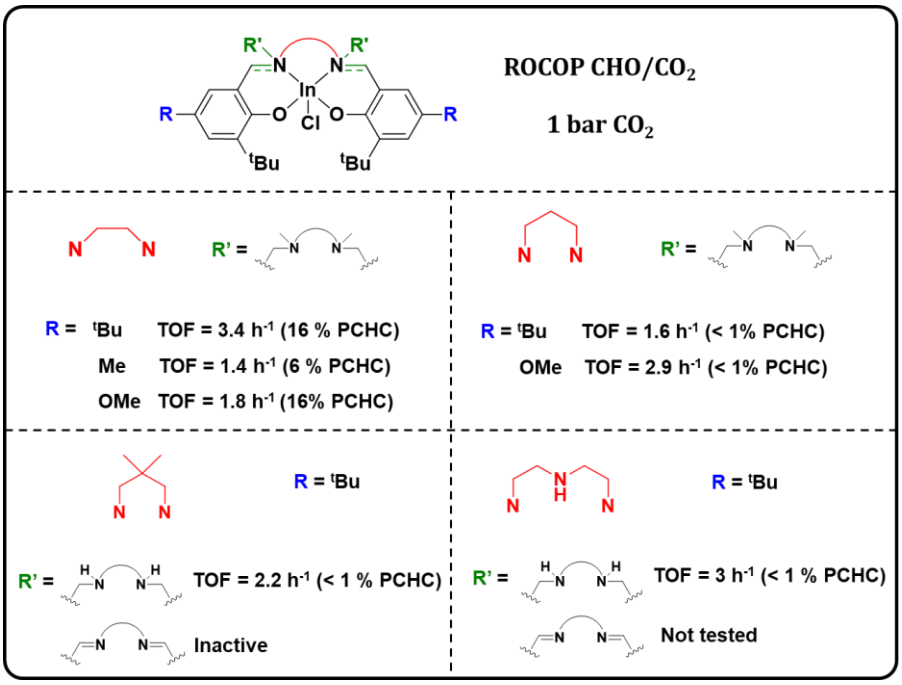


Figure 5.3. Summary of mononuclear In(III) complexes tested for ROCOP of CHO/CO_2, without co-catalyst addition, and their respective activity and selectivity.

5.2. Future work

5.2.3. Heterodinuclear catalysts

In terms of the heterodinuclear catalysts, future experiments should focus on understanding and characterizing the catalyst and mechanisms.

- Mechanism: To complement the experimental studies a computation study, using DFT, could be performed to try to understand the influences of different metal centres and to attribute roles in the catalytic cycles to the two metals. Studies should also target isolation of catalytic intermediates to compare ground state structures of different adducts and intermediates, for example by comparing angle and bond distances of metal–epoxide and metal–carbonate model complexes. To isolate the intermediates, crystallisation of the catalyst in a non-coordinated solvent saturated with a CO_2 atmosphere and crystallisations with a controlled amount of epoxide, with and without the presence of CO_2, should be explored.

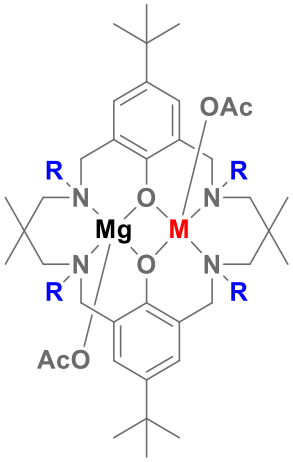
- Synergic Catalysis: Williams and co-workers previously reported a detailed study of the ROCOP of CHO/CO_2 with the MgCo catalyst. The Eyring analysis and comparisons revealed that the Mg(II) centre reduces the barrier to the epoxide coordination primarily through reduced transition state entropy. The Co(II) centre is responsible for reducing the transition state enthalpy and is proposed to provide the carbonate nucleophile.[2] A clear target for future work would be to conduct an Eyring analysis of selected catalysts, for example, MgFe (fast) and MgCr (slow). Such studies should be used to understand whether similar transition entropy and enthalpy contributions are observed. Due to the capacity of MgCo to copolymerise epoxide/anhydride, the enthalpy and entropy studies could be also performed for this system and compared with the results reported for CHO/CO_2 using the same catalyst

– such studies would also be important to understand the generality of the insights into synergic catalysis.

- High-pressure copolymerisation experiments: Due to the physical limitations that may occur in copolymerisations conducted at 1 bar CO_2 in neat epoxide (such as viscosity and CO_2 dissolution limitations) the series of catalysts should also be tested using high-pressure conditions and using *in situ* ATR-IR spectroscopic monitoring. Such studies would be useful to confirm if the catalytic activity order remains the same under different conditions.

New Ligands and Catalysts

- Inspired by the addition of donor R groups to the In(III) catalysts in chapter 4, the bimetallic catalysts could also be ligand modified. For example, changing from N–H to N–Me groups could be used to increase electron-donating characteristics. Such a substitution at the amines should maintain the flexibility of the macrocycle (allowing the catalyst to access the bowl conformation) whilst increasing electron donation to the metal centres, Scheme 5.1. It would be useful to test such a ligand in coordination chemistry with MgCo and MgFe (most active catalysts) and with MgCr and MgCu to better understand the balance of Lewis acidity and lability.

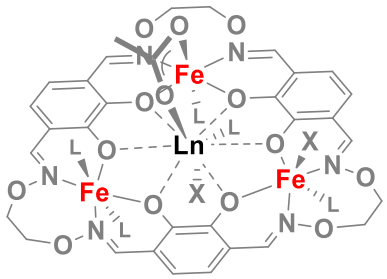


M(II) = Cr, Fe, Co, Cu

R = Me, H

Scheme 5.1. Potential heterodinuclear macrocycle catalyst systems.

- Recent work from Nozaki and co-workers used a multinuclear catalyst featuring Co(II) and Ln(III) and showed high activity in CHO/CO_2 ROCOP.[3] Inspired by this finding, it may be possible to replace the Co(II) for Fe(II) to produce a new multinuclear catalyst of high activity but utilising lower cost and lower toxicity iron, Scheme 5.2.



L = MeOH X = OAc

Ln = La, Ce, Pr,Nd, Eu, Gd

Scheme 5.2. Potential multinuclear catalysts.

5.2.2. Mononuclear Catalysts

To complete the series of mononuclear metal catalysts the following work is recommended:

- Compare catalysts which all feature ^{t}Bu *para*-phenyl substituents to understand how the ligand backbone and N–Me groups influence catalytic activity and selectivity. The ROCOP of CHO/CO_2 should be performed under the same conditions as in chapter 4, at 1 bar CO_2. The catalysts with N,N,2,2-tetramethyl-1,3-propanediamine and 1,7-dimethyldiethylenetriamine backbones should be synthesised from the amine precursor reported in chapter 4. A summary of the catalysts that should be synthesised to complete the catalytic comparison is shown in boxes, Figure 5.4.

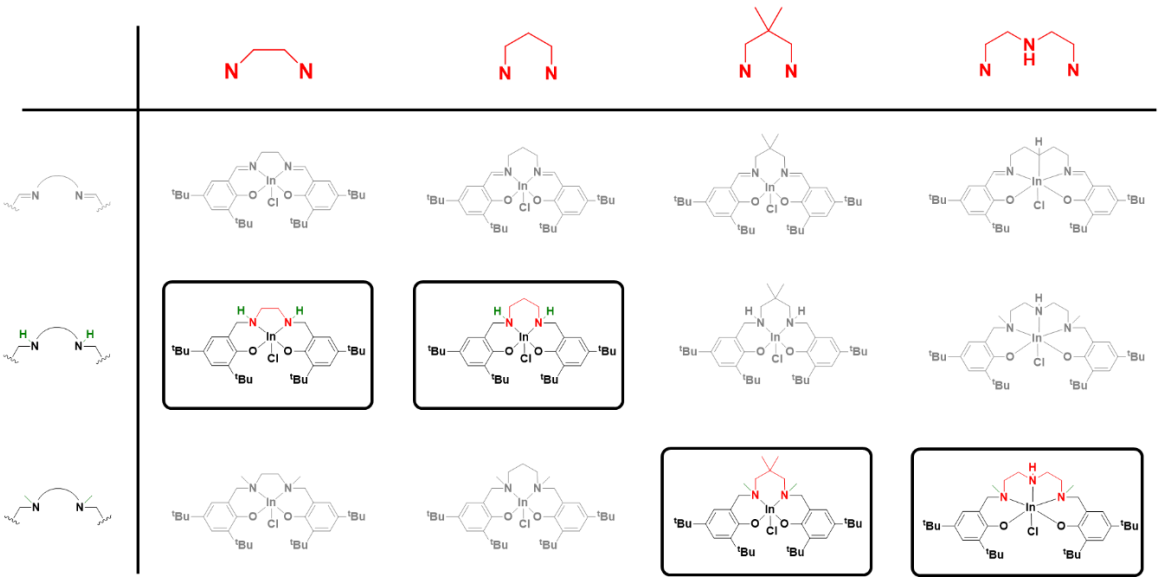


Figure 5.4. Summary of In(III) catalysts systems with diamine backbone and nitrogen environment variations. Highlighted the systems that were not accessed and tested yet.

- To understand the balance between ligand flexibility and metal Lewis acidity, a full comparison of the different *para*-phenyl substituents and ligand backbones should be conducted using the ligands with N–Me groups. To complete this study, the catalysts shown in boxes in Figure 5.5 should be synthesised.

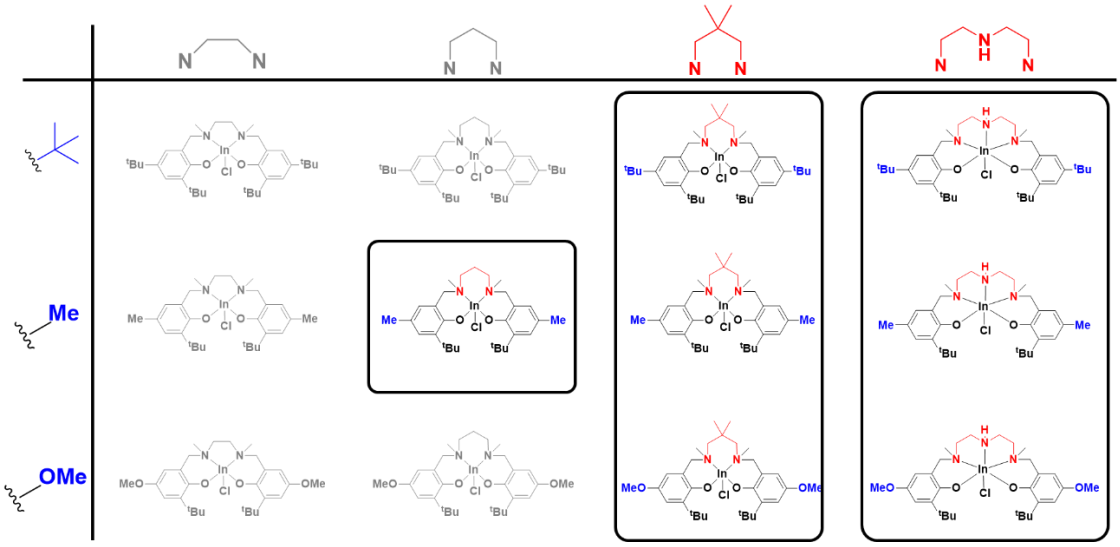


Figure 5.5. Summary of In(III) catalysts systems with diamine backbone and *para*-phenolate sites variations (for N–Me systems). Highlighted the systems that were not accessed and tested yet.

- Once all catalysts have been compared, the best ligand structure should be obtained and used for further study with different metal centres and co-ligands. In terms of the metal centre, larger ionic radii metals should facilitate the *cis*-coordination of epoxide and initiating group, and so targets should include Ln(III) metal centres. In terms of co-ligands, using alkoxides is likely to reduce initiation periods compared to the chloride ligands tested in Chapter 4.

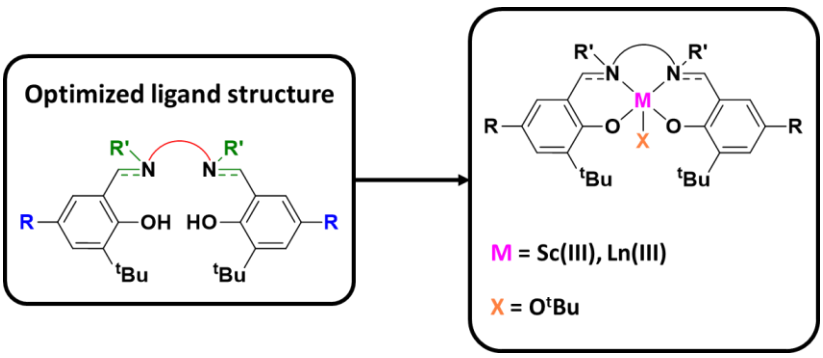


Figure 5.6. Potential future catalysts obtained from the optimized ligand structure.

- Considering that metal salen and salan catalysts are extensively applied for ring-opening polymerisation (ROP) of lactide (LA),[4-8] these catalysts should also be tested for polyester synthesis by lactide ROP. If they are successful in that catalysis, they may also have potential in switch catalysis, where by mixtures of lactone,

anhydride, epoxide and carbon dioxide are selectively enchained.[9-11] Such switch catalysis using carbon dioxide and lactide combinations could be a powerful means to improve polymer scope using renewable resources and to tune factors such as crystallinity, glass transition temperatures, mechanical responses and degradation rates.

5.4. References

1. Thevenon, A.; Cyriac, A.; Myers, D.; White, A. J. P.; Durr, C. B.; Williams, C. K., Indium Catalysts for Low-Pressure CO_2/Epoxide Ring-Opening Copolymerization: Evidence for a Mononuclear Mechanism? *J. Am. Chem. Soc.* **2018,** *140*, 6893-6903.
2. Deacy, A. C.; Kilpatrick, A. F. R.; Regoutz, A.; Williams, C. K., Understanding metal synergy in heterodinuclear catalysts for the copolymerization of CO_2 and epoxides. *Nat. Chem.* **2020,** *12* (4), 372-380.
3. Asaba, H.; Iwasaki, T.; Hatazawa, M.; Deng, J.; Nagae, H.; Mashima, K.; Nozaki, K., Alternating Copolymerization of CO_2 and Cyclohexene Oxide Catalyzed by Cobalt–Lanthanide Mixed Multinuclear Complexes. *Inorg. Chem.* **2020,** *59* (12), 7928-7933.
4. Myers, D.; White, A. J. P.; Forsyth, C. M.; Bown, M.; Williams, C. K., Phosphasalen Indium Complexes Showing High Rates and Isoselectivities in rac-Lactide Polymerizations. *Angew. Chem. Int.* **2017,** *56* (19), 5277-5282.
5. Aluthge, D. C.; Ahn, J. M.; Mehrkhodavandi, P., Overcoming aggregation in indium salen catalysts for isoselective lactide polymerization. *Chem. Sci.* **2015,** *6* (9), 5284-5292.
6. Nomura, N.; Ishii, R.; Akakura, M.; Aoi, K., Stereoselective Ring-Opening Polymerization of Racemic Lactide Using Aluminum-Achiral Ligand Complexes: Exploration of a Chain-End Control Mechanism. *J. Am. Chem. Soc.* **2002,** *124* (21), 5938-5939.
7. Maudoux, N.; Roisnel, T.; Dorcet, V.; Carpentier, J.-F.; Sarazin, Y., Chiral (1,2)-Diphenylethylene-Salen Complexes of Triel Metals: Coordination Patterns and Mechanistic Considerations in the Isoselective ROP of Lactide. *Chem. Eur. J.* **2014,** *20* (20), 6131-6147.
8. Nomura, N.; Ishii, R.; Yamamoto, Y.; Kondo, T., Stereoselective Ring-Opening Polymerization of a Racemic Lactide by Using Achiral Salen– and Homosalen–Aluminum Complexes. *Chem. Eur. J.* **2007,** *13* (16), 4433-4451.
9. Stößer, T.; Williams, C. K., Selective Polymerization Catalysis from Monomer Mixtures: Using a Commercial Cr-Salen Catalyst To Access ABA Block Polyesters. *Angew. Chem. Int.* **2018,** *57* (21), 6337-6341.
10. Stößer, T.; Sulley, G. S.; Gregory, G. L.; Williams, C. K., Easy access to oxygenated block polymers via switchable catalysis. *Nat. Commun.* **2019,** *10* (1), 2668.
11. Kernbichl, S.; Reiter, M.; Mock, J.; Rieger, B., Terpolymerization of β-Butyrolactone, Epoxides, and CO_2: Chemoselective CO_2-Switch and Its Impact on Kinetics and Material Properties. *Macromolecules* **2019,** *52* (21), 8476-8483.

Chapter 6

Experimental

6.1. General Comments

All solvents and reagents were obtained from commercial sources and used as received unless stated otherwise. All metal complexes were synthesised under anhydrous conditions, using a nitrogen-vacuum Schlenk line or a nitrogen-filled glovebox. Common organic solvents used in complex synthesis were obtained from a SPS system, degassed by three freeze-pump-thaw cycles and stored over activated 3 Å or 4 Å molecular sieves under nitrogen. Cyclohexene oxide was dried over calcium hydride for 5 days and purified via fractional distillation under inert atmosphere, it was then degassed by three freeze-pump-thaw cycles and stored under N_2. All anhydrous deuterated solvents were dried over calcium hydride overnight, and purified via vacuum transfer and stored under inert atmosphere with 4 Å molecular sieves. Deuterated MeOH was obtained in individual glass ampoule and used as received. Research grade carbon dioxide (BOC, 99.99 %) was dried through two drying columns (Micro Torr, Model number: MC1-804FV) in series. The norbornene anhydride was purified by dissolving in benzene, filtered and recrystalized in chloroform. The anhydride was also sublimed and stored under nitrogen atmosphere. The full characterisation of some complexes were not possible due to limitation caused by COVID-19 2020 outbreak.

6.2. Instrumentation

6.2.1. Attenuated Total Reflection Infrared Spectroscopy (ATR-IR)

In situ ATR-IR measurements were performed on a Mettler-Toledo ReactIR ic.10 spectrometer equipped with a MCT detector and a silver halide DiComp probe. The reported plots were obtained after one point base line corrections and the monitoring

bands were selected from the overlap of individual IR spectra of monomer and polymers.

6.2.2. FT-IR

The IR measurements were performed in a Varian FTS-7000 Fourier Transform Infrared Spectrometer. During the measurement the samples were obtained in air with minimal exposure time for the samples.

6.2.3. Matrix-Assisted Laser Desorption/Ionization – Time of Flight (MALDI-ToF)

MALDI-ToF analysis were performed on a Bruker MALDI Autroflex Speed and the data was analysed using mmass software.

Catalyst: It was a mixture of 20 μL of a 0.016 M solution of catalyst in THF with 80 μL of a 0.16 M solution of DCTB. 2 μL of the mixture was spotted onto the sample plate.

Polymer: It was a mixture of 5 μL of a solution of isolated polymer in THF (0.01 g mL^{-1}) with 50 μL of 0.16 M solution of DCTB and 2 μL of a 0.1 M solution of potassium trifluoroacetate (KTFA) as the ionising agent. 2 μL of the mixture was spotted onto the sample plate

6.2.4. Nuclear Magnetic Resonance (NMR) spectroscopy

NMR experiments were performed on Bruker Avance III HD nanobay NMR equipment with 9.4 T magnet, 400 MHZ. Bruker Avance III HD nanobay NMR equipped with a 11.75 T magnet, 500 MHz or Bruker Avance NMR equipped with a 11.75 T magnet and a 13C detect cryoprobe. NMR spectra were processed and analysed using MestreNova and Bruker TopSpin software.

- Diffusion Ordered NMR Spectroscopy (DOSY)

The DOSY experiments were performed on a 500 MHz Bruker Avance NMR equipped with a 11.75 T magnet and the molecular weight was estimated using a linear calibration obtained from the diffusion coefficients of standard compounds as shown below.

$$D = \frac{k_B T}{n\pi\eta r}$$

Stoke-Einstein equation: k_b in the Boltzman constant, T the temperature, η the solvent viscosity, and r the hydrodynamic radius.

$$D = A(MW)^{\alpha}$$

$$\log(D) = \alpha \log(MW) + \log(A)$$

Where A and α are intrinsic constants of the deuterated solvent used.

The values of log (A) and α were obtained from the literature[1] from a linear plot of log (D) vs log (MW) measured from the calibration using the diffusion coefficients and molecular weight of hexamethyldisilazane ($HN(SiMe_3)_2$); $Zn(HMDS)_2$; diketiminate ligand $HC(C(Me)N\text{-}2,6\text{-}^{i}Pr_2C_6H_3)_2$ (BDIH) and (BDI)Zn(HMDS) in toluene-d_8 and THF-d_8. The values are: α = -0.5626 and log (A) = -7.505 in THF-d_8 and α = -0.5777 and log(A) = -7.558 in toluene-d_8.[1]

6.2.5. Elemental Analysis

Elemental analysis was carried out by Mr Stephen Boyer at London Metropolitan University, North Campus, Holloway Road, London N7 7DD and Microanalysis laboratory at Department of Chemistry, University of Cambridge, Lensfield Road, Cambridge, CB2 1EW.

6.2.6. X-ray Diffraction

Crystal structures were recorded and solved by Dr. Ryan Kerr and Dr. Andreas Phanopoulos. The crystal sample was isolated in nitrogen-filled glovebox. Diffraction data was collected on an Oxford Diffraction Supernova diffractometer with Cu K_α (λ = 1.5417 Å) radiation, processed using CrysAlisPro. Structures were solved by SHELXT and full-matrix least squares refinements based on F2 were performed in SHELXL, as incorporated in the Olex2 package.

6.2.7. Cyclic Voltammetry

Cyclic voltammograms were recorded in a N_2 glovebox using a PalmSens EmStat Blue potentiostat under computer control with three electrodes: Au disc (2.0 mm^2) as the working electrode, Pt wire as the counter electrode and a Ag wire as the pseudo-reference electrode. The measurement was performed with a solution of 5 mM of sample with 0.1 M of $[^nBu_4N][PF_6]$ in 10 mL of THF. Potentials are reported relative to $[Fc]^+/[Fc]$ measured by ferrocene reference added to the solution.

6.2.8. Superconducting Quantum Interference Device (SQUID) Magnetometry

SQUID data was obtained with a Quantum Design MPMS-5 magnetometer, at a field of 0.1 Tesla and temperature range of 2 – 300 K. Samples were weighed (ca. 30 mg) and stored into gelatine capsules and then placed into a plastic straw. All this procedure was performed in a nitrogen-filled glovebox and the sample was carried out to the equipment inside a Schlenk with inert atmosphere. The magnetic susceptibility values were corrected using the diamagnetic Pascal constants.[2]

6.2.9. Size Exclusion Chromatography (SEC)

Analyses of PCHC were performed on a Shimadzu LC-20AD instrument with two mixed bed PSS SDV linear S columns in series, with HPLC grade THF as the eluent at 40 °C. The polymer samples were dissolved in HPLC grade THF and filtered before the analysis. Polymer molecular weight (M_n) was calibrated against polystyrene standards.

6.3. Chapter 3

6.3.1. Polymerisation procedure

Epoxide/CO_2 copolymerisation – General procedure

The polymerisation was performed in neat epoxide. A Schlenk was charged with 6.0 mL of epoxide, catalyst (0.015 mmol) and 1,2-cyclohexenadiol (CHD) (0.034 g, 0.3 mmol) in a glovebox (N_2 atmosphere). The Schlenk was removed from the glovebox, connected to a triple manifold Young tap CO_2/N_2/vacuum Schlenk line. The system was submitted to 1 bar of CO_2 after five rapid vacuum/CO_2 cycles, the ATR-IR probe was inserted, the system was placed into a preheated oil bath. The final conversion was obtained from the ^{1}H NMR of the aliquot taken when the reaction was stopped (cooling the system to room temperature and exposing to air). GPC analysis was carried out on the crude product. The polycarbonate was isolated by dissolving in DCM, passing through a silica plug, precipitating with methanol and dried under vacuum before MALDI-ToF analysis be conducted.

Cyclohexene oxide (CHO): Reaction performed using CHO (6.0 mL, 59.4 mmol) at 100 °C, monitoring the signal at 1750 cm^{-1} by ATR-IR. Polymer conversion was obtained following the ^{1}H NMR signals for CHO and PCHC. Signals typically used to calculate polymer conversion in a CHO/CO_2 reaction: ^{1}H NMR (400 MHz, $CDCl_3$,

δ (ppm)): 3.05 (CHO), 4.60 (PCHC backbone), 4.35 (PCHC end group), 3.50 (PCHC end group), 3.95 (cyclic carbonate) and 3.45 (polyether).

Vinyl cyclohexene oxide (vCHO): Reaction performed using vCHO (6.0 mL, 46.2 mmol) at 100 °C, monitoring the signal at 1753 cm^{-1} or 1264 cm^{-1} by ATR-IR. Signals typically used to calculate polymer conversion in a vCHO/CO_2 reaction: ^{1}H NMR (400 MHz, $CDCl_3$, δ (ppm)): 5.70 (vCHO and PvCHC, C_{ar}–C**H**=O), 4.77 (PvCHC backbone) 2.42 (PvCHC backbone).

Cyclopentene oxide (CPO): Reaction performed using CPO (6.0 mL, 69.0 mmol) at 80 °C, monitoring by ATR-IR the signal at 1754 cm^{-1}. Signals typically used to calculate polymer conversion in a CPO/CO_2 reaction: ^{1}H NMR (400 MHz, $CDCl_3$, δ (ppm)): 4.94 (PCPC backbone), 4.69 (PCPC end group), 4.12 (PCPC end group), 3.39 (CPO).

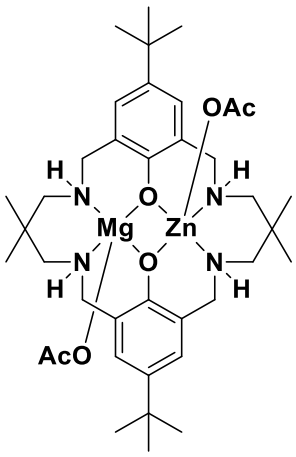
3,4-Epoxytetrahydrofuran (ETHF): Reaction performed using ETHF (6.0 mL, 86.4 mmol) at 80 °C, monitoring by ATR-IR the signal at 1756 cm^{-1}. Signals typically used to calculate polymer conversion in a ETHF/CO_2 reaction: ^{1}H NMR (400 MHz, $CDCl_3$, δ (ppm)): 5.16 (polymer backbone), 4.93 (polymer end group), 3.77 (ETHF).

<u>NA/CHO copolymerisation</u>

The polymerisation was performed in neat CHO. A Schlenk was charged with 6.0 mL of epoxide, catalyst (0.015 mmol), 1,2-cyclohexenadiol (CHD) (0.034 g, 0.3 mmol) and (0.25 g, 0.15 mmol) of NA in N_2 atmosphere. The ATR-IR probe was inserted and the reaction monitored at 100 °C, by analysing the anhydride resonance signal at 1784 cm^{-1}. The reaction was performed until complete consumption of NA, confirmed by IR and ^{1}H NMR. ^{1}H NMR (400 MHz, $CDCl_3$, δ (ppm)): 6.14 (polymer backbone), 4.72 (polymer

end group), 3.25 (polymer), 3.14 (polymer) and complete disappearance of signals at 3.00 and 2.37 (NA).

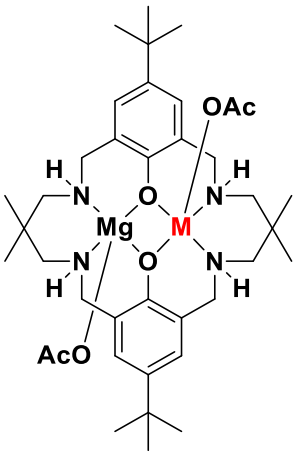
6.3.2. Synthesis of LMgZn(OAc)$_2$



The synthesis was performed according to the literature procedures.[3, 4] LH$_2$, (0.50 g, 0.91 mmol), synthesised previously by members of Williams group, was dissolved in 5 mL of THF in a Schlenk and then a solution of ZnEt$_2$ (0.11 g, 0.91 mmol) in 5 mL of THF was added. The reaction mixture was stirred for 16 h. After this time, 5 mL of THF was added to the reaction and the solution was cooled to -78 °C whilst stirring and then a solution of MgBr$_2$ (0.17g, 0.91 mmol) in THF (10 mL) was added, dropwise, over 15 min. The reaction mixture was stirred at -78 °C, for 15 min, and then at room temperature for 30 min. The solvent was removed and the white powder was dried *in vacuo* overnight to yield the product [LMgZnBr$_2$] (0.67 g, 0.83 mmol, 91 %). To a solution of [LMgZnBr$_2$] (0.67 g, 0.83 mmol) in THF (5 mL), was added K(OAc) (0.16 g, 1.66 mmol) in 5 mL of THF and the mixture was stirred for 16 h at room temperature. The resulting solid (KBr) was removed by filtration and the solvent was removed *in vacuo.* The complex was extracted with DCM several times. The solution was dried *in vacuo* to give the complex LMgZn(OAc)$_2$. (Yield: 0.30 g, 0.42 mmol, 50 %).

^{1}H NMR (400 MHz, d_4-MeOD, δ (ppm)): 7.05 (s, 4H, Ph**H**), 4.22–4.16 (m, 2H, Ph–C**H**$_2$–NH), 4.02–3.94 (m, 2H, Ph–C**H**$_2$–NH), 3.30–3.22 (m, 4H, Ph–C**H**$_2$–NH), 2.95–2.60 (m, 6H, C**H**$_2$–C(CH$_3$)$_2$), 1.70 (br s, 6H, C**H**$_3$–COO), 1.28 (s, 18H, C(C**H**$_3$)$_2$), 1.04–0.97 (m, 12H, C(C**H**$_3$)$_3$). ^{13}C NMR (126 MHz, d_4-MeOD, δ (ppm)): 162.6 (**C**$_{ar}$–O); 138.4 (**C**$_{ar}$–C(CH$_3$)$_3$); 129.4 (**C**$_{ar}$–H); 129.1 (**C**$_{ar}$–H); 125.5 (**C**$_{ar}$–(CH$_2$)–NH); 125.3 (**C**$_{ar}$–(CH$_2$)–NH); 124.8 (**C**$_{ar}$–(CH$_2$)–NH); 124.6 (**C**$_{ar}$–(CH$_2$)–NH); 64.2 (HN-**C**H$_2$-C(CH$_3$)$_2$); 64.1 (HN–**C**H$_2$–C(CH$_3$)$_2$); 63.3 (HN–**C**H$_2$–C(CH$_3$)$_2$); 63.2 (HN–**C**H$_2$–C(CH$_3$)$_2$); 56.9 (HN–**C**H$_2$–Ph); 56.1 (HN–**C**H$_2$–Ph); 35.3 (**C**(CH$_3$)$_2$); 34.7 (**C**(CH$_3$)$_2$); 34.4 (Ar–C(**C**H$_3$)$_3$); 32.1 (Ar–**C**(CH$_3$)$_3$); 28.9 (C(**C**H$_3$)$_2$); 28.7 (C(**C**H$_3$)$_2$); 24.0 (**C**H$_3$-COO); 21.5 (C(**C**H$_3$)$_2$); 21.2 (C(**C**H$_3$)$_2$). Elemental analysis for $C_{38}H_{60}MgN_4O_6Zn$ (756.37 g mol^{-1}): Found (Calcd.): C, 59.35 (60.17); H, 7.64 (7.97); N, 7.04 (7.39) %. MS (MALDI-ToF): m/z 697.18 [LMgZn(OAc)]$^+$; 657.26 [LMgMg(OAc)]$^+$ and 737.18 [LZnZn(OAc)]$^+$. IR: 3300 cm^{-1} (ν_{NH}), 1591 cm^{-1} ($\nu_{(COO)\text{-}as}$), 1419 cm^{-1} ($\nu_{(COO)\text{-}sy}$) and 922 cm^{-1} ($\delta_{(COO)\text{-}}$).

6.3.3. General procedure 1 – Synthesis of LMgM(OAc)$_2$



M (II) =		
	Mg	2
	Cr	3
	Mn	4
	Fe	5
	Co	6
	Ni	7
	Cu	8

The synthesis of the heterobimetallic systems were performed following an adapted literature procedure.[5] Mg(N(SiMe$_3$)$_2$)$_2$ (0.31 g, 0.91 mmol) in THF (2.5 mL) was added to a solution of H$_2$L (0.50 g, 0.91mmol) also in THF (2.5 mL) and stirred for 2 h. M(OAc)$_2$ (0.91 mmol) was added and the solution was stirred for 16 h at 100 °C in a J-Young ampoule. The solution was reduced *in vacuo* and the product was washed with pentane at least 3 times to afford the final complex.

Complex 2 (MgMg): Using general procedure 1, reaction using Mg(OAc)$_2$ (0.13 g, 0.91 mmol) gives the title product as a white powder (Yield: 0.46 g, 0.64 mmol, 70 %), ^{1}H NMR (500 MHz, d$_4$-MeOD, δ (ppm)): 7.02 (s, 4H, Ph**H**), 4.00 (d, *J* = 11.8 Hz, 4H, Mg–HN–C**H**$_2$–Ph), 3.22 (d, *J* = 11.8 Hz, 4H, Mg–HN–C**H**$_2$–Ph), 2.75 (d, *J* = 11.7 Hz, 4H, Mg–HN–C**H**$_2$–C(CH$_3$)$_2$), 2.64 (d, *J* = 11.7 Hz, 4H, Mg–HN–C**H**$_2$–C(CH$_3$)$_2$), 1.90 (br, s, (C**H**$_3$)COO), 1.23 (s, 18H, C(C**H**$_3$)$_2$), 1.23 (s, 6H, C(C**H**$_3$)$_2$), 1.02 (s, 6H, C(C**H**$_3$)$_2$). ^{13}C NMR (126 MHz, d$_4$-MeOD, δ (ppm)): 162.5 (**C**$_{ar}$–O); 138.1 (**C**$_{ar}$–C(CH$_3$)$_3$); 129.4 (**C**$_{ar}$–H); 125.5 (**C**$_{ar}$–(CH$_2$)–NH); 63.2 (Mg-HN-**C**H$_2$-C(CH$_3$)$_2$); 56.2 (Mg-HN-**C**H$_2$-Ph); 35.3 (**C**(CH$_3$)$_2$); 34.4 (**C**(CH$_3$)$_2$); 32.1 (Ar–C(**C**H$_3$)$_3$); 28.9 (C(**C**H$_3$)$_2$); 21.5 (C(**C**H$_3$)$_2$). Elemental analysis for C$_{38}$H$_{60}$Mg$_2$N$_4$O$_6$ (716.42 g mol^{-1}): Found (Calcd.): C, 63.10

(63.61); H, 8.67 (8.55); N, 7.70 (7.64) %. MS (MALDI-ToF): m/z 657.27 $[LMgMg(OAc)]^+$. IR: 3308 cm^{-1} (ν_{NH}), 1595 cm^{-1} ($\nu_{(COO)-as}$), 1423 cm^{-1} ($\nu_{(COO)-sy}$) and 924 cm^{-1} ($\delta_{(COO)-}$).

Complex 3 (MgCr): Using a modification of general procedure 1, reaction using $Cr(OAc)_2$ (0.15 g, 0.91 mmol) at room temperature for 72 h gives the title product as a blue powder (Yield: 50 %). MS (MALDI-ToF): m/z 685.19 $[LMgCr(OAc)]^+$; 657.23 $[LMgMg(OAc)]^+$, 696.75 $[LMgMg(OAc)]^+$ with K^+ and 713.15 $[LCrCr(OAc)]^+$. IR: 3307 cm^{-1} (ν_{NH}), 1593 cm^{-1} ($\nu_{(COO)-as}$), 1421 cm^{-1} ($\nu_{(COO)-sy}$) and 924 cm^{-1} ($\delta_{(COO)-}$).

Complex 4 (MgMn): Using general procedure 1, reaction using $Mn(OAc)_2$ (0.16 g, 0.91 mmol) gives the title product as an off white powder (Yield: 0.46 g, 0.62 mmol, 68 %). Elemental analysis for $C_{38}H_{60}MgMnN_4O_6$ (747.37 g mol^{-1}): Found (Calcd.): C, 60.85 (61.01); H, 8.01 (8.08); N, 7.45 (7.49) %. MS (MALDI-ToF): m/z 688.19 $[LMgMn(OAc)]^+$; 657.22 $[LMgMg(OAc)]^+$ and 719.14 $[LMnMn(OAc)]^+$. IR: 3308 cm^{-1} (ν_{NH}), 1583 cm^{-1} ($\nu_{(COO)-as}$), 1415 cm^{-1} ($\nu_{(COO)-sy}$) and 926 cm^{-1} ($\delta_{(COO)-}$).

Complex 5 (MgFe): Using general procedure 1, reaction using $Fe(OAc)_2$ (0.16 g, 0.91 mmol) gives the title product as a light brown powder (Yield: 0.51 g, 0.68 mmol, 75 %). Elemental analysis for $C_{38}H_{60}MgFeN_4O_6$ (748.37 g mol^{-1}): Found (Calcd.): C, 61.56 (60.93); H, 8.67 (8.07); N, 7.70 (7.48) %. MS (MALDI-ToF): m/z 689.28 $[LMgFe(OAc)]^+$; 657.30 $[LMgMg(OAc)]^+$ and 721.26 $[LFeFe(OAc)]^+$. IR: 3308 cm^{-1} (ν_{NH}), 1587 cm^{-1} ($\nu_{(COO)-as}$), 1421 cm^{-1} ($\nu_{(COO)-sy}$) and 924 cm^{-1} ($\delta_{(COO)-}$).

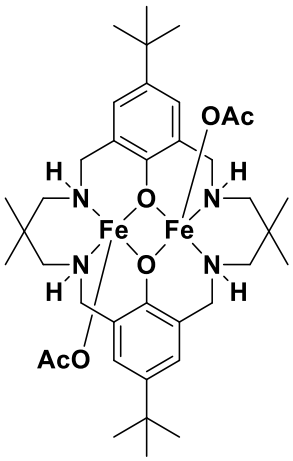
Complex 6 (MgCo): Using general procedure 1, reaction using $Co(OAc)_2$ (0.16 g, 0.91 mmol) gives the title product as a pale pink powder (Yield: 0.52 g, 0.68 mmol, 75 %). Elemental analysis for $C_{38}H_{60}MgCoN_4O_6$ (751.37 g mol^{-1}): Found (Calcd.): C, 60.51 (60.68); H, 7.89 (8.04); N, 7.31 (7.45) %. MS (MALDI-ToF): m/z 692.26

[LMgCo(OAc)]$^+$; 657.27 [LMgMg(OAc)]$^+$ and 727.22 [LCoCo(OAc)]$^+$. IR: 3300 cm^{-1} (ν_{NH}), 1587 cm^{-1} ($\nu_{(COO)-as}$), 1419 cm^{-1} ($\nu_{(COO)-sy}$) and 925 cm^{-1} ($\delta_{(COO)-}$).

Complex 7 (MgNi): Using general procedure 1, reaction using $Ni(OAc)_2$ (0.16 g, 0.91 mmol) gives the title product as a pale blue powder (Yield: 0.53 g, 0.71 mmol, 78 %). Elemental analysis for $C_{38}H_{60}MgNiN_4O_6$ (750.37 g mol^{-1}): Found (Calcd.): C, 60.26 (60.70); H, 8.08 (8.04); N, 7.30 (7.45) %. MS (MALDI-ToF): m/z 691.20 [LMgNi(OAc)]$^+$; 657.24 [LMgMg(OAc)]$^+$, 675.42 [LMgMg(OAc)]$^+$·H_2O and 725.18 [LNiNi(OAc)]$^+$. IR: 3290 cm^{-1} (ν_{NH}), 1587 cm^{-1} ($\nu_{(COO)-as}$), 1419 cm^{-1} ($\nu_{(COO)-sy}$) and 937 cm^{-1} ($\delta_{(COO)-}$).

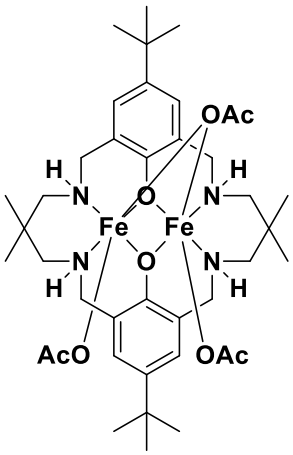
Complex 8 (MgCu): Using general procedure 1, reaction using $Cu(OAc)_2$ (0.17 g, 0.91 mmol) gives the title product as a green powder (Yield: 0.45 g, 0.59 mmol, 65 %). Elemental analysis for $C_{38}H_{60}MgCuN_4O_6$ (755.37 g mol^{-1}): Found (Calcd.): C, 60.25 (60.31); H, 8.02 (7.99); N, 7.43 (7.40) %. MS (MALDI-ToF): m/z 696.28 [LMgCu(OAc)]$^+$; 657.29 [LMgMg(OAc)]$^+$, 676.17 [LMgMg(OAc)]$^+$·H_2O. IR: 3306 cm^{-1} (ν_{NH}), 1591 cm^{-1} ($\nu_{(COO)-as}$), 1421 cm^{-1} ($\nu_{(COO)-sy}$) and 914 cm^{-1} ($\delta_{(COO)-}$).

6.3.4. Synthesis of complex 9, LFeIIFeII(OAc)$_2$



The bis-potassium complex was synthesised following a literature procedure.[6] A solution of K(N(SiMe$_3$)$_2$) (0.22 g, 1.08 mmol) in 5.0 mL of THF was added to a solution of H$_2$L (0.30 g, 0.54 mmol) in 5.0 mL of THF and left stirring for 16 h at 100 °C. Volatiles were removed and hexane was added to the oil and evaporated under vacuum (this procedure was repeated three times) to isolate crude bis-potassium complex (LK$_2$) as a white powder (70 % yield). A solution of Fe(OAc)$_2$ (0.07 g, 0.40 mmol) in THF (5.0 mL) was added in a solution of LK$_2$ (0.13 g, 0.20 mmol) in THF (5.0 mL). The solution was stirred at 100 °C during 16 h. The precipitate was filtered and the volatiles were removed *in vacuo*, washed with hexane and dried overnight to obtain the title product as a red solid (62.0 mg, 0.08 mmol, 40 %). MS (MALDI-ToF): m/z 721.31 [LFeFe(OAc)]$^+$. IR: 3298 cm^{-1} (ν_{NH}), 1595 cm^{-1} ($\nu_{(COO)\text{-}as}$), 1421 and 1375 cm^{-1} ($\nu_{(COO)\text{-}sy}$) and 921 cm^{-1} ($\delta_{(COO)\text{-}}$).

6.3.5. Synthesis of complex 10, LFeIIFeIII(OAc)$_3$



A solution of Fe(OAc)$_2$ (0.19 g, 1.08 mmol) in THF (5.0 mL) was added to a H_2L (0.30 g, 0.54 mmol) in THF (5.0 mL). The mixture was stirring for 16 h at 100 °C. The volatiles were removed and the mixture was washed first with toluene, then with pentane and dried overnight to afford the title product as a purple solid (0.27 g, 0.32 mmol, 60 % yield). MS (MALDI-ToF): m/z 721.31 $[LFeFe(OAc)]^+$. Elemental analysis for $C_{40}H_{63}Fe_2N_4O_8 \cdot C_4H_6FeO_4$ (LFeIIFeIII(OAc)$_3$·Fe(OAc)$_2$): Found (Calcd.): C, 53.41 (52.14); H, 6.87 (6.86); N, 5.92 (5.53) %. IR: 3296 cm^{-1} (ν_{NH}), 1710 cm^{-1} ($\nu_{(C=O)st}$ of acetic acid or Fe(OAc)$_2$), 1596 and 1564 cm^{-1} ($\nu_{(COO)-as}$), 1425–1363 cm^{-1} ($\nu_{(COO)-sy}$) and 925 cm^{-1} ($\delta_{(COO)-}$).

6.4. Chapter 4

6.4.1. Polymerisation

Polymerisation procedure (1bar)

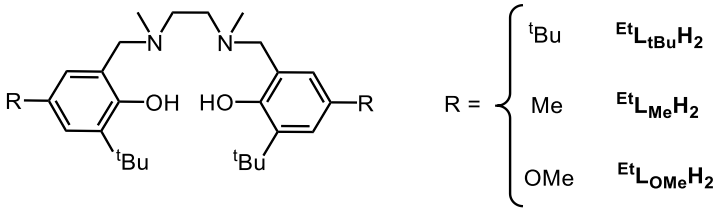
The polymerisation was performed in neat CHO. A Schlenk was charged with CHO (2.0 mL, 1.94 mmol) and catalyst (0.03 mmol) in a glovebox (N_2 atmosphere). The system was submitted to 1 bar of CO_2 (following the same procedure as described in section 6.3.1) and reacted at 60 °C for 48 h. The polymer conversion was analysed by ^{1}H NMR of an aliquot taken at the end of the polymerisation. The polymerisation was stopped by cooling the system to room temperature and exposing to air.

Polymerisation procedure (high pressure)

The polymerisation was performed in neat CHO. A high pressure reactor was charged with CHO (6.0 mL, 59.30 mmol) and catalyst (0.03 mmol), under N_2, in a glovebox. The reactor was closed before removing from the glovebox and then, the system was submitted to a 40 bar pressure of CO_2 and reacted at 80 °C for 24 h. When specified, PPNCl was added in a ratio of 1:1 [Cat]:[PPNCl]. The polymer conversion was analysed by ^{1}H NMR of an aliquot taken in the end of the polymerisation. Polymerisation was stopped by cooling the system to room temperature, depressurising and opening to air.

6.4.2. Synthesis of ligands

- **General procedure 2 – Salan synthesis – C_2 backbone ($^{Et}L_RH_2$) where R = ^{t}Bu, Me and OMe**



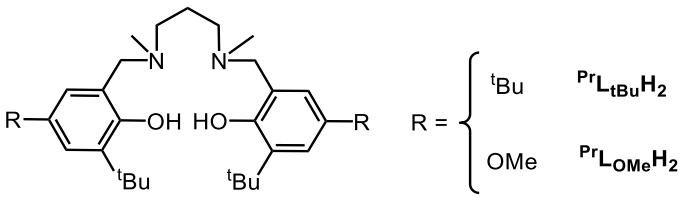
The ligand synthesis was performed following a modified literature procedure.[7] Phenol (80.0 mmol) was added to a round bottom flask and dissolved in methanol (80 mL). Formaldehyde (30 mL, 37% aq.) and *N,N*-dimethylethane-1,2-diamine (4.3 mL, 40.0 mmol) were added and the solution was heated to reflux for 17 hours. After cooling to room temperature, the precipitate was isolated and washed with methanol and dried under vacuum.[7]

$^{Et}L_{tBu}H_2$: Using general procedure 2, reaction using 2,4-di-*tert*-butylphenol (16.5 g, 80.0 mmol) gives the title product as a white powder. Yield: 17.9 g, 32.4 mmol, 81 %. ^{1}H-NMR (400 MHz, C_6D_6, 298 K). δ (ppm): 10.79 (s, 2H, O**H**), 7.51 (d, J = 2.4 Hz, 2H, Ar–**H**), 6.88 (d, J = 2.4 Hz, 2H, Ar–**H**), 3.25 (s, 4H, Ar–C**H**$_2$–N), 2.12 (s, 4H, N–(C**H**$_2$)$_2$–N), 1.78 (s, 6H, N–C**H**$_3$), 1.71 (s, 18H, Ar–C(C**H**$_3$)$_3$), 1.36 (s, 18H, Ar–C(C**H**$_3$)$_3$). ^{13}C-NMR (125.8 MHz, C_6D_6, 298 K). δ (ppm): 155.1 (**C**$_{ar}$) ; 140.8 (**C**$_{ar}$) ; 136.2 (**C**$_{ar}$) ; 123.6 (**C**$_{ar}$H); 123. 3 (**C**$_{ar}$H); 121.7 (**C**$_{ar}$); 62.8 (Ar–**C**H$_2$–N) ; 53.7 (N–(**C**H$_2$)$_2$–N); 41.0 (N–**C**H$_3$); 35.4 (C$_{ar}$–**C**(CH$_3$)$_3$); 34.4 (C$_{ar}$–**C**(CH$_3$)$_3$); 32.0 (C(**C**H$_3$)$_3$); 30.1 (C(**C**H$_3$)$_3$). Elemental analysis for $C_{34}H_{56}N_2O_2$ (524.43 g mol^{-1}): Found (Calcd.): C, 77.70 (77.81); H, 10.65 (10.76); N, 5.21 (5.34) %.

$^{Et}L_{Me}H_2$: Using general procedure 2, reaction using 3.94 g (24.0 mmol) of 2-*tert*-butyl-*p*-creasol and further recrystalised with pentane gives the title product as a white powder. Yield: 48 % (2.54 g, 5.76 mmol). ^{1}H-NMR (500 MHz, $CDCl_3$, 298 K). δ (ppm): 10.63 (s, 2H, O**H**); 6.99 (d, J = 2.2 Hz, 2H, Ar–**H**); 6.63 (d, J = 2.2 Hz, 2H, Ar–**H**); 3.63 (s, 4H, Ar–C**H**$_2$–N); 2.61 (s, 4H, N–(C**H**$_2$)$_2$–N); 2.25 (s, 6H, N–C**H**$_3$); 2.24 (s, 6H, Ar–C**H**$_3$); 1.39 (s, 18H, Ar–C–(C**H**$_3$)$_3$). ^{13}C-NMR (125.8 MHz, C_6D_6, 298 K). δ (ppm): 154.5 (**C**$_{ar}$); 136.5 (**C**$_{ar}$); 127.3 (**C**$_{ar}$); 127.2 (**C**$_{ar}$); 126.8 (**C**$_{ar}$); 121.9 (**C**$_{ar}$); 62.8 (Ar–**C**H$_2$–N); 53.7 (N–(**C**H$_2$)$_2$–N); 41.6 (N–**C**H$_3$); 34.7 (**C**–(CH$_3$)$_3$); 29.7 (C–(**C**H$_3$)$_3$) ; 20.9 (Ar–**C**H$_3$). Elemental analysis for $C_{28}H_{44}N_2O_2$ (440.34 g mol^{-1}): Found (Calcd.): C, 77.70 (76.32); H, 10.65 (10.06); N, 5.21 (6.36) %.

$^{Et}L_{OMe}H_2$: Using general procedure 2, reaction using 4.33 g (24.0 mmol) of 3-*tert*-Butyl-4-hydroxyanisole gives the title product as a white powder (Yield: 62 %, 3.51 g, 7.44 mmol). ^{1}H-NMR (500 MHz, $CDCl_3$, 298 K). δ (ppm): 10.35 (s, 2H, O**H**); 6.79 (d, J = 3.0 Hz, 2H, Ar–**H**); 6.38 (d, J = 3.0 Hz, 2H, Ar–**H**); 3.74 (s, 6H, O–C**H**$_3$); 3.63 (s, 4H, Ar–C**H**$_2$–N); 2.60 (s, 4H, N–(C**H**$_2$)$_2$–N); 2.24 (s, 6H, N–C**H**$_3$); 1.39 (s, 18H, Ar–C(C**H**$_3$)$_3$). ^{13}C-NMR (125.8 MHz, C_6D_6, 298 K). δ (ppm): 151.81 (**C**$_{ar}$–O); 150.7 (O–**C**H$_3$); 138.1 (**C**$_{ar}$); 122.4 (**C**$_{ar}$); 112.9 (**C**$_{ar}$); 111.2 (**C**$_{ar}$); 62.7 (Ar–**C**H$_2$–N); 55.8 (N–(**C**H$_2$)$_2$–N); 53.7 (Ar–O**C**H$_3$); 41.6 (N–**C**H$_3$); 35.0 (**C**(CH$_3$)$_3$); 29.5 (C(**C**H$_3$)$_3$).

- **General procedure 3: Salan synthesis – C_3 backbone ($^{Pr}L_RH_2$) where R = ^{t}Bu and OMe**



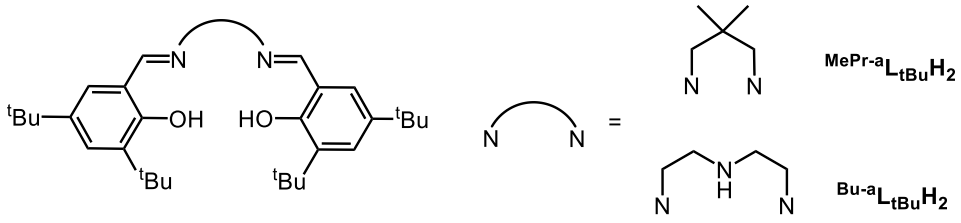
Phenol (80.0 mmol) was added to a round bottom flask and dissolved in methanol (80 mL). Formaldehyde (30 mL, 37% aq.) and *N,N*-dimethyl-1,3-propanediamine (5.0 mL, 40.0 mmol) were added and the solution brought to reflux for 17 hours. After cooling to room temperature, the precipitate was isolated and washed with methanol and dried under vacuum.[7]

$^{Pr}L_{tBu}H_2$: Using general procedure 3, reaction using 2,4-di-*tert*-butylphenol (16.5 g, 80.0 mmol) gives the title product as a white powder. Yield: 5.1 g, 9.42 mmol, 24 %. ^{1}H-NMR (500 MHz, C_6D_6, 298 K). δ (ppm): 11.09 (s, 2H, –O**H**); 7.50 (d, J = 2.4 Hz, 2H, Ar–**H**); 6.91 (d, J = 2.4 Hz, 2H, Ar–**H**); 3.29 (s, 4H, Ar–C**H**$_2$–N–); 1.96 (br, 4H, ,–N–C**H**$_2$–CH$_2$) ; 1.80 (s, 6H, N–C**H**$_3$); 1.71 (s, 18H, Ar–C(C**H**$_3$)$_3$); 1.38 (s, 18H, Ar–C–(C**H**$_3$)$_3$); 1.28 (quint, 2H, N–CH$_2$–C**H**$_2$–CH$_2$). ^{13}C-NMR (126 MHz, C_6D_6, 298 K). δ (ppm): 155.2 (**C**$_{ar}$); 140.8 (**C**$_{ar}$); 136.1 (**C**$_{ar}$); 123.6 (**C**$_{ar}$H); 123.2 (**C**$_{ar}$H); 121.8 (**C**$_{ar}$); 62.5 (Ar–**C**H$_2$–N); 54.6 (N–**C**H$_2$–CH$_2$–); 40.9 (N–**C**H$_3$); 35.4 (C$_{ar}$–**C**–(CH$_3$)$_3$); 34.4 (C$_{ar}$–**C**(CH$_3$)$_3$); 32.0 (C–(**C**H$_3$)$_3$); 30.1 (C–(**C**H$_3$)$_3$); 24.8 (N–CH$_2$–**C**H$_2$–CH$_2$). Elemental analysis for $C_{35}H_{58}N_2O_2$ (538.45 g mol^{-1}): Found (Calcd.): C, 78.81 (78.01); H, 11.32 (10.85); N, 5.28 (5.20) %.

$^{Pr}L_{OMe}H_2$: Using a modification of general procedure 3, reaction using 4.33 g (24.0 mmol) 3-*tert*-butyl-4-hydroxyanisole, after reflux, hydrochloric acid (1 M solution in diethyl ether) was added to the system. The precipitate obtained was washed with cold ether and then neutralised with sodium hydrogen carbonate (1 M, aqueous solution,

excess). The solvent was removed under reduced pressure and then recrystallised from hot ethanol to access the title product. 22% yield (1.30 g, 2.64 mmol). ^{1}H-NMR (500 MHz, $CDCl_3$, 298 K). δ (ppm): 10.69 (s, 2H, –O**H**); 6.79 (d, J = 3.0 Hz, 2H, Ar–**H**); 6.39 (d, J = 3.0 Hz, 2H, Ar–**H**); 3.74 (s, 6H, O–C**H**$_3$); 3.62 (s, 4H, Ar–C**H**$_2$–N–); 2.44 (t, J = 7.3 Hz, 4H, N–C**H**$_2$–CH_2–C**H**$_2$); 2.27 (s, 6H, N–C**H**$_3$); 1.78 (quint, J = 7.4 Hz, 2H, N–CH_2–C**H**$_2$–CH_2); 1.39 (s, 18H, Ar–C(C**H**$_3$)$_3$). ^{13}C-NMR (126 MHz, C_6D_6, 298 K). δ (ppm): 151.8 (**C**$_{ar}$–O); 150.7 (**C**$_{ar}$–OCH_3); 137.9 (**C**$_{ar}$); 122.5 (**C**$_{ar}$–H); 112.7 (**C**$_{ar}$–H); 111.1 (**C**$_{ar}$); 62.3 (Ar–**C**H_2–N); 55.8 (O–**C**H_3) 54.6 (N–**C**H_3); 41.3 (N–**C**H_2–CH_2–**C**H_2); 34.9 (**C**$(CH_3)_3$); 29.5 (C(**C**$H_3)_3$); 24.8 (N–CH_2–**C**H_2–CH_2). Elemental analysis for $C_{29}H_{46}N_2O_4$ (486.35 g mol^{-1}): Found (Calcd.): C, 68.92 (71.57); H, 9.53 (9.52); N, 5.62 (5.76) %.

- **General procedure 4 – Salen synthesis – C_3 and C_4 backbone (**$^{MePr\text{-}a}L_{tBu}H_2$ **and** $^{Bu\text{-}a}L_{tBu}H_2$**)**



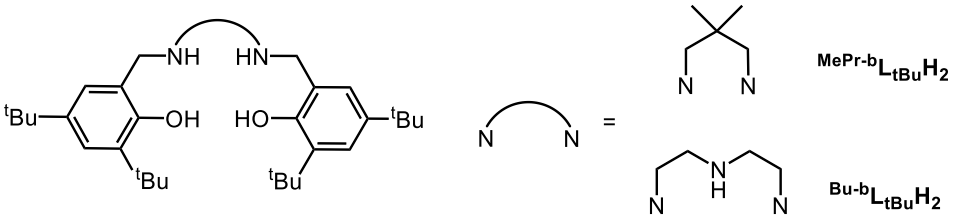
3,5-Di-*tert*-butyl-2-hydroxybenzaldehyde (10.0 g, 42.7 mmol) was added to a round bottom flask and dissolved in ethanol (50 mL). The correspondent diamine (21.3 mmol) was added dropwise and the solution brought to reflux for 2 hours. [8, 9]

$^{MePr\text{-}a}L_{tBu}H_2$**:** Using general procedure 4, reaction using 2,2-dimethyl-1,3-propanediamine (2.56 mL, 21.3 mmol). After reflux the yellow precipitate was filtered and washed with methanol and dried under vacuum to access the title product as a yellow powder. (10.2 g, 19.0 mmol, 89% yield). ^{1}H-NMR (500 MHz, C_6D_6, 298 K).

δ (ppm): 14.28 (s, 2H, –O**H**), 7.85 (s, 2H, Ar–C**H**=N–), 7.60 (d, J = 2.5 Hz, 2H, Ar–**H**), 7.04 (d, J = 2.5 Hz, 2H, Ar–**H**), 3.09 (s, 4H, –N–C**H**$_2$–C–), 1.68 (s, 18H, Ar–C(C**H**$_3$)$_3$), 1.35 (s, 18H, Ar–C(C**H**$_3$)$_3$), 0.86 (s, 6H, C(C**H**$_3$)$_2$). ^{13}C-NMR (126 MHz, C_6D_6, 298 K). δ (ppm): 167.2 (N=**C**H); 159.0 (**C**$_{ar}$–OH); 140.3 (**C**$_{ar}$); 137.2 (**C**$_{ar}$); 127.1 (**C**$_{ar}$H); 126.5 (**C**$_{ar}$H); 118.7 (**C**$_{ar}$); 68.2 (N–C**H**$_2$–C–); 35.5 (**C**(CH$_3$)$_2$); 34.3 (C$_{ar}$–**C**(CH$_3$)$_3$); 31.8 (C$_{ar}$–C(**C**H$_3$)$_3$); 29.8 (C$_{ar}$–C(**C**H$_3$)$_3$); 24.4 (C(**C**H$_3$)$_2$). Elemental analysis for $C_{35}H_{54}N_2O_2$ (534.42 g mol^{-1}): Found (Calcd.): C, 78.50 (78.60); H, 10.10 (10.18); N, 5.23 (5.24) %.

$^{Bu\text{-}a}L_{tBu}H_2$: Using general procedure 4, reaction using 2.30 mL (21.3 mmol) of 2,2'-diaminodiethylamine,[10] after reflux, the solvent was removed under reduced pressure. The yellow oil product was dissolved in ether and the solvent was removed under vacuum, after 3 cycles of solubilising and removing solvent, gives the title product as a yellow powder. (8.9 g, 16.6 mmol, 78 % yield). ^{1}H-NMR (500 MHz, C_6D_6, 298 K). δ (ppm): 14.20 (s, 2H, –O**H**), 7.84 (s, 2H, Ar–C**H**=N–), 7.58 (d, J = 2.5 Hz, 2H, Ar–**H**), 6.98 (d, J = 2.5 Hz, 2H, Ar–**H**), 3.18 (t, J = 6.1 Hz, 4H, N–(C**H**$_2$)$_2$–N), 2.52 (t, J = 6.1 Hz, 4H, N–(C**H**$_2$)$_2$–N), 1.66 (s, 18H, Ar–C(C**H**$_3$)$_3$), 1.33 (s, 18H, Ar–C(C**H**$_3$)$_3$), 0.68 (br, N**H**). ^{13}C-NMR (126 MHz, C_6D_6, 298 K). δ (ppm): 167.2 (N=**C**H), 158.9 (**C**$_{ar}$–OH), 140.2 (**C**$_{ar}$), 137.2 (**C**$_{ar}$), 127.0 (**C**$_{ar}$H), 126.4 (**C**$_{ar}$H), 60.0 (N–(**C**H$_2$)$_2$–N), 50.1 (N–(**C**H$_2$)$_2$–N), 35.5 (C$_{ar}$–**C**(CH$_3$)$_3$), 34.3 (C$_{ar}$–**C**(CH$_3$)$_3$), 31.8 (C$_{ar}$–C(**C**H$_3$)$_3$), 29.8 (C$_{ar}$–C(**C**H$_3$)$_3$). Elemental analysis for $C_{34}H_{53}N_3O_2$ (535.41 g mol^{-1}): Found (Calcd.): C, 76.03 (76.22); H, 10.02 (9.97); N, 7.80 (7.84) %.

- **General procedure 5 – Salan synthesis – C_3 and C_4 backbone ($^{MePr\text{-}b}L_{tBu}H_2$ and $^{Bu\text{-}b}L_{tBu}H_2$)**



$^{MePr\text{-}b}L_{tBu}H_2$ or $^{Bu\text{-}b}L_{tBu}H_2$ (17.1 mmol) was added to a round bottom flask and dissolved in methanol (50 mL). Excess of sodium borohydride (6.5 g, 172.0 mmol) was added slowly (the round bottom flask was placed into an ice bath during the process) and the mixture was stirred during 16 hours at room temperature. Water was slowly added to the system and left stirring for more 16 h. The white precipitate was isolated, washed with water and dried under vacuum. The solid was recrystallized in methanol, washed one more time with water and left drying under vacuum during 48 hours.[11, 12]

$^{MePr\text{-}b}L_{tBu}H_2$: Using general procedure 5, reaction using 9.15 g (17.1 mmol) of $^{MePr\text{-}a}L_{tBu}H_2$ gives the title product as a light yellow powder. Yield: 8.5 g, 15.8 mmol, 92 % yield (before recrystallisation). ^{1}H-NMR (500 MHz, C_6D_6, 298 K). δ (ppm): 11.03 (s, 2H, –O**H**), 7.51 (d, J = 2.5 Hz, 2H, Ar–**H**), 6.97 (d, J = 2.5 Hz, 2H, Ar–**H**), 3.54 (d, J = 4.8 Hz, 4H, Ar–C**H**$_2$–N), 1.95 (d, J = 7.9 Hz, 4H, N–C**H**$_2$-C), 1.72 (s, 18H, Ar–C(C**H**$_3$)$_3$), 1.39 (s, 18H, Ar–C–(C**H**$_3$)$_3$), 0.85 (m, br, 0.85, 2H, N**H**), 0.51 (s, 6H, CH_2–C(C**H**$_3$)$_2$). ^{13}C-NMR (126 MHz, C_6D_6, 298 K). δ (ppm): 155.4 (**C**$_{ar}$–O), 140.8 (**C**$_{ar}$), 136.3 (**C**$_{ar}$), 123.7 (**C**$_{ar}$), 123.2 (**C**$_{ar}$H), 122.6 (**C**$_{ar}$), 57.3 (N–**C**H_2-C), 54.4 (Ar–**C**H_2–N), 35.4 (C_{ar}–**C**$(CH_3)_3$), 34.4 (CH_2–**C**$(CH_3)_2$), 34.1 (C_{ar}–**C**$(CH_3)_3$), 32.0 (C(**C**$H_3)_3$), 30.1 (C(**C**$H_3)_3$) ; 23.9 (CH_2–C(**C**$H_3)_2$). Elemental analysis for $C_{35}H_{58}N_2O_2$ (538.45 g mol^{-1}): Found (Calcd.): C, 78.10 (78.01); H, 10.87 (10.85); N, 5.23 (5.20) %.

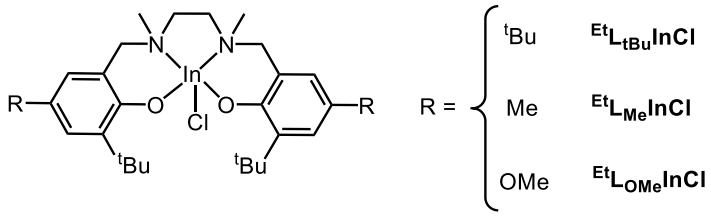
$^{Bu\text{-}b}L_{tBu}H_2$: Using general procedure 5, reaction using 9.0 g (16.8 mmol) of $^{Bu\text{-}a}L_{tBu}H_2$ gives the title product as a yellow powder. Yield = 7.3 g, 13.4 mmol, 80 %. ^{1}H-NMR (500 MHz, C_6D_6, 298 K). δ (ppm): 7.50 (d, J = 2.5 Hz, 2H, Ar–H), 6.95 (d, J = 2.5 Hz, 2H, Ar–H), 3.59 (s, 4H, Ar–C**H**$_2$–N), 2.18–2.14 (m, 4H, N–(C**H**$_2$)$_2$–N), 2.14–2.09 (m, 4H, N–(C**H**$_2$)$_2$–N), 1.72 (s, 18H, Ar–C(C**H**$_3$)$_3$), 1.39 (s, 18H, Ar–C(C**H**$_3$)$_3$). ^{13}C-NMR (126 MHz, C_6D_6, 298 K). δ (ppm): 155.6 (**C**$_{ar}$–OH), 140.6 (**C**$_{ar}$), 136.3 (**C**$_{ar}$), 123.5 (**C**$_{ar}$), 123.1 (**C**$_{ar}$H), 122.6 (**C**$_{ar}$H), 53.6 (Ar–**C**H$_2$–N), 48.4 (N–(**C**H$_2$)$_2$–N), 48.2 (N–(**C**H$_2$)$_2$–N), 35.4 (C_{ar}–**C**(CH$_3$)$_3$), 34.4 (C_{ar}–**C**(CH$_3$)$_3$), 32.1 (C_{ar}–C(**C**H$_3$)$_3$), 30.1 (C_{ar}–C(**C**H$_3$)$_3$). Elemental analysis for $C_{34}H_{57}N_3O_2$ (539.45 g mol^{-1}): Found (Calcd.): C, 75.50 (75.65); H, 10.62 (10.64); N, 7.75 (7.78) %.

6.4.3. Catalyst synthesis

General procedure 6

This procedure was adapted from literature.[18] Pro-ligand (1.36 mmol) was added to a Schlenk and dissolved in THF (20 mL), at 25 °C. $K[N(SiMe_3)_2]$ (0.54 g, 2.71 mmol) was added to the solution and the mixture was stirred during 16 hours and $InCl_3$ (0.30 g, 1.36 mmol) was added. The mixture was stirred for more 16 hours. The solution was filtered and the solvent was removed under reduced pressure to afford the desired catalyst. The product was washed with cold hexane unless specified.

- **$^{Et}L_RInCl$ where R = ^{t}Bu, Me, OMe**

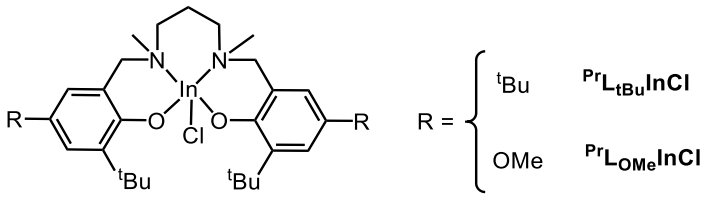


$^{Et}L_{tBu}InCl$: Using general procedure 6, reaction using (0.71 g, 1.36 mmol) $^{Et}L_{tBu}H_2$ gives the title product as a white powder. 64 % yield (0.58 g, 0.87 mmol). ^{1}H-NMR (400 MHz, C_6D_6, 298 K) δ (ppm): ^{1}H-NMR (400 MHz, C_6D_6, 298 K) δ (ppm): 7.68 (d, J = 2.5 Hz, 2H, Ar–**H**), 6.83 (d, J = 2.5 Hz, 2H, Ar–**H**), 4.26 (d, J = 12.1 Hz, 2H, Ar–C**H**$_2$–N), 2.50 (d, J = 12.1, 2H, Ar–C**H**$_2$–N); 2.04-1.95 (m, N–(C**H**$_2$)$_2$–N); 1.72-1.58 (m, N–(C**H**$_2$)$_2$–N); 1.91 (s, 18H, Ar–C(C**H**$_3$)$_3$), 1.79 (s, 6H, N–C**H**$_3$), 1.46 (s, 18H, Ar–C(C**H**$_3$)$_3$). ^{13}C-NMR (126 MHz, C_6D_6, 298 K). δ (ppm): 161.2 (**C**$_{ar}$); 140.4 (**C**$_{ar}$); 138.1 (**C**$_{ar}$); 125.4 (**C**$_{ar}$H); 120.5 (**C**$_{ar}$); 63.9 (Ar–**C**H$_2$–N); 54.7 (N–(**C**H$_2$)$_2$–N); 43.3 (N–**C**H$_3$); 35.9 (C$_{ar}$–**C**(CH$_3$)$_3$); 34.3 (C$_{ar}$–**C**(CH$_3$)$_3$); 32.2 (C(**C**H$_3$)$_3$); 32.0 (C(**C**H$_3$)$_3$). Elemental analysis for $C_{34}H_{54}ClInN_2O_2$ (672.29 g mol^{-1}): Found (Calcd.): C, 60.66 (60.67); H, 8.18 (8.09); N, 4.09 (4.16) %.

$^{Et}L_{Me}InCl$: Using general procedure 6, reaction using (0.60 g, 1.36 mmol) $^{Et}L_{Me}H_2$ gives the title product. 40 % yield (0.32 g, 0.54 mmol). ^{1}H-NMR (500 MHz, C_6D_6, 298 K) δ (ppm): 7.37 (d, J = 2.3 Hz, 2H, Ar–**H**); 6.49 (d, J = 2.3 Hz, 2H, Ar–**H**); 4.21 (d, J = 12.2 Hz, 2H, Ar–C**H**$_2$–N); 2.43 (d, J = 12.2Hz, 2H, Ar–C**H**$_2$–N); 2.35 (s, 6H, N–**C**H$_3$); 2.0 (m, 2H, N–C**H**$_2$); 1.88 (s, 18H, C(C**H**$_3$)$_3$); 1.75 (s, 6H, C_{ar}–C**H**$_3$); 1.61 (m, 2H, N–C**H**$_2$). ^{13}C-NMR (126 MHz, C_6D_6, 298 K). δ (ppm): 161.2 (**C**$_{ar}$–O); 140.8 (**C**$_{ar}$); 129.5 (**C**$_{ar}$); 149.2 (**C**$_{ar}$); 128.6 (**C**$_{ar}$); 124.5 (**C**$_{ar}$–H); 121.1 (**C**$_{ar}$–H); 63.5 (Ar–**C**H$_2$–N); 54.8 (N–(**C**H$_2$)$_2$–N); 43.3 (N–**C**H$_3$); 35.6 (C_{ar}–**C**–(CH$_3$)$_3$); 30.3 (C–(**C**H$_3$)$_3$); 21.2 (C_{ar}–**C**H$_3$). Elemental analysis for $C_{28}H_{42}ClInN_2O_2$ (588.20 g mol^{-1}): Found (Calcd.): C, 57.83 (57.11); H, 7.59 (7.19); N, 4.51 (4.76) %.

$^{Et}L_{OMe}InCl$: Using general procedure 6, reaction using (0.64 g, 1.36 mmol) $^{Et}L_{OMe}H_2$ gives the title product. 60 % yield (0.50 g, 0.82 mmol): ^{1}H-NMR (500 MHz, C_6D_6, 298 K) δ (ppm): 7.28 (d, J = 3.1 Hz, 2H, Ar–**H**); 6.40 (d, J = 3.1 Hz, 2H, Ar–**H**); 4.20 (d, J = 12.2 Hz, 2H, Ar–C**H**$_2$–N); 3.60 (s, 6H, O–C**H**$_3$); 2.37 (d, J = 12.2 Hz, 2H, Ar–C**H**$_2$–N); 1.93 (m, 4H, N–C**H**$_2$–CH$_2$–C**H**$_2$); 1.86 (s, 18H, Ar–C(C**H**$_3$)$_3$); 1.74 (s, 6H, N–C**H**$_3$); 1.57 (m, 2H, N–CH$_2$–C**H**$_2$–CH$_2$). ^{13}C-NMR (126 MHz, C_6D_6, 298 K). δ (ppm): 157.6 (**C**$_{ar}$–O); 150.8 (**C**$_{ar}$–OCH$_3$); 142.1 (**C**$_{ar}$); 121.0 (**C**$_{ar}$); 114.8 (**C**$_{ar}$–H); 114.2 (**C**$_{ar}$–H); 63.4 (Ar–**C**H$_2$–N); 55.5 (N–(**C**H$_2$)$_2$–N); 54.6 (Ar–O**C**H$_3$); 43.3 (N–**C**H$_3$); 35.9 (**C**(CH$_3$)$_3$); 30.1 (C(**C**H$_3$)$_3$). Elemental analysis for $C_{28}H_{42}ClInN_2O_4$ (620.19 g mol^{-1}): Found (Calcd.): C, 54.29 (54.16); H, 6.95 (6.82); N, 4.41 (4.51) %.

- **$^{Pr}L_xInCl$ where X = ^{t}Bu, OMe**

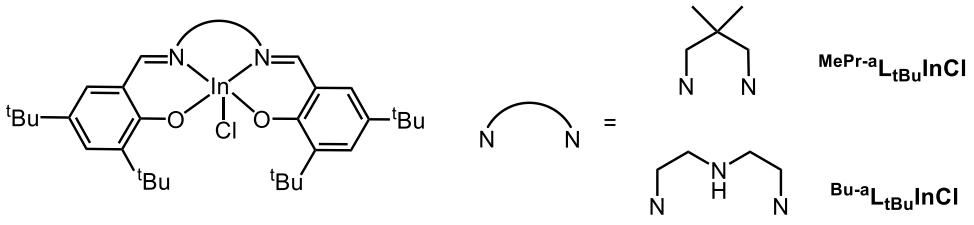


$^{Pr}L_{tBu}InCl$: Using general procedure 6, reaction using (0.73 g, 1.36 mmol) $^{Pr}L_{tBu}H_2$, gives the title product as a white powder. The product was washed with cold hexane and further crystalized using a mixture of THF and hexane held at -40 °C over 5 days. Yield: 0.60 g, 0.87 mmol, 64%. ^{1}H-NMR (500 MHz, C_6D_6, 298 K) δ (ppm): 7.67 (d, J = 2.5 Hz, 2H, Ar–**H**); 6.76 (d, J = 2.5 Hz, 2H, Ar–**H**); 5.04 and 2.89 (d, J = 13.8 Hz, 2H, Ar–C**H**$_2$–N), 4.24 and 2.64 (d, J = 12.8 Hz, 2H, Ar–C**H**$_2$–N), 3.62 (THF), 2.38–2.24 (m, 2H, N–C**H**$_2$–CH$_2$–C**H**$_2$), 1.91 (s, 18H, Ar–C(C**H**$_3$)$_3$); 1.89 (s, 6H, N–C**H**$_3$); 1.45 (s, 18H, Ar–C(C**H**$_3$)$_3$), 1.41 (THF), 1.12–1.02 (m, 2H, N–CH$_2$–C**H**$_2$–CH$_2$), 0.95-0.88 and 0.40-0.31 (m, 2H, N–C**H**$_2$–CH$_2$–C**H**$_2$). ^{13}C-NMR (126 MHz, C_6D_6, 298 K). δ (ppm): 162.1 (**C**$_{ar}$); 139.9 (**C**$_{ar}$); 137.4 (**C**$_{ar}$); 128.4 (**C**$_{ar}$); 125.3 (**C**$_{ar}$H); 125.2 (**C**$_{ar}$H); 124.9 (**C**$_{ar}$); 124.8 (**C**$_{ar}$); 124.7 (**C**$_{ar}$); 119.8 (**C**$_{ar}$); 119.7 (**C**$_{ar}$); 118.6 (**C**$_{ar}$); 68.1 (THF); 67.0 (C$_{ar}$–**C**H$_2$–N); 60.6 (N–**C**H$_2$–CH$_2$–**C**H$_2$); 59.5 (N–**C**H$_2$–CH$_2$–**C**H$_2$); 44.4 (N–**C**H$_3$), 35.9 (**C**(CH$_3$)$_3$); 34.3 (**C**(CH$_3$)$_3$); 32.3 (C(**C**H$_3$)$_3$); 30.5 (C(**C**H$_3$)$_3$); 25.8 (THF); 21.0 (N–CH$_2$–**C**H$_2$–CH$_2$). Elemental analysis for $C_{35}H_{56}ClInN_2O_2$·C_4H_7O·KCl ($^{Pr}L_{tBu}$InCl·THF and KCl): Found (Calcd.): C, 56.53 (56.25); H, 7.94 (7.63); N, 3.55 (3.36) %. MS (MALDI-ToF): m/z 651.37 [$^{Pr}L_{tBu}In$]$^+$.

$^{Pr}L_{OMe}InCl$: Using general procedure 6, reaction using (0.66 g, 1.36 mmol) $^{Pr}L_{OMe}H_2$, gives the title product. 30 % yield (0.26 g, 0.41 mmol). ^{1}H-NMR (500 MHz, C_6D_6, 298 K) δ (ppm): 7.27 (d, J = 3.2 Hz, 2H, Ar–**H**); 6.40 (d, J = 3.2 Hz, 2H, Ar–**H**); 3.69 (THF); 3.61 (s, 6H, O–C**H**$_3$); 3.18 and 2.71 (br, Ar–C**H**$_2$–N); 2.45 (t, J = 12.4 Hz, 2H, N–C**H**$_2$–CH$_2$) ;

1.93 (s, 6H, N–C**H**$_3$); 1.83 and 1.72 (s, 18H, Ar–C(C**H**$_3$)$_3$); 1.46 (br, N–C**H**$_2$–CH$_2$); 1.42 (THF). ^{13}C-NMR (126 MHz, C_6D_6, 298 K). δ (ppm): 158.5 (**C**$_{ar}$–O); 150.4 (**C**$_{ar}$–O(CH$_3$)) ; 141.4 (**C**$_{ar}$); 120.5 (**C**$_{ar}$); 114.8 (**C**$_{ar}$–H); 114.0 (**C**$_{ar}$–H) ; 66.4 (C$_{ar}$–**C**H$_2$–N) ; 60.0 (N–**C**H$_2$–CH$_2$–**C**H$_2$); 55.7 (O–**C**H$_3$); 44.7 (N–**C**H$_3$); 35.8 (C$_{ar}$–**C**(CH$_3$)$_3$); 30.2 (C(**C**H$_3$)$_3$). Elemental analysis for $C_{29}H_{44}ClInN_2O_4$ (634.20 g mol^{-1}): Found (Calcd.): C, 55.57 (54.86); H, 7.15 (6.99); N, 4.33 (4.41) %.

- **$^{MePr\text{-}a}L_{tBu}InCl$ and $^{Bu\text{-}a}L_{tBu}InCl$**

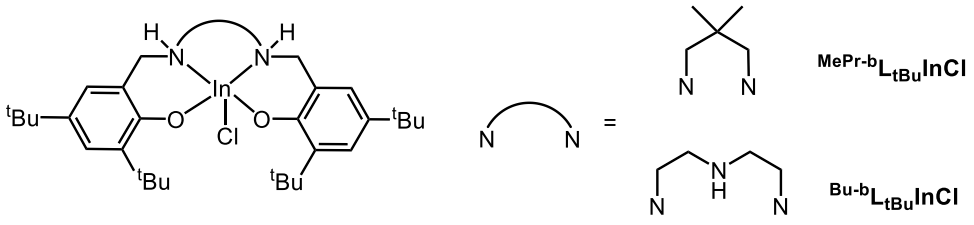


$^{MePr\text{-}a}L_{tBu}InCl: Using general procedure 6, reaction using (0.73 g, 1.36 mmol) $^{MePr\text{-}a}L_{tBu}H_2$, gives the title product as a yellow powder. 53 % yield (0.49 g, 0.72 mmol). ^{1}H-NMR (500 MHz, C_6D_6, 298 K). δ (ppm): 7.74 (d, J = 2.7 Hz, 2H, C$_{ar}$–**H**); 7.34 (s, 2H, N=C**H**); 6.79 (d, J = 2.7 Hz, 2H, C$_{ar}$–**H**); 3.63 (d, J = 13.0 Hz, 2H, N–C**H**$_2$–C); 2.31 (d, J = 13.0 Hz, 2H, N–C**H**$_2$–C); 1.79 (s, 18H, C(C**H**$_3$)$_3$); 1.37 (s, 18H, C(C**H**$_3$)$_3$); 0.47 (s, 3H, C(C**H**$_3$)$_2$), 0.35 (s, 3H, C(C**H**$_3$)$_2$). ^{13}C-NMR (126 MHz, C_6D_6, 298 K). δ (ppm): 174.8 (N=**C**H); 169.8 (**C**$_{ar}$–O); 143.0 (**C**$_{ar}$); 137.5 (**C**$_{ar}$); 131.1 (**C**$_{ar}$–H); 130.0 (**C**$_{ar}$–H); 117.3 (**C**$_{ar}$); 73.9 (N–**C**H$_2$–C(CH$_3$)$_2$–**C**H$_2$); 36.2 (CH$_2$(**C**(CH$_3$)$_2$CH$_2$); 34.6 (C$_{ar}$–**C**(CH$_3$)$_3$); 34.1 (C$_{ar}$–**C**(CH$_3$)$_3$); 31.6 (C(**C**H$_3$)$_3$); 30.3 (C(**C**H$_3$)$_3$); 26.6 (C(**C**H$_3$)$_2$); 21.2 (C(**C**H$_3$)$_2$). Elemental analysis for $C_{35}H_{52}ClInN_2O_2$ (682.28 g mol^{-1}): Found (Calcd.): C, 61.45 (61.54); H, 7.50 (7.67); N, 4.00 (4.10) %.

$^{Bu\text{-}a}L_{tBu}InCl: Using general procedure 6, reaction using (0.73 g, 1.36 mmol) $^{Bu\text{-}a}L_{tBu}H_2$, gives the title product as a yellow powder. 40 % yield (0.37 g, 0.54 mmol). ^{1}H-NMR

(500 MHz, $CDCl_3$, 298 K). δ (ppm): 8.23 (s, 2H, C**H**=N) ; 7.36 (d, J = 2.7 Hz, Ar–**H**); 6.83 (d, J = 2.7 Hz, Ar–**H**); 3.80–3.63 (br, N–C**H**$_2$–CH_2); 3.51 (br, N–CH_2–C**H**$_2$); 3.01 (br, N–CH_2–C**H**$_2$); 1.44 (br, C(C**H**$_3$)$_3$); 1.25 (br, C(C**H**$_3$)$_3$), 1.22 (br, C(C**H**$_3$)$_3$), 1.04 (br, C(C**H**$_3$)$_3$). ^{13}C-NMR (126 MHz, C_6D_6, 298 K). δ (ppm): 171.4 (**C**$_{ar}$); 170.6 (**C**$_{ar}$); 169.1 (**C**$_{ar}$); 142.1 (**C**$_{ar}$); 136.0 (**C**$_{ar}$); 129.8 (**C**$_{ar}$H); 128.0 (**C**$_{ar}$H); 117.2 (**C**$_{ar}$); 54.4 (N–**C**H_2–CH_2) ; 48.8 (N–CH_2–**C**H_2); 35.3 (**C**(CH_3)$_3$); 33.8 (**C**(CH_3)$_3$); 31.3 (C(**C**H_3)$_3$); 29.6 (C(**C**H_3)$_3$).

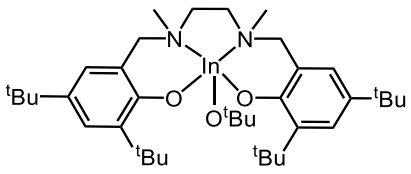
- **$^{MePr\text{-}b}L_{tBu}InCl$ and $^{Bu\text{-}b}L_{tBu}InCl$**



$^{MePr\text{-}b}L_{tBu}InCl$: Using general procedure 6, reaction using 0.50 g (0.93 mmol) of $^{MePr\text{-}b}L_{tBu}H_2$, gives the title product as an off-white powder. 58 % yield (0.37 g, 0.54 mmol) ^{1}H-NMR (500 MHz, Toluene-d_8, 298 K). δ (ppm): 7.47 (d, J = 2.6 Hz, 1H, C_{ar}–**H**); 7.43 (d, J = 2.7 Hz, 1H, C_{ar}–**H**); 7.20 (d, J = 2.6 Hz, 1H, C_{ar}–**H**); 6.90 (d, J = 2.7 Hz, 1H, C_{ar}–**H**); 4.75 (d, J = 13.0 Hz, 1H, Ar–C**H**$_2$–N); 4.65 (d, J = 11.0 Hz, 1H, Ar–C**H**$_2$–N); 3.95 (d, J = 11.0 Hz, 1H, Ar–C**H**$_2$–N); 3.48 (d, J = 13.0 Hz, Ar–C**H**$_2$–N); 3.32 (d, J = 13.8 Hz, 1H, N–C**H**$_2$–C); 3.24 (d, J = 13.8 Hz, 1H, N–C**H**$_2$–C); 3.06 (d, J = 12.5 Hz, 1H, N–C**H**$_2$–C); 2.57 (d, J = 12.5 Hz, 1H, N–C**H**$_2$–C); 1.81 (s, 9H, C(C**H**$_3$)$_3$); 1.49 (s, 9H, C(C**H**$_3$)$_3$)); 1.46 (s, 9H, C(C**H**$_3$)$_3$); 1.30 (s, 9H, C(C**H**$_3$)$_3$); 1.23 (s, 3H, C(C**H**$_3$)$_2$); 0.86 (s, 3H, C(C**H**$_3$)$_2$). ^{13}C-NMR (126 MHz, Toluene-d_8, 298 K). δ (ppm): 164.6 (**C**$_{ar}$–O); 164.0 (**C**$_{ar}$–O); 139.4 (**C**$_{ar}$); 138.3 (**C**$_{ar}$); 137.2 (**C**$_{ar}$); 135.3 (**C**$_{ar}$); 127.3 (**C**$_{ar}$–H); 125.8 (**C**$_{ar}$–H); 124.7 (**C**$_{ar}$–H); 122.5 (**C**$_{ar}$–H); 72.7 (N–**C**H_2–C); 66.9 (C_{ar}–**C**H_2–N); 65.6 (N–**C**H_2–C); 60.0 (C_{ar}–**C**H_2–N); 39.4 (**C**(CH_3)$_2$); 36.5 (**C**(CH_3)$_3$); 35.9 (**C**(CH_3)$_3$); 34.6 (**C**(CH_3)$_3$); 34.5 (**C**(CH_3)$_3$); 32.8 (C(**C**H_3)$_3$); 32.3 (C(**C**H_3)$_3$); 32.1 (C(**C**H_3)$_3$); 31.5 (C(**C**H_3)$_3$); 31.1 (C(**C**H_3)$_2$); 30.3 (C(**C**H_3)$_2$).

$^{Bu\text{-}b}L_{tBu}InCl$: Using general procedure 6, reaction using 0.44 g (0.82 mmol) of $^{Bu\text{-}b}L_{tBu}H_2$, gives the title product. 32 % yield (0.18 g, 0.27 mmol). The NMR experiments were made at low temperature (-25 °C / 248 K). ^{1}H-NMR (500 MHz, Toluene-d_8, 248 K). δ (ppm): 7.55 (s, 2H, C_{ar}–**H**); 6.58 (s, 2H, C_{ar}–**H**); 5.19 (d, J = 12.5 Hz, 2H, Ar-C**H**$_2$–N); 3.82 (N**H**); 2.99 (br, 2H, N–CH_2C**H**$_2$–N); 2.91 (d, J = 12.5, 2H, Ar-C**H**$_2$–N); 2.03 (br, N–CH_2C**H**$_2$–N); 1.79 (s, 18H, C(C**H**$_3$)$_3$); 1.65 (br, N–C**H**$_2$$CH_2$–N); 1.48 (br, N–C**H**$_2$$CH_2$–N); 1.39 (s, 18H, C(C**H**$_3$)$_3$); ^{13}C-NMR (126 MHz, C_6D_6, 248 K). δ (ppm): 163.2 (**C**$_{ar}$); 137.80 (**C**$_{ar}$); 126.1 (**C**$_{ar}$–H); 125.7 (**C**$_{ar}$); 123.3 (**C**$_{ar}$–H); 121.1 (**C**$_{ar}$); 52.5 (C_{ar}-**C**H_2–N); 43.7 (N–**C**$H_2$$CH_2$–N); 42.0 (N–$CH_2$**C**$H_2$–N); 36.6 (**C**(C$H_3$)$_3$); 34.5 (**C**(C$H_3$)$_3$); 32.6 (C(**C**$H_3$)$_3$); 31.3 (C(**C**$H_3$)$_3$).

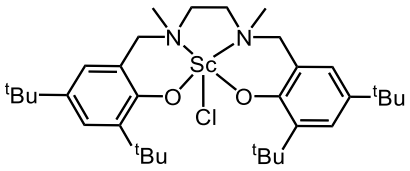
- **Catalyst synthesis ($^{Et}L_{tBu}InO^tBu$)**



The complex $^{Et}L_{tBu}$InCl (0.30 g, 0.45 mmol) was added to a Schlenk and dissolved in THF. KO^{t}Bu (0.051 g, 0.45 mmol) was added and the mixture was stirred for 4 hours. The solution was filtered and the solvent was removed under vacuum to obtain $^{Et}L_{tBu}$InO^{t}Bu with 60 % yield (0.20 g, 0.27 mmol). ^{1}H-NMR (400 MHz, C_6D_6, 298 K) δ (ppm): 7.66 (d, J = 2.6 Hz, 2H, Ar–**H**), 6.83 (d, J = 2.6 Hz, 2H, Ar–**H**), 3.97 (d, J = 12.3 Hz, 2H, Ar–C**H**$_2$–N), 2.62(d, J = 12.3 Hz, 2H, Ar–C**H**$_2$–N), 2.05 (s, 6H, CH_2–N(C**H**$_3$)–CH_2), 1.74 (t, J = 10.8 Hz, 4H, N–C**H$_2$C H$_2$**); 1.86 (s, 18H, Ar–C(C**H**$_3$)$_3$), 1.46 (s, 18H, Ar–C(C**H**$_3$)$_3$), 1.40 (br, O–C(C**H**$_3$)$_3$). ^{13}C-NMR (126 MHz, C_6D_6, 298 K). δ (ppm): 161.7 (**C**$_{ar}$); 139.0 (**C**$_{ar}$); 138.4 (**C**$_{ar}$); 125.0 (**C**$_{ar}$); 124.8 (**C**$_{ar}$H); 124.5 (**C**$_{ar}$H); 63.5 (Ar–**C**H_2–N); 50.7 (**C**(CH_3)$_3$); 47.7 (N–**C**H_2**C**H_2–N); 43.1 (N–**C**H_3); 40.6 (C(**C**H_3)$_3$); 33.0 (**C**(CH_3)$_3$);

31.4 (O–C(**C**H_3)$_3$); 30.3 (C(**C**H_3)$_3$). Elemental analysis for $C_{38}H_{63}InN_2O_3$ (710.39 g mol^{-1}): Found (Calcd.): C, 64.15 (64.22); H, 8.77 (8.93); N, 3.95 (3.94) %.

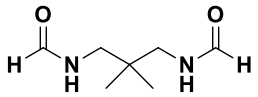
- **Catalyst synthesis ($^{Et}L_{tBu}ScCl$)**



This procedure was adapted from literature.[18] The ligand $^{Et}L_{tBu}H_2$ (0.71 g, 1.36 mmol) was added to a Schlenk and dissolved in THF (20 mL), at 25 °C. K[N(SiMe$_3$)$_2$] (0.54 g, 2.71 mmol) was added to the solution and the mixture was stirred during 16 hours and then $ScCl_3$ (0.21 mg, 1.36 mmol) was added. The mixture was stirred for 16 hours. The solution was filtrated and the solvent was removed under reduced pressure, the solid was washed with cold hexane to afford the complex $^{Et}L_{tBu}ScCl$ with 30 % yield (0.25 g, 0.41 mmol). ^{1}H-NMR (400 MHz, C_6D_6, 298 K) δ (ppm): 7.59 (d, J = 2.6 Hz, 1H, Ar–**H**), 7.53 (d, J = 2.6 Hz, 1H, Ar–**H**); 7.03 (d, J = 2.6 Hz, 1H, Ar–**H**), 6.92 (d, J = 2.6 Hz, 1H, Ar–**H**); 5.02 (d, J = 13.0 Hz, 1H, Ar–C**H**$_2$–N), 4.59 (d, J = 13.3 Hz, 1H, Ar–C**H**$_2$–N), 3.05 (d, J = 13.3 Hz, 1H, Ar–C**H**$_2$–N), 2.88-2.78 (m, 2H, N–C**H**$_2$–C**H**$_2$), 2.74 (d, J = 13.0 Hz, 1H, Ar–C**H**$_2$–N); 1.31 (s, 2H, N–C**H**$_2$–C**H**$_2$), 2.58 (s, 3H, N–C**H**$_3$), 1.79 (s, 9H, Ar–C(C**H**$_3$)$_3$), 1.68 (s, 3H, N–C**H**$_3$), 1.54 (s, 9H, Ar–C(C**H**$_3$)$_3$), 1.38 (s, 9H, Ar–C(C**H**$_3$)$_3$), 1.35 (s, 9H, Ar–C(C**H**$_3$)$_3$). ^{13}C-NMR (126 MHz, C_6D_6, 298 K) δ (ppm): 159.9 (**C**$_{ar}$–O); 159.3 (**C**$_{ar}$–O); 139.0 (**C**$_{ar}$); 138.0 (**C**$_{ar}$); 136.7 (**C**$_{ar}$); 136.3 (**C**$_{ar}$); 128.4 (**C**$_{ar}$); 125.5 (**C**$_{ar}$H); 124.8 (**C**$_{ar}$H); 124.7 (**C**$_{ar}$H); 124.6 (**C**$_{ar}$H); 124.4 (**C**$_{ar}$), 66.0(Ar–**C**H$_2$–N) ; 64.6 (Ar–**C**H$_2$–N); 56.6 (N–**C**H$_2$CH$_2$); 52.0 (N–CH$_2$**C**H$_2$); 51.2 (N–**C**H$_3$); 42.0 (N–**C**H$_3$); 36.0 (C$_{ar}$–**C**(CH$_3$)$_3$); 35.6 (C$_{ar}$–**C**(CH$_3$)$_3$); 34.3 (C$_{ar}$–**C**(CH$_3$)$_3$); 34.2 (C$_{ar}$–**C**(CH$_3$)$_3$); 32.1 (C(**C**H$_3$)$_3$); 32.0 (C(**C**H$_3$)$_3$); 31.6 (C(**C**H$_3$)$_3$); 30.3 (C(**C**H$_3$)$_3$). MS (MALDI-ToF): m/z 567.41 [$^{Et}L_{tBu}Sc$]$^+$.

6.4.4. Synthesis of *N,N'*-Dimethyl-2,2-dimethylpropane-1,3-diamine

This synthesis was adapted from the literature.[13, 14]



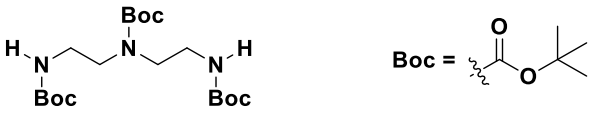
18 mL (0.15 mol) of 2,2-dimethyl-1,3-propanediamine was added to 59 mL (0.96 mol) of methyl formate (HCOOMe) at neat conditions and the mixture was refluxed for 16 h. The volatile were removed under vacuum and the residue was scratched with hexane. The product was further recrystalised from a mixture of hexane and acetone to access yellow crystals (C1). Yield: 89 % (21 g, 0.13 mol). ^{1}H-NMR (400 MHz, C_6D_6, 298 K) δ (ppm): 7.68 (s, 2H, C**H**=O); 5.51 (br, 2H, N**H**); 2.67 (d, J = 6.9 Hz, 4H, N–C**H**$_2$–C); 0.51 (s, 6H, C(C**H**$_3$)$_2$). ^{13}C-NMR (100 MHz, C_6D_6, 298 K). δ (ppm): 160.3 (**C**H=O); 43.1 (N–**C**H$_2$–C); 35.1 (**C**(CH$_3$)$_2$); 22.5 (C(**C**H$_3$)$_2$).



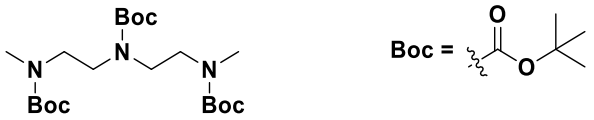
The diamine C1 (9.88 g, 62.5 mmol) was added in small portions, and slowly, to a mixture of $LiAlH_4$ (10 g, 263.5 mmol) in 250 mL of Et_2O at 0 °C. After the addition was finished, the reaction was left stirred at room temperature during 20 h. The mixture was then slowly hydrolysed with a mixture of Et_2O and H_2O (the round bottom flask was placed into an ice bath during the process) and the white solid was removed by filtration (through Celite) and the filtrate was dried over $MgSO_4$, filtered and the volatiles were removed under vacuum to afford a pale yellow oil (d = 0.82 g mL^{-1}) with 25 % yield (2.03 g, 15.6 mmol). ^{1}H-NMR (400 MHz, C_6D_6, 298 K) δ (ppm): 5.3 (br, N**H**); 2.29 (s, 4H, N–C**H**$_2$–C); 2.26 (s, 6H, N–C**H**$_3$); 0.88 (s, 6H, C(C**H**$_3$)$_2$). ^{13}C-NMR (100 MHz,

C_6D_6, 298 K). δ (ppm): 62.1 (N–**C**H_2–C); 37.1 (N–**C**H_3); 35.4 (**C**$(CH_3)_2$); 24.0 (C(**C**$H_3)_2$). Data is in accordance with the literature.[13, 14]

6.4.5. Synthesis of *N*-Methyl-*N'*-[2-(methylamino)ethyl]-1,2-ethanediamine

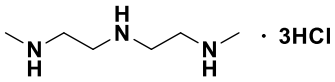


The synthesis was performed following a procedure adapted from the literature.[15-17] Di-*tert*-butyldicarbonate (7.3 g, 33 mmol) was added to a mixture of diethylenetriamine 1.02 g (1.07 mL, 9.90 mmol) in methanol (15 mL) and the system was left stirring during 72 h. After this time water was added to the system and the product was extracted with ether, washed with brine and dried over $MgSO_4$. The volatiles were removed under vacuum to afford a white powder P1 (oil that crystallises at room temperature) with 87 % yield (3.5 g, 8.61 mmol). ^{1}H-NMR (400 MHz, $CDCl_3$, 298 K) δ (ppm): 5.02 and 4.94 (s, br, 2H, N**H**); 3.39–3.17 (m, 8H, N–(C**H**$_2)_2$–N); 1.47 (s, 9H, O–C(C**H**$_3)_3$); 1.42 (s, br, 18H, O–C(C**H**$_3)_3$). ^{13}C-NMR (100 MHz, $CDCl_3$, 298 K) δ (ppm): 156.0 (**C**H=O); 46.9 (N–(**C**$H_2)_2$–N); 39.2 (N–(**C**$H_2)_2$–N); 28.2 (C(**C**$H_3)_3$); 26.5 (**C**$(CH_3)_3$).



A solution of P1 in dry DMF was added slowly and under N_2 atmosphere to a suspension of NaH also in dry DMF (the round bottom flask was placed into an ice bath during the process). The mixture was stirred during 1 h at room temperature and then methyl iodide was added dropwise. After 16h the reaction was slowly quenched with water (the round bottom flask was placed into an ice bath during the process) and the

product was extracted into DCM and washed with brine. The crude product was purified with column chromatography using a mixture of 30 % ethyl acetate/hexane as the eluent to access a clear and viscous oil (P2). ^{1}H-NMR (400 MHz, $CDCl_3$, 298 K) δ (ppm): 3.32 (d, J = 15.4 Hz, 8H, N–(C**H**$_2$)$_2$–N); 2.87 (s, 6H, N–C**H**$_3$); 1.45 and 1.44 (s, br, 27H, O–C(C**H**$_3$)$_3$).



1.20 g (2.78 mmol) of P2 was dissolved in ethanol and 2 м HCl (8 mL) in ether was added. The system was stirred for 5 h and the white precipitate was filtered and dried under vacuum to access the desired product with 90 % yield (0.33 g, 2.50 mmol). ^{1}H-NMR (400 MHz, D_2O, 298 K) δ (ppm): 3.57–3.52 (m, 4H, N–(C**H**$_2$)$_2$–N); 3.50–3.46 (m, 4H, N–(C**H**$_2$)$_2$–N); 2.83 (s, 6H, N–C**H**$_3$). ^{13}C-NMR (100 MHz, D_2O, 298 K) δ (ppm): 44.2 (N–(**C**H$_2$)$_2$–N); 43.5 (N–(**C**H$_2$)$_2$–N); 32.9 (N–**C**H$_3$). Data is in accordance with the literature.[15]

6.5. References

1. Thevenon, A.; Garden, J. A.; White, A. J. P.; Williams, C. K., Dinuclear Zinc Salen Catalysts for the Ring Opening Copolymerization of Epoxides and Carbon Dioxide or Anhydrides. *Inorg. Chem.* **2015,** *54* (24), 11906-11915.
2. Bain, G. A.; Berry, J. F., Diamagnetic Corrections and Pascal's Constants. *J. Chem. Edu.* **2008,** *85* (4), 532.
3. Garden, J. A.; Saini, P. K.; Williams, C. K., Greater than the Sum of Its Parts: A Heterodinuclear Polymerization Catalyst. *J. Am. Chem. Soc.* **2015,** *137* (48), 15078-15081.
4. Trott, G.; Garden, J. A.; Williams, C. K., Heterodinuclear zinc and magnesium catalysts for epoxide/CO_2 ring opening copolymerizations. *Chem. Sci.* **2019,** *10* (17), 4618-4627.
5. Deacy, A. C.; Kilpatrick, A. F. R.; Regoutz, A.; Williams, C. K., Understanding metal synergy in heterodinuclear catalysts for the copolymerization of CO_2 and epoxides. *Nat. Chem.* **2020,** *12* (4), 372-380.
6. Deacy, A. C.; Durr, C. B.; Garden, J. A.; White, A. J. P.; Williams, C. K., Groups 1, 2 and Zn(II) Heterodinuclear Catalysts for Epoxide/CO_2 Ring-Opening Copolymerization. *Inorg. Chem.* **2018,** *57* (24), 15575-15583.
7. Schneider, F.; Zhao, T.; Huhn, T., Cytotoxic heteroleptic heptacoordinate salan zirconium(IV)-bis-chelates-synthesis, aqueous stability and X-ray structure analysis. *Chem. Comm.* **2016,** *52*, 10151-10154.
8. Morris, G. A.; Zhou, H.; Stern, C. L.; Nguyen, S. T., A general high-yield route to bis (salicylaldimine) zinc (II) complexes: Application to the synthesis of pyridine-modified salen-type zinc (II) complexes. *Inorg. Chem.* **2001,** *40* (13), 3222-3227.
9. Herrmann, W. A.; Rauch, M. U.; Artus, G. R. J., Multiple Bonds between Main Group Elements and Transition Metals. 153.1 Rhenium (V) Oxo Complexes with Tetradentate Schiff Bases: Structural Considerations. *Inorg. Chem.* **1996,** *35* (7), 1988-1991.
10. Lazar, A.; Thiel, W. R.; Singh, A. P., Synthesis and characterization of 3-[N,N′-bis-3-(salicylidenamino)ethyltriamine] Mo(vi)O2@SBA-15: a highly stable and reusable catalyst for epoxidation and sulfoxidation reactions. *RSC Advances* **2014,** *4* (27), 14063-14073.
11. Thevenon, A.; Garden, J. A.; White, A. J. P.; Williams, C. K., Dinuclear Zinc Salen Catalysts for the Ring Opening Copolymerization of Epoxides and Carbon Dioxide or Anhydrides. *Inorg. Chem.* **2015,** *54*, 11906-11915.
12. Yeori, A.; Goldberg, I.; Shuster, M.; Kol, M., Diastereomerically-specific zirconium complexes of chiral salan ligands: isospecific polymerization of 1-hexene and 4-methyl-1-pentene and cyclopolymerization of 1, 5-hexadiene. *J. Am. Chem. Soc.* **2006,** *128* (40), 13062-13063.
13. Qian, F.; McCusker, J. E.; Zhang, Y.; Main, A. D.; Chlebowski, M.; Kokka, M.; McElwee-White, L., Catalytic Oxidative Carbonylation of Primary and Secondary Diamines to Cyclic Ureas. Optimization and Substituent Studies. *J. Org. Chem.* **2002,** *67* (12), 4086-4092.
14. Betschart, C.; Schmidt, B.; Seebach, D., Anwendungsbreite der reduktiven Kupplung aromatischer Aldimin-Derivate mit niedervalenten Titan-Reagenzien zu 1,2-Diarylethylendiaminen. *Helv. Chim. Acta* **1988,** *71* (8), 1999-2021.

15. Truong, T.-T.; Coates, G. W.; Abruña, H. D., High power organic cathodes using thin films of electropolymerized benzidine polymers. *Chem. Comm.* **2015,** *51* (78), 14674-14677.
16. Edwards, M. L.; Prakash, N. J.; Stemerick, D. M.; Sunkara, S. P.; Bitonti, A. J.; Davis, G. F.; Dumont, J. A.; Bey, P., Polyamine analogs with antitumor activity. *J. Med. Chem.* **1990,** *33* (5), 1369-1375.
17. Larsson, P.-F.; Astvik, P.; Norrby, P.-O., New efficient ligand for sub-mol % copper-catalyzed C–N cross-coupling reactions running under air. *Beilstein J. Org. Chem.* **2012,** *8*, 1909-1915.
18. Thevenon, A.; Cyriac, A.; Myers, D.; White, A. J. P.; Durr, C. B.; Williams, C. K., Indium Catalysts for Low-Pressure CO_2/Epoxide Ring-Opening Copolymerization: Evidence for a Mononuclear Mechanism? *J. Am. Chem. Soc*. **2018**, 140, 6893-6903.

Chapter 7

Appendices

7.1. Chapter 3

7.1.1. SQUID Magnetometry

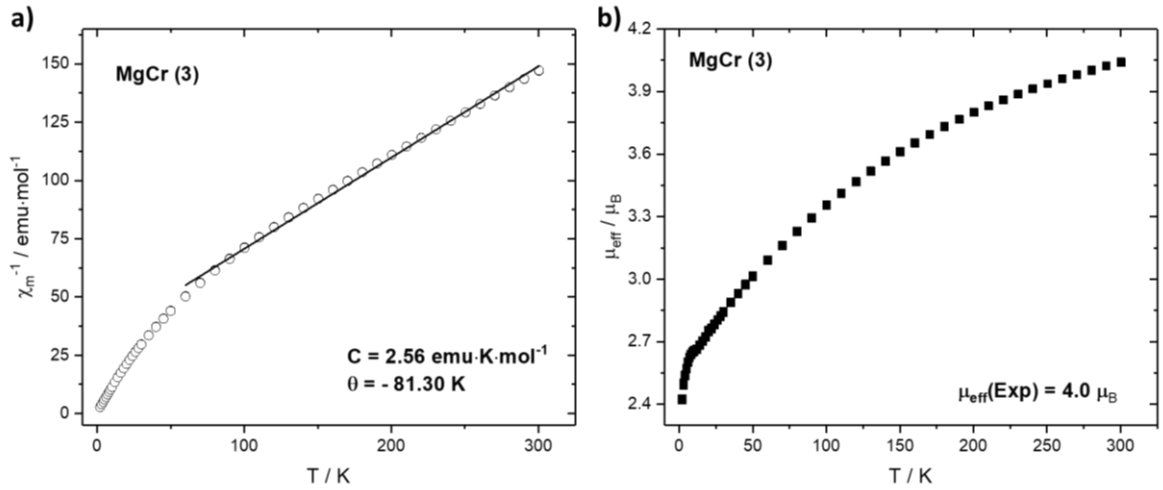


Figure A.1. Magnetic data for complex **3** (MgCr) a) Inverse of molar susceptibility *vs*. temperature, ∘ experimental data, – fitting of the curve (fitting 60 – 300 K). b) Effective magnetic moment *vs.* temperature graph.

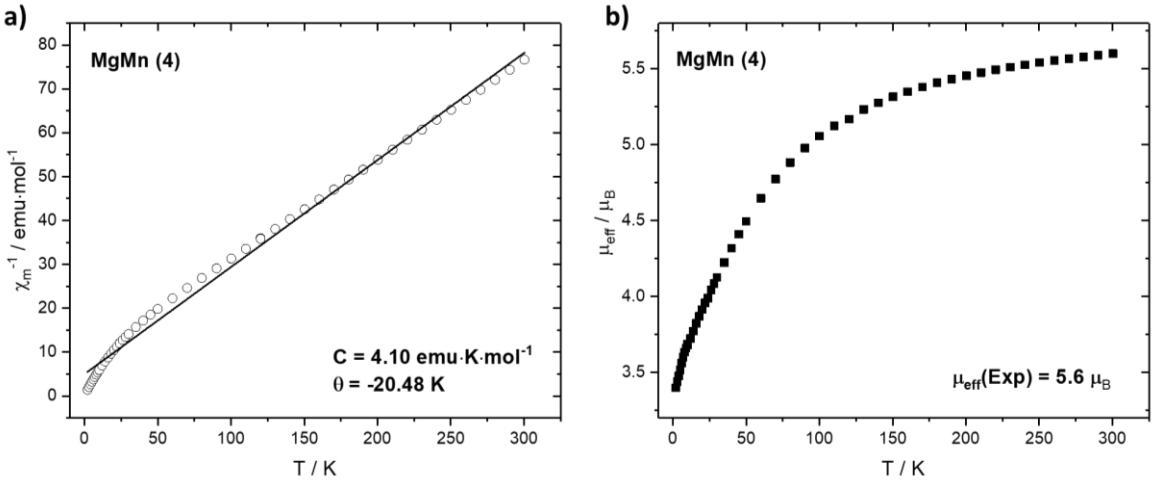


Figure A.2. Magnetic data for complex **4** (MgMn) a) Inverse of molar susceptibility *vs*. temperature, ∘ experimental data, – fitting of the curve. b) Effective magnetic moment *vs.* temperature graph.

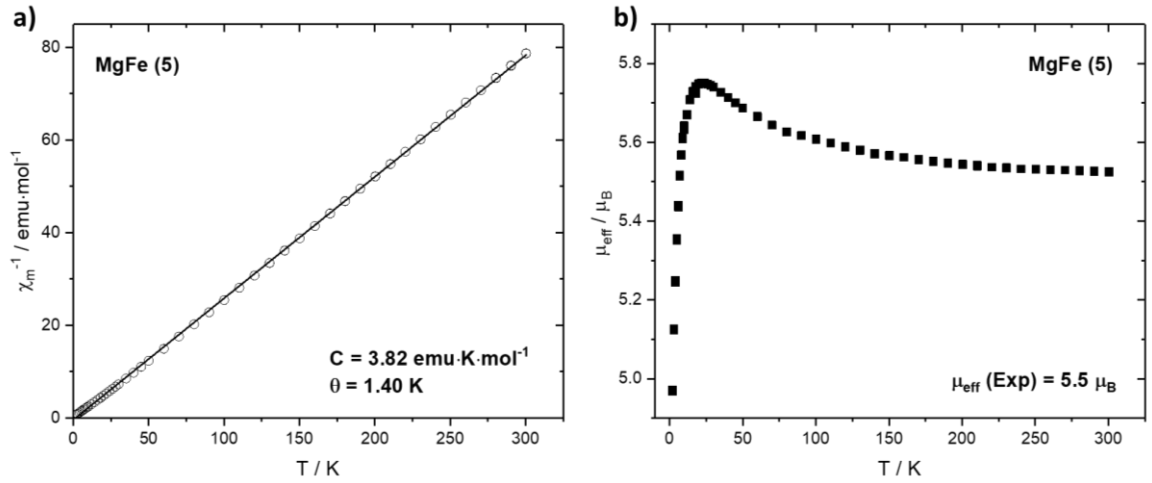


Figure A.3. Magnetic data for complex **5** (MgFe) a) Inverse of molar susceptibility *vs*. temperature, ∘ experimental data, – fitting of the curve. b) Effective magnetic moment *vs.* temperature graph.

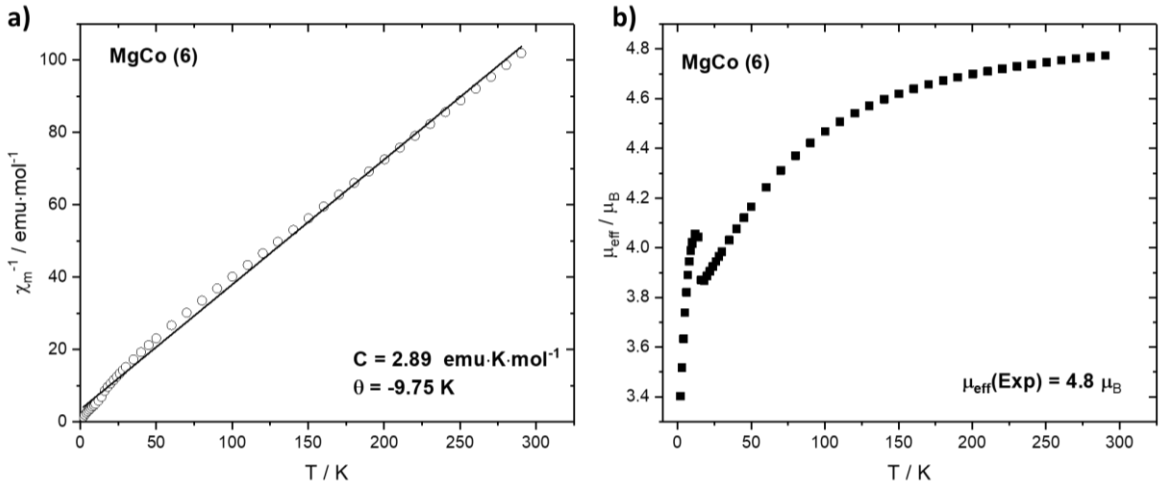


Figure A.4. Magnetic data for complex **6** (MgCo) a) Inverse of molar susceptibility *vs*. temperature, ∘ experimental data, – fitting of the curve. b) Effective magnetic moment *vs.* temperature graph.

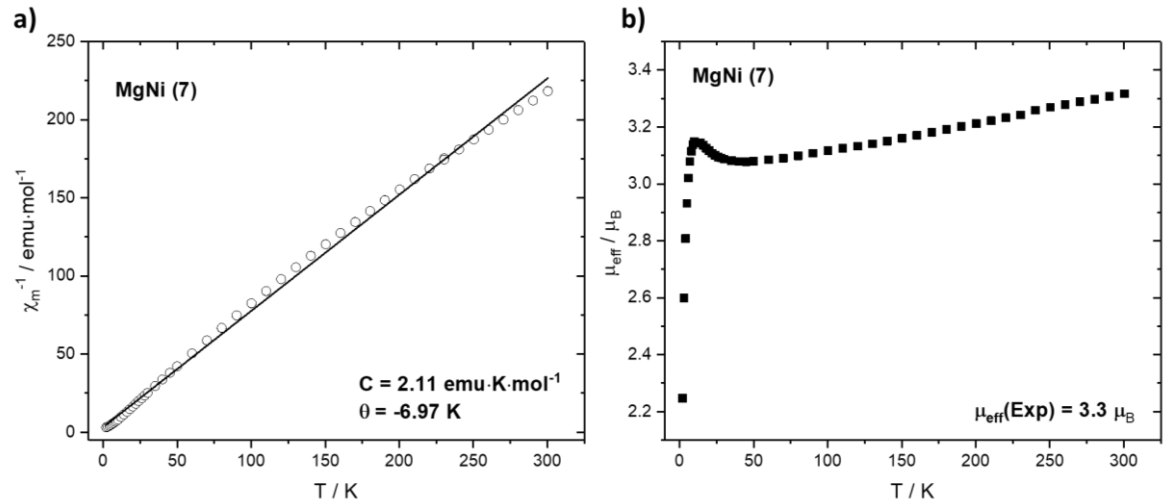


Figure A.5. Magnetic data for complex **7** (MgNi) a) Inverse of molar susceptibility *vs*. temperature, ∘ experimental data, – fitting of the curve. b) Effective magnetic moment *vs.* temperature graph.

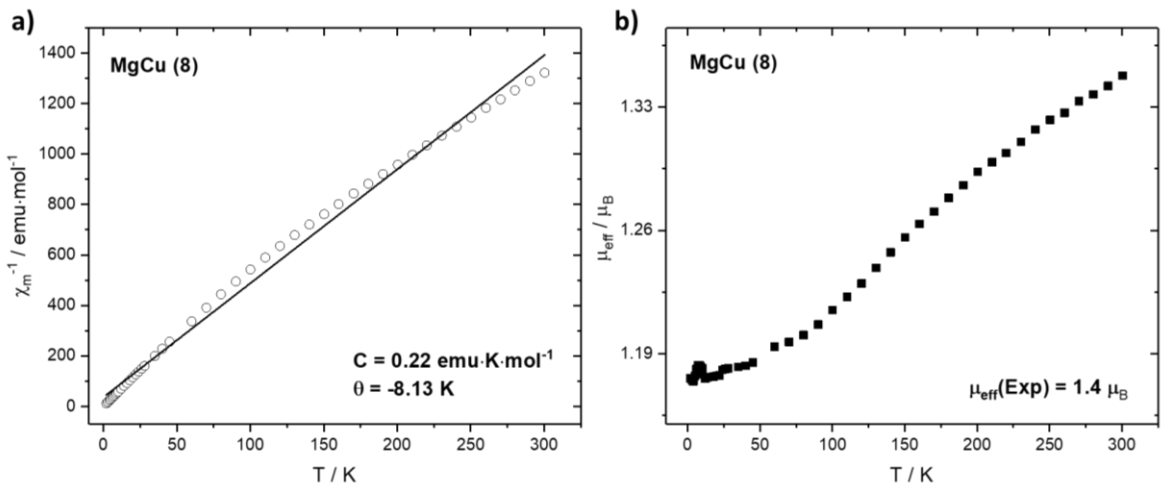


Figure A.6. Magnetic data for complex **8** (MgCu) a) Inverse of molar susceptibility *vs*. temperature, ∘ experimental data, – fitting of the curve. b) Effective magnetic moment *vs.* temperature graph.

Table A.1. Diamagnetic correction calculated for the ligand macrocycle.[1]

	$\chi_{diamagnetic}$		Total
2 O	2 x (-4.60x10^{-6})	=	-9.2x10^{-6}
4 N	4 x (-4.61x10^{-6})	=	-18.44x10^{-6}
12 C_{ring}	12 x (-6.24x10^{-6})	=	-74.88x10^{-6}
22 C	22 x (-6.00x10^{-6})	=	-132x10^{-6}
60 H	60 x (-2.93x10^{-6})	=	-175.8x10^{-6}
2 Benzene	2 x (-1.4x10^{-6})	=	-2.8x10^{-6}
Total (ligand)		=	-413.12x10^{-6} emu mol^{-1}

Table A.2. Other diamagnetic constants used in this work.[1]

	$\chi_{diamagnetic}$ (emu mol^{-1})		$\chi_{diamagnetic}$ (emu mol^{-1})
(-OAc)	-31.5x10^{-6}	**Fe(III)**	-10x10^{-6}
Mg(II)	-5x10^{-6}	**Co(II)**	-12x10^{-6}
Cr(II)	-15x10^{-6}	**Ni(II)**	-12x10^{-6}
Mn(II)	-14x10^{-6}	**Cu(II)**	-11x10^{-6}
Fe(II)	-13x10^{-6}		

Table A.3. Diamagnetic correction values for complexes **3**–**10**.

Complex	Formula	$\chi_{diamagnetic}$ (emu mol^{-1})
3	$C_{38}H_{60}MgCrN_4O_6$	496.12 x10^{-6}
4	$C_{38}H_{60}MgMnN_4O_6$	495.12 x10^{-6}
5	$C_{38}H_{60}MgFeN_4O_6$	494.12 x10^{-6}
6	$C_{38}H_{60}MgCoN_4O_6$	493.12 x10^{-6}
7	$C_{38}H_{60}MgNiN_4O_6$	493.12 x10^{-6}
8	$C_{38}H_{60}MgCuN_4O_6$	492.12 x10^{-6}
9	$C_{38}H_{60}Fe_2N_4O_6$	502.12 x10^{-6}
10	$C_{40}H_{63}Fe_2N_4O_8$	530.62 x10^{-6}

7.1.2. ROCOP of CO_2 and CHO

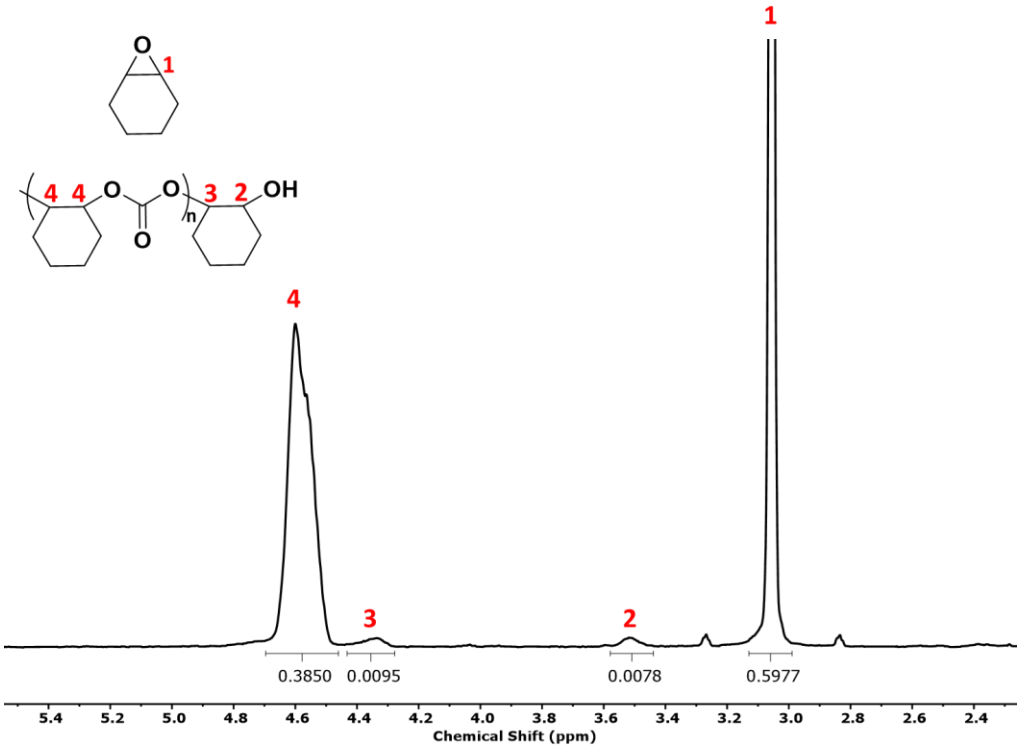


Figure A.7. ^{1}H NMR spectrum of a crude reaction mixture for one of the runs of the ROCOP of CO_2 and CHO with MgFe catalyst.

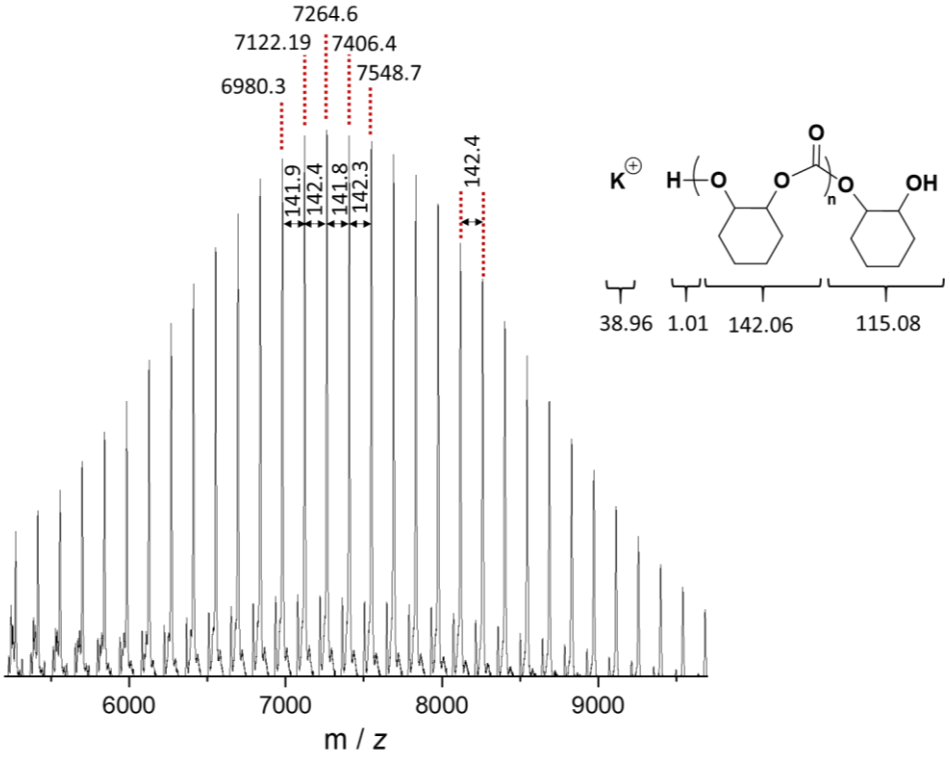


Figure A.8. MALDI-ToF spectrum of isolated polymer from one of the runs of the ROCOP of CO_2 and CHO with MgFe catalyst.

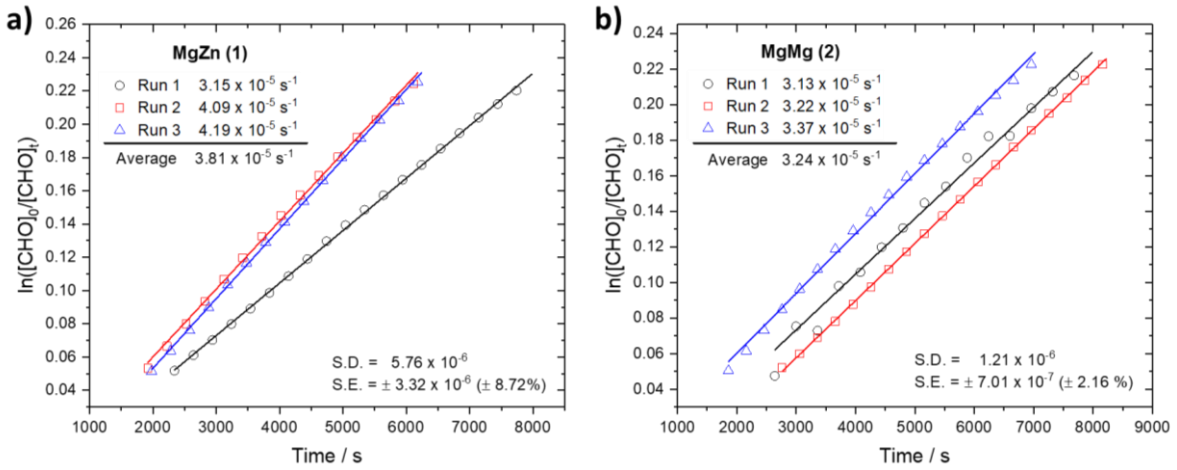


Figure A.9. Logarithm of epoxide concentration vs. time for three ROCOP runs with a) MgZn (**1**) (For clarity, every 5th data point is shown) and b) MgMg (**2**) (For clarity, every 5th data point is shown). Reaction conditions: CHO:CHD:Cat = 4000:20:1, 100°C.

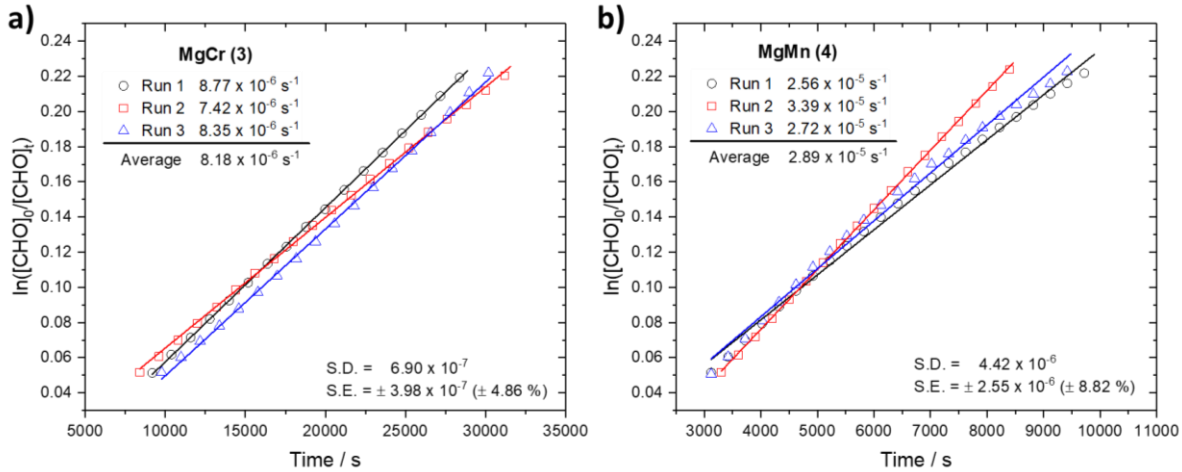


Figure A.10. Logarithm of epoxide concentration vs. time for three ROCOP runs with a) MgCr (**3**) (For clarity, every 20th data point is shown) and b) MgMn (**4**) (For clarity, every 5th data point is shown). Reaction conditions: CHO:CHD:Cat = 4000:20:1, 100°C.

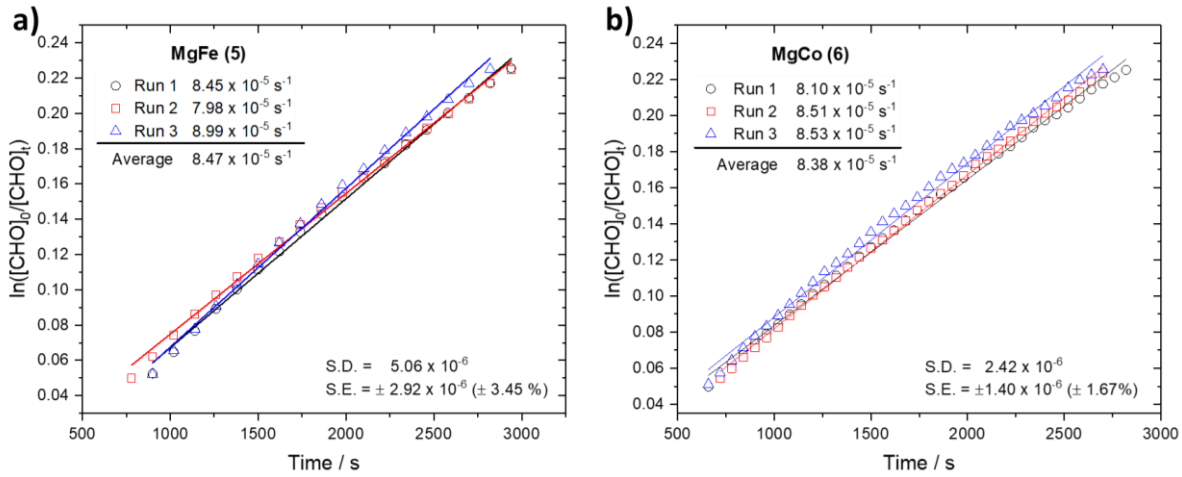


Figure A.11. Logarithm of epoxide concentration vs. time for three ROCOP runs with a) MgFe (**5**) (For clarity, every 2nd data point is shown). and b) MgCo (**6**). Reaction conditions: CHO:CHD:Cat = 4000:20:1, 100°C.

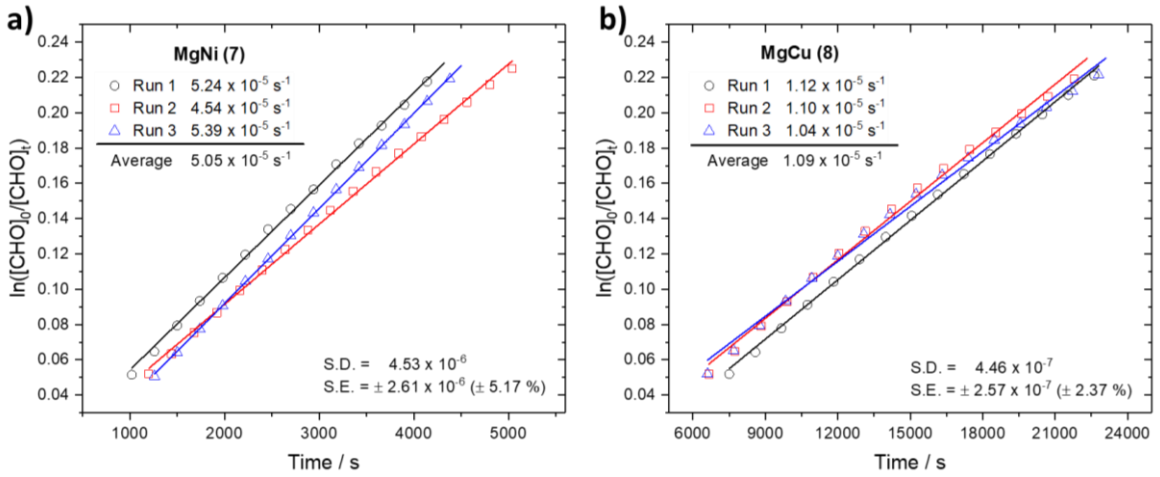


Figure A.12. Logarithm of epoxide concentration vs. time for three ROCOP runs with a) MgNi (**7**) (For clarity, every 4th data point is shown) and b) MgCu (**8**). (For clarity, every 18th data point is shown). Reaction conditions: CHO:CHD:Cat = 4000:20:1, 100°C.

7.1.2. ROCOP of CO_2 and alternative epoxides

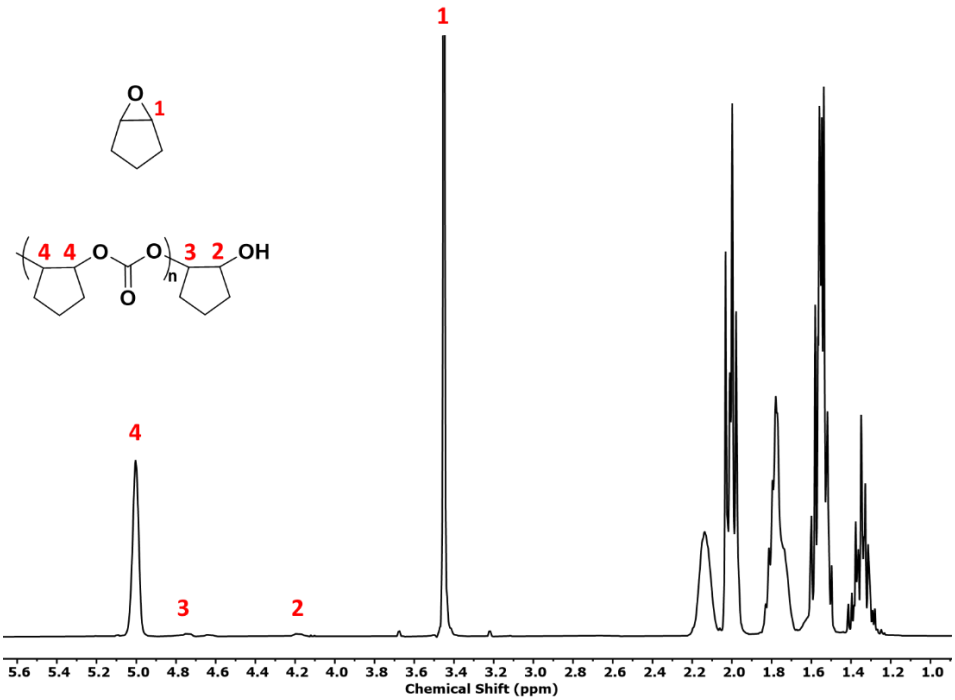


Figure A.13. ^{1}H NMR spectrum of a crude reaction mixture for the ROCOP of CO_2 and CPO with MgCo catalyst.

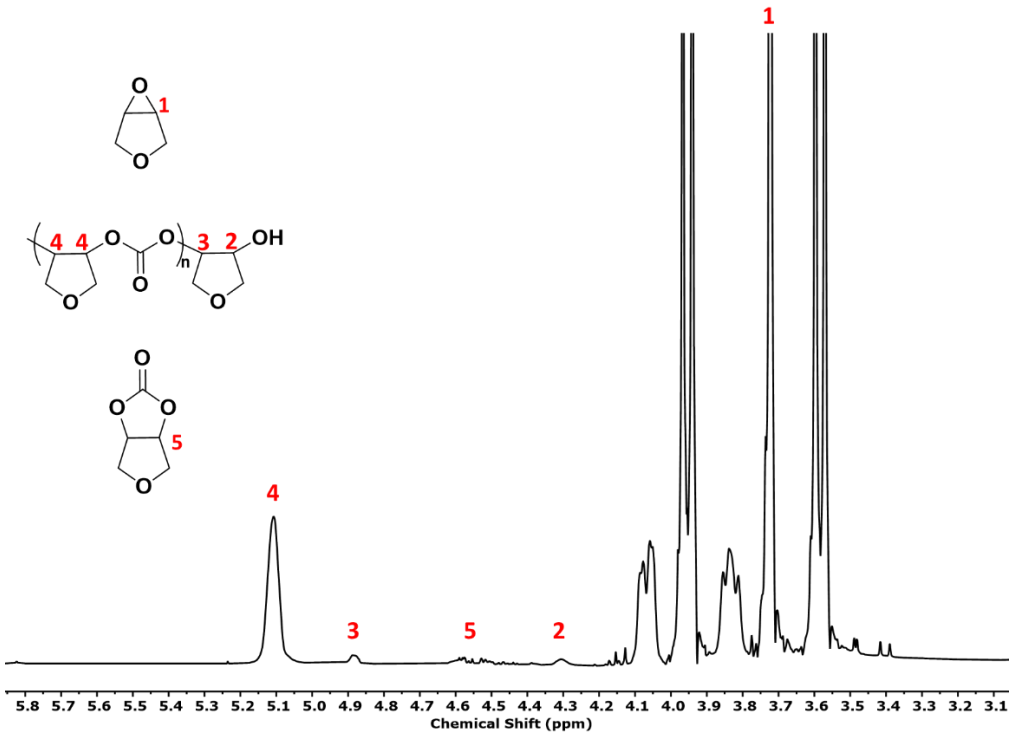


Figure A.14. ^{1}H NMR spectrum of a crude reaction mixture for the ROCOP of CO_2 and ETHF with MgCo catalyst.

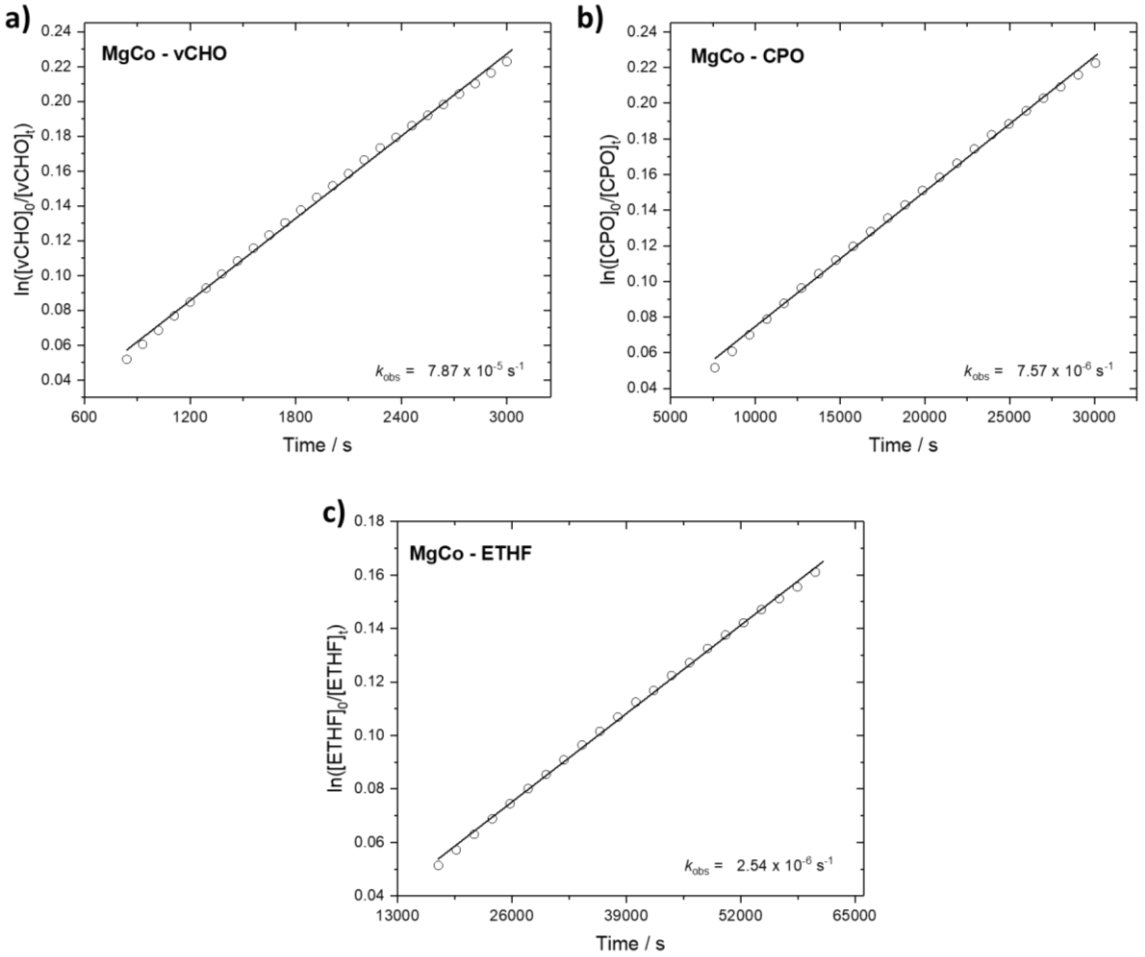


Figure A.15. Logarithm of epoxide concentration vs. time for ROCOP of epoxides/CO_2 using MgCo. a) vCHO/CO_2, Reaction conditions: vCHO:CHD:Cat = 3100:20:1, 100°C (5–20% conversion – For clarity, every 3rd data point is shown); b) CPO/CO_2, CPO:CHD:Cat = 4600:20:1, 80 °C (5–20% conversion – For clarity, every 17th data point is shown) and c) ETHF/CO_2, ETHF:CHD:Cat = 5800:20:1, 80 °C (3–15% conversion – For clarity, every 34th data point is shown)

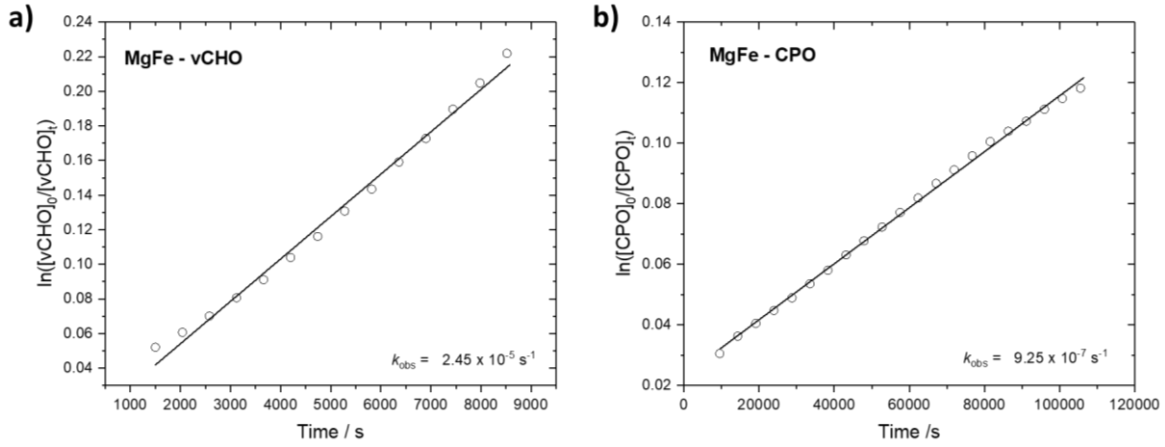


Figure A.16. Logarithm of epoxide concentration vs. time for ROCOP of epoxides/CO_2 using MgFe. a) vCHO/CO_2, reaction conditions: vCHO:CHD:Cat = 3100:20:1, 100°C (5–20% conversion – For clarity, every 9th data point is shown); b) CPO/CO_2, reaction conditions: CPO:CHD:Cat = 4600:20:1, 80 °C (3–12% conversion – For clarity, every 80th data point is shown).

7.1.3. GPC

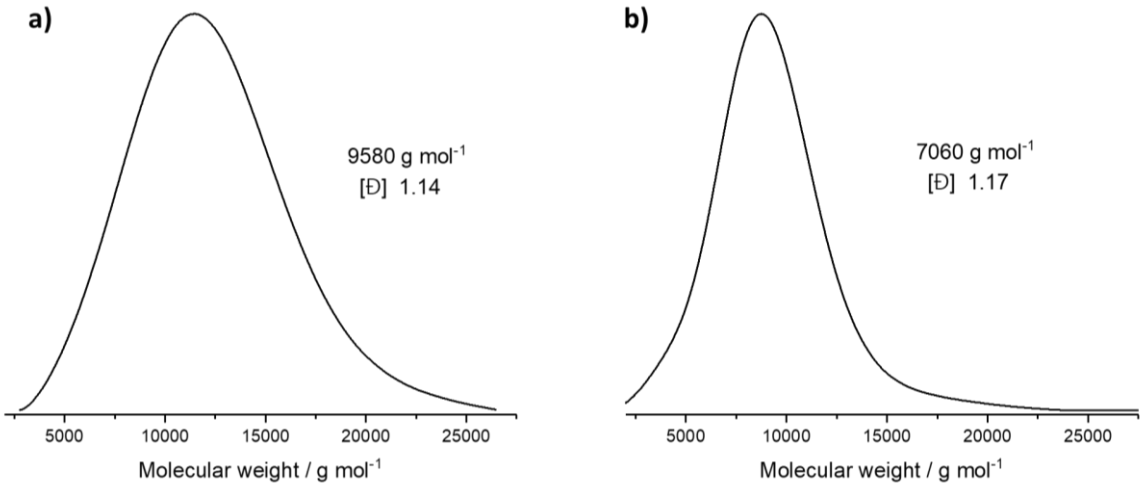


Figure A.17. GPC traces for a) vCHO/CO_2 and b) CPO/CO_2 copolymerisation with MgCo.

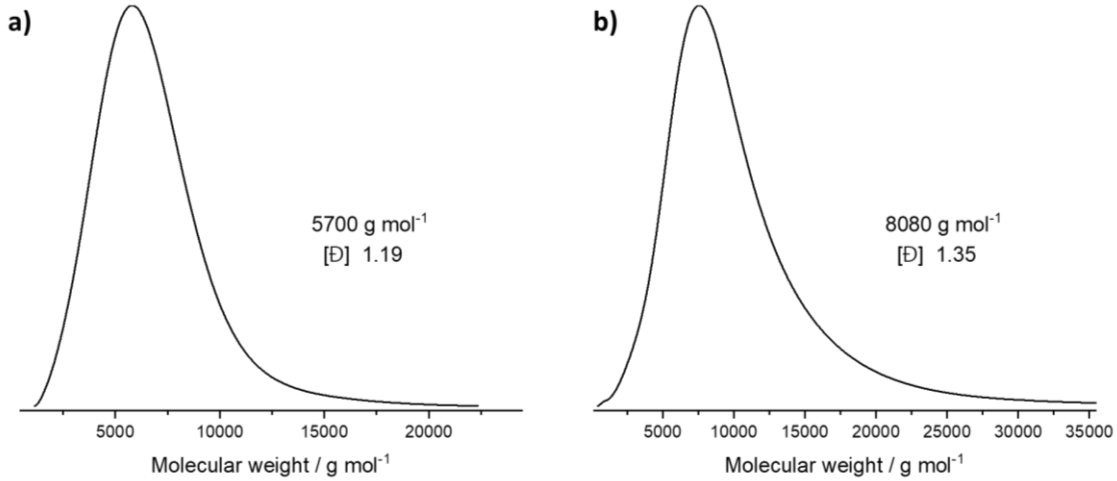


Figure A.18. GPC traces for a) vCHO/CO_2 and b) CPO/CO_2 copolymerisation with MgFe.

7.1.3. ROCOP of NA and CHO

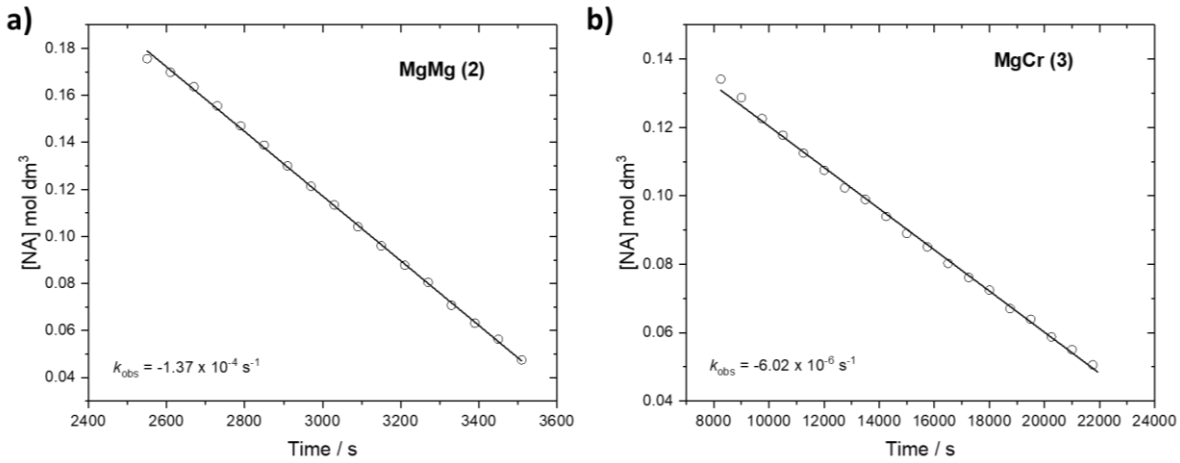


Figure A.19. Concentration vs. time plots (30–80% conversion) for the ROCOP of NA and CHO using a) MgMg (**2**) (For clarity, every 2nd data point is shown) and b) MgCr (**3**) (For clarity, every 25th data point is shown). Reaction conditions: CHO:NA:CHD:Cat = 4000:100:20:1, 100 °C.

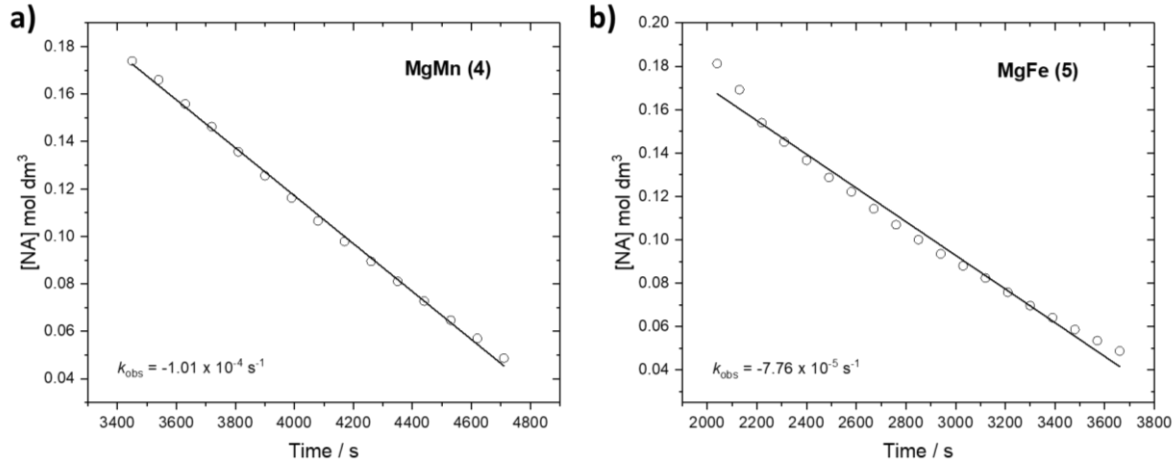


Figure A.20. Concentration vs. time plots (30–80% conversion) for the ROCOP of NA and CHO using a) MgMn (**4**) (For clarity, every 3rd data point is shown) and b) MgFe (**5**) (For clarity, every 3rd data point is shown). Reaction conditions: CHO:NA:CHD:Cat = 4000:100:20:1, 100 °C.

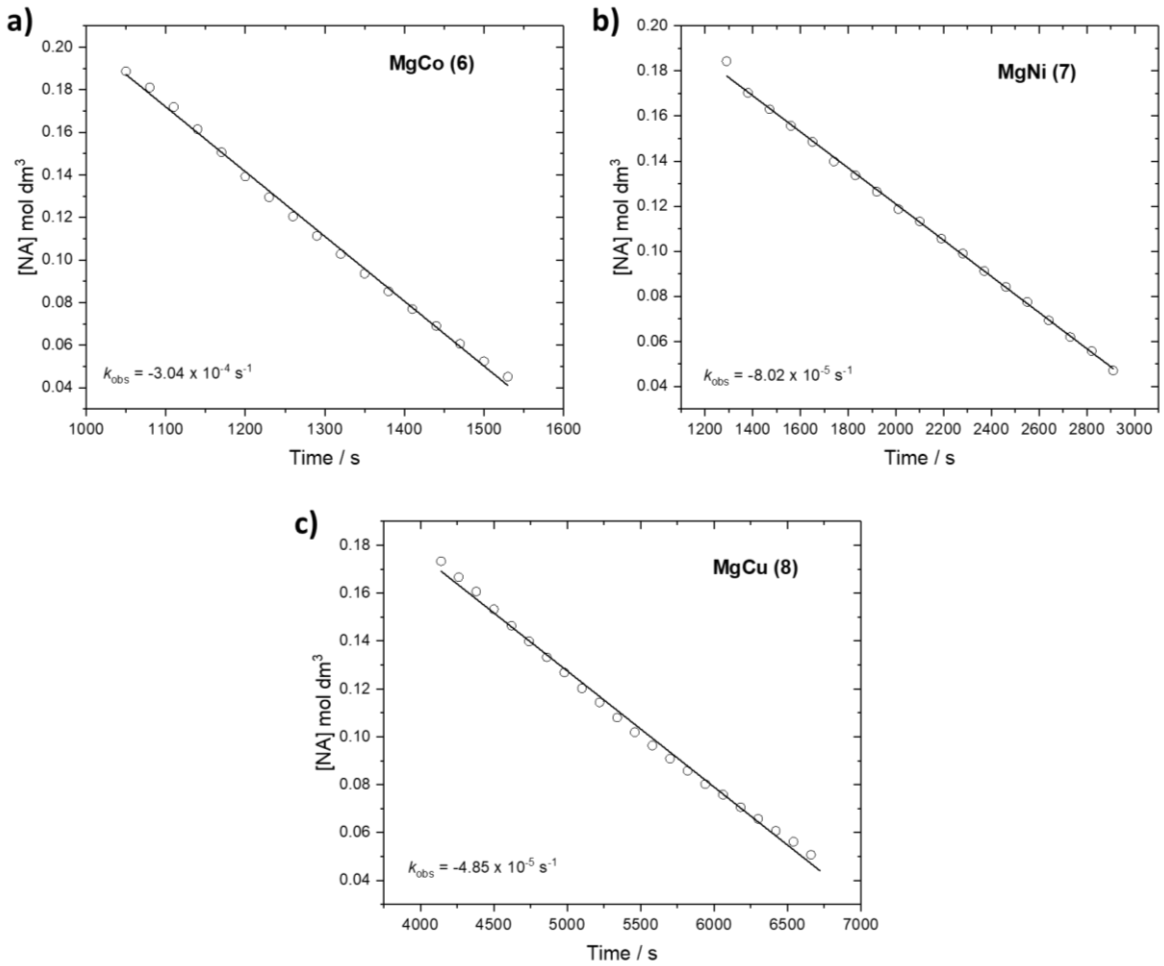


Figure A.21. Concentration vs. time plots (30–80% conversion) for the ROCOP of NA and CHO using a) MgCo (**6**); b) MgNi (**7**) (For clarity, every 3rd data point is shown) and c) MgCu (**8**) (For clarity, every 2nd data point is shown). Reaction conditions: CHO:NA:CHD:Cat = 4000:100:20:1, 100 °C.

7.1.4. X-Ray Crystallography

Table A.4. Summary of crystallographic refinement for complexes MgFe (**5**) and MgNi (**7**).

Compound	**[LMgFe(OAc)$_2$]**	**[LMgNi(OAc)$_2$H$_2$O]·Tol**
Chemical Formula	$C_{37.98}H_{60}Fe_{0.67}Mg_{1.3}N_4O_{6.65}$	$C_{47.5}H_{70}N_5O_{7.5}Mg_{1.25}Ni_{1.25}$
Formula weight	747.89	934.86
T (°C)	150.0(2)	150(2)
Crystal system	Monoclinic	Monoclinic
Space group	I2/a	$P2_1/c$
a (Å)	12.7301(5)	15.8872(2)
b (Å)	31.128(3)	16.18380(10)
c (Å)	20.5420(12)	36.3194(2)
α (°)	90	90
β (°)	91.990(5)	92.2320(10)
γ (°)	90	90
Volume (Å^3)	8135.2(9)	9331.19(14)
Z	8	8
ρ_{calcd} (g cm^{-3})	1.221	1.331
μ (mm^{-1})	2.644	1.322
2Θ range for data collection (°)	7.506 to 157.018	7.254 to 152.406
Reflections collected	47757	53417
Radiation	CuKα (λ = 1.54184)	CuKα (λ = 1.54184)
R_1(obs) [a]	0.1445	0.0573
wR_2(all)[b]	0.3018	0.1254
Goodness-of-fit on F^2	1.055	1.023
Largest diff. peak and hole (e Å^{-3})	0.43/-0.63	0.93/-0.56

- Bond lengths and angles for complex MgFe (**5**)

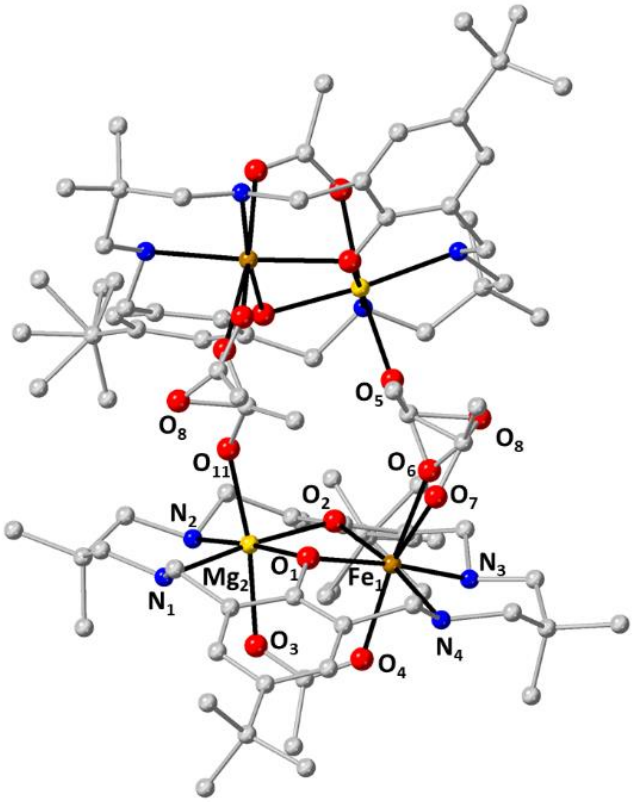


Table A.5. Key bond lengths for complex MgFe (**5**).

Bond	Bond Length (Å)	Bond	Bond Length (Å)
Fe01–Mg02	3.0083(17)	Mg02–O3	2.144(3)
Fe01–O4	2.137(3)	Mg02–O1	2.048(5)
Fe01–O1	2.103(4)	Mg02–O2	2.087(3)
Fe01–O2	2.069(5)	Mg02–N1	2.169(4)
Fe01–N3	2.175(4)	Mg02–N2	2.181(6)
Fe01–N4	2.153(7)		
Fe01–O7	2.034(7)		

Table A.6. Selected angles for MgFe (**5**).

Bond	Bond Angle (°)	Bond	Bond Angle (°)
O4–Fe01–Mg02	78.72(9)	O1–Mg02–N2	173.44(19)
O4–Fe01–N3	84.69(15)	O2–Mg02–Fe01	43.39(13)
O4–Fe01–N4	80.3(2)	O2–Mg02–O3	94.65(14)
O1–Fe01–Mg02	42.84(13)	O2–Mg02–N1	174.93(15)
O1–Fe01–O4	88.31(13)	O2–Mg02–N2	92.05(19)
O1–Fe01–N3	171.62(17)	N1–Mg02–Fe01	133.22(14)
O1–Fe01–N4	91.70(19)	N1–Mg02–N2	89.40(17)

O2–Fe01–Mg02	43.86(10)	N2–Mg02–Fe01	130.95(14)
O2–Fe01–O4	92.57(15)	C23–O4–Fe01	124.6(3)
O2–Fe01–O1	84.02(17)	C23–O3–Mg02	123.4(3)
O2–Fe01–N3	91.69(19)	Mg02–O1–Fe01	92.88(19)
O2–Fe01–N4	171.8(2)	C1–O1–Fe01	125.3(3)
N3–Fe01–Mg02	130.67(16)	C1–O1–Mg02	124.9(3)
N4–Fe01–Mg02	129.79(15)	Fe01–O2–Mg02	92.75(18)
N4–Fe01–N3	91.6(2)	C12–O2–Fe01	125.7(3)
O7–Fe01–Mg02	115.3(2)	C12–O2–Mg02	125.6(4)
O7–Fe01–O4	156.0(3)	C7–N1–Mg02	108.9(3)
O7–Fe01–O1	90.2(2)	C8–N1–Mg02	118.4(3)
O7–Fe01–O2	111.1(3)	C8–N1–C7	110.3(4)
O7–Fe01–N3	98.1(2)	C18–N3–Fe01	108.6(3)
O7–Fe01–N4	75.8(3)	C19–N3–Fe01	115.1(4)
O3–Mg02–Fe01	80.11(10)	C19–N3–C18	109.9(5)
O3–Mg02–N1	80.60(13)	C10–N2–Mg02	116.2(5)
O3–Mg02–N2	85.98(19)	C10–N2–C11	107.4(4)
O1–Mg02–Fe01	44.28(10)	C11–N2–Mg02	106.8(5)
O1–Mg02–O3	88.44(15)	C21–N4–Fe01	116.0(6)
O1–Mg02–O2	84.95(18)	C21–N4–C22	109.6(5)
O1–Mg02–N1	93.11(17)	C22–N4–Fe01	109.1(5)

- Bond lengths and angles for complex MgNi (**7**)

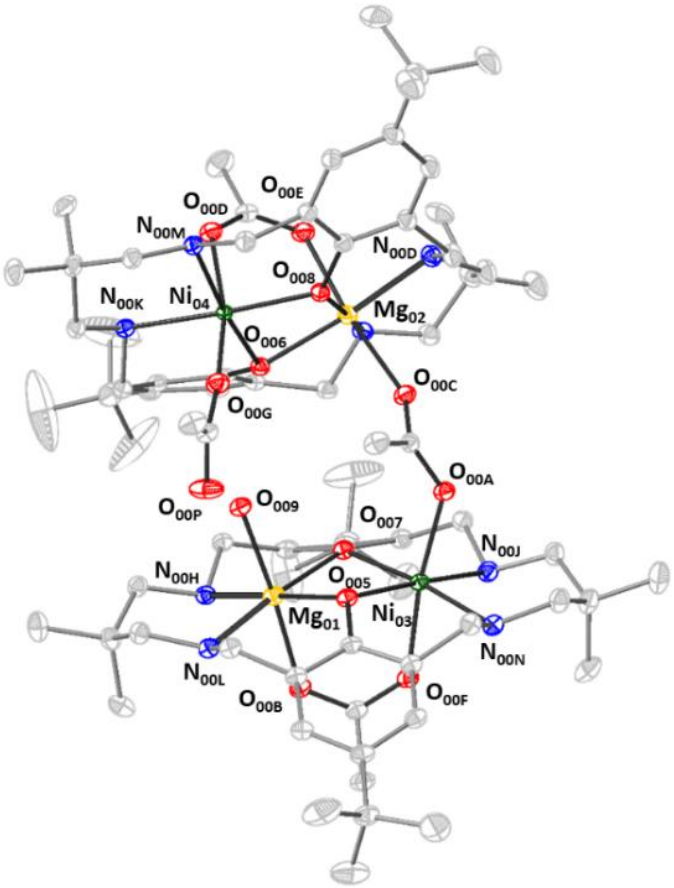


Table A.6. Selected bond lengths for complex MgNi (**7**).

Bond	Bond Length (Å)	Bond	Bond Length (Å)
Mg01–Ni03	3.0413(5)	Ni03–O00A	2.0545(13)
Mg01–O005	2.0988(13)	Ni03–O00F	2.1082(13)
Mg01–O007	2.0655(13)	Ni03–N00J	2.1404(16)
Mg01–O009	2.0783(12)	Ni03–N00N	2.1455(16)
Mg01–O00B	2.0874(12)	Ni04–O006	2.0954(12)
Mg01–N00H	2.1175(16)	Ni04–O008	2.0559(13)
Mg01–N00L	2.1168(16)	Ni04–O00D	2.1075(14)
Mg02–N00O	2.1280(16)	Ni04–O00G	2.0293(15)
Ni03–O005	2.0872(13)	Ni04–N00K	2.1598(16)
Ni03–O007	2.0673(13)	Ni04–N00M	2.1789(15)

Table A.7. Selected angles for MgNi (**7**).

Bond	Bond Angle (°)	Bond	Bond Angle (°)
O005–Mg01–Ni03	43.25(3)	O007–Ni03–N00N	173.86(6)
O005–Mg01–N00H	175.21(5)	O00A–Ni03–Mg01	109.66(4)

O005–Mg01–N00L	93.16(6)	O00A–Ni03–O005	96.65(5)
O007–Mg01–Ni03	42.64(4)	O00A–Ni03–O007	93.69(5)
O007–Mg01–O005	82.74(5)	O00A–Ni03–O00F	172.16(6)
O007–Mg01–O009	89.70(5)	O00A–Ni03–N00J	88.18(6)
O007–Mg01–O00B	94.60(5)	O00A–Ni03–N00N	91.90(6)
O007–Mg01–N00H	93.51(5)	O00F–Ni03–Mg01	78.07(4)
O007–Mg01–N00L	174.74(6)	O00F–Ni03–N00J	87.44(6)
O009–Mg01–Ni03	104.12(4)	O00F–Ni03–N00N	81.55(6)
O009–Mg01–O005	92.42(5)	N00J–Ni03–Mg01	131.46(5)
O009–Mg01–O00B	175.56(6)	N00J–Ni03–N00N	89.30(6)
O009–Mg01–N00H	90.53(6)	N00N–Ni03–Mg01	132.59(5)
O009–Mg01–N00L	93.78(6)	O006–Ni04–Mg02	44.01(4)
O00B–Mg01–Ni03	79.88(4)	O006–Ni04–O00D	90.86(5)
O00B–Mg01–O005	89.24(5)	O006–Ni04–N00K	93.04(5)
O00B–Mg01–N00H	88.09(5)	O006–Ni04–N00M	172.39(6)
O00B–Mg01–N00L	82.01(6)	O008–Ni04–Mg02	43.43(4)
N00H–Mg01–Ni03	132.22(4)	O008–Ni04–O006	83.60(5)
N00L–Mg01–Ni03	132.39(4)	O008–Ni04–O00D	93.66(6)
N00L–Mg01–N00H	90.40(6)	O008–Ni04–N00K	173.15(6)
O006–Mg02–Ni04	43.68(3)	O008–Ni04–N00M	92.53(5)
O006–Mg02–N00I	93.41(5)	O00D–Ni04–Mg02	78.87(4)
O006–Mg02–N00O	173.85(6)	O00D–Ni04–N00K	80.39(6)
O008–Mg02–Ni04	42.57(4)	O00D–Ni04–N00M	82.83(6)
O008–Mg02–O006	82.48(5)	O00G–Ni04–Mg02	114.29(4)
O008–Mg02–O00E	91.97(5)	O00G–Ni04–O006	98.89(6)
O008–Mg02–N00I	171.43(6)	O00G–Ni04–O008	96.17(6)
O008–Mg02–N00O	92.24(6)	O00G–Ni04–O00D	166.84(6)
O00C–Mg02–Ni04	114.42(4)	O00G–Ni04–N00K	90.23(6)
O00C–Mg02–O006	94.84(5)	O00G–Ni04–N00M	88.02(6)
O00C–Mg02–O008	100.95(5)	N00K–Ni04–Mg02	131.17(5)
O00C–Mg02–O00E	165.92(6)	N00K–Ni04–N00M	90.10(6)
O00C–Mg02–N00I	86.85(6)	N00M–Ni04–Mg02	129.90(5)
O00C–Mg02–N00O	89.24(6)	Ni03–O005–Mg01	93.19(5)
O00E–Mg02–Ni04	78.97(4)	C00S–O005–Mg01	121.73(11)
O00E–Mg02–O006	92.35(5)	C00S–O005–Ni03	121.18(11)
O00E–Mg02–N00I	80.64(6)	Ni04–O006–Mg02	92.31(5)
O00E–Mg02–N00O	84.65(6)	C00Q–O006–Mg02	121.84(11)
N00I–Mg02–Ni04	130.70(5)	C00Q–O006–Ni04	121.23(10)
N00O–Mg02–Ni04	130.27(5)	Mg01–O007–Ni03	94.77(5)
N00O–Mg02–N00I	91.40(6)	C00R–O007–Mg01	124.02(11)
O005–Ni03–Mg01	43.55(4)	C00R–O007–Ni03	124.20(11)

O005–Ni03–O00F	88.13(5)	Ni04–O008–Mg02	94.00(5)
O005–Ni03–N00J	174.12(6)	C015–O008–Mg02	124.16(11)
O005–Ni03–N00N	93.86(6)	C015–O008–Ni04	126.22(11)
O007–Ni03–Mg01	42.59(4)	C00W–O00A–Ni03	131.63(12)
O007–Ni03–O005	82.99(5)	C00U–O00B–Mg01	124.15(12)
O007–Ni03–O00F	93.06(5)	C00W–O00C–Mg02	141.63(12)
O007–Ni03–N00J	93.40(6)	C01F–O00D–Ni04	127.64(12)
C00U–O00F–Ni03	125.51(11)	C01F–O00E–Mg02	127.91(13)

7.2. Chapter 4

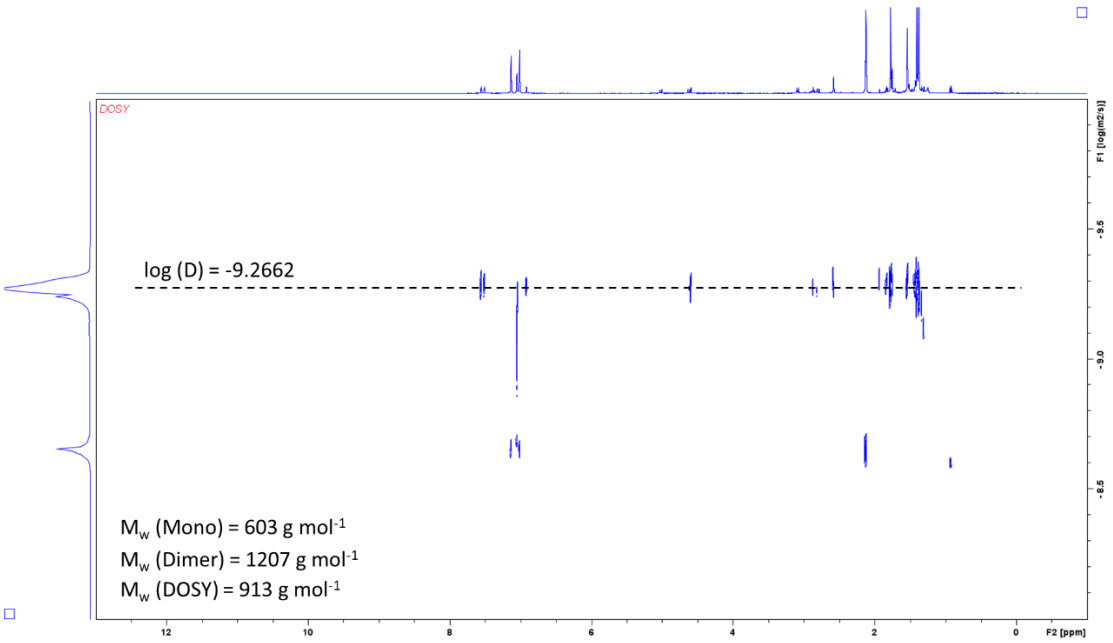


Figure A.22. ^{1}H DOSY NMR spectrum of complex $^{Et}L_{tBu}ScCl$ in Toluene-d_8, 298 K.

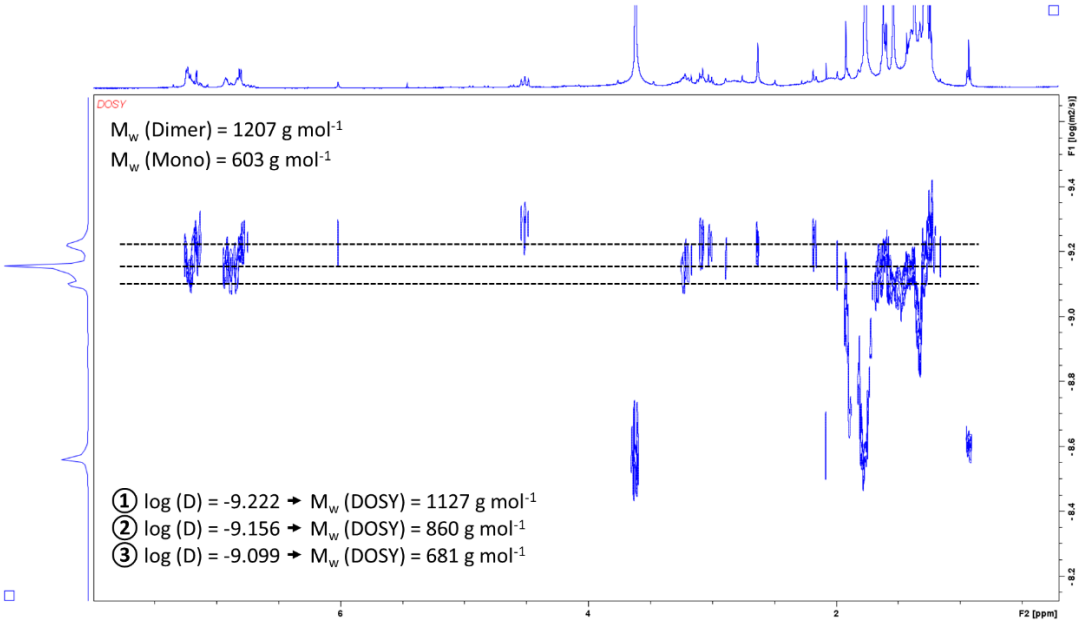
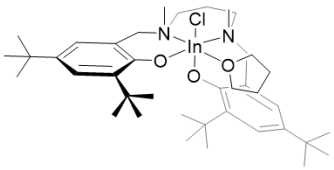
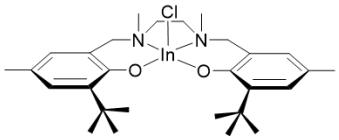


Figure A.23. ^{1}H DOSY NMR spectrum of complex $^{Et}L_{tBu}ScCl$ in THF-d_8, 298 K.

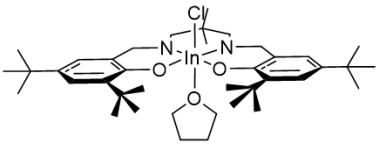
7.2.1. X-Ray Crystallography



$^{Pr}L_{tBu}InCl$



$^{Et}L_{Me}InCl$



$^{MePr\text{-}a}L_{tBu}InCl$

Table A.8. Summary of crystallographic refinement for complexes $^{Pr}L_{tBu}InCl$, $^{Et}L_{Me}InCl$ and $^{MePr\text{-}a}L_{tBu}InCl$.

Compound	$^{Pr}L_{tBu}InCl$	$^{Et}L_{Me}InCl$	$^{MePr\text{-}a}L_{tBu}InCl$
Chemical Formula	$C_{35}H_{56}ClInN_2O_2$	$C_{29}H_{45}ClInN_2O_2$	$C_{51}H_{84.39}ClInN_2O_6$
Formula weight	687.08	603.94	971.86
T (°C)	150.0(10)	150.01(10)	150.01(10)
Crystal system	Triclinic	Monoclinic	Monoclinic
Space group	P-1	$P2_1/n$	$P2_1/c$
a (Å)	11.8292(3)	14.1497(2)	16.8268(2)
b (Å)	14.0696(3)	15.5092(2)	26.4404(2)
c (Å)	15.5258(3)	17.9884(3)	11.83120(10)
α (°)	97.601(2)	90	90
β (°)	108.798(2)	108.147(2)	98.0290(10)
γ (°)	94.925(2)	90	90
Volume (Å^3)	2401.83(10)	3751.21(10)	5212.19(9)
Z	3	4	4
ρ_{calcd} (g cm^{-3})	1.425	1.604	1.238
μ (mm^{-1})	6.917	8.770	4.455
2Θ range for data collection (°)	6.102 to 154.45	6.984 to 153.448	5.304 to 154.612
Reflections collected	44627	34926	37698
Radiation	CuKα (λ = 1.54184)	CuKα (λ = 1.54184)	CuKα (λ = 1.54184)
R_1(obs) [a]	0.0624	0.0418	0.0716
wR_2(all)[b]	0.1843	0.0722	0.1811
Goodness-of-fit on F^2	1.111	1.008	1.068
Largest diff. peak and hole (e Å^{-3})	4.03/-0.72	0.50/-0.54	1.76/-0.64

- Bond lengths and angles for complex $^{Pr}L_{tBu}InCl$

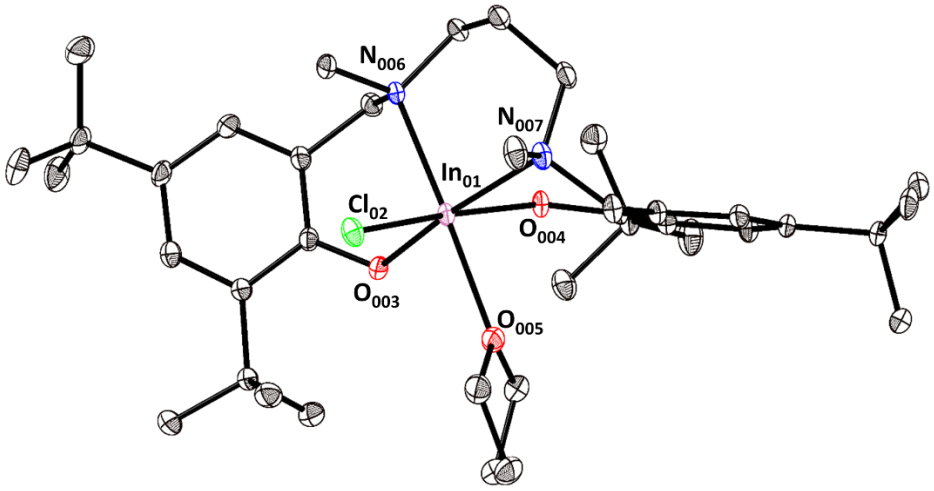


Table A.9. Key bond lengths for complex $^{Pr}L_{tBu}InCl$.

Bond	Bond Length (Å)	Bond	Bond Length (Å)
In01–Cl02	2.4259(10)	In01–O005	2.292(3)
In01–O003	2.097(3)	In01–N006	2.308(3)
In01–O004	2.086(3)	In01–N007	2.369(3)

Table A.10. Selected angles for complex $^{Pr}L_{tBu}InCl$.

Bond	Bond Angle (°)	Bond	Bond Angle (°)
O003–In01–Cl02	97.49(9)	O004–In01–N007	80.24(11)
O003–In01–O005	85.82(11)	O005–In01–Cl02	88.51(9)
O003–In01–N006	89.25(12)	O005–In01–N006	174.71(12)
O003–In01–N007	169.72(12)	O005–In01–N007	92.21(12)
O004–In01–Cl02	170.91(8)	N006–In01–Cl02	94.03(9)
O004–In01–O003	89.55(11)	N006–In01–N007	92.31(12)
O004–In01–O005	86.26(11)	N007–In01–Cl02	92.54(9)
O004–In01–N006	91.80(12)		

- Bond lengths and angles for complex $^{Et}L_{Me}InCl$

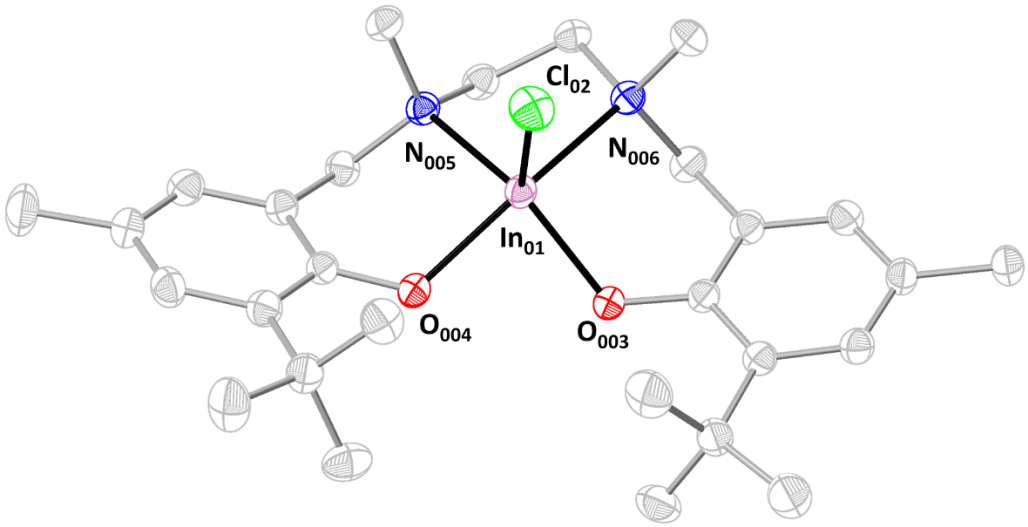


Table A.11. Key bond lengths for complex $^{Pr}L_{tBu}InCl$.

Bond	Bond Length (Å)	Bond	Bond Length (Å)
In01–Cl02	2.3661(6)	In01–N005	2.2743(19)
In01–O003	2.0447(16)	In01–N006	2.349(2)
In01–O004	2.0672(17)		

Table A.12. Selected angles for complex $^{Pr}L_{tBu}InCl$.

Bond	Bond Angle (°)	Bond	Bond Angle (°)
O003–In01–Cl02	118.86(5)	O004–In01–N005	86.79(7)
O003–In01–O004	86.09(6)	O004–In01–N006	152.99(7)
O003–In01–N005	132.78(7)	N005–In01–Cl02	107.53(5)
O003–In01–N006	87.76(7)	N005–In01–N006	78.26(7)
O004–In01–Cl02	109.30(5)	N006–In01–Cl02	96.69(5)

- Bond lengths and angles for complex $^{MePr\text{-}a}L_{tBu}InCl$

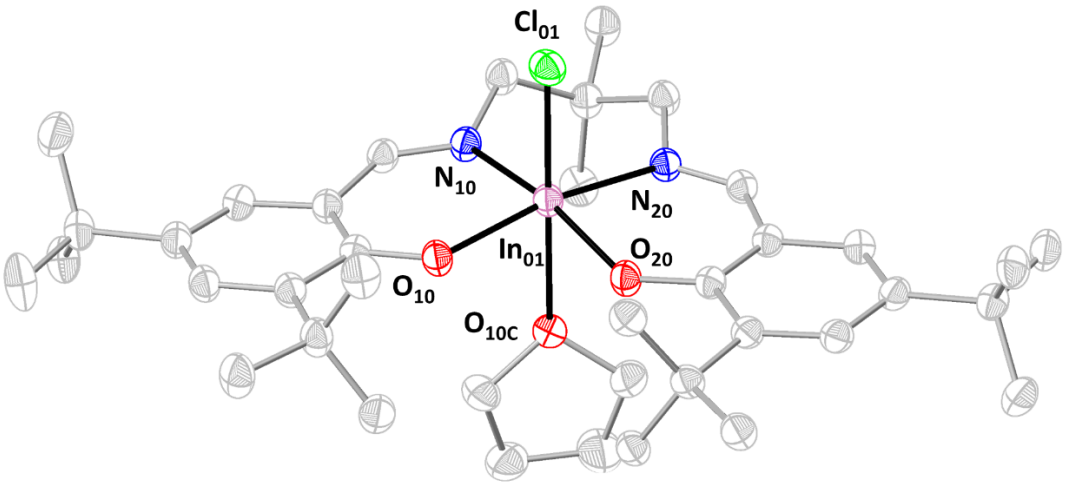


Table A.13. Key bond lengths for complex $^{MePr\text{-}a}L_{tBu}InCl$.

Bond	Bond Length (Å)	Bond	Bond Length (Å)
In1–Cl1	2.4427(11)	In1–N20	2.210(3)
In1–O10	2.069(2)	In1–N10	2.197(3)
In1–O20	2.059(3)	In1–Cl1	2.4427(11)
In1–O10C	2.449(3)		

Table A.14. Selected angles for complex $^{MePr\text{-}a}L_{tBu}InCl$.

Bond	Bond Angle (°)	Bond	Bond Angle (°)
Cl1–In1–O10C	178.64(8)	O20–In1–N20	87.64(11)
O10–In1–Cl1	99.25(9)	O20–In1–N10	165.91(12)
O10–In1–O10C	81.74(11)	N20–In1–Cl1	94.52(8)
O10–In1–N20	166.13(12)	N20–In1–O10C	84.46(11)
O10–In1–N10	87.17(10)	N10–In1–Cl1	93.35(9)
O20–In1–Cl1	100.72(9)	N10–In1–O10C	85.76(11)
O20–In1–O10	91.40(10)	N10–In1–N20	90.40(11)
O20–In1–O10C	80.16(11)		

7.3. References

1. Bain, G. A.; Berry, J. F., Diamagnetic Corrections and Pascal's Constants. *J. Chem. Edu.* **2008,** *85* (4), 532.